Technische Universität München
TUM School of Medicine and Health

Targeting of the Homeostatic Orchestrator AMPK by Drug Repurposing Exposes a Metabolic Vulnerability of PDAC Cells

Carolin Desiree Schneider

Vollständiger Abdruck der von der TUM School of Medicine and Health der Technischen Universität München zur Erlangung eines

Doctor of Philosophy (Ph.D.)

genehmigten Dissertation.

Vorsitz: Prof. Dr. Marc Schmidt-Supprian

Betreuer: Prof. Dr. Günter Schneider

Prüfende der Dissertation:

1. Prof. Dr. Maximilian Reichert
2. Prof. Dr. Oliver Krämer
3. Prof. Dr. Julia Mayerle

Die Dissertation wurde am 25.09.2023 bei der TUM School of Medicine and Health der Technischen Universität München eingereicht und durch die TUM School of Medicine and Health am 08.01.2024 angenommen.

Table of Contents

Acknowledgments

Foremost, I would like to thank Prof. Dr. Günter Schneider for granting me the opportunity to be a part of his research group and to embark on this exciting project. I am immensely thankful for the many enthusiastic and challenging discussions, for helping me to develop scientific critical thinking, and for his valuable scientific guidance.

I would also like to thank Prof. Dr. Roland Schmid and the Klinik und Poliklinik für Innere Medizin II, Klinikum rechts der Isar as well as Prof. Dr. Michael Ghadimi and the Klinik für Allgemein-, Viszeral- und Kinderchirurgie, Universitätsmedizin Göttingen for providing an excellent research environment.

Moreover, I express my sincere appreciation to the members of my thesis advisory committee Prof. Dr. Maximilan Reichert and Prof. Dr. Oliver Krämer for their continuous mentorship and expertise during my PhD journey.

My special thanks go to M.Sc. Lukas Krauß, for being an incredible support in so many ways. We made a great team, inside and outside the lab.

I owe my gratitude to Dr. Felix Orben and Dr. Constanza Tapia Contreras who performed the PDO experiments; M.Sc. Stefanie Höfer and Prof. Dr. Bernhard Küster who made it possible to perform and analyze the Kinobeads assay; Dr. Felix Schicktanz, PD Dr. Katja Steiger, and Prof. Dr. Wilko Weichert who conducted the pathological evaluation; Abdallah M. Alfayomy and Prof. Dr. Wolfgang Sippl who performed the molecular docking analysis, M.Sc. Angela Bosnakovska and Prof. Dr. Peter Rehling who helped with the Seahorse assay; Dr. Christian Schneeweis who was of fundamental help with the cloning and transduction experiments; Christin Kellner, Prof. Dr. Elisabeth Heßmann and Dr. Chiara Falcomatà who generously shared their cell line models and Dr. Maren Sitte, Dr. Gabriela Salinas-Riester, Dr. Rupert Öllinger and Prof. Dr. Roland Rad who performed the RNA-Seq experiments.

Moreover, I want to thank Franziska Génevaux, Jorina Hilbert, and B.Sc.Thorsten Richter who supported this project with a lot of dedication and hard work.

Furthermore, I thank all the members of AG Geisler, AG Grade, AG Rad, and, AG Saur for their valuable collaboration and the enriching atmosphere they have fostered throughout our work together.

Last but not least, I would like to thank my family for their constant encouragement, understanding, and belief in me which has been invaluable to my PhD journey.

List of Figures

List of Tables

Abbreviations

°C	Degrees celsius
2D	Two-dimensional
3D	Three-dimensional
53BP1	p53-binding protein 1
ABL	Abelson murine leukemia
ADP	Adenosine diphosphate
AGC	Automatic gain control
AID	Autoinhibitory domain
AMP	Adenosine monophosphate
AMPK	AMP-activated protein kinase
AMPKi	AMPK inhibitor
Å	Ångström
APS	Ammonium persulfate
ARE	Androgen receptor
ATG	Autophagy-related gene
ATP	Adenosine triphosphate
AUC	Area under curve
Axin	Axis inhibition protein
BCR	Breakpoint cluster region
BSA	Bovine serum albumin
c-NHEJ	Canonical non-homologous end joining
Ca^{2+}	Calcium
CAA	2-Chloroacetamide
CAF	Cancer-associated fibroblast
CAK	CDK-activating kinase complex
CBS	Cystathionine-beta-synthase
CBM	Carbohydrate-binding module
CDK	Cyclin-dependent kinase
ChREBP	Carbohydrate-response element-binding protein
CO_2	Carbon dioxide
CoA	Coenzyme A
CREB	Cyclic AMP response element binding protein

CPT1	Carnitine palmitoyltransferase 1
CTD	Carboxy-terminal domain
DAB	3,3′-Diaminobenzidin
ddH_2O	Double-distilled water
DMEM	Dulbecco´s Modified Eagle's Medium
DMSO	Dimethyl sulfoxide
DNA	Deoxyribonucleic acid
DRP1	Dynamin-related protein 1
DTT	Dithiothreitol
EC50	Effective concentration 50
ECAR	Extracellular acidification rate
ECM	Extracellular matrix
EDTA	Ethylenediaminetetraacetic acid
et al.	et alii
EMT	Epithelial-to-mesenchymal transition
ERK	Extracellular signal-regulated kinase
EtOH	Ethanol
FAS	Fatty acid synthase
FC	Fold change
FCS	Fetal calf serum
FDA	U.S. Food and Drug Administration
FOLFIRINOX	FOL: folinic acid/leucovorin, F: fluorouracil/5-FU, IRIN: irinotecan/Camptosar, OX: oxaliplatin/Eloxatin
FoxO	Forkhead box O
g	Gram
GLUT	Glucose transporter
GPX	Glutathione peroxidase
GSEA	Gene set enrichment analysis
GSH	Glutathione, reduced
GSSH	Glutathione, oxidized
h	Hour/s
hEGF	Human epidermal growth factor
HEK	Human embryonic kidney
HCD	High energy collisional dissociation

HPLC	High performance liquid chromatography
IHC	Immunohistochemistry
IC50	Inhibitory concentration 50
kDa	Kilodalton
KO	Knockout
l	Litre
LacZ	Beta-galactosidase
LC3	Microtubule-associated protein 1A/1B-light chain 3
LC-MS/MS	Liquid chromatography-tandem mass spectrometry
LFQ	Label-free quantification
LKB1	Liver kinase B1
Log	Logarithmic transformation
M	Molar
m, milli	Thousandth
MEK	Mitogen activated protein kinase
mg	Milligram
ml	Millilitre
mm	Millimetre
mM	Millimolar
µ, micro	Millionth
µl	Microliter
µm	Micrometre
µM	Micromolar
min	Minute
nab	Albumin-bound
NADPH	Nicotinamide adenine dinucleotide phosphate
NES	Normalized enrichment score
nM	Nanomolar
NRF2	Nuclear factor erythroid 2–related factor 2
NSCLC	Non-small-cell lung cancer
OCR	Oxygen consumption rate
OPLS	Optimized potentials for liquid simulations
P-	Phospho-
PanIN	Pancreatic intraepithelial neoplasia

PBS	Phosphate buffered saline
PCR	Polymerase chain reaction
PD-CL	Patient-derived cell line
PDAC	Pancreatic ductal adenocarcinoma
PDGF	Platelet derived growth factor
PDHc	Pyruvate dehydrogenase complex
PDO	Patient-derived organoid
PET	Positron emission tomography
PGC-1α	Peroxisome proliferator-activated receptor gamma coactivator 1-alpha
PGC-1β	Peroxisome proliferator-activated receptor gamma coactivator 1-beta
PGK	Phosphoglycerate kinase
pH	Power of hydrogen
PI3K	Phosphoinositide 3-kinase
PKA	Protein kinase A
pKd	Logarithmic transformation of dissociation constant
PROTAC	Proteolysis targeting chimera
PTM	Post-translational modification
RAF	Rapidly accelerated fibrosarcoma
RIPA	Radioimmunoprecipitation assay
RMSD	Root-mean-square deviation
RNA	Ribonucleic acid
RNA-Seq	RNA sequencing
ROS	Reactive oxygen species
rpm	Revolutions per minute
rRNA	Ribosomal RNA
RSK	Ribosomal 6 kinase
RT	Room temperature
sc	Single cell
SDS	Sodium dodecyl sulphate
sec	Seconds
Ser	Serine
sh	Short hairpin

si	Silencing
SREBP	Sterol-response element-binding protein
ss	Single sample
TAE	Tris-acetate-EDTA
TBS	TRIS buffered saline
TBS-T	TBS + Tween20
TCA	Tricarboxylic acid
TEMED	N,N,N',N'-Tetramethylethylendiamin
Thr	Threonine
TIF1A	Transcription initiation factor IA
TIP3P	Transferable intermolecular potential with 3 points
TME	Tumor microenvironment
TPM	Transcripts per kilobase million
TRIS	Tris-(hydroxymethyl)-aminomethane
TUM	Technical University of Munich
V	Volt
v/v	Volume per volume
w/v	Weight per volume

This list provides a summary of abbreviations mentioned in this thesis, including protein names not included in the section 'Human and Murine Gene Names and Symbols’.

Human and Murine Gene Names and Symbols

Human gene symbol	Murine gene symbol	Name
ACC1	*Acc1*	Acetyl-CoA carboxylase 1
ACC2	*Acc2*	Acetyl-CoA carboxylase 1
ACVR1	*Acvr1*	Activin A receptor type 1
ARMC10	*Armc10*	Armadillo repeat containing 10
ATM	*Atm*	Ataxia telangiectasia mutated
BCL2	*Bcl2*	B-cell lymphoma 2
BECN1	*BECN1*	Beclin 1
BMPR1A	*Bmpr1a*	bone morphogenetic protein receptor type 1A
BMPR1B	*Bmpr1b*	bone morphogenetic protein receptor type 1B
BRCA1	*Brca1*	Breast cancer type 1
BRCA2	*Brca2*	Breast cancer type 2
CDK1	*Cdk1*	Cyclin-dependent kinase 1
CDK4	*Cdk4*	Cyclin-dependent kinase 4
CDK6	*Cdk6*	Cyclin-dependent kinase 6
CDK7	*Cdk7*	Cyclin-dependent kinase 7
CDK16	*Cdk16*	Cyclin-dependent kinase 16
CDKN2A	*Cdkn2a*	Cyclin-dependent kinase inhibitor 2A
CDKN2B	*Cdkn2b*	Cyclin-dependent kinase inhibitor 2B
DNML1	*Dnm1l*	Dynamin 1 like
EEF2K	*Eef2k*	Eukaryotic elongation factor-2 kinase
EXO1	*Exo1*	Exonuclease 1
FASN	*Fasn*	Fatty acid synthase
FOXO1	*Foxo1*	Forkhead box O1
FOXO3	*Foxo3*	Forkhead box O3
HDAC4	*Hdac4*	Histone deacetylase 4
HDAC5	*Hdac5*	Histone deacetylase 5
HMBS	*Hmbs*	Hydroxymethylbilane synthase
HMGCR	*Hmgcr*	3-hydroxy-3-methylglutaryl-Coenzyme A reductase
HMOX1	*Hmox1*	Heme oxygenase 1
HSF1	*Hsf1*	Heat shock factor 1

IDH1	*Idh1*	Isocitrate dehydrogenase 1
KIT	*Kit*	KIT proto-oncogene receptor tyrosine kinase
KRAS	*Kras*	Kirsten rat sarcoma virus
MAPK1, ERK2	*Mapk1, Erk2*	Mitogen-activated protein kinase 1
MAPK3, ERK1	*Mapk3, Erk1*	Mitogen-activated protein kinase 3
MFF	*Mff*	Mitochondrial fission factor
MLH1	*Mlh1*	MutL homolog 1
MSH2	*Msh2*	MutS homolog 2
MSH6	*Msh6*	MutS homolog 6
MTOR	*Mtor*	Mechanistic target of rapamycin kinase
NFE2L2	*Nfe2l2*	Nuclear factor erythroid 2–like factor 2
PAK4	*Pak4*	p21-activated kinase 4
PALB2	*Palb2*	Partner and localizer of BRCA2
PARK2	*Park2*	Parkin RBR E3 ubiquitin protein ligase
PDHA1	*Pdha1*	Pyruvate dehydrogenase E1 alpha 1
PIK3C3, VPS34	*Pik3c3, Vps34*	Phosphatidylinositol 3-kinase catalytic subunit type 3
PIK3R4, VPS15	*Pik3r4, Vps15*	Phosphoinositide-3-kinase regulatory subunit 4
PINK1	*Pink1*	PTEN induced kinase 1
PPARGC1A	*Ppargc1a*	Peroxisome proliferator-activated receptor gamma coactivator 1-alpha
PPARGC1B	*Ppargc1b*	Peroxisome proliferator-activated receptor gamma coactivator 1-beta
PRKAA1	*Prkaa1*	Protein kinase AMP-activated catalytic subunit alpha 1
PRKAA2	*Prkaa2*	Protein kinase AMP-activated catalytic subunit alpha 2
PRKAB1	*Prkab1*	Protein kinase AMP-activated non-catalytic subunit beta 1
PRKAB2	*Prkab2*	Protein kinase AMP-activated non-catalytic subunit beta 2
PRKAG1	*Prkag1*	Protein kinase AMP-activated non-catalytic subunit gamma 1
PRKAG2	*Prkag2*	Protein kinase AMP-activated non-catalytic subunit gamma 2
PRSS1	*Prss1*	Protease, serine 1
PTEN	*Pten*	Phosphatase and tensin homolog
RACK1	*Rack1*	Receptor for activated C kinase 1

RPTOR	*Rptor*	Regulatory associated protein of mTOR complex 1
SKP2	*Skp2*	S-phase kinase-associated protein 2
SLC2A1	*Slc2a1*	solute carrier family 2 member 1
SLC2A4	*Slc2a4*	solute carrier family 2 member 4
SPINK1	*Spink1*	Serine peptidase inhibitor, Kazal type 1
STK11	*Stk11*	Serine/threonine kinase 11
TFE3	*Tfe3*	Transcription factor binding to IGHM enhancer
TFEB	*Tfeb*	Transcription factor EB
TP53	*Tp53*	Transformation-related protein 53
TP53BP1	*Tp53bp1*	TP53-binding protein 1
TSC2	*Tsc2*	Tuberous Sclerosis Complex 2
TWIST1	*Twist1*	Twist basic helix-loop-helix transcription factor 1
TXN	*Txn1/2*	Thioredoxin
TXNIP	*Txnip*	Thioredoxin interacting protein
ULK1	*Ulk1*	UNC-51 like kinase

This list provides a summary of the genes mentioned in this thesis, including the genes for the proteins that are mentioned when the protein is encoded by a single gene.

Abstract

Pancreatic ductal adenocarcinoma (PDAC) is a highly heterogeneous disease with immense resistance to both standard-of-care as well as experimental drugs, making it almost universally fatal.

The disease's remarkable metabolic plasticity has been identified as a key factor in its progression and drug resistance. As such, targeting metabolic regulators at the apex of the metabolic hierarchy, such as the AMP-activated protein kinase (AMPK), may hold promise for overcoming the unfavorable prognosis of PDAC. AMPK is a sophisticated metabolic gatekeeper that orchestrates the energy homeostasis in all eukaryotic cells. The presented results define a context-dependent function of AMPK in PDAC and show that the kinase may be crucial for the redox homeostasis of PDAC cells. This discovery provides opportunities for therapeutic strategies that leverage oxidative stress in combination with AMPK inhibitors (AMPKi) as an avenue to overcome drug resistance in PDAC.

Currently, available AMPK targeting compounds are often criticized for their broad-spectrum kinase inhibitory effects and are considered experimental without imminent clinical translation. To accelerate the discovery of potential AMPK inhibitors that could be fast-tracked for clinical application, a drug repurposing approach was employed. Through a comprehensive drug screen of compounds under clinical investigation, the p21-activated kinase 4 (PAK4) inhibitor PF-3758309 was identified as a potential AMPK inhibitor. Proteomic inhibitor selectivity profiling further validated that PF-3758309 binds to AMPK and further experiments showed efficient blocking of AMPK downstream signaling at nanomolar concentrations. Notably, PF-3758309 demonstrated nanomolar efficacy in cellular PDAC models across species.

The presented data provide evidence that AMPK can be inhibited by PF-3758309, thereby targeting a central metabolic orchestrator. The observed cross-species response of PDAC cells towards PF-3758309 is the basis of further development of the scaffold to a selective AMPKi and underscores the clinical relevance of drug repurposing.

Zusammenfassung

Das duktale Adenokarzinom des Pankreas (PDAC) ist eine sehr heterogene Erkrankung mit immenser Resistenz sowohl gegenüber Standardbehandlungen als auch experimentellen Medikamenten. PDAC zählt daher zu den tödlichsten Krebserkankungen der heutigen Zeit.

Die bemerkenswerte metabolische Plastizität der Krankheit wurde als Schlüsselfaktor für ihr Fortschreiten und ihre Arzneimittelresistenz identifiziert. Daher kann die Hemmung von Stoffwechselregulatoren an der Spitze der Stoffwechselhierarchie, wie z. B. AMP-aktivierte Proteinkinase (AMPK), vielversprechend sein, um die fatale Prognose von PDAC zu verbessern. AMPK ist ein ausgeklügelter metabolischer Torwächter, der die Energiehomöostase in allen eukaryotischen Zellen orchestriert. Unsere Ergebnisse definieren eine Subtyp-abhängige Funktion von AMPK in PDAC und zeigen, dass die Kinase entscheidend für die Redox-Homöostase von PDAC-Zellen ist. Diese Entdeckung bietet Möglichkeiten für therapeutische Strategien, die oxidativen Stress in Kombination mit AMPK-Inhibitoren (AMPKi) als vielversprechenden Weg zur Überwindung von Arzneimittelresistenzen bei PDAC nutzen.

Leider werden derzeit verfügbare AMPK-Targeting-Wirkstoffe oft wegen ihrer Kinase-Hemmwirkung mit breitem Spektrum kritisiert und als experimentell ohne bevorstehende klinische Translation angesehen. Um die Entdeckung potenzieller AMPK-Inhibitoren mit klinischer Relevanz zu beschleunigen, haben wir den Ansatz des Drug Repurposing angewendet. Drug Repurposing bedeutet bestehende Arzneimittel für eine alternative Verwendungsmöglichkeit zu gebrauchen. Durch ein umfassendes Arzneimittel-Screening von Verbindungen, die sich in der klinischen Prüfung befinden, identifizierten wir den p21-aktivierten Kinase 4 (PAK4)-Inhibitor PF-3758309 als potentiellen AMPK Inhibitor. Proteomische Inhibitor-Selektivitätsexperiemente bestätigten, dass PF-3758309 an AMPK bindet, und weitere Experimente zeigten eine effiziente Blockierung der nachgeschalteten AMPK-Signalübertragung bei nanomolaren Konzentrationen. Bemerkenswerterweise zeigte PF-3758309 eine speziesübergreifende nanomolare Wirksamkeit in zellulären Assays.

Unsere Daten belegen, dass AMPK durch PF-3758309 gehemmt werden kann, wodurch ein zentraler metabolischer Integrator angegriffen wird. Die beobachtete speziesübergreifende Reaktion von PDAC-Zellen auf PF-3758309 positioniert diesen Inhibitor als Baustein für die Entwicklung selektiver AMPK Inhibitoren und unterstreicht die Relevanz des Arzneimittel Repurposing.

Introduction

1 Pancreatic Cancer

1.1 Current Status

Pancreatic cancer is one of the most aggressive and fatal malignancies and according to recent statistical data the third leading cause of cancer-related death in the United States (Siegel et al. 2022) as well as in Germany (Robert Koch Institute 2022) (Figure 1). These statistics are driven by rising incidences and no meaningful improvements in therapy regimens or screening approaches. In Germany, the absolute number of new cases of pancreatic cancer has almost trebled since the 1970s (Robert Koch Institute 2022), and while for other cancer types, the 5-year survival rate almost passed the 90% mark, pancreatic cancer continues to have the lowest 5-year survival among all cancer types of only 11% (Robert Koch Institute 2022; Siegel et al. 2022).

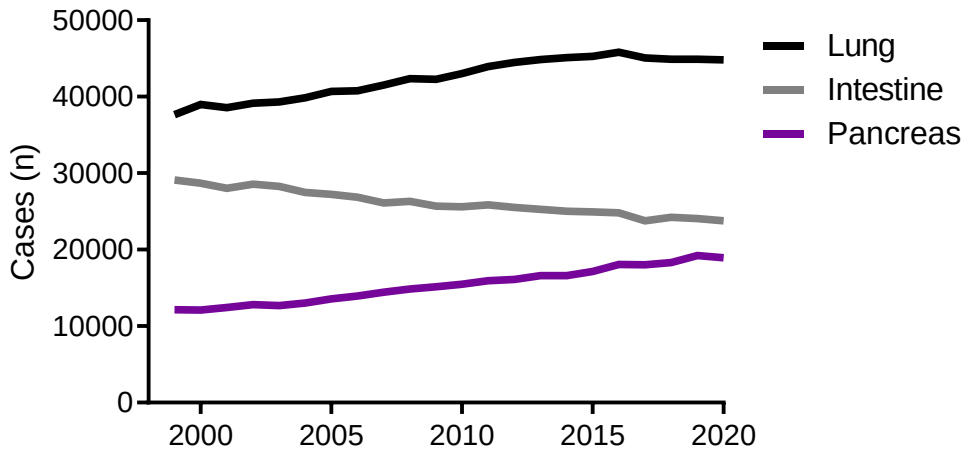

Figure 1 | Mortality of the three most prominent cancer entities in Germany. Cancer entities are color-coded. The mortality of cancer of the pancreas is continuously rising. n: absolute number. (Robert Koch Institute 2022)

Complete surgical resection is the only curable therapeutic option. However, less than 20% of patients are suitable for pancreatectomy (Barugola et al. 2009) seeing that most patients are diagnosed when the tumor is already locally advanced or metastasized (Siegel et al. 2022; Siegel, Miller, and Jemal 2017). After surgery, 60-70% of patients eventually suffer from recidivism of the disease (Nishio et al. 2017; Topal et al. 2022). As such, nearly all patients are offered conventional chemotherapy as first-line treatment. After showing marginal efficacy in clinical trials, Gemcitabine was approved as standard-of-care by the U.S. Food and Drug Administration (FDA) for metastatic pancreatic cancer in 1996 (Burris et al. 1997, 1997; Carmichael et al. 1996; Casper et al. 1994). Depending on the performance status of the

patient, a combination therapy of gemcitabine with albumin-bound (nab) paclitaxel (Von Hoff et al. 2013) or the multi-drug regimen FOLFIRINOX (5-Fluorouracil, Leucovorin, Irinotecan, and Oxaliplatin) (Conroy et al. 2011) is prescribed which improved survival time compared to gemcitabine monotherapy from 6.7 to 8.5 months in the gemcitabine with nab-paclitaxel group or from 6.8 to 11.1 months in the FOLFIRINOX group. These therapies, however, are associated with frequent serious adverse events.

The predominately chemotherapeutic treatment approach for pancreatic cancer stands in stark contrast to the advancements observed in therapeutic options for other cancer types. For instance, the development of targeted therapies for driver mutations, such as tyrosine-kinase inhibitors, has led to a tripling of the 5-year survival rate in chronic myeloid leukemia, from 22% in the mid-1970s to 70% (Sasaki et al. 2015; Siegel et al. 2023). In addition, significant improvements in survival outcomes have been observed for metastatic melanoma patients with the advent of first-generation and second-generation immunotherapies, along with targeted therapies like BRAF and MEK inhibitors (Berk-Krauss et al. 2020; Siegel et al. 2023). Since then, the combination therapy of BRAF and MEK inhibitors has gained tumor-agnostic approval for BRAF-mutant unresectable and metastatic solid tumors (Mullard 2022). However, in the case of pancreatic cancer, fewer targetable mutations have been identified, posing challenges for developing effective therapeutic strategies. Thus, driving research in the field of pancreatic cancer is essential to bring about significant advancements and breakthroughs in the treatment of this disease, similar to those witnessed in other cancer entities.

1.2 Pathobiology of PDAC

The pancreas is a vital organ within both the digestive and endocrine systems. It consists of three distinct cell types that contribute to its overall function: (i) acinar cells which are crucial for the production of digestive enzymes, (ii) ductal cells that form a network of channels to facilitate the transportation of the pancreatic enzymes to the duodenum, (iii) and endocrine cells found in the islets of Langerhans which are responsible for hormone production and release.

Pancreatic ductal adenocarcinoma (PDAC), the predominant type of pancreatic cancer, arises from the exocrine compartment of the organ and accounts for over 90% of all pancreatic cancer cases. Rarer tumor types of the pancreas include other exocrine tumors such as squamous cell carcinoma, adenosquamous carcinoma or colloid carcinoma, and neuroendocrine tumors. The understanding of PDAC carcinogenesis has greatly improved through decades of research and is described by the punctuated evolution progression model shown in Figure 2.

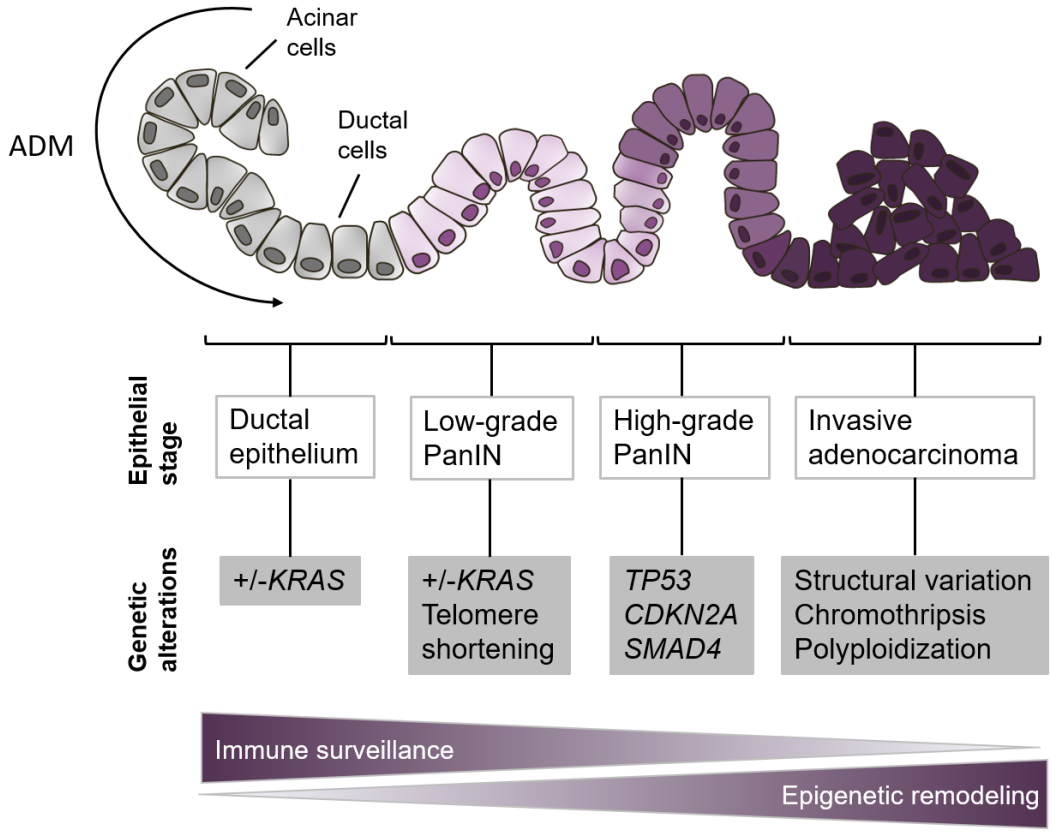

Figure 2 | Punctuated evolution progression model for pancreatic cancer. The diagram illustrates the sequence of genetic events during the transformation of normal pancreatic epithelial cells into aberrant precursor lesions, eventually leading to invasive PDAC. PDAC precursor cells can potentially emerge from acinar cells through ADM or from pre-existing ductal cells. Histologically normal epithelium may carry activating *KRAS* mutations. Early events arising in low-grade PanINs are somatic changes in the *KRAS* oncogene and telomere shortening. High-grade PanINs acquire inactivation of the tumor suppressor genes *TP53*, *CDKN2A*, and/or *SMAD4*. Invasive adenocarcinomas are characterized by more structural and copy number variants, and genomic instability leading to chromothripsis and polyploidization. Mutations in additional genes that are not illustrated in this example may also occur during tumor progression. Besides genetic alterations, advanced PDAC is characterized by vast epigenetic changes and loss of immune surveillance. ADM: Acinar-to-ductal metaplasia, *CDKN2A:* Cyclin-dependent kinase inhibitor 2A, KRAS: Kirsten rat sarcoma virus, PanIN: Pancreatic intraepithelial neoplasia, *SMAD4*: SMAD family member 4, *TP53:* Transformation-related protein 53.

PDAC is thought to initiate through two possible cell types. Firstly, it may arise directly from ductal cells. Alternatively, PDAC can develop through a process called acinar-to-ductal metaplasia (ADM), where acinar cells undergo transdifferentiation into cells that resemble ductal cells (Friedlander et al. 2009; Kopp et al. 2012). The pancreatic tissue then undergoes further remodeling, leading to the formation of pancreatic intraepithelial neoplasia (PanIN), which progresses through three distinct stages (types 1, 2, and 3) from low-grade to high-grade, reflecting increasing degrees of dysplasia. Other routes include PDAC development

from larger pre-neoplastic lesions, such as intraductal papillary mucinous neoplasms and mucinous cystic neoplasms (Kleeff et al. 2016). The increasing dysplasia is associated with accumulating genetic alterations. 90% of PanINs of all grades harbor activating Kirsten rat sarcoma virus (*KRAS*) mutations suggesting this event to be the initiation and making PDAC the most Ras-addicted of all cancers (Australian Pancreatic Cancer Genome Initiative et al. 2015; Biankin et al. 2012; Jones et al. 2008; Makohon-Moore et al. 2018). Activated KRAS can, in turn, activate multiple signaling pathways, including the rapidly accelerated fibrosarcoma (RAF)-mitogen-activated protein kinase (MEK)-extracellular regulated protein kinases (ERK) signaling pathway, phosphoinositide 3-kinase (PI3K)-protein kinase B (AKT)—mechanistic target of rapamycin (mTOR) signaling pathway, and other signaling pathways involved in cell proliferation and growth. Further progressed lesions are associated with the subsequent mutational inactivation of cyclin-dependent kinase inhibitor 2A (*CDKN2A*), and in highest-grade lesions, loss of transformation-related protein (*TP53*), and SMAD family member 4 (*SMAD4*) is detected. PDAC suppressor gene inactivations can occur simultaneously with complex largescale chromosomal rearrangements accelerating the sudden onset of a full-blown invasive and metastatic PDAC (Australian Pancreatic Cancer Genome Initiative et al. 2015; Notta et al. 2016). Moreover, a high number of infrequently mutated genes occurring at a prevalence below 2% contribute to the genetic landscape of the disease (Kleeff et al. 2016). Nevertheless, genetic alterations are not enough to explain PDAC evolution in its entirety. Accumulating evidence suggests that changes in the epigenetic landscape regulating the expression of cancer-related genes contribute in tandem with genetic alterations to its pathobiology (Lomberk et al. 2018).

In most individuals, the described process is entirely somatic, while up to 10% of patients with PDAC have a germline predisposition (Klein et al. 2004; Shi, Hruban, and Klein 2009). Risk factors and inherited syndromes associated with PDAC are listed in Table 1.

Table 1 | Risk factors and hereditary syndromes linked with pancreatic cancer. The relative risk for risk factors and the lifetime risk for genetic syndromes are listed. For genetic syndromes, associated genes are given in brackets. The table is adapted from (Ryan, Hong, and Bardeesy 2014). PRSS1: Serine protease 1, SPINK1: Serine peptidase inhibitor Kazal type 1, STK11: serine/threonine kinase 11, CDKN2A: cyclin dependent kinase inhibitor 2A, MLH1: mutL homolog 1, MSH2/6: mutS homolog 2/6, BRCA1/2: Breast cancer type 1/2, PALB2: Partner and localizer of BRCA2, ATM: Ataxia-telangiectasia mutated, TP53: transformation-related protein 53.

VARIABLE	APPROXIMATE RISK
Risk factor	
Nonhereditary and chronic pancreatitis	2-6
Smoking	2-3
Diabetes mellitus	2
Obesity, inactivity, or both	2
Non-O blood group	1-2
Genetic syndrome and associated genes	
Hereditary pancreatitis (PRSS1, SPINK1)	50
Peutz-Jeghers syndrom (STK11)	30-40
Familial atypical multiple mole and melanoma syndrome (CDKN2A)	10-20
Hereditary nonpolyposis colon cancer (Lynch syndrome) (MLH1, MSH2, MSH6)	4
Hereditary breast and ovarian cancer syndromes (BRCA1, BRCA2, PALB2)	1-2
Ataxia-telangiectasia (ATM)	Unknown
Li-Fraumeni syndrome (TP53)	Unknown

1.3 Multi-Therapy Resistance

PDAC is a highly heterogeneous disease with immense resistance against the standard of care as well as novel experimental drugs. This multi-therapy resistance has tumor cell-intrinsic and extrinsic roots.

Tumor Cell-Extrinsic Factors

One main tumor cell-extrinsic factor confounding PDAC treatment response is its heterogeneous tumor microenvironment (TME). TME is a collective term for the tumor-surrounding blood vessels, immune cells, fibroblasts, signaling molecules, and the extracellular matrix (ECM). To establish a niche for unrestrained growth, the PDAC cells interact and reprogram these surrounding cells.

Late-stage PDAC provokes an extreme desmoplastic reaction completely destroying the tissue architecture of the pancreas. The desmoplastic reaction denotes the activation and proliferation of cancer-associated fibroblasts (CAFs) and the excessive deposition of ECM proteins secreted by them. Only 10-20% of the pancreatic tumor mass are actual malignant

cells, while the majority of the bulk originates from CAFs and ECM proteins. This dense stroma creates a mechanical barrier around the tumor cells, preventing appropriate vascularization and thus limiting chemotherapy exposure as well as nutrient uptake and oxygen supply. Given the abundance of CAFs and their widely appreciated tumor-supporting and resistance-driving function, there have been strong efforts to modulate CAF activity to enhance the effect of chemotherapy, but breakthroughs fail to appear (Gunderson et al. 2019; Tran et al. 2013).

Another prominent feature of PDAC is its immunosuppressive phenotype. It has been shown that PDAC almost completely blocks the infiltration of effector T-cells and only allows the presence of regulatory T-cells making PDAC an immunologically “cold” tumor (Clark et al. 2007; Hiraoka et al. 2006; Tang et al. 2014). Immunotherapy which is considered a treatment revolution in other cancer entities is dependent on the infiltration of effector T-cells, but in PDAC, the described immunologic features nullify the effect of such therapeutic concepts (Yarchoan, Hopkins, and Jaffee 2017).

Tumor-Cell Intrinsic Factors

Besides the mentioned cell-extrinsic features fostering drug resistance, PDAC bears multiple tumor cell-intrinsic elements making it a disease extremely hard to treat.

KRAS

Since *KRAS* is the most frequently mutated oncogenic driver in PDAC, there has been a long history of researchers trying to either target downstream signaling which is, however, associated with severe side effects due to the essentiality of the pathway or to design and optimize covalent inhibitors that specifically target mutated KRAS. One recent milestone was the development of $KRAS^{G12C}$-specific inhibitors, namely Sotorasib and Adagrasib, which have shown promising clinical efficacy in lung cancer patients (Jänne et al. 2022; Skoulidis et al. 2021). Currently, Sotorasib is under investigation to determine its safety and tolerability in combination with standard chemotherapy in pancreatic cancer (NCT05251038). In PDAC, only 1% of *KRAS*-mutated tumors harbor $KRAS^{G12C}$ mutations and could potentially benefit from these compounds, while the predominant variant is $KRAS^{G12D}$. A recent study published in Nature Medicine claims to have developed a non-covalent $KRAS^{G12D}$ inhibitor that showed great efficacy in human PDAC cell lines (Anon 2022). These compounds bear great therapeutic potential, but the first results of the clinical trials also reveal that approximately two-thirds of patients do not respond to selective KRAS blockage (Jänne et al. 2022; Skoulidis et al. 2021).

Thus, targeting mutated KRAS may not be enough and we need to continue exploring alternative therapies.

Molecular Diversity Beyond Mutations

For decades, PDAC has been treated as one disease entity with chemotherapy as the sole therapy option since the mutational profile is dominated by four main genes i.e. *KRAS, TP53, CDKN2A, SMAD4*. However, these mutations poorly correlate with treatment response. Advances in large-scale sequencing technologies led to the development of increasingly sophisticated molecular tumor classifications with the goal to find subtype-specific therapies. Initially, two main transcriptional-based subtypes emerged, a classical subtype with a better prognosis which tends to respond to chemotherapy, and a basal-like subtype that is rather undifferentiated and associated with a poorer clinical outcome and chemotherapy resistance (Aung et al. 2018; Chan-Seng-Yue et al. 2020; Moffitt et al. 2015). This concept has been expanded by recent studies suggesting that not only basal-like and classical cell populations coexist in the same tumor but a continuum of these phenotypes (Nicolle et al. 2020) which are also able to switch from one transcriptional state into the other in response to environmental cues (Raghavan et al. 2021). These studies show that the plasticity of PDAC is higher than anticipated and this binary classification system is not enough to inform about the right treatment decisions.

Accumulating evidence indicates that each patient needs individual therapy. In recent years, molecular tumor profiling and molecular studies have led to the discovery of pivotal genes and pathways that are dysregulated or mutated in cancer. Concurringly, the arsenal of drugs targeting these alterations with high efficacy is continuously expanding. Prototype clinical trials have already proven the success of matching targeted therapies based on molecular profiling. In the Know Your Tumor registry trial, 1082 PDAC patients underwent molecular testing and in 26% of the patients, actionable alterations were detected (Pishvaian et al. 2020). Of the patients analyzed, the patients who received a matched therapy the overall median survival was 2.39 years compared to 1.32 years when no actionable alteration was found. More ongoing clinical trials testing the efficacy of targeted drugs in molecularly matched patients are DRUP (NCT02925234), TAPUR (NCT02693535), and MATCH (NCT02465060) (Flaherty et al. 2020). The I-PREDICT Trial expanded the concept by the administration of multi-drug combinations targeting multiple identified molecular alterations based upon recommendations from a molecular tumor board (Sicklick et al. 2019). While these trials are the beginning of a new area of precision oncology, we need to further improve this patient-centric therapy approach.

As discussed above, the high level of heterogeneity of PDAC emerges from a molecular diversity beyond mutations. Global epigenetic, microenvironmental, and tissue-specific alterations have been shown to contribute to the diverse nature of PDAC seen in the clinic. To obtain a comprehensive understanding of each patient's tumor, it is imperative to conduct an extensive molecular characterization encompassing transcriptomics, proteomics, immune profiling, and metabolic subtyping. The integration of these layers of data could help to deconvolute the individual molecular makeup of the PDAC of specific patients with the absolute goal to find potential vulnerabilities and therapeutic windows.

Especially the metabolic characterization of PDACs is a research field of recent interest. Metabolic reprogramming is a multifaceted process and has been linked with PDAC development and progression as well as clinical parameters including patient survival and resistance toward standard chemotherapy. Understanding the metabolic landscape of PDAC and exploiting this knowledge to target specific metabolic pathways could be a promising approach to developing novel clinical treatment regimens.

1.4 Metabolic Reprogramming and Vulnerabilities of PDAC

According to Hanahan and Weinberg, deregulated cellular energetics represents one of the fourteen hallmarks of cancer (Hanahan 2022; Hanahan and Weinberg 2011), a fact appreciated since the postulation of the Warburg hypothesis in the early 20th century (Warburg 1956). The chronic and often uncontrolled cell proliferation that represents the essence of neoplastic diseases involves not only deregulated control of cell proliferation but also corresponding adjustments of energy metabolism to fuel cell growth and division. Otto Warburg observed that even in the presence of oxygen, cancer cells favor glycolysis over oxidative phosphorylation for adenosine triphosphate (ATP) production and energy synthesis (Warburg 1956). Regarding the fact that glycolysis is 15-18 times less effective in energy production, cancer cells exhibit a drastically increased glucose uptake. This cancer phenotype has been translated into clinical application for the imaging of tumors by noninvasively visualizing glucose uptake using positron emission tomography (PET) with a radiolabeled analog of glucose (18F-fluorodeoxyglucose, FDG) as a tracer.

In the past decade, numerous studies have investigated the heterogeneity and complexity of cancer metabolism beyond the Warburg effect. In-depth studies of the metabolic landscape of PDAC and the discovery of metabolic bottlenecks are crucial to eventually developing novel therapeutic approaches. In this chapter, the current knowledge of PDAC metabolism will be summarized (Figure 3).

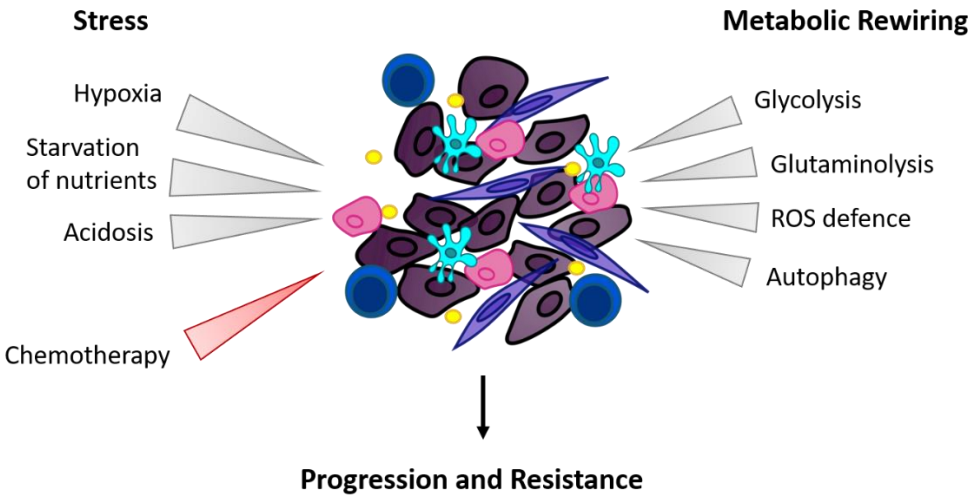

Figure 3 | Metabolic rewiring in PDAC. PDAC cells face severe metabolic stresses including hypoxia, starvation of nutrients, and acidosis caused by oncogene activation, high proliferation, the dense microenvironment, and in some cases chemotherapeutic treatment. To cope with the metabolic stresses, PDAC cells undergo global metabolic rewiring which ensures their survival and ultimately bolsters the progression and resistance of the disease.

Oncogenes are far-reaching drivers of the bioenergetics and metabolic traits of cancer cells. In PDAC, mutation of *KRAS* is the signature event and has been shown to alter the reliance of PDAC cells on specific metabolic pathways In 2012 Ying et al. established a conditional $Kras^{G12D}$ expressing mouse model and found that $Kras^{G12D}$ controls the expression of multiple rate-limiting enzymes of glycolysis increasing glycolytic fueling. Moreover, they found that the glycolysis intermediates were directed into biosynthetic pathways boosting O-glycan biosynthesis, steroid biosynthesis, and non-oxidative pentose-phosphate-pathway for pyrimidine synthesis. (Ying et al. 2012)

PDAC cells have demonstrated a significant dependency on the maintenance of redox homeostasis. Redox homeostasis refers to the balance of oxidant production, especially reactive oxygen species (ROS), and their elimination. ROS levels play a critical role in cellular signaling and gene expression regulation, with physiological levels being necessary for normal cellular function. However, uncontrolled ROS production can lead to the oxidation of proteins, DNA, and lipids, potentially triggering programmed cell death. Elimination of ROS is secured by antioxidant systems including glutathione (GSH) and thioredoxin (TXN) which require NADPH as a reduction equivalent. Tilting of this redox balance towards oxidation is commonly referred to as oxidative stress.

Redox homeostasis is a highly controversial topic in cancer. In cancer cells, ROS levels are often elevated due to increased metabolic rates, gene mutations, relative hypoxia, and in some cases chemotherapy. Although high ROS levels have been discussed to have pro-tumorigenic

properties, the maintenance of redox homeostasis seems as crucial for cancer cells as for normal cells.

For instance, KRAS has been shown to induce the expression of Nuclear factor erythroid 2–related factor 2 (NRF2), a master transcription factor of antioxidant genes. Consistent with these findings, interference with NRF2 hampered $KRAS^{G12D}$-induced proliferation (DeNicola et al. 2011:2).

Moreover, studies by Son et al. have demonstrated that KRAS controls the expression of key enzymes requisite for glutaminolysis (Son et al. 2013). This elevated glutaminolysis which is characteristic of PDAC cells, is believed to stem, among other factors, from its role in redox metabolism. Since the pyruvate generated out of glycolysis is not channeled into the tricarboxylic acid cycle (TCA cycle), but reduced to lactate, PDAC cells rely upon the anaplerotic metabolite glutamine. The rewiring of glutaminolysis is used to uphold the TCA flux while using aspartate as an intermediate for the generation of NADPH from NADP+. In turn, NADPH is needed to preserve the GSH pool, which serves as one of the primary safeguards of redox homeostasis.

Notably, the cytosolic enzyme isocitrate dehydrogenase 1 (IDH1) has been identified as another critical player in this context. IDH1 catalyzes the reversible conversion of isocitrate to α-ketoglutarate, utilizing NADP+ or NADPH as a cofactor, depending on the direction of the reaction. Thereby, IDH1 is coupled to antioxidant defense. It is mutated up to 80% in a subtype of brain cancer as well as 16% in intrahepatic cholangiocarcinoma underscoring the cancer-driving force of this metabolic enzyme. Notably, the mutant IDH1 inhibitor Ivosidenib has exhibited substantial advancements in the treatment of *IDH1*-mutated intrahepatic cholangiocarcinoma leading to its FDA approval (A. X. Zhu et al. 2021).

Although the mutation rate in PDAC is low, Vazier-Gohar et al. discovered IDH1 as a potential target in PDAC, especially under glucose deprivation (Vaziri-Gohar et al. 2022). A clinical trial started this year will examine the efficacy of Ivosidenib targeting the wildtype IDH1, in conjunction with standard-of-care mFOLFIRINOX in the neoadjuvant setting (NCT05209074).

Recent studies performing *in vivo* and *in vitro* CRISPR screens to identify metabolic vulnerabilities in PDAC cells have highlighted the essentiality of heme biosynthesis. Specifically, heme oxygenase 1 (HMOX1) (X. G. Zhu et al. 2021) and hydroxymethylbilane synthase (HMBS) (Biancur et al. 2021) have emerged as critical players in PDAC. These enzymes play vital roles in ROS detoxification, further emphasizing the significance of redox regulation in PDAC cells.

Moreover, pancreatic cancers exhibit constitutively high levels of autophagy when compared to other cancers (S. Yang et al. 2011). Autophagy is a highly selective and conserved pathway

that degrades cellular components, such as defective organelles and aggregates of misfolded protein through lysosomes. Notably, inhibition of autophagy has been shown to impair tumor growth (S. Yang et al. 2011; X. G. Zhu et al. 2021). In light of these findings, the autophagy inhibitor hydroxychloroquine has been tested in combination with gemcitabine and nab-paclitaxel. Although the overall survival at 1 year among patients with metastatic pancreatic cancer was not improved, the response rate was higher suggesting a potential therapeutic window as a neoadjuvant option (Karasic et al. 2019).

Furthermore, a comprehensive epigenomic study conducted in 2017 revealed a reciprocal feedback loop between metabolism and cancer characteristics, demonstrating that metabolites can manipulate gene expression by affecting epigenetic marks on histones and DNA. McDonald et al. reported that anabolic glucose metabolism significantly impacts global chromatin modifications driving malignant epigenetic programs in metastatic pancreatic cancer (McDonald et al. 2017). This research highlights the active role of metabolism in shaping cellular signaling and steering major cellular decisions to sustain continuous proliferation and cell survival.

As already mentioned, the until to date established PDAC classifications are insufficient to guide clinical decisions. Deamen et al. propelled research in this field by using metabolite-based subtyping of PDAC cell lines for treatment stratification. In this study, they found three metabolic subtypes: slow proliferating, lipogenic, and glycolytic. The subtypes significantly correlated with enriched sensitivity to a variety of metabolic inhibitors. This study highlights that understanding the essential metabolic pathways of PDAC may provide novel therapeutic strategies and opens opportunities for personalized therapies. (Daemen et al. 2015)

Besides fostering cancer proliferation, emerging studies refer to an association between metabolic reprogramming and cancer drug resistance. Resistance to chemotherapy or molecularly targeted therapies is a major cause of tumor relapse and death. Using organoids established from the same patient pre- and post-chemotherapy, Peschke *et al.* could show a metabolic switch towards oxidative phosphorylation and lipogenesis after therapy (Peschke et al. 2022). Congruently with this observation, the inhibition of fatty acid biosynthesis (Orlistat) can overcome gemcitabine resistance in an *in vivo* orthotopic implantation model (Tadros et al. 2017). Moreover, Masoud *et al*. showed that targeting complex I in the PDAC subtype with high oxidative phosphorylation activity is synergistic with gemcitabine treatment (Masoud et al. 2020). These studies support that metabolic reprogramming underlies the development of drug resistance and point to potential metabolic vulnerabilities of resistant cancer cells. Hence, therapeutic strategies that combine metabolic targeting in combination with chemotherapeutic drugs could display a promising avenue to overcome drug resistance in PDAC.

The concept of targeting metabolic subtypes has been challenged by recent studies showing remarkable metabolic plasticity of PDAC tumor cells and reverting metabolic patterns upon treatment. Targeting metabolic regulators at the apex of the metabolic hierarchy and thus targeting metabolic plasticity itself, could be a way to restrain the high resilience of the disease.

2 AMPK

2.1 Structure of AMPK

Monitoring nutrient availability in the surrounding microenvironment and meeting energy needs are controlled by highly conserved and sophisticated systems. Among them, adenosine monophosphate-activated kinase (AMPK) has a unique position in cellular energy homeostasis (Herzig & Shaw, 2018).

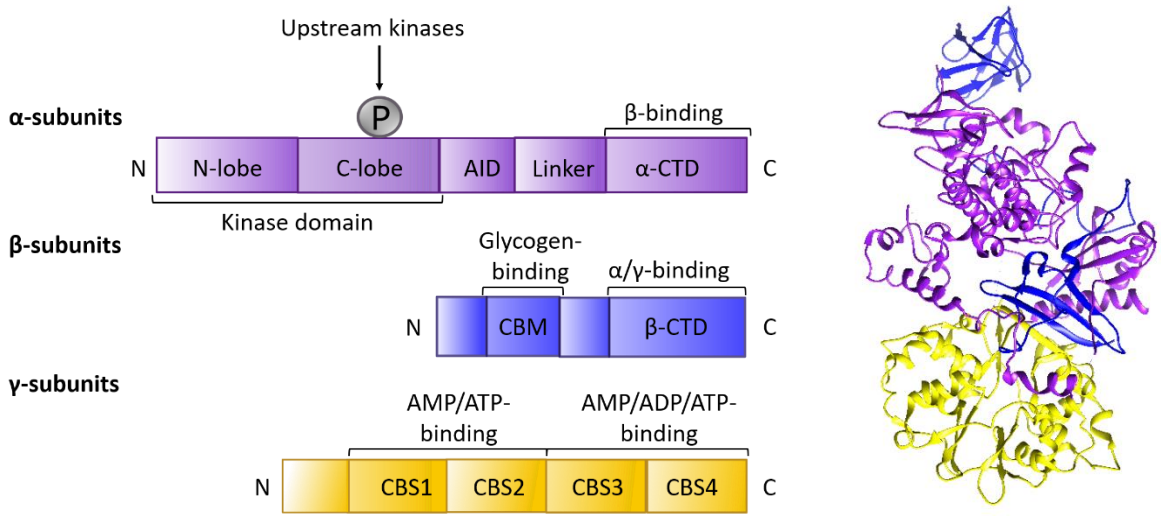

Figure 4 | Domain structure of AMPK. AMPK subunits are color-coded (α: purple. β: blue. γ: yellow) and domains are indicated. **Left:** Domain structure of α-, β-, γ-subunits of AMPK. **Right:** 3-Dimensional structure of active AMPK. Drawn by Chimera 1.16 using PDB file 4RER. AMP: Adenosine monophosphate, ADP: Adenoside diphosphate, AID: autoinhibitory domain, ATP: Adenosine triphosphate, CBS: cystathionine-β-synthase, CBM: carbohydrate-binding module, CTD: Carboxy-terminal domain.

It is a heterotrimeric complex composed of three subunits, the catalytic α-subunit, the scaffolding β-subunit, and the regulatory γ-subunit (Figure 4). There are two isoforms of the α (encoded by *PRKAA1* and *PRKAA2*) and β (encoded by *PRKAB1* and *PRKAB2*) subunit and three isoforms of the γ (encoded by *PRKAG1*, *PRKAG2,* and *PRKAG3*) subunit, giving rise to twelve possible combinations of the protein. The existence of multiple isoforms of AMPK subunits has been known for decades, but the functional relevance of the different isoforms

remains only partially understood. The α-subunit contains the Serine/Threonine kinase domain with the N-terminal lobe (N-lobe), the C-terminal lobe (C-lobe), and the critical residue Threonine 172 (Thr172) as well as an autoinhibitory domain (AID) which is followed by a linker and the carboxy-terminal domain (α-CTD). In its inactive state, the α-AID interacts with the Serine/Threonine kinase domain. The β-subunit harbors the carbohydrate-binding module (CBM) which functions as a binding pocket for glycogen. The functional significance of this remains unelusive, although it may serve to colocalize AMPK with downstream targets in glycogen particles, such as glycogen synthase. The β-CTD joins with both the α-CTD and the γ-subunit, thus forming the structural core of the complex. The γ-subunit enables AMPK to respond to changes in the ATP-to-Adenosine monophosphate (AMP) ratio as it contains four tandem cystathionine-β-synthase (CBS) domains that bind AMP, Adenosine diphosphate (ADP), and ATP competitively.

2.2 Mechanism of Action

AMPK can be activated by canonical and non-canonical mechanisms (Figure 5).

Canonical Activation

The canonical activation mechanism involves allosteric activation by AMP binding to the CBS repeats, preferentially CBS3, and promotion of Thr172 phosphorylation. Superseding of ATP from the CBS sides of the γ-subunit by binding of AMP, and to a lesser extent, ADP leads to a conformational change that physically shields Thr172 from dephosphorylation. By this allosteric mechanism, AMPK can sense the energy status and restore the energy homeostasis of the cell. Upon phosphorylation of Thr172 by upstream kinases, the activity of AMPK can further increase by more than 100-fold.

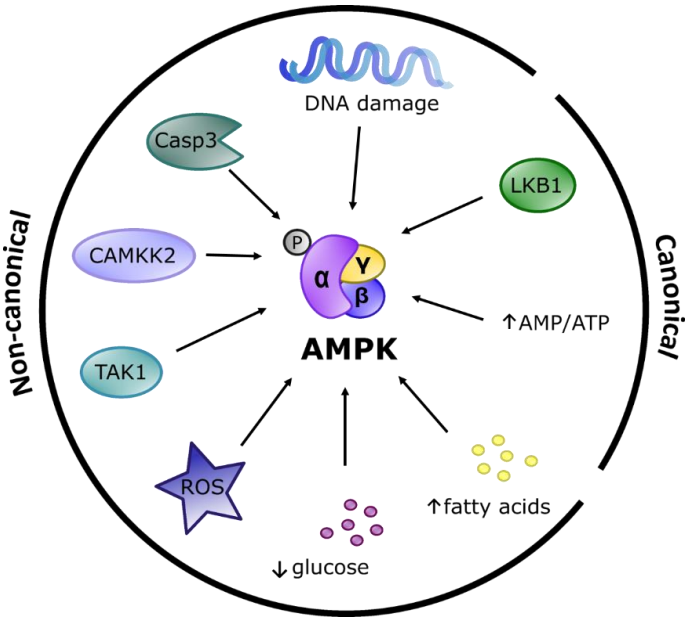

Figure 5 | Mechanisms of canonical and non-canonical activation of AMPK. Canonical activation mechanisms include a high AMP/ATP ratio resulting in the binding of AMP, and phosphorylation of AMPK by LKB1 at Thr172. Non-canonical activation mechanisms are triggered by diverse physiological cues including low levels of glucose, high levels of fatty acids, and the presence of ROS or DNA damage. Besides LKB1, the kinases TAK1 and CAMKK2 have been shown to phosphorylate AMPK. Furthermore, Casp3 is capable to cause nuclear accumulation of AMPKα1 by cleaving its nuclear export sequence. AMP: Adenosine monophosphate, ATP: Adenosine triphosphate, CAMMK2: Calcium/calmodulin-dependent protein kinase kinase 2, Casp3: Caspase 3, LKB1: Liver kinase B1, ROS: Reactive oxygen species, TAK1: Transforming growth factor-β-activated kinase 1.

The two major upstream kinases of AMPK are the liver kinase B1 (LKB1, *STK11*) (canonical) and the Ca^{2+}/calmodulin-activated protein kinase kinase (CaMKK2) (non-canonical). *STK11* has been well characterized as a tumor suppressor gene encoding a ubiquitously expressed and evolutionarily conserved serine-threonine kinase, originally associated with the inherited cancer disorder Peutz-Jeghers Syndrome (Hemminki et al. 1997, 1998; Jenne et al. 1998). It is one of the most commonly mutated genes in sporadic human lung cancer, particularly in multiple subtypes of non-small cell lung carcinoma (NSCLC). LKB1 functions as a heterotrimer with the kinase-dead STE20-related kinase STRAD and the STE20 family scaffolding protein MO25 and is responsible for the majority of AMPK activation under energy stress. AMPK activation by LKB1 requires N-myristoylation of the β-subunit (Mitchelhill et al., 1997; Oakhill et al., 2010) which facilitates recruitment to cellular membranes where LKB1 is localized. LKB1 is constitutively bound to axis inhibition protein (Axin), acting as a scaffold for AMPK. AMP binding to the γ-subunit induces a conformational change that enables the formation of a ternary complex of LKB1-Axin-AMPK. This complex promotes AMPK phosphorylation and activation.

Non-Canonical Activation

In LKB1 deficient tumors, CAMKK2 has been shown to sustain residual AMPK phosphorylation. CAMKK2 responds to increased intracellular calcium flux triggered by metabolic hormones including vascular endothelial growth factor (Stahmann et al. 2010), ghrelin (Y. Yang et al. 2011), or thyroid hormones (Sinha et al. 2015) and subsequently activates AMPK. In addition, CAMKK2 is the executive kinase leading to AMPK activation in response to DNA-damaging agents (Li et al. 2019:1). Recent findings by Cheratta et al. expose further insights. Cheratta et al. showed that upon DNA damage, Caspase 3 cleaves the nuclear export sequence of AMPKα1 leading to its nuclear retention and subsequent phosphorylation by CAMKK2 (Cheratta et al. 2022). Whether there is a third upstream kinase of AMPK, the transforming growth factor-β-activated kinase 1 (TAK1), is still the subject of debate, however, accumulating evidence suggests that TAK1 indeed phosphorylates AMPK, particularly in the context of cytoprotective autophagy (Herrero-Martín et al. 2009; Jia et al. 2020).

Growing appreciation is given to AMPK activation through AMP-independent mechanisms. AMPK has been shown to become activated under acute glucose deprivation even when ATP levels are stable by a mechanism involving the glycolytic enzyme aldolase. Aldolase catalyzes the cleavage of fructose-1,6-bisphosphate to dihydroxyacetone phosphate and Glycerinaldehyd-3-phosphate. When the glucose levels in the cell drop and consequently the fructose-1,6-bisphosphate levels, aldolase promotes the formation of the supercomplex of vacuolar-type ATPase, ragulator, AXIN, and LKB1 at the lysosomal membrane where a pool of AMPK resides. The proximity of LKB1 and AMPK then causes AMPK phosphorylation and activation. (Zhang et al. 2017)

The tertiary structure of the AMPK subunits forms an allosteric drug and metabolite (ADaM) site, a cleft between the N-lobe of the kinase domain and the β-CBM (Langendorf and Kemp 2015). The AdaM site was reported to be critical for a new level of regulation wherein fatty acyl-CoA esters per se allosterically activate AMPK (Pinkosky et al. 2020).

AMPK was also described as a redox-sensing protein and activated in response to oxidative stress. Zmijewski et al. showed that the presence of H_2O_2 can induce S-glutathionylation of the AMPKα and AMPKβ subunits and upregulate AMPK activity (Zmijewski et al. 2010). Even though a comprehensive picture is yet to emerge, the evidence points to AMPK at the core between cellular metabolism and cellular redox status.

The activation status of AMPK is also supervised by phosphatases coordinating dephosphorylation including protein phosphatase 2A (Joseph et al. 2015), protein phosphatase 2C (Woods et al. 2017) and Mg2+-/Mn2+-dependent protein phosphatase 1E (Voss et al. 2011).

Phosphorylation Sites

AMPKα subunits are also phosphorylated at other sites than Thr172. These sites include the serine/threonine-rich (ST) loop at the C-terminus of the α-CTD and the α-linker. The ST loop of AMPKα1 is the target of AKT (Hawley et al. 2014) as well as cyclic AMP-dependent kinase (PKA) (Hurley et al. 2006; Ning, Xi, and Clemmons 2011). Phosphorylation of Ser485 by AKT and PKA as well as also through autophosphorylation inhibits the activating phosphorylation at Thr172 and consequent AMPK activation. The ST loop of AMPKα2 has been previously reported to be phosphorylated at Thr485 by cyclin-dependent kinase (CDK) 1 (Lu et al. 2021) and potentially at several sites by CDK4 (Lopez-Mejia et al. 2017:4). A study published in Nature Metabolism discovered two phosphorylation sites in the α-linker (Ser347 in AMPKα1 and at Ser345 in AMPKα). These sites are fundamental for the reciprocal relationship between AMPK and its metabolic counterpart, mTOR. mTOR is a central integrator of nutrient and growth factor signals that activates numerous biosynthetic pathways, especially protein translation, and overall cellular growth. Ling et al. show that mTOR phosphorylates AMPK leading to reduced phosphorylation of Thr172 (Ling et al. 2020:1).

Motif of AMPK

AMPK has been reported to directly phosphorylates more than 100 target proteins on at least 130 sites tuning almost every metabolic pathway there is to restore energy balance (Steinberg and Hardie 2022). The central phosphorylation motif for AMPK has been established using variants of peptides known to be phosphorylated by AMPK (Weekes et al. 1993) and later confirmed using unbiased chemical screens (Schaffer et al. 2015). The frequency plot of the recognition motif of AMPK shown in Figure 6 represents the occurrence of amino acids based on 126 sites on 103 target proteins and is in line with the mentioned functional studies.

Figure 6 | Consensus phosphorylation motif of AMPK. Generated using Weblogo.berkeley.edu using 126 phosphorylation sites of 103 target proteins. The height of the letter indicates the frequency of that amino acid at that position. Amino acids are described with one letter abbreviation. C: C-terminal, N: N-terminal.

Fatty Acid and Cholesterol Metabolism

Generally, AMPK blocks a wide range of anabolic reactions to minimize ATP consumption and at the same time activates catabolic reactions to stimulate ATP production. Biosynthetic processes which consume huge amounts of energy include lipogenesis. AMPK inhibits the first step in fatty acid synthesis through the phosphorylation of acetyl-CoA carboxylase (ACC) 1 and ACC2 at Ser79 and Ser212 preventing the conversion of acetyl-CoA to malonyl-CoA. Malonyl-CoA also serves as an allosteric inhibitor of the fatty acid transporter carnitine palmitoyltransferase 1 (CPT1) which sits in the outer mitochondrial membrane. The fall of malonyl-CoA concentrations reactivates CPT1 and thus the transport of fatty acids into mitochondria for β-oxidation. Moreover, AMPK inhibits 3-hydroxy-3-methylglutaryl-coenzyme-A-reductase (HMGCR), which catalyzes the rate-limiting step in cholesterol synthesis through phosphorylation at Ser871/Ser872 (Sato, Goldstein, and Brown 1993). Lipid synthesis is also governed by transcriptional programs of the sterol-response element-binding proteins (SREBPs) and carbohydrate-response element-binding proteins (ChREBPs). AMPK phosphorylates SREBP-1c at Ser372 and Ser374 of SREBP2 and suppresses proteolytic cleavage needed for nuclear translocation and target gene expression (Li et al. 2011). AMPK can further suppress the transcriptional lipogenic program through phosphorylation ChREBP at Ser568 which inhibits the DNA binding capacity of ChREBP (Kawaguchi et al. 2002). ChREBP is responsible for the transcription of important lipogenic enzymes including ACC and fatty acid synthase (FAS).

Carbohydrate Metabolism

AMPK controls many facets of carbohydrate metabolism including glucose import, gluconeogenesis, and glycogen synthesis. Glucose import is regulated by the interaction of AMPK with thioredoxin-interacting protein (TXNIP). Under high-glucose conditions, TXNIP sequesters and internalizes the membrane-bound glucose transporter (GLUT) 1 by endocytosis (Wu et al. 2013:1). Upon energy stress, AMPK phosphorylates TXNIP on Ser308 leading to its rapid degradation and the retention of GLUT1 transporters on the cell surface for continuous glucose uptake (Wu et al. 2013:1). In addition, AMPK orchestrates gluconeogenic gene expression programs. Responsible for the transcription of enzymes in gluconeogenesis is the cyclic AMP response element binding protein (CREB). AMPK disrupts gluconeogenesis via Ser 171 phosphorylation of transducer of regulated CREB activity 2 (TORC2) (Koo et al. 2005). Phosphorylation of TORC2 blocks its nuclear entry where it would otherwise enhance CREB-dependent transcription (Koo et al. 2005). Class IIa Histone deacetylases (HDACs) have been also identified as AMPK substrates that steer gluconeogenesis (Mihaylova et al.

2011). Phosphorylation of HDAC4 and HDAC5 by AMPK leads to their nuclear exclusion and prevents the activation of forkhead box O (FoxO) transcription factor family via deacetylation that would otherwise initiate a gluconeogenic gene expression (Mihaylova et al. 2011). Glycogen synthesis is also controlled by AMPK. AMPK phosphorylates glycogen synthase (GYS) 1 and GYS2 inhibiting glycogen synthesis (Bultot et al. 2012).

Protein and rRNA Synthesis

Protein synthesis is tightly governed by the interrelationship of AMPK and mTOR which serves as a signaling hub for regulating cellular metabolism, energy homeostasis, and cell growth. AMPK adjusts protein synthesis through the inhibition of mTORC1 by I) phosphorylation and activation of tuberous sclerosis complex 2 (TSC2) (Inoki, Zhu, and Guan 2003), a negative regulator of mTORC1, and II) phosphorylation and inhibition of regulatory-associated protein of mTOR (RPTOR), a subunit of the mTORC1 complex (Gwinn et al. 2008).
Besides inhibition of mTOR, AMPK blocks ribosomal RNA synthesis through Ser635 phosphorylation and inhibition of transcription initiation factor IA (TIF1A), which is essential for the assembly of the functional transcription initiation complexes of RNA-polymerase I (Hoppe et al. 2009). AMPK also inhibits protein elongation, through phosphorylation and activation of eEF2K (eukaryotic elongation factor 2 kinase), an inhibitor of translational elongation (Leprivier et al. 2013:2).

DNA Damage

DNA damage has been shown to activate AMPK in the nucleus by the Ca^{2+}-CAMKK2 pathway (Li et al. 2019). Activated AMPK phosphorylates exonuclease 1 (EXO1) at Ser746 which inhibits the recruitment of EXO1 to stressed replication forks. This mechanism safeguards aberrant fork processing and preserves genome stability. Moreover, AMPK regulates a key mediator which facilitates canonical non-homologous end joining (c-NHEJ): p53-binding protein 1 (53BP1) (Y. Jiang et al. 2021). Jiang et al. proved that AMPK-mediated phosphorylation of 53BP1 at Ser1317 promotes 53BP1 recruitment to DNA damage sites, thus promoting c-NHEJ activity for efficient double-strand break repair. The AMPK-53BP1 axis is crucial for the maintenance of genomic integrity.

Autophagy and Cell Cycle

Autophagy is the degradation of intracellular cargo by lysosomes to either remove damaged organelles or to ensure the availability of critical metabolic intermediates in case of metabolic

shortage. The discovery of lysosomes by Christian de Duve more than 60 years ago bore a new research field and earned its pioneer a Nobel Prize in Physiology or Medicine in 1974. Essential genes were termed autophagy-related genes (*ATG*). Autophagy starts with the recruitment of ATGs to phosphatidylinositol 3-kinase catalytic subunit type 3 (*PIK3C3, VPS34*) complexes. It follows the nucleation of the autophagic cargo and the formation of a vesicle trapping the cargo, termed the autophagosome. The autophagosome subsequently fuses with lysosomes forging the autolysosome where the cargo is degraded.

AMPK pulls the strings of the autophagic process at numerous critical layers. The balance between mTOR and AMPK activation not only orchestrates protein synthesis but also the autophagic machinery (Kim et al. 2011). Under nutrient-rich conditions, mTOR suppresses the autophagy regulator unc-51-like autophagy-activating kinase 1 (ULK1) (Kim et al. 2011). To survive nutrient deprivation, AMPK phosphorylates and activates ULK1 at Ser555 triggering the autophagic cascade (Egan et al. 2011; Kim et al. 2011). Weerasekara et al. propose that under hypoxia, AMPK can bypass ULK1 and directly phosphorylates ATG9A at Ser761 leading to the recruitment of ATG9A to microtubule-associated protein 1A/1B-light chain 3 (LC3)-positive autophagosomes (Weerasekara et al. 2014).

Supplementary to the control of kinases important for the initiation of the autophagic cascade, AMPK regulates VSP34 complexes which are important for vesicle trafficking and autophagic processes depending on their composition. Theses pro-autophagy VPS34 complexes include VPS34, VPS15, Beclin1 (BECN1), and the autophagic-specific subunit ATG14L (Kim et al. 2013). AMPK inhibits the non-autophagic VPS34 complexes by phosphorylating Thr163/Ser165 of VPS34. The presence of ATG14L in the pro-autophagic complexes ensures that AMPK phosphorylates BECN1 at Ser91/94 and not VPS34 which induces the formation of the autophagosome (Kim et al. 2013). Moreover, Zhang et al. determined Thr388 as another phosphorylation site on BECN1 which serves as a critical determinant for the cellular decision between autophagy and apoptosis (Zhang et al. 2016). BECN1 is phosphorylated by AMPK at Thr388 leading to increased interaction with VPS34 and ATG14L and consequently inducing autophagy (Zhang et al. 2016). Intriguingly, phosphorylation at Thr388 also inhibits the interaction of BECN1 with the anti-apoptotic protein B-cell lymphoma 2 (BCL2), releasing BCL2 which counteracts apoptosis (Zhang et al. 2016).

Another important player in autophagosome formation is the receptor for activated C kinase 1 (RACK1) which acts as a scaffold, transiently binding multiple ATG proteins at phagophore assembly sites. Phosphorylation of RACK1 at Thr50 by AMPK has been shown to enhance its direct binding to VPS15, ATG14L, and BECN1, thereby promoting the assembly of the autophagy-initiation complex (Zhao et al. 2015:1).

Transcriptional control of autophagy is governed by transcription factor E3 (TFEB) and transcription factor binding to IGHM enhancer (TFE3). They are controlled by a two-pronged system. I) mTORC1 controls TFEB and TFE3 cytosolic retention by directly phosphorylating TFEB at Ser211 (Martina et al. 2012) and Ser142 (Settembre et al. 2012) and TFE3 at Ser321 (Martina et al. 2014:3). Inhibition of mTOR by AMPK ergo leads to their nuclear import. II) Moreover, AMPK-mediated multisite phosphorylation of TFEB and TFE3 on three serine residues leads to TFEB and TFE3 transcriptional activity (Paquette et al. 2021).

Moreover, studies show the connection between autophagy and cell cycle genes which are controlled by AMPK. Liang et al. provide evidence that AMPK phosphorylates the cyclin-dependent kinase inhibitor 1B (CDKN1B, $p27^{Kip1}$) at Thr198, thereby increasing $p27^{Kip1}$ stability (Liang et al. 2007). They show that $p27^{Kip1}$ accumulation is the determinant of whether starved cells enter the autophagy cell survival pathway or undergo rapid cell death. Additionally, Dohmen et al. identified cyclin Y as an AMPK substrate, where phosphorylation of cyclin Y at Ser326 promotes its interaction with the CDK16 and stimulates its catalytic activity (Dohmen et al. 2020). Functional analysis revealed that cyclin Y/CDK16 induces autophagy.

Mitochondrial Dynamics

Mitochondria undergo fission or fusion in response to changes in cellular metabolism. Dysfunctional mitochondrial parts can be recycled by fission and subsequent mitophagy to sustain mitochondrial health.

The mitochondrial fission factor (MFF) has been revealed as a direct target of AMPK. AMPK phosphorylates MFF at Ser155 and Ser172 which serves as the receptor for the dynamin-related protein 1 (DRP1) of the mitochondrial fission machinery (Toyama et al. 2016). Once recruited, DRP1 further assembles around the mitochondrial tubule to initiate mitochondrial fission.

By global quantitative phosphoproteomic analysis, another effector of AMPK-dependent mitochondrial dynamics was identified, the armadillo repeat containing 10 (ARMC10). The work of Chen et al. shows that ARMC10 sits in the outer mitochondrial membrane and can be directly phosphorylated by AMPK at Ser45 which promotes mitochondrial fission (Chen et al. 2019).

Another crucial signaling pathway that sustains mitochondrial health is the already-mentioned AMPK-ULK1 axis. Important downstream effectors are the ubiquitin kinase Phosphatase and tensin homolog (PTEN)-induced kinase 1 (PINK1) and the Parkin RBR E3 ubiquitin protein ligase (PARK2). The activation of PINK1 is one of the earliest events in mitophagy which leads

to the subsequent recruitment of PARK2. PARK2 coats damaged mitochondria with ubiquitin which triggers mitophagy. Hung et al. found that ULK1 phosphorylates Ser108 of PARK2 in an AMPK-dependent manner. They show that this phosphorylation event is required for the phosphorylation of PARK2 by PINK1 on Ser65 initiating mitophagy (Hung et al. 2021).

The peroxisome-proliferator-activated receptor γ coactivator 1α (PGC-1α) is considered a master regulator of mitochondrial biogenesis and is described as a mediator of the transcriptional outputs triggered by metabolic enzymes including AMPK. Jäger et al demonstrated that AMPK directly phosphorylates PGC-1α at Thr177 and Ser538 which mediates an increase in PGC-1α protein action on the PGC-1α promoter (Jäger et al. 2007). In 2010 Leick et al expanded this remark and showed that PGC-1α is the crucial element through which AMPK increases GLUT4 expression (Leick et al. 2010). It is important to note that Leick et al. used AICAR as an AMPK activator and genetic studies are missing to validate their findings.

Redox Homeostasis

In addition to its energy-adjusting capabilities, AMPK acts as a redox sensor for maintaining redox homeostasis.

AMPK functions through the phosphorylation of antioxidant transcription factors including members of the FoxO transcription factor family. It was shown that AMPK phosphorylates FoxO1 at Thr649 (Yun et al. 2014) as well as FoxO3 at at least three sites (Greer et al. 2007:3) to launch FoxO-dependent transcription of ROS detoxification enzymes. It is important to mention that especially FoxO3 modulates also the expression of autophagy-related genes (Greer et al. 2007).

Moreover, AMPK directly phosphorylates NRF2 at Ser550, promoting the nuclear accumulation of NRF2 for androgen receptor (ARE) -mediated gene transcription and protection from ROS (Joo et al. 2016:2).

AMPK also indirectly monitors the GSH pool, one of the most essential redox homeostasis safeguards. GSH in its reduced form is considered to be one of the most important scavengers of ROS. Glutathione peroxidase (GPX) uses GSH to eliminate H_2O_2 -generating oxidized GSH (GSSG). NADPH is required for the regeneration of GSH. Fatty acid synthesis consumes NADPH and the inhibition of the acetyl-CoA carboxylases ACC1 and ACC2 by AMPK decreases NADPH consumption in fatty-acid synthesis while increasing NADPH production through fatty-acid oxidation (Jeon, Chandel, and Hay 2012). This, in turn, allows NADPH to be used for GSH regeneration.

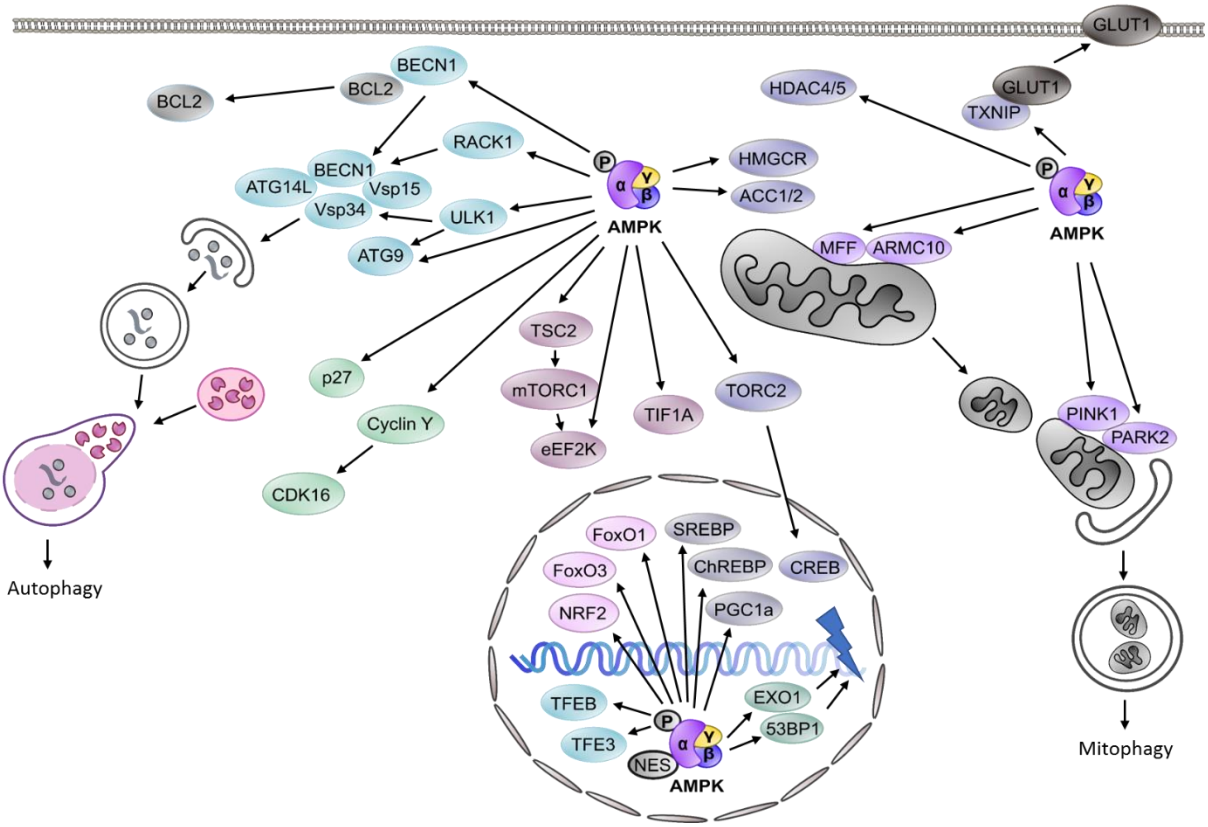

Figure 7 | Network of AMPK downstream effectors. AMPK orchestrates a wide plexus of processes to safeguard cellular homeostasis. These processes include fatty acid, cholesterol, and carbohydrate metabolism as well as protein and rRNA synthesis. Moreover, AMPK plays a role in the DNA damage response, autophagy, and cell cycle control. The contribution of AMPK in mitochondrial dynamics and redox homeostasis has also been shown. For a detailed description see the text. 53BP1: p53-binding protein 1, ACC1/2: Acetyl-CoA carboxylase 1/2, ARMC10: Armadillo repeat containing 10, ATG: autophagy-related genes, BCL2: Anti-apoptotic protein B-cell lymphoma 2, BECN1: Beclin1, CDK16: Cyclin-dependent kinase 16, ChREBPs: Carbohydrate-response element-binding proteins, DRP1: Dynamin-related protein 1, eEF2K: eukaryotic elongation factor 2 kinase, EXO1: Exonuclease 1, FoxO1/3: Forkhead box O 1/3, GLUT1: Glucose transporter 1, HDAC4/5: Histone deacetylase 4/5, HMGCR: 3-Hydroxy-3-methylglutaryl-coenzyme-A-reductase, MFF: Mitochondrial fission factor, mTORC1: Mechanistic target of rapamycin complex 1, NES: Nuclear export sequence, NRF2: nuclear factor erythroid 2-related factor 2, p27: Cyclin-dependent kinase inhibitor 1B, PARK2: Parkin, PGC-1α: Peroxisome-proliferator-activated receptor γ coactivator 1α, PINK1: PTEN-induced kinase 1, RACK1: Receptor for activated C kinase 1, SREBP: sterol-response element-binding protein, TFE3: Transcription factor binding to IGHM enhancer 3, TFEB: Transcription factor EB, TIF1A: Transcription initiation factor IA, TORC2: Transducer of regulated CREB activity 2, TXNIP: Thioredoxin-interacting protein, ULK1: Unc-51-like autophagy-activating kinase 1, Vsp34: Phosphatidylinositol 3-kinase catalytic subunit type 3

Overall, AMPK phosphorylates a broad spectrum of downstream effectors which affects almost every aspect of cellular metabolism. Depending on the subcellular location where AMPK is activated, the spectrum of downstream targets changes.

Regarding the fact that AMPK significantly shapes the metabolic plasticity of cells towards various stresses, the idea of targeting AMPK in the context of cancer has been highly discussed. The following section provides an overview of the current state of studies examining the involvement of AMPK in cancer and whether it is a rational target for therapeutic intervention.

2.3 AMPK as Chameleon in Cancer

The role of AMPK in cancer is highly controversial and AMPK has shown both, cancer-promoting and cancer-inhibiting properties.

Cancer-Suppressor

Through its well-established role in inhibiting mTOR and thereby activating a metabolic checkpoint, AMPK has been thought to be a mere tumor suppressor (Gwinn et al. 2008; Inoki et al. 2003). Moreover, AMPK phosphorylates and activates the most classical tumor suppressor there is, TP53 (Jones et al. 2005). Compelling evidence for the growth-restrictive abilities of AMPK comes also from the frequent mutation of its upstream kinase, LKB1, in various cancer types, which suggests that malignant cells need to overcome the tumor-suppressive functions of AMPK. In fact, Faubert et al. demonstrated that loss of AMPKα1 accelerates Myc-driven lymphomagenesis *in vivo*, providing further support for the role of AMPK as the gatekeeper of oncogenic metabolic rewiring (Faubert et al. 2013).

Cancer-Promoter

This one-dimensional concept which suggests AMPK to be a plain tumor suppressor has been challenged by a myriad of studies showing the aftermath of AMPK signaling is highly context-dependent.

Already in 2006, Laderoute et al. observed that the proliferation of H-Ras-transformed mouse embryonic fibroblasts was strongly impaired when AMPKa was not present manifesting in a decreased tumor volume in xenografts (Laderoute et al. 2006). Several further studies demonstrate the importance of AMPK for tumors especially under nutrient deprivation (Jeon et al. 2012; Leprivier et al. 2013) or in the presence of oxidative stress (Cai et al. 2020).

AMPK in PDAC

As in other cancer entities, the role of AMPK in PDAC is a conflicting topic among researchers in the field. Kumazoe et al. investigated AMPK in the context of the cancer stem cell compartment of PDAC (Kumazoe et al. 2017). By using a siRNA approach, they found that the LKB1 signaling is indispensable for PDAC stem cells. The growth alteration caused by LKB1 siRNA was rescued by PGC-1β and FoxO3, transcription factors crucial for mitochondrial health. Kumazoe et al. provide insight into the metabolic basis of the observed effect. By halting the TCA cycle through the knockdown of the rate-limiting enzyme pyruvate dehydrogenase E1 subunit alpha 1 (PDHA1), PDAC cells lost their stemness properties. Their work proves the importance of the LKB1-AMPK-PGC-1β-PDHA1 pathway for the acquirement of the cancer stem cell phenotype of PDAC cells. In the same year, Chen et al. published a paper proposing the opposite (Chen et al. 2017:1). According to the evaluation of IHC stainings of different stages of human PDAC, loss of AMPK activation was associated with pancreatic cancer progression. They validated their findings *in vitro* by using the siRNA approach and migration assay. They suggest that loss of AMPK promotes the activation of heat shock factor 1 (HSF1) which in turn promotes the invasion and metastasis of pancreatic cancer.

Other studies, however, have demonstrated the critical role of AMPK in responding to environmental stresses. In 2019, Hu et al. found that hypoxia induces AMPK activation (Hu et al. 2019). They used pharmacological AMPK inhibition and showed that AMPK inhibition strongly impaired the survival, migration, and invasion ability of PDAC cells upon normoxia, however, the effect was more pronounced under hypoxia.

Despite global efforts, the function of AMPK in cancer and specifically in PDAC remains incompletely understood. These studies suggest that quite subtle differences in the type of cancer, and the context of AMPK action, can markedly affect the outcome and conclusion of each study and picture AMPK to be an impeccable example of „Context matters“.

3 Kinases as Therapeutic Targets in Cancer

3.1 Lessons from Kinase Inhibitor Development

Kinase inhibitors have been successfully implemented into clinical practice and transformed cancer therapy. In 2001, Imatinib received FDA approval as the first well-characterized kinase inhibitor. Imatinib blocks the Abelson tyrosine kinase (ABL), which is expressed as a deregulated fusion protein, namely breakpoint cluster region (BCR) –ABL, in nearly all cases of chronic myeloid leukemia and has shown spectacular efficacy. Although not designed on purpose, Imatinib also inhibits two other protein kinases (the KIT proto-Oncogene receptor

tyrosine kinase (KIT) and platelet-derived growth factor (PDGF) receptors) and it has proved to be equally effective in cancers, which overexpress or express the mutated form of these kinases. Imatinib is thus a great example of the utility of polypharmacology. Polypharmacology refers to the phenomenon that a drug acts on multiple targets. Most kinase inhibitors bind to the ATP binding pocket of the enzyme which is highly conserved among kinases. The consequent promiscuous target profile of compounds has both advantages and disadvantages. By inhibiting multiple nodes belonging to a network of interacting kinases polypharmacology can enhance the efficacy of a drug. In other cases, it can also blur the discovery of the primary target and complicate linking individual targets with the observed drug effect. In some cases, the clinical efficacy might even be explained entirely by off-target effects which were initially not taken into consideration.

Traditionally, drugs were discovered by phenotypic assays or by rational design for specific targets of interest. Thus, hitherto drug discovery approaches never investigate the full potential of a particular drug or the underlying pharmacophore. In the last decades, the rise of advanced technologies in medicinal chemistry, biochemistry, mass spectrometry, and bioinformatics have significantly facilitated ligand discovery, selectivity profiling, and target identification on a proteome-wide scale. In parallel, the global information on inhibitor target profiles was integrated into public and private molecular databases. These cumulative efforts opened novel avenues for the use of polypharmacology for research purposes and for unlocking the full potential of one particular compound.

3.2 Drug Repurposing

In a study published in JAMA in 2020, the investment required to bring a new antineoplastic agent to the market was estimated to be $2771.6 million (Wouters, McKee, and Luyten 2020). These statistics are driven by multifold challenges faced by the global pharmaceutical industry and include high attrition rates and stringent regulatory requirements.

Drug repurposing is an endeavor for identifying new uses for approved or investigational drugs that are outside the scope of the original clinical use. In theory, drug repurposing could decrease drug development costs, increase drug approval rates, and decrease attrition rates while maximizing the clinical application of the repurposed molecule. Moreover, this strategy could help to target proteins of biomedical significance for which no specific inhibitor has been developed until now.

In a multitude of cases where drugs failed in clinical trials the mode(s) of action of the kinase inhibitors was insufficiently understood. This hampers the adequate use and full exploitation of these very advanced molecules. Today, we are in an era where we can characterize drugs

better than ever before which is playing to the strengths of drug repurposing. By building upon the available *in vitro*, *in vivo,* and clinical data of compounds which includes, depending on the stage of development, the target profile, pharmacokinetics, and safety properties, drug repurposing allows skipping the initial development phase thereby reducing overall costs and risks. As a consequence, compounds rapidly advance into disease-oriented research and if successful, into clinical application. Taken together, the concept of drug repurposing bears immense value to the pharma industry and more importantly to patients.

3.3 Targeting AMPK

Currently, there are only two AMPK inhibitors (AMPKi) available, namely Dorsomorphin (also known as Compound C) and BAY 3827 (as reported by Lemos et al. 2021). However, these compounds have been documented to harbor activities against off-target kinases. Dorsomorphin, for instance, has been shown to inhibit not only AMPK but also bone morphogenetic protein (BMP) signaling by targeting activin A receptor Type 1 (ACVR1), BMP receptor type 1A (BMPR1A) and BMP receptor type 1B (BMPR1B) (Yu et al. 2008). On the other hand, BAY 3827 has been described as a potent AMPK inhibitor with additional activity against ribosomal 6 kinase (RSK) family members (Lemos et al. 2021). It is important to note that both compounds have not been tested in clinical trials and are considered experimental compounds at this stage. To expedite the discovery of potential AMPK inhibitors, drug repurposing approaches could be explored, which may identify compounds that are already further along in clinical development and have the potential for fast-track clinical applications.

4 Aims

Metabolic plasticity has been widely appreciated as a crucial factor in the progression of cancer. Thus, targeting central metabolic orchestrators could have therapeutic utility. AMPK, being at the apex of the metabolic hierarchy, has been investigated in the context of cancer, however, present data on whether AMPK is a tumor-promoter or suppressor are controversial. In this thesis, I aimed to investigate the role of AMPK in PDAC. Moreover, I used the concept of drug repurposing to find a developmentally advanced AMPK inhibitor.

Material and Methods

5 Material

Table 2 | Instruments.

Instruments	Company
AS2000 Maxwell® 16 instrument	Promega, Madison, WI, USA
Axiovert 25 Inverse Microscope	Carl Zeiss, Oberkochen, Germany
Clariostar 4300741	BMG Labtech, Ortenberg, Germany
Dionex UltiMate 3000 nano HPLC System	ThermoFisher Scientific, Waltham, MA, USA
Eppendorf Multipipette E3X	Eppendorf AG, Hamburg, Germany
Eppendorf Reference/Research Pipettes	Eppendorf AG, Hamburg, Germany
FLUOstar® OPTIMA	BMG Labtech, Champigny-sur-Marne, France
Freezer	Robert Bosch Hausgeräte GmbH, Gerlingen, Germany
Fridge	Siemens AG, Munich, Germany
Horizontal shaker	Titertek Instruments, Inc., Huntsville, AL, USA
IncuCyte S3	Sartorius AG, Göttingen, Germany.
Liquid handling pin tool	V&P Scientific Inc., San Diego, CA, USA
Laminar flow HERAsafe	Heraeus Holding GmbH, Hanau, Germany
Microcentrifuge Mini Star	VWR, Radnor, PA, USA
Multi-Blot Floating E-Clip Style Replicator – 96 FP6 pins (Manual Pintool)	V&P Scientific Inc., San Diego, CA, USA
Multiskan FC	ThermoFisher Scientific, Waltham, MA, USA
NanoDrop 1000	Peqlab Biotechnologie GmbH, Erlangen, Germany
Neubauer counting chamber 0,100mm	Hecht Assistent, Sondheim an der Rhön, Germany
NextSeq 500 System	Illumina, San Diego, CA, USA
Odyssey Fc	LI-COR, Bad Homburg vor der Höhe, Germany
Orbitrap Fusion™ Lumos™ Tribrid™	ThermoFisher Scientific, Waltham, MA, USA
Stripettor ultra pipetting aid	Corning Incorporated, New York, NY, USA
T100 Thermal Cycler	Bio-Rad Laboratories GmBH, Hercules, CA, USA
ThermoMixer® C	Eppendorf AG, Hamburg, Germany

Vacuboy, Vacuum Hand Operator	Integra Biosciences AG, Zizers, Switzerland
Waterbath 1083	GFL Gesellschaft für Labortechnik mbH, Burgwedel, Germany
Western Blot System Mini-PROTEAN Tetra System	Bio-Rad Laboratories GmBH, Hercules, CA, USA
XF96e Extracellular Flux Analyzer	Agilent, Santa Clara, CA, USA

Table 3 | Kits.

Kits	Catalog Number	Company
Caspase-Glo® 3/7 Assay	G8091	Promega, Madison, WI, USA
CellTiter-Glo® Luminescent Cell Viability Assay	G7570	Promega, Madison, WI, USA
GeneJET PCR Purification Kit	K0701	ThermoFisher Scientific, Waltham, MA, USA
Maxwell® 16 LEV simplyRNA Purification Kits	AS1280	Promega, Madison, WI, USA
NEBuilder HiFi DNA Assembly Cloning Kit	E5520S	New England Biolabs., Ipswich, MA, USA
NucleoSpin Plasmid, Mini kit	740588.250	Macherey-Naggel GmbH, Düren, Germany
NucleoSpin Plasmid Transfection-grade	740490.10	Macherey-Naggel GmbH, Düren, Germany

Table 4 | Reagents.

Reagents	Catalog Number	Company
2-Deoxy-D-glucose	S4701	Selleck Chemicals, Houston, TX, USA
2-Propanol (Isopropanol)	CN09.1	Carl Roth, Karlsruhe, Germany
2-Mercaptoethanol, 98%	4227.3	Carl Roth, Karlsruhe, Germany
3,3,5-Triiodo-L- thyronine	T2877	Sigma-Aldrich, St. Louis, MO, USA
30% Acrylamide/Bisacrylamide-stock solution (29:1)	A124	Carl Roth, Karlsruhe, Germany
A83-01	72022_C	STEMCELL Technologies, Vancouver, BC, Canada
Acetic acid	6755	Carl Roth, Karlsruhe, Germany
ACK Lysing Buffer	A1049201	ThermoFisher Scientific, Waltham, MA, USA
Agarose	3810	Carl Roth, Karlsruhe, Germany

Albumin	11930.03	SERVA Electrophoresis GmbH, Rosenheim, Germany
Alkopharm absolut (Ethanol 80%)	60870	BrüggemannAlcohol Heilbronn GmBh, Heilbronn, Germany
Antimycin A	J63522.MA	ThermoFisher Scientific, Waltham, MA, USA
APS	9592	Carl Roth, Karlsruhe, Germany
Aqua	0082423E	B. Braun Melsungen AG, Melsungen, Germany
B-27	17504044	ThermoFisher Scientific, Waltham, MA, USA
Bovine Pituitary Extract	P1476	Sigma-Aldrich, St. Louis, MO, USA
Bradford reagent 5x	39222.03	SERVA Electrophoresis GmbH, Rosenheim, Germany
Bromophenol Blue	CAS 115-39-9	Santa Cruz Biotechnology, Heidelberg, Germany
BSA, Molecular Biology Grade	B6917	Sigma-Aldrich, St. Louis, MO, USA
CCCP	S6494	Selleck Chemicals, Houston, TX, USA
Cell Recovery Solution, 100 mL Corning®	354253	ThermoFisher Scientific, Waltham, MA, USA
Cholera toxin	C8052	Sigma-Aldrich, St. Louis, MO, USA
Crystal violet powder	C0775	Sigma-Aldrich, St. Louis, MO, USA
Cultrex Reduced Growth Factor Basement Membrane Extract, Type 2	3536-005-02	R&Dsystems, Minneapolis, MN, USA
Demineralized water (ddH_2O)	7732-18-5	SAV Liquid Production GmbH, Flintsbach am Inn, Germany
D-Glucose	G8270	Sigma-Aldrich, St. Louis, MO, USA
Dexamethasone	D1756	Sigma-Aldrich, St. Louis, MO, USA
Dimethylsulfoxide (DMSO)	A3672	AppliChem GmbH, Darmstadt, Germany
dNTP-Mix	331550	Biozym Scientific GmbH, Hessisch Oldendorf, Germany
DMEM/F12-500 mL	11330032	ThermoFisher Scientific, Waltham, MA, USA

DraI	R0129S	New England Biolabs., Ipswich, MA, USA
Dulbecco´s Modified Eagles Medium; high glucose	D5796	Sigma-Aldrich, St. Louis, MO, USA
Dulbecco's Phosphate Buffered Saline (PBS)	D8537	Sigma-Aldrich, St. Louis, MO, USA
EDTA (Versen) 1% (w/v) in PBS w/o CA^{2+}	L 2113	Biochrom GmbH, Berlin, Germany
Ethanol 100%	27669	Otto Fischar GmbH & Co. KG; Saarbrücken, Germany
Ethidium promide solution	E1510	Sigma-Aldrich, St. Louis, MO, USA
Fetal Calf Serum (FCS) Superior	S 0615	Sigma-Aldrich, St. Louis, MO, USA
hGastrin I	10047-33-3	Tocris Bioscience, Bristol, United Kingdom
Gateway™ LR Clonase™ II Enzym-Mix	11791100	ThermoFisher Scientific, Waltham, MA, USA
Glucose	A2494001	ThermoFisher Scientific, Waltham, MA, USA
Glutamine	25030081	Thermo Fisher Scientific, Munich, Germany
Glycerine	56-81-5	Carl Roth, Karlsruhe, Germany
Glycine	3790	Carl Roth, Karlsruhe, Germany
hEGF	E9644	Merck Schuchardt, Hohenbrunn, Germany
hFGF	100-26	PeproTech, Cranbury, NJ, USA
Immobilon Forte Western HRP substrate	WBLUF0500	Merck Schuchardt OHG, Hohenbrunn, Germany
Keratinocyte-SFM Medium (1x)	17005042	ThermoFisher Scientific, Waltham, MA, USA
LB-Agar powder	X.969.2	Carl Roth, Karlsruhe, Germany
LB-Medium powder	X968.1	Carl Roth, Karlsruhe, Germany
Lipofectamine 2000 Transfection Reagent	11668030	ThermoFisher Scientific, Waltham, MA, USA
Matrigel®, Growth Factor Reduced (GFR) Basement Membrane Matrix, LDEV-free, Corning®	354230	ThermoFisher Scientific, Waltham, MA, USA
Methanol	8388	Carl Roth, Karlsruhe, Germany
mNoggin	250-38	PeproTech, Cranbury, NJ, USA
Natrium Chloride (NaCl)	3957	Carl Roth, Karlsruhe, Germany

Natrium acide	S2002	Merck Schuchardt, Hohenbrunn, Germany
Neuregulin	100-03	PeproTech, Cranbury, NJ, USA
Nicotinamide	N3376	Sigma-Aldrich, St. Louis, MO, USA
NPO_4	74385	Sigma-Aldrich, St. Louis, MO, USA
Nu-Serum IV, Corning®	355100	ThermoFisher Scientific, Waltham, MA, USA
Oligomycin	S1478	Selleck Chemicals, Houston, TX, USA
Opti-MEM with GlutaMAX, Gibco	12559099	ThermoFisher Scientific, Waltham, MA, USA
Page Ruler Prestained Protein Ladder	26616X4	ThermoFisher Scientific, Waltham, MA, USA
Penicillin/Streptomycin	15140-122	Thermo Fisher Scientific, Munich, Germany
PF-3758309	S7094	Selleck Chemicals, Houston, TX, USA
Phosphatase inhibitor 100x	39050	SERVA Electrophoresis GmbH, Rosenheim, Germany
Polybrene Infection / Transfection Reagent	TR-1003	Sigma-Aldrich, St. Louis, MO, USA
Primocin	Ant-pm-1	Invivogen, San Diego, CA, USA
Propidium Iodide	P4170	Sigma-Aldrich, St. Louis, MO, USA
Powdered milk	T145	Carl Roth, Karlsruhe, Germany
Protease inhibitor 25x	CO-RO	Roche Diagnostics GmbH, Penzberg, Germany
rCutSmart™ Buffer	B6004S	New England Biolabs., Ipswich, MA, USA
REDTaq® ReadyMix™ PCR Reaction Mix	R2523	Sigma-Aldrich, St. Louis, MO, USA
RLT Buffer	79216	QIAGEN GmbH, Hilden, Germany
Rock inhibitor Y-27632	72304	STEMCELL Technologies, Vancouver, BC, Canada
Rotenone	S2348	Selleck Chemicals, Houston, TX, USA
PureLink™ RNase A, 10 mL, Invitrogen	1772940	ThermoFisher Scientific, Waltham, MA, USA
Puromycin	ant-pr-1	Invivogen, San Diego, CA, USA

Pyruvate	11360070	ThermoFisher Scientific, Waltham, MA, USA
Q5 High-Fidelity DNA Polymerase	M0491S	New England Biolabs., Ipswich, MA, USA
Quick-Load® Purple 1 kb DNA Ladder	N0552S	New England Biolabs., Ipswich, MA, USA
Recovery Cell Culture Freezing Medium	12648010	ThermoFisher Scientific, Waltham, MA, USA
RPMI 1640 Medium, GlutaMAX™ Supplement	61870044	ThermoFisher Scientific, Waltham, MA, USA
SDS, ultra pure	2326	Carl Roth, Karlsruhe, Germany
Seahorse XF Base Medium	102353-100	Agilent, Santa Clara, CA, USA
Sodiumdeoxychelate	D6750	Sigma-Aldrich, St. Louis, MO, USA
T4 DNA Ligase	M0202S	New England Biolabs., Ipswich, MA, USA
T4 DNA Ligase Reaction Buffer	B0202S	New England Biolabs., Ipswich, MA, USA
TRIS	4855	Carl Roth, Karlsruhe, Germany
TrypLE™ Express Enzyme (1x), 100 mL	12604013	ThermoFisher Scientific, Waltham, MA, USA
Trypsin – EDTA Solution 10x	T2610	Sigma-Aldrich, St. Louis, MO, USA
Tween 20	9127	Carl Roth, Karlsruhe, Germany
TEMED	8142	Carl Roth, Karlsruhe, Germany
V&P	VP 110A	V&P Scientific Inc., San Diego, CA, USA
XbaI	R0145S	New England Biolabs., Ipswich, MA, USA
Y-27632	HY-10071	Hycultec GmBh, Beutelsbach, Germany

Table 5 | Products.

Products	Catalog Number	Company
24-well Polypropylene Microplates, clear, Corning®	142475	ThermoFisher Scientific, Waltham, MA, USA
384-well White/Clear Bottom Polystyrene Microplates, Corning®	3765	ThermoFisher Scientific, Waltham, MA, USA

96-well Polypropylene Microplates, clear, Corning®	3343	ThermoFisher Scientific, Waltham, MA, USA
Acclaim™ PepMap™ 100 C18	164946	ThermoFisher Scientific, Waltham, MA, USA
Cell Scraper	83.1830	Sarstedt AG & Co.KG, Nümbrecht, Germany
Cellstar Cell culture bottle	660175	Greiner BIO-ONE, Kremsmünster, Austria
CELLSTAR® Polypropylen Röhrchen	227261	Greiner BIO-ONE, Kremsmünster, Austria
Costar® TC-Treated Multiple Well Plates 24-well, Corning®	CLS3527	Sigma-Aldrich, St. Louis, MO, USA
Costar® TC-Treated Multiple Well Plates 6-well, Corning®	CLS3516	ThermoFisher Scientific, Waltham, MA, USA
Eppendorf Safe-Lock Tubes, 1.5 mL	0030120086	Eppendorf AG, Hamburg, Germany
Eppendorf Safe-Lock Tubes, 2mL	0030120094	Eppendorf AG, Hamburg, Germany
Falcon® Round-Bottom Polystyrene Tubes	38055	STEMCELL Technologies, Vancouver, BC, Canada
Filtropur	20003477	Sarstedt AG & Co.KG, Nümbrecht, Germany
Gel Saver-Tip II	GSII054R	Kisker Biotech GmbH & Co. KG, Steinfurt, Germany
Nitrocellulose Blotting Membrane	10600001	Bio-Rad Laboratories GmBH, Hercules, CA, USA
PCR® MICROPLATE, Axygen	PCR-96-LP-AP-C	ThermoFisher Scientific, Waltham, MA, USA
Platemax CyclerSeal Sealing Film, Axygen	PCR-TS	ThermoFisher Scientific, Waltham, MA, USA
Safe seal tube, 1.5 mL	72.706	Sarstedt AG & Co.KG, Nümbrecht, Germany
Screw cap tube, 15 ml, (LxØ): 120 x 17 mm, PP, with print	62.554.100	Sarstedt AG & Co.KG, Nümbrecht, Germany
Screw cap tube, 50 ml, (LxØ): 114 x 28 mm, PP, with print	62.547.254	Sarstedt AG & Co.KG, Nümbrecht, Germany
Seahorse XF96 V3 PS Cell Culture Microplates	101085-004	Agilent, Santa Clara, CA, USA
Tissue-culture treated culture dishes, Corning®	CLS430599	ThermoFisher Scientific, Waltham, MA, USA
Whatman® cellulose chromatography papers	WHA3030917	Merck Schuchardt, Hohenbrunn, Germany

Table 6 | Organisms.

Organisms	Catalog Number	Company
One Shot™ Stbl3™ Chemically Competent *E. coli*	C737303	ThermoFisher Scientific, Waltham, MA, USA

Table 7 | Plasmids.

Plasmids	Catalog Number	Company
pENTR/D-TOPO	10780335	ThermoFisher Scientific, Waltham, MA, USA
pLenti PGK Puro Dest	19068	Addgene, Watertown, MA USA
pMD2.G	12259	Addgene, Watertown, MA USA
psPAX2	12260	Addgene, Watertown, MA USA

Table 8 | Buffers and Solutions.

Buffers and Solutions	Composition
0.2% Crystal violet	0.2% (w/v) Crystal Violet powder
	2% (v/v) Ethanol
KCM Buffer (5x)	0.5 M KCl
	0.15 M $MCaCl_2$
	0.25 mL $MgCl_2$
Laemmli Buffer (5x)	250 mM Tris-HCl (pH 6.8)
	4% (w/v) SDS
	40% (v/v) Glycerol
	0.05% (w/v) Bromphenolblue
	5% (v/v) β-Mercaptoethanol
LB-Agar	4% (w/v) LB-Agar powder
	100 µM (v/v) Ampicillin
LB-Medium	2.5% (w/v) LB-Medium powder
	50 µM Ampicillin
Running buffer (1x)	192 mM Glycine
	25 mM TRIS
	3.47 mM SDS
Transfer buffer (1x)	192 mM Glycine
	25 mM TRIS
	20% (v/v) Methanol

Resolving gel (7.5%)	390 mM Tris-HCl, pH 8.8
	7.5% (v/v) Acrylamide
	0.1% (v/v) SDS
	0.05% (v/v) APS
	0.05% (v/v) TEMED
Resolving gel (10%)	390 mM Tris-HCl, pH 8.8
	10% (v/v) Acrylamide
	0.1% (v/v) SDS
	0.05% (v/v) APS
	0.05% (v/v) TEMED
Stacking gel buffer	125 mM Tris-HCl, pH 6.8
	4.4% (v/v) Acrylamide
	0.1% (v/v) SDS
	0.05% (v/v) APS
	0.2% (v/v) TEMED
RIPA buffer	150 mM NaCl
	10 mM TRIS
	0.1% (w/v) Sodiumdeoxychelate
	0.1% (w/v) SDS
	1% (v/v) NPO_4
	1x Protease inhibitor
	1x Phosphatase inhibitor
TBS-T (1x) buffer, pH 7.6	20 mM TRIS
	150 mM NaCl
	0.1% (v/v) Tween 20
5% TBS-T Milk	5% (w/v) Powdered milk
	1x TBS-T
TAE Buffer, pH 8.0	40 mM Tris-HCl
	1 M EDTA
	20 mM acetic acid

Table 9 | Antibodies.

Antibodies	Dilution	Catalog Number	Company
Acetyl-CoA Carboxylase (ACC) (C83B10), rabbit	1:1,000	#3676S (RRID:AB_2219397)	Cell Signaling Technology, Danvers, MA, USA

AMPKα (D63G4), rabbit	1:1,000	#5832S (RRID:AB_10624867)	Cell Signaling Technology, Danvers, MA, USA
Anti-AMPK alpha 1 antibody [Y365]		ab32047 (RRID: AB_722764)	Abcam, Cambridge, UK
Anti-α-Tubulin (T5168), mouse	1:1,000	#89494 (RRID:AB_477579)	Sigma-Aldrich, St. Louis, MO, USA
Anti-β-Actin (A5316), mouse	1:2,000	#059M4770V (RRID:AB_476743)	Sigma-Aldrich, St. Louis, MO, USA
Phospho-Acetyl-CoA Carboxylase (P-ACC) (Ser79) (D7D11), rabbit	1:1,000	#11818S (RRID:AB_2687505)	Cell Signaling Technology, Danvers, MA, USA
Phospho-AMPKα (Thr172) (40H9), rabbit	1:1,000	#2535S (RRID:AB_331250)	Cell Signaling Technology, Danvers, MA, USA
HSP90 alpha/beta Antikörper (F-8)	1:1,000	sc-13119 (RRID:AB_675659)	Santa Cruz Biotechnology, Heidelberg, Germany
Mouse IgG (H+L chain) Rabbit Polyclonal Antibody	1:10,000	R1253HRP	OriGene Technologies, Rockville, MD, USA
Rabbit IgG (H+L chain) Goat Polyclonal Antibody	1:10,000	R1364HRP	OriGene Technologies, Rockville, MD, USA

Table 10 | Primers.

Description	Sequence	Function
muPrkaa1-pENTR-fwd	5‘ TGT ACA AAA AAG CAG GCT TTC CAC CAT GCG CAG ACT CAG TTC C 3’	Gibson Assembly of pENTR and *Prkaa1*
muPrkaa1-pENTR-rev	5‘ TTT GTA CAA GAA AGC TGG GTT TAC TGT GCA AGA ATT TTA ATT AGA TTT GC 3‘	Gibson Assembly of pENTR and *Prkaa1*
Primer PGK-fwd	5‘ GTG TTC CGC ATT CTG CAA G 3’	Sequencing of PGK Vector
Primer PGK-rev	5‘ CAT AGC GTA AAA GGA GCA ACA 3’	Sequencing of PGK Vector
5’ primer Mycoplasma I	5‘ CGC CTG AGT AGT ACG TTC GC 3‘	Mycoplasma detection
5’ primer Mycoplasma II	5‘ CGC CTG AGT AGT ACG TAC GC 3‘	Mycoplasma detection
5’ primer Mycoplasma III	5‘ TGC CTG GGT AGT ACA TTC GC 3‘	Mycoplasma detection

5' primer Mycoplasma IV	5' TGC CTG AGT AGT ACA TTC GC 3'	Mycoplasma detection
5' primer Mycoplasma V	5' CGC CTG AGT AGT ATG CTC GC 3'	Mycoplasma detection
5' primer Mycoplasma VI	5' CAC CTG AGT AGT ATG CTC GC 3'	Mycoplasma detection
5' primer Mycoplasma VII	5' CGC CTG GGT AGT ACA TTC GC 3'	Mycoplasma detection
3' primer Mycoplasma I	5' GCG GTG TGT ACA AGA CCC GA 3'	Mycoplasma detection
3' primer Mycoplasma II	5' GCG GTG TGT ACA AAA CCC GA 3'	Mycoplasma detection
3' primer Mycoplasma III	5' GCG GTG TGT ACA AAC CCC GA 3'	Mycoplasma detection

Table 11 | Software.

Software	Manufacturer/Website
Adobe Illustrator CC 2018	Adobe Inc., San José, CA, USA
Axio Vision 4.8	Carl Zeiss, Oberkochen, Germany
ChatGPT	https://chat.openai.com/
Chimera Autodock Vina	https://www.cgl.ucsf.edu/chimera/
ConfGen	Schrödinger, LLC, NY, USA
Cutoff Finder	https://molpathoheidelberg.shinyapps.io/CutoffFinder_v1/
Desmond	Schrödinger, LLC, NY, USA
Drop-seq pipeline v1.0	McCarroll Lab, Harvard Medical School, Boston, MA, USA
Epik	Schrödinger, LLC, NY, USA
FlowJo 10.8.1	BD Biosciences, Heidelberg, Germany
GeneTrail 3.0	Chair for Bioinformatics, Saarland University, Germany
Glide	Schrödinger, LLC, NY, USA
GraphPad Prism 9.00	GraphPad Software, San Diego, CA, USA
GSEA v4.3.2	https://www.gsea-msigdb.org/
Image Studio Lite Version 5.2	LI-COR Biotechnology, Lincoln, NE, USA
Inkscape 1.2.2	https://inkscape.org/
Ligprep	Schrödinger, LLC, NY, USA
Maestro	Schrödinger, LLC, NY, USA
MaxQuant v1.6.12.0	https://www.maxquant.org/
NEBuilder® Assembly Tool	https://nebuilder.neb.com/
Office 365	Microsoft Corporation, Redmond, WA, USA

PyMol	Schrödinger, LLC, NY, USA
R v4.3	https://www.R-project.org/.
SnapGene	GSL Biotech LLC, San Diego, CA, USA
Seahorse Wave Desktop Software	Agilent, Santa Clara, CA, USA
STRING 11.5	https://string-db.org/

6 2D Cell Culture

Patient-derived cell lines (PD-CLs) were kindly provided by Prof. Dr. Elisabeth Heßmann (8/1/17).

Cells were cultivated either in DMEM high glucose supplemented with 10% (v/v) FCS or in the case of primary human cell lines with Keratinocyte-SFM Medium with 10% (v/v) FCS, 0.5 mg/ml bovine pituitary extract and 0.05 ng/ml at 37°C and 5% CO2. After reaching 80-90% confluency, cells were sub-cultured. Specifically, the medium was removed, and cells were washed once with PBS before 0.05% EDTA in PBS was added to detach the cells from the flask. Cells were diluted in a pre-warmed growth medium and the cell suspension was either recultured or used for subsequent experiments. Volumes are listed in Table 12.

Table 12 | Volumes used for different flask sizes.

Flask	Culture medium [ml]	PBS [ml]	EDTA [ml]	Cryo-tubes
T25	6	3	1	2-3
T75	10	5	2	5-6
T175	25	10	3	7-9

Freezing of Cell Lines

First, the medium was discarded and cells were washed with PBS twice. 0.05% EDTA in PBS was added to detach the cells from the flask. Detached cells were resuspended with 5 ml PBS, transferred into a 15 ml falcon, and centrifuged for 5 minutes at 4°C and 1000 rpm. The supernatant was aspirated and the pellet was dissolved in a freezing medium constituting of culture medium supplemented with 20% (v/v) FCS and 10% (v/v) DMSO. In the case of primary human cell lines, the pellet was dissolved in 80% (v/v) FCS and 10% (v/v) DMSO. 1 ml of the cell suspension was transferred to each cryo-tube. Cells were stored at -150°C until the next use.

Thawing of Cell Lines

Cryo-tubes with frozen cells, stored at -150°C, were quickly thawed in a prewarmed water bath. The thawed cell suspension was transferred to a 15 ml falcon with 5 ml PBS and centrifuged for 5 minutes at 4°C and 1000 rpm. The supernatant was aspirated and the pellet was dissolved in 6 ml of culture medium which was transferred to a T25 flask for culturing.

7 3D Cell Culture

The establishment and culturing of patient-derived organoids (PDOs) were performed as described by (Orben et al. 2022) or as described in the next section. The primary patient-derived PDAC organoids were isolated from resected primary pancreatic cancer following the Tuveson protocol. Tumor samples were obtained from the Institute of Pathology at the University Medical Center Göttingen (UMG), and the primary PDAC tissue underwent molecular characterization at the Institute of Human Genetics (UMG) through gene panel sequencing. To cultivate the primary patient-derived PDAC organoids, cells were resuspended in Matrigel Growth Factor Reduced (GFR) Basement Membrane Matrix-Phenol Red-free-LDEV-free in 24-well plates. Cultivation medium was added after Matrigel solidification. PDO media consisted of Advanced DMEM/F-12 medium, supplemented with 10 nM HEPES, 1X-GlutaMAX, 0.1% BSA, 10% R-spondin1-Conditioned medium (R-spondin1-Conditioned medium overexpressing cell line HEK293T, provided by the Institute of Pathology at the University Medical Center Göttingen (UMG)), 1x B-27, 10 nM Nicotinamide, 1.25 mM 100 ng/mL hFGF10, 10 nM hGastrin I, 500 nM A83-01, 10.5 µM Y-27632. PDOs were maintained at 37°C and 5% CO_2.

8 Mycoplasma Testing

Routine testing for Mycoplasma infections was performed every month by a multiplexed PCR-based method. To generate the DNA template, 2 ml of the culture medium from the confluent cell culture was centrifuged at 250 g for 2 minutes. The supernatant was transferred to a new 1.5 ml tube and centrifuged again at 20.000 g for 10 minutes. The pellet was resuspended in 50 µl PBS and heat-inactivated at 95 °C for 3 minutes. Primers for PCR are listed in Table 10. Premixes of 5’ primers and 3’ primes were prepared before the PCR. For the 5’ primer premix, 10 µl of each 5‘ primer and 30 µl ddH_2O were mixed. For the 3’ primer premix, 10 µl of each 3‘ primer and 70 µl ddH_2O were mixed. To perform the PCR, 15µl Premix, 2 µl 5´primer dilution, 2 µl 3´primer dilution, and 9 µl ddH_2O were mixed before adding 2 µl of the template. PCR program is depicted in Table 13.

Table 13 | Mycoplasma PCR program.

Temperature	Time	Cycles
95°C	15 minutes	
95°C	1 minutes	x40
60°C	1 minutes	
74°C	1minutes	
72°C	10 minutes	
25°C	Pause	

9 CellTiter-Glo® Luminescent Cell Viability Assay

Growth Curves

To determine the growth rate of cell lines, 1000 cells per well were seeded in 100 µl of growth medium in at least technical triplicates in white 96 well plates. After 24-hour intervals, 25 µl of CellTiter-Glo® Reagent prepared according to the manufacturer's instructions was added to each well and incubated for 20 minutes on an orbital shaker protected from light. Luminescence was measured on a microplate reader. Experiments were performed in technical triplicates and at least in biological triplicates.

Pharmacotyping of 2D Cell Lines

For pharmacotyping of 2D cell lines, 1000 cells per well were seeded in a white 96 well plate in 100 µl of growth medium. After 24 hours of incubation at 37°C and 5% CO_2, cells were treated with 20 µl of drug dilution per well. After a further 72 hours of incubation at 37°C and 5% CO_2, 25 µl of CellTiter-Glo® Reagent prepared according to the manufacturer's instructions was added to each well and incubated for 20 minutes on an orbital shaker protected from light. Luminescence was measured on a microplate reader. Experiments were performed in technical triplicates and at least in biological triplicates.

Pharmacotyping of 3D Cell Lines

The pharmacotyping experiments of PDOs were performed as described by (Orben et al. 2022) as described in the next section. PDOs were digested to a single-cell suspension using TrypLE Express Enzyme. 1250 cells/well were mixed in a total volume of 50 µl/well containing 10% of Cultrex Reduced Growth Factor Basement Membrane Extract, Type 2 and seeded into 384 well white plates for cell viability assays. After 24 hours, cells were treated with 10 µl of drug dilution. All plates were incubated at 37°C and 5% CO_2. After 72 hours of treatment, cell viability

was measured by adding 15 µl of CellTiter-Glo® Luminescent Assay. Luminescence was measured using a plate reader.

10 Life Cell Imaging

For life cell imaging, 1250 cells per well were seeded in a clear 384 well plate and treated as described above. The plates were incubated for 7 days without media change and imaged using Incucyte® SX5 Live-Cell Analysis System (Sartorius), standard software, every 4 hours.

11 Clonogenic Assay

To analyze the long-term effects of drug treatments and genetic knockouts on cell survival and proliferation, clonogenic assays were performed. Volumes for specific well sizes are listed in Table 14.

Table 14 | Volumes used for different well plates.

Well plate	Medium [ml]	Drug [ml]	Total Medium [ml]	Crystal violet [µl]	1% SDS
6	2	1	3	750	1.5 ml
12	1	1	2	500	1 ml
24	0.5	0.5	1	200	600 µl
48	0.25	0.25	0.5	100	300 µl

Cells were seeded in 6, 12, 24, or 48 well plates and after 24 hours, inhibitors were added. When the control wells were 80-90% confluent (about 7-10 days after seeding), the medium was removed and the cells were washed with PBS twice followed by the addition of crystal violet solution and incubation on a shaker for 10 minutes at room temperature. Then the plates were washed with ddH_2O until clean, air-dried, and scanned for visualization. For quantification, 1% SDS was added to each well and the plate was incubated on a shaker until the stain was completely solubilized. Absorbance measurements were performed at 570 nm in a photo spectrometer.

12 Drug Screening

The cherry-picked compound library was purchased from Selleck Chemicals. Drugs were chosen based on their previously discovered effectiveness in pancreatic cancer cells. The compound library was diluted in 384 well plates in DMSO in 7 concentrations of each compound to attain the following final treatment concentrations: 10 µM, 3.3 µM, 1.1 µM,

0.37 µM, 0.12 µM, 0.04 µM, 0.014 µM and DMSO as control. For each cell line, the optimal cell number was determined by growth curves. For each screen, cells were seeded in white 96 well plates in 100 µl culture medium using a Multidrop Combi dispenser (ThermoFisher). The screening was conducted as one biological replicate performed as technical duplicates. After 24 hours of incubation, cells were treated with the diluted compound library using a liquid handling manual pin tool according to the following steps. Each cleaning step includes 3x dipping in the designated solution and 15 seconds of drying on a blotting paper afterward. Before each screen and at the end, the pin tool was cleaned according to the left flow chart in Figure 8. During drug treatment, the pin tool was cleaned according to the right flow chart in Figure 8. For the drug treatment, the pin tool was dipped 3x in each drug library plate and directly dipped 3x in the 96 well plate.

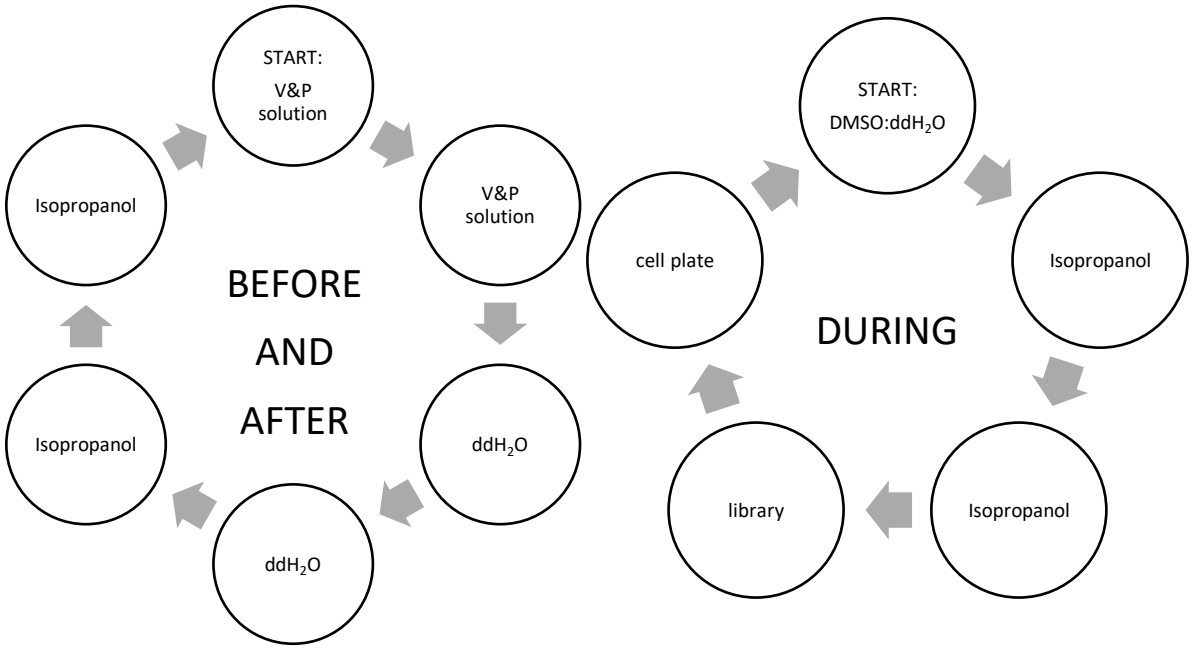

Figure 8 | Usage of liquid handling manual pin tool. Left: The pin tool underwent the following cleaning procedure before and after usage. First, it was dipped three times in a V&P solution and left to dry for 15 seconds on Whatman paper. This step was repeated once. Then, the pin tool was dipped three times in ddH_2O and again left to dry for 15 seconds on Whatman paper. This step was also repeated once. Finally, the pin tool was dipped three times in isopropanol and left to dry for 15 seconds on Whatman paper. Again, this step was repeated once. **Right:** The drug screen was conducted using the following procedure. Initially, the pin tool was dipped three times in a solution of DMSO:ddH_2O (1:1) and then left to dry for 15 seconds on Whatman paper. Subsequently, the pin tool was dipped three times in isopropanol and again left to dry for 15 seconds on Whatman paper. Following that, the pin tool was dipped three times in the compound library and then dipped three times in the cell plate.

To control for differing growth rates, cell viability was also measured 24 hours after seeding, and doubling times in hours were calculated by dividing cell viability at the endpoint by the cell

viability 24 hours after seeding. Cell viability was measured using the CellTiter-Glo® Luminescent Assay (Promega) as described in section 9.

Dose-response curves were generated using the R package GRmetrics. Only drugs for which a sigmoid curve could be fitted (coefficient of determination, $r2>0.9$, $p<0.05$) were considered for further analysis. Half maximal inhibitory concentration (IC50) and area under the curve (AUC) were used as drug sensitivity measures. For each modified cell line and its corresponding control cell line, the fold change of the IC50 (FC(IC50)) and delta AUC (ΔAUC) were calculated, and drugs were ranked according to these measures. Drug sensitivity parameters are summarized in Table 22 and 23.

13 Caspase 3/7 Assay

To evaluate apoptosis, 1000 cells per well were seeded in 100 µl of growth medium in a white 96-well plate. After 48 hours, the caspase 3/7 assay (Promega) was used according to the instructions provided by the manufacturer. Experiments were performed as two technical replicates and three biological replicates.

14 Seahorse Assay

Glycolysis Stress Test

XF96e Extracellular Flux Analyzer was used to evaluate the rate of extracellular acidification in cells. The manufacturer's instructions for the Seahorse XF Glycolysis Stress Test Kit User Guide (103020-400, Agilent Technologies) were followed when completing the assay. For this assay, 35,000 cells were plated on a Seahorse Plate. The next day, XF DMEM Buffer (supplemented with 1 mM pyruvate and 2 mM glutamine) was used to test the media's initial acidification, and subsequent extracellular acidification rate (ECAR) measurements were taken after the addition of 10 mM glucose, 3 mM oligomycin, and 50 mM 2-deoxy-D-glucose.

Mito Stress Test

According to instructions provided by the manufacturer in the Seahorse XF Cell Mito Stress Test Kit User Guide (103016-400, Agilent Technologies), the Seahorse XF96e Extracellular Flux Analyzer was used to measure the oxygen consumption rate (OCR) in cells. For the analysis, 35,000 cells were plated onto a Seahorse Plate. The next day, in XF DMEM buffer supplemented with 1 mM pyruvate, 2 mM glutamine, and 10 mM glucose, baseline respiration

was assessed. Following the addition of 3 M Oligomycin, 1.5 M CCCP, and 0.5 M Antimycin/Rotenone, OCR was further measured under varying metabolic conditions.

15 Transcriptomic Analysis

mRNA Isolation

For RNASeq, cells were seeded in 6-well plates. Cell numbers were adjusted to their growth rate. mRNA extraction was performed on ice. The growth medium of cultured cells was discarded, and cells were washed twice with 500 µl PBS. Cell extracts were obtained using 300 µl of 1x RLT buffer containing 1:100 β-Mercaptoethanol per well of a 6-well plate. Cells were scraped from the plate, transferred to 1.5 ml tubes, and isolated using the Maxwell 16 LEV simplyRNA Tissue Kit, following the manufacturer's instructions. RNA concentration was measured using a Nandrop spectrophotometer and samples were stored at -80°C.

Bulk RNA-Seq

RNA-Seq was performed at the Sequencing Core Unit at the TranslaTUM, Technical University Munich (TUM) or the NGS Integrative Genomics Core Unit, University Medical Center Göttingen (UMG).

For the RNASeq performed at the Sequencing Core Unit at the TranslaTUM, library preparation for bulk-sequencing of poly(A)-RNA was done as previously described (Parekh et al. 2016). Subsequent steps were performed as previously published (Krauß et al. 2022:2). For the RNASeq performed at the NGS Integrative Genomics Core Unit, University Medical Center Göttingen (UMG), sequence images were transformed with Illumina software BaseCaller to BCL files, which was demultiplexed to fastq files with bcl2fastq v2.20. The sequencing quality was asserted using FastQC (http://www.bioinformatics.babraham.ac.uk/projects/fastqc/). Sequences were aligned to the reference genome Homo sapiens (GRCh38.p13, https://www.ensembl.org/Homo_sapiens/Info/Index) using the RNA-Seq alignment tool (Dobin et al. 2013) (version 2.7.8a) allowing for 2 mismatches within 50 bases. Subsequently, read counting was performed using featureCounts (Liao, Smyth, and Shi 2014).

RNA-Seq analysis was performed with R-Studio (R version 4.0.2 (2020-06-22), open-source license) and DEseq2. Genes with sum (read counts) < n (sequenced samples) were removed and the remaining counts were normalized and transformed using regularized log

transformation (rlog) implemented in the DEseq2 package. RNA-Seq can be accessed by PRJEB63203.

Cluster Analysis

Analysis of RNA-Seq of murine *Kras*^{G12D} cell lines (n=38) was based on data generated by the Rad lab (Mueller et al. 2018). Information for metastasis formation (No, Yes), the grading of the respective tumors (Undifferentiated, G3, G2, G1) and murine PDAC clusters (mClusters) (C1, C2a, C2b, C2c, outlier) were derived from the mentioned publication. The cellular morphology (mesenchymal, quasi-epithelial, quasi-mesenchymal, epithelial) of the cell lines was determined by microscopic investigation. AMPK subunits were hierarchically clustered (method: average, distance: euclidean) and the resulting cluster tree was stratified into three main clusters.

GSEA

For gene set enrichment analysis (GSEA) between groups, the open-source tool GSEA v4.3.2 was used. For single sample GSEA (ssGSEA), the R package GSVA (Hänzelmann, Castelo, and Guinney 2013) was used. Genesets HALLMARK and KEGG were downloaded from the MSigDB homepage (RRID:SCR_016863).

scRNA-Seq Analysis

Single cell nuclear transcriptomic data of 43 primary PDAC tumor specimens was downloaded from GSE202051. H5ad files were converted to H5seurat files with R (V. 4.2.2) and Rstudio (V. 2023.3 using the packages Seurat (V. 4.3.0) and SeuratDisk (V. 0.0.0.9020). Subsequent analyses were performed with package Seurat (V. 4.3.0). Cell subtypes were filtered for untreated cells according to the provided annotations using the subtype function of Seurat. Additionally, the percentage of expressed mitochondrial genes was determined using PercentageFeatureSet(data pattern ="^MT-") and cells with mitochondrial genes > 5% were filtered out. Principle component analysis (PCA) was performed using the subsetted data with npcs=40. Subsequently, UMAP was performed with dims=1:20 and reduction “pca”. Visualization of single cells and *PRKAA1* expression density was performed using the additinal packages Nebulosa (V. 1.8) and viridis (V. 0.6.2) and the functions DimPlot, plot_density (reduction=”umap” and provided annotations) as well as DotPlot.

16 Western Blot

Protein Extraktion

Protein extraction was performed on ice. Growth medium of cultured cells was discarded, and cells were washed twice with PBS. Cell extracts were obtained using 100 µl of 1x RIPA buffer containing 1x protease-inhibitor as well as 1x phosphatase inhibitor per 10 cm cell culture dish. Cells were scraped from the plate, transferred to 1.5 ml tubes, centrifuged for 15 minutes at 4°C and 16,000x g and the supernatant was stored at -80°C.

Bradford Assay

The protein concentration of cell extracts was estimated using Bradford assay. 300 µl of 1x Bradford reagent (diluted 1:5 in ddH_2O from stock) was pipetted in each well of 96 wells plates. The standard curve was computed with 0, 0.5, 1, 2, 4, and 8 µg of BSA standard. 1 µl of protein extract was added to each well in triplicates. Absorbance measurements were performed at 595 nm in a photospectrometer and subsequently, the extinction coefficient was calculated. Protein extracts were adjusted to desired protein concentrations in 1x Laemmli buffer.

SDS-PAGE and Western Blotting

For sodium dodecyl sulfate–polyacrylamide gel electrophoresis (SDS-PAGE), the Western Blot System Mini-PROTEAN Tetra System (Bio-Rad, Hercules, California, USA) was used. Depending on the protein size, 7.5-12% gels were prepared according to Table 8. The gels were run with 1x running buffer (192 mM Glycine, 25 mM TRIS, 3.47 mM SDS) for 2-3 hours at 80-120 V. For Western blotting, gels were transferred onto nitrocellulose membranes in 1x transfer buffer (192 mM Glycine, 25 mM TRIS, 20% (v/v) Methanol) for 2 hours at 350 mA. To minimize unspecific antibody binding, membranes were blocked with 5% skim milk in 1x TBS and subsequently incubated with a primary antibody overnight at 4°C. Prior to incubation with a secondary antibody for 2 hours at room temperature, the membranes were washed with 0.1% Tween in 1x TBS 3 times for 15 minutes. After incubation with the secondary antibody, the washing steps were repeated as described before. Depending on the fluorescent secondary antibody used, membranes were scanned with Odyssey Fc at 488 nm, 700 nm, or 800 nm to visualize specific protein bands. To detect chemiluminescent secondary antibodies, membranes were incubated in HRP substrate for 10 seconds before scanning with ChemiDoc MP (Bio-Rad). For quantification, Image Studio Light version 5.2 software was used. For phosphorylation level analysis, the same lysates were transferred to two separate membranes and incubated either with phospho- or pan-antibodies. First, phospho- and pan-bands were

normalized each to their respective loading control. Subsequently, the relative phosphorylation levels were calculated. Antibodies and dilutions can be found in Table 9.

17 Kinobead Assay

Dose-dependent competition pulldown assays using kinobeads ε were performed as previously described (Reinecke et al. 2019). In brief, cell lysate (2.5 mg protein per pulldown) was incubated with different concentrations of compound solution (0.3 nM, 1 nM, 3 nM, 10 nM, 30 nM, 100 nM, 300 nM, 1000 nM, 3000 nM, 30000 nM) or vehicle for 45 min at 4 °C. Subsequently, the pulldown assay was performed by adding beads to the compound-incubated lysate for another 30 minutes at 4 °C. Enriched proteins were reduced and alkylated for 30 minutes at room temperature using 50 mM DTT and 50 mM CAA, respectively, followed by tryptic on-bead digest at 37 °C overnight. Peptides were eluted and desalted on C18 material, dried down and stored at -20 °C until measurement. From the vehicle experiment, unbound proteins were subjected to a second pulldown experiment with fresh beads ('pulldown of pulldown', PDPD). This allows to estimate the protein depletion from the lysate upon the pulldown experiment and enables the calculation of apparent Dissociation constant (Kd) values (Kdapp) from effective concentration 50 (EC50) values as described by Heinzlmeir (Heinzlmeir, Stephanie 2017).

Liquid chromatography-Tandem mass spectrometry (LC-MS/MS) measurement was carried out on a micro-flow LC system built by combining a modified Vanquish pump with the autosampler of the Dionex UltiMate 3000 nano HPLC System (Thermo Scientific) coupled to an Orbitrap Fusion Lumos Tribrid instrument (Thermo Scientific). Dried peptides were reconstituted in 0.1% formic acid and loaded directly onto an Acclaim PepMap 100 C18 column (2 µm particle size, 1 mm ID × 150 mm, Thermo Scientific) heated at 55 °C. Samples were separated using a 15-min linear gradient of 7-32% solvent B (solvent A: 0.1% formic acid, 3% DMSO in HPLC grade water; solvent B: 0.1% formic acid, 3% DMSO in ACN) at a flow rate of 50 µl/minutes. Peptides were ionized using an electrospray voltage of 3.5 kV, a capillary temperature of 325 °C, and a vaporizer temperature of 125 °C. Sheath, aux and sweep gas were used at a flow rate of 32, 5, and 0, respectively. MS1-spectra were acquired in the orbitrap at a resolution of 120,000 using a maximum injection time of 50 ms and an AGC target value of 4x10e5. Ions were fragmented by high energy collisional dissociation (HCD) using a normalized collision energy of 35. MS2-spectra were acquired in the linear ion trap in rapid scan mode using a maximum injection time of 10 ms and an automatic gain control (AGC) target value of 1x10e4. The cycle time was 0.6 s, with isolation windows of 0.4 m/z and dynamic exclusion of 12 s.

For identification and quantification of peptides and proteins, raw files were searched against the UniProtKB Mouse Reference Proteome database (UP000000589, downloaded on April 20th 2022) using MaxQuant (v1.6.12.0), with label-free quantification (LFQ) and 'match-between-runs' enabled. The results were filtered for potential contaminants, reversed hits and proteins identified only by post-translational modifications (PTMs). For data analysis, LFQ intensities were normalized to vehicle control to retrieve residual binding at each drug dose. The resulting ratios were fitted to a four-parameter log-logistic regression model using the 'drc' package in R to retrieve curve parameters. The mass spectrometry proteomics data will be deposited to the ProteomeXchange Consortium (http://proteomecentral.proteomexchange.org) via the massIVE data repository (https://massive.ucsd.edu/) and can be accessed via the identifier MSV000092202 (reviewer account: MSV000092202_reviewer, password reviewers_access).

18 Cloning

Agarose Gel Electrophoresis

For agarose gel electrophoresis, 1.5% agarose gels were used. Therefore, a 1.5% agarose gel solution with 1x TAE buffer was microwaved until the agarose was completely dissolved. 0.5 µg/µl ethidium bromide was added to the cooled agarose gel solution. Next, the gel solution was poured into the assembled gel tray with combs in place to create wells for loading. Following polymerization, the gel was placed in an electrophoresis chamber, covered with 1x TAE buffer supplemented with 0.5 µg/µl ethidium bromide. Samples with 1x loading dye (Thermo Fisher Scientific), as well as Quick-Load® Purple 1 kb DNA Ladder (New England Biolabs), were loaded onto the gel. The gels were run for 1.5-2 hours at 120 V (or until sufficient separation). Using a UV transilluminator, DNA fragment bands were visualized.

Insert DNA Isolation

Murine PDAC cells were cultured as described. To harvest cells, the growth medium of cultured cells was discarded, and cells were washed twice with PBS. Cells were scraped from the plate, transferred to 1.5 ml tubes, and centrifuged for 15 minutes at 4°C and 16,000x g, the supernatant was discarded and the cells were stored at -80°C. 100 µl of 50 mM NaOH was added and tubes were placed in a heat block at 100°C for 30 minutes. Afterward, 30 µl 1 M TRIS pH 7.4 were added to neutralize.

Vector Linearization

The pENTR vector was linearized by restriction digest with XbaI and DraI (New England Biolabs) according to the manufacturer's instructions. Briefly, 1 µg pENTR plasmid DNA was mixed with 5 µL 10x CutSmart Buffer (New England Biolabs), 1 µL XbaI, 1 µL DraI in 50 µl reaction volume adjusted with H_2O and incubated at 37°C for 60 minutes.

HiFi DNA Assembly

NEBuilder HiFi DNA Assembly Cloning Kit (New England Biolabs) is an improved version based on the principle of Gibson assembly. Gibson assembly is an *in vitro* recombination method created by Daniel G. Gibson (Gibson et al., 2009) for assembling multiple overlapping DNA molecules in one reaction. For HiFi DNA assembly, the following steps were performed. Overlapping ends of DNA fragments which are required for HiFi DNA assembly were generated by PCR and specifically designed primers. These PCR primers require two components, an overlap sequence that is complementary to adjacent fragments and a gene-specific sequence that is required for PCR-amplification of the target sequence. For the design of primers, NEBuilder® Assembly Tool was used (https://nebuilder.neb.com/). PCR primers were purchased from Eurofins and are listed in Table 10. Fragments were amplified using Q5 High-Fidelity DNA Polymerase (New England Biolabs) and the designed primers. Reactions were set up on ice according to Table 15.

Table 15 | Components of Gibson Assembly.

Components	**Amount**
Q5 Reaction Buffer (5x)	5 µl
10 mM dNTPs	0.5 µl
10 µM Forward primer	1.25 µl
10 µM Reverse primer	1.25 µl
Template cDNA: 1 ng-1 µg	Plasmid: 1 pg-1 ng
Q5 High Fidelity DNA Polymerase	0.25 µl
Q5 High GC Enhancer (5 x)	5 µl
Nuclease-free H_2O	To 25 µl

Reactions were gently mixed, spun, and transferred to a PCR machine. For thermocycling, the PCR program in Table 16 was used.

Table 16 | Thermocycling conditions for PCR using Q5 High-Fidelity DNA Polymerase.

Temperature	Time	Cycles
98°C	1 minutes	
98°C	10 seconds	x35
50-72°C	30 seconds	
72°C	30 seconds/kb	
72°C	2 minutes	
4°C	Pause	

PCR products were verified by agarose gel electrophoresis. Prior to assembly, PCR fragments were purified using GeneJET PCR Purification Kit (Thermo Fisher Scientific) and concentrations were measured using a Nanodrop. In the final step, PCR products and restriction enzyme-digested vectors are assembled using NEBuilder HiFi DNA Assembly Master Mix (New England Biolabs). For optimal efficiency of the reaction, 75-100 ng of vector with 2-fold excess of insert were used. Reactions were set up on ice according to Table 17 and subsequently incubated in a thermocycler for 15-30 minutes at 50°C.

Table 17 | Components for HiFi DNA Assembly.

Components	Amount
DNA Molar Ratio	vector:insert = 1:2
Total amount DNA	0.03-0.2 pmol
NEBuilder HiFi DNA Assembly Master Mix (2 x)	5 µl
Deionized H_2O	5-x µl

Until transformation, samples were stored on ice.

Gateway Cloning

After assembly of *Prkaa1* into the pENTR entry vector, the *Prkaa1* insert was shuttled into the destination vector pLenti PGK Puro Dest (#19068) via Gateway Cloning using the Gateway® LR Clonase® II enzyme mix (Thermo Fisher Scientific) according to the manufacturer's instructions. 100 ng of the pENTR-vector with the *Prkaa1* insert sequence were mixed with 100 ng of the destination vector and adjusted with H2O to a volume of 8 µL. Next, 2 µL of LR Clonase enzyme were added and incubated at 25°C for 2 hours. Until transformation, samples were stored on ice.

KCM-based Transformation

For amplification of the assembled plasmids, the plasmids were introduced into competent Stbl3 bacteria by KCM-based transformation. Specifically, Stbl3 bacteria were thawed on ice and transformation was performed according to Table 18.

Table 18 | Protocol for KCM-based transformation.

Components	Volume
KCM buffer	20 µl
ddH_2O	75 µl
HiFi assembly reaction	5 µl
Stb3 bacteria	100 µl

The transformation mix was first incubated for 20 minutes on ice and subsequently for 10 minutes at room temperature. Then, 1 ml LB-Medium was added and incubated for 1 hour at 30/37°C and 600 rpm. 100 µl of transformed bacteria were spread on prewarmed selection LB-agar plates supplemented with 100 µg/ml ampicillin. Plates were incubated overnight at 30/37°C depending on the appropriate growth temperature of the vector. Plates were subsequently screened for positive clones by colony-PCR and stored at 4°C.

Colony-PCR

To verify the insert of interest was incorporated into the vector, colony-PCR was performed. Following PCR and agarose gel electrophoresis, successfully transformed colonies are identified based on the predicted size of the PCR amplicons. A reaction master mix was prepared on ice according to Table 19.

Table 19 | Components for colony-PCR of 25 µl reaction.

Components	Amounts
Primer fwd/rev (10 µl)	1 µl each
S-Mix	12.5 µl
Deionized H_2O	to 25 µl

Single colonies were picked with a 10 µl tip and rinsed in a PCR tube with 25 µl of PCR-mix each. Afterward, the 10 µl tip was thrown into 14 ml round bottom tubes with 6 ml liquid LB-medium supplemented with 50 µg/ml ampicillin. The PCR was performed in a thermocycler according to the PCR program shown in Table 20.

Table 20 | Thermocycling conditions for colony-PCR.

Temperature	Time	
95°C	3 minutes	
95°C	45 seconds	40x
50°C	1 minutes	
72°C	1 minutes 30 seconds	
72°C	2 minutes	
4°C	Pause	

Finally, positive colonies holding the assembled plasmid were identified by agarose gel electrophoresis. The already occulated LB-medium with the colonies was used in the next step for plasmid DNA isolation.

Plasmid DNA isolation and Sequencing

To isolate plasmid DNA of bacteria, 6 ml liquid LB-medium supplemented with 50 µg/ml ampicillin in 14 ml round bottom tubes were prepared. A single bacterial colony was picked and transferred to each tube. The tubes were incubated for 12 hours at 200 rpm at 30/37°C depending on the vector. 4 ml of each overnight culture was then used for plasmid DNA isolation by NucleoSpin® Plasmid kit (MACHEREY-NAGEL GmbH & Co.). DNA concentration was estimated by measuring the absorbance at 260 nm (A260) in a nanodrop. Isolated good-quality plasmids were sent for Sanger sequencing to ensure the nucleotide sequence of the insert was correct. Sequencing files were downloaded and SnapGene software as well as Basic Local Alignment Search Tool (httpa://blast.ncbi.nlm.nih.gov/Blast) was used for sequence analysis. The pLenti PGK puro *Prkaa1* construct was deposited to Addgene (#204356).

19 Lentiviral transduction

HEK293 cells were seeded in a T75 flask. On the following day, the transduction cocktail was prepared. First, 1.1 µg/µl psPAX2, 0.46 µg/µl pMD2.G, and 2 µg of the plasmid diluted in 10 µl H_2O were mixed and added to 270 µl of Opti-MEM which was finally supplemented with 18 µl Lipofectamine. The cocktail was incubated at room temperature for 30 minutes and subsequently added to the HEK cells. After 24 hours of incubation, the transduction cocktail was removed and DMEM with 30% (v/v) FCS was added. The lentivirus-containing

supernatant was harvested after 24 and 48 hours, centrifuged at 500 g for five minutes, filtered and stored at -80°C.

For lentiviral transduction, 100,000 cells were seeded in a 6-well plate. The next day, the media was replaced with 1 ml of the lentivirus-containing medium with 8 µg/ml Polybrene. After 8 hours, 1 ml of culture medium was added. After 24 hours, the medium was changed to a culture medium. After additional 24 hours, transduced cells were selected with the respective selection marker. A control well with untransfected cells was treated with the selection marker as well to control for optimal selection time.

20 Immunohistochemistry

Immunohistochemistry Staining

Immunohistochemistry (IHC) was performed using a Bond RXm system (Leica, Wetzlar, Germany, all reagents from Leica) with a primary antibody against AMPKα (Clone Y365, Dilution 1:400) as well as P-AMPKα (Clone Thr172, Dilution: 1:100). Briefly, slides were deparaffinized using deparaffinization solution. For AMPKα the tissue samples were pretreated with Epitope retrieval solution 1 (corresponding to citrate buffer pH 6) for 30 minutes, for p-AMPKα Epitope retrieval solution 2 (corresponding to EDTA buffer pH 8) was applied for 30 minutes. Antibody binding was detected with a polymer refine detection kit without post primary reagent and visualized with DAB as a dark brown precipitate. Counterstaining was done with hematoxyline.

Descriptive Semiquantitative Score for P-AMPKa and AMPKa Immunohistochemistry

IHC staining for AMPKα and p-AMPKα was performed on Tissue Microarrays (TMA) of 107 patients (cohort previously described; (Noll et al. 2016)) with PDAC. The IHC slides were evaluated in relation to the intensity of the staining reaction and proportion of positive tumor cells. Regarding the intensity, we discriminated between negative, low, medium, high cytoplasmic staining of tumor cells.

21 Docking Analysis

For the docking study, the structures of AMPKα, CDK7, and PAK4 (Table 21) were downloaded from the Protein Databank (http://www.rcsb.org). The inhibitor PF-03758309 has been cocrystallized with PAK4 (PDB ID 2X4Z) and was used to test the docking method. The

following steps of protein preparation were executed using the graphical user interface of Maestro (Schrödinger, LLC 2021e). Subsequently, Schrödinger's Protein Preparation Wizard was used to prepare the protein structures for ligand docking by adding hydrogen atoms, filling in missing side chains, capping the chains' termini, and optimizing the hydrogen bond network (at pH 7.4) (Epik, Schrödinger, LLC 2021; Madhavi Sastry et al. 2013). Finally, an energy minimization step was executed using OPLS 2005 as a force field (Harder et al. 2016; Jorgensen, Maxwell, and Tirado-Rives 1996; Jorgensen and Tirado-Rives 1988; Shivakumar et al. 2010). The prepared structure was solvated with the aid of TIP3P water molecules and neutralized with chloride ions in an orthorhombic box with a margin of 10 Å to the protein surface. Desmond was used afterward in order to perform an additional energy minimization step in the presence of water (Bowers et al. 2006; D.E; Shaw Research 2021). The minimized protein-ligand-complex served as a template for generating the receptor grid assigning the docked inhibitor as the center of the grid. All inhibitor structures for docking were prepared using Schrödinger's Ligprep (Schrödinger, LLC 2021d) in standard settings including Epik (Greenwood et al. 2010; Schrödinger, LLC 2021b; Shelley et al. 2007) for the generation of ionization states and utilizing the OPLS 2005 force field. Confgen was used afterward to generate 64 diverse conformers per inhibitor (Schrödinger, LLC 2021a; Watts et al. 2010). These conformers served as an input for the subsequent docking procedure for which Schrödinger's Glide was used in Standard Precision (SP) mode (Friesner et al. 2004, 2006; Halgren et al. 2004; Schrödinger, LLC 2021c). Resulting binding poses were visualized using PyMOL (Schrödinger, LLC n.d.) and MOE 2019.01 (Chemical Computing Group ULC 2019). The described docking setup was first tested with the cocrystallized inhibitors (PF-03758309 in PAK4, related pyrazolo[1,5-a]pyrimidines in CDK7, and Staurosporine in AMPKα) to check whether RMSD values below 1.2 Å can be reproduced (Table 21).

22 Statistical Analysis

Graphs were generated using Graph Pad Prism 9, R v4.3, and GSEA v4.3.2. Statistical analysis for each experiment is described in the figure legends. All data were obtained from at least three independent experiments unless otherwise stated. The resulting p-values are indicated in the respective figures. A comparison was considered significant if the p-value was equal to or below 0.05. In cases where multiple statistical tests were performed on the same dataset, a Bonferroni correction was applied to account for false-positive results.

Results

Contributions of authors other than myself are acknowledged in the figure legends. Data generated in collaboration with students under my supervision is also indicated in the text or in the figure legends, where appropriate.

23 AMPKα Is Upregulated in a Subtype of PDAC

To investigate the role of AMPK in PDAC, we reviewed the TCGA data set (https://www.cancer.gov/tcga) for AMPK subunit expression in PDAC (Figure 9) (Tang et al. 2017). We found that all subunits of AMPK1 (*PRKAA1, PRKAB1, PRKAG1*) were significantly upregulated in PDAC compared to normal tissue.

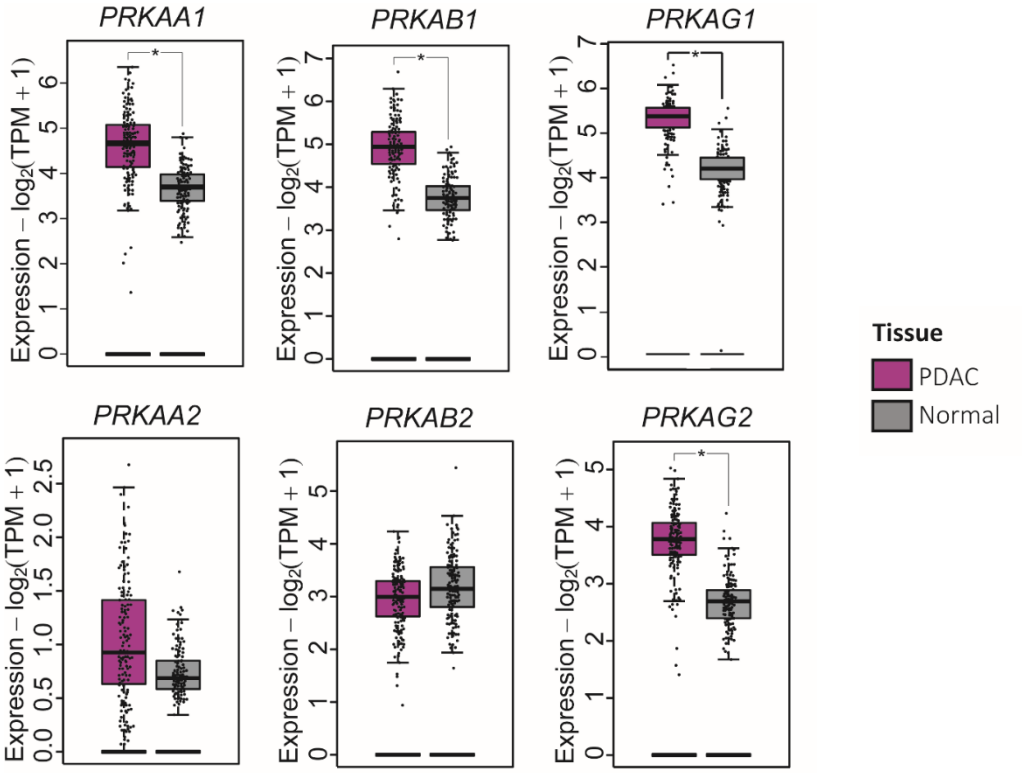

Figure 9 | mRNA expression of AMPK subunits in PDAC compared to normal tissue. Adapted from http://gepia2.cancer-pku.cn/ and https://www.cancer.gov/tcga. The PAAD dataset with 179 samples was matched to 171 GTEx samples. Tissues are color-coded (purple: PDAC, grey: Normal). mRNA expression is shown in log_2(TPM+1). Log_2FC cutoff: 0.58, p-value cutoff: 0.05. One-way ANOVA was performed. PAAD/PDAC: Pancreatic adenocarcinoma, GTEx: Genotype-Tissue Expression project, TPM: Transcripts per million.

We further corroborated our findings by leveraging single-cell RNA sequencing (scRNA-Seq) data (GSE202051) (Hwang et al. 2022). A dataset of 108,917 cells was generated from surgical samples obtained from 18 PDAC patients (Figure 10a). We analyzed *PRKAA1*

expression across different cell types and observed the highest average expression in malignant epithelial cells (Figure 10b,c,d).

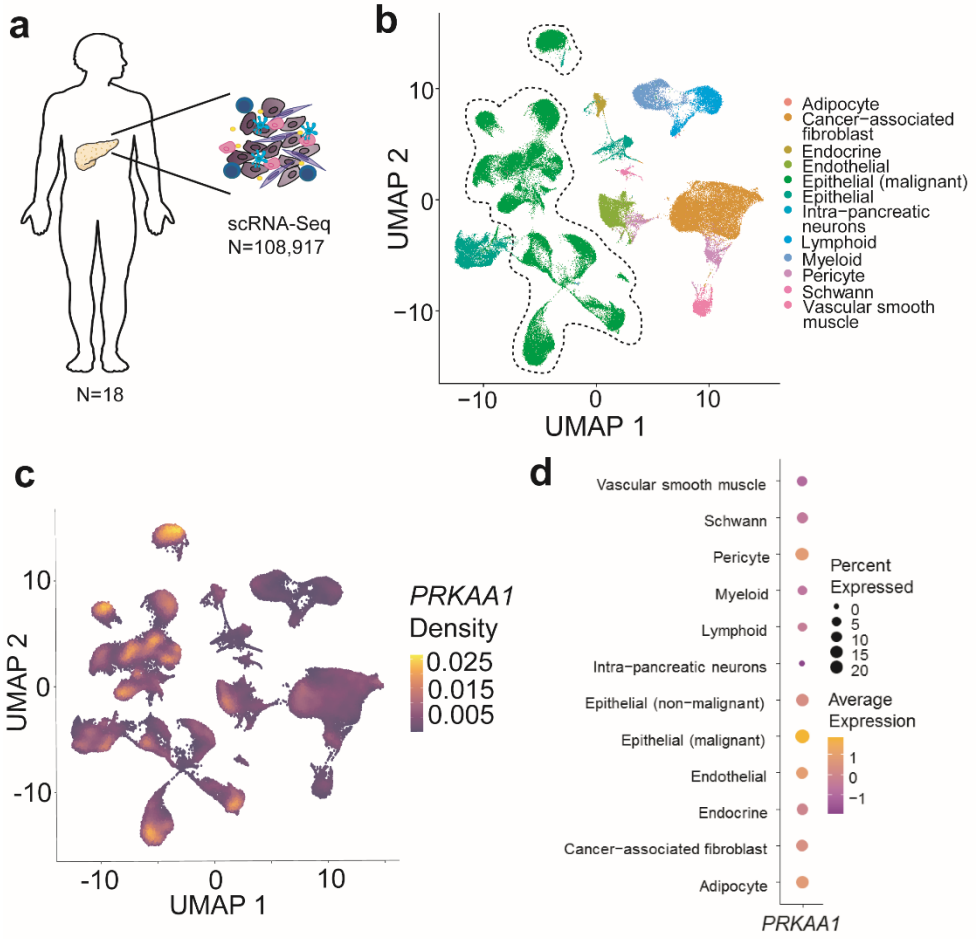

Figure 10 | scRNA-seq analysis of treatment-naive PDAC tissue to investigate *PRKAA1*. a, Surgical samples of 18 treatment-naive PDAC patients were used for scRNA-Seq. In total, 108,917 single cells were analyzed as shown in **b, c,** and **d,**. **b,** UMAP with color-coded cell types. **c,** UMAP with color-coded density of *PRKAA1* expression. **d,** Dot plot depicting the expression of *PRKAA1* for distinct cell types. Cell types are shown in rows. The percentage (%) of cells expressing *PRKAA1* is indicated by circle size. The average expression of *PRKAA1* by cell type is color-coded. Data were analyzed by Lukas Krauß (Technical University Munich, Prof. Dr. Günter Schneider) and myself. scRNA-Seq: single-cell RNA-Seq, UMAP: Uniform Manifold Approximation and Projection.

To validate the protein expression of PRKAA1 in human PDACs, we conducted immunofluorescent staining for AMPKα and Thr172 phosphorylated AMPKα in a cohort of 107 treatment-naïve patients. Our results showed heterogeneous expression of both AMPKα and P-AMPKα among PDAC patients (Figure 11a).

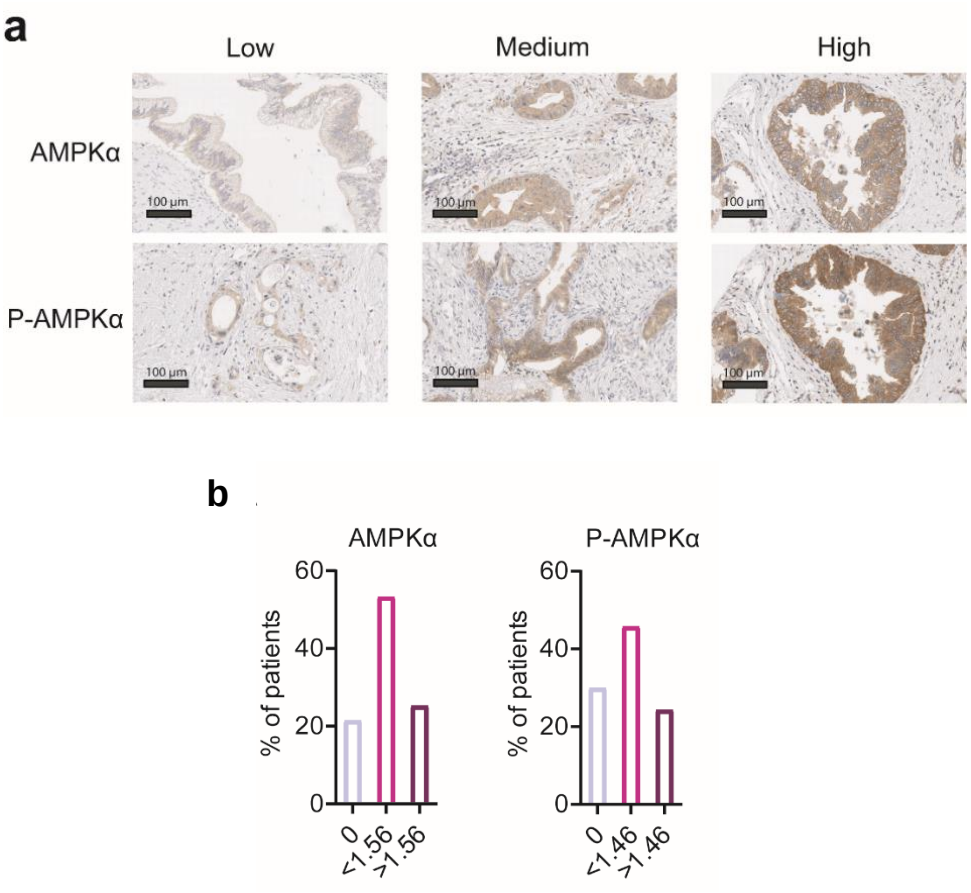

Figure 11 | AMPKα and P-AMPKα immunofluorescent staining of human PDAC cohort. a, Immunohistochemistry staining of P-AMPK and AMPK in a cohort of 107 PDAC patients. Intensities of stained PDAC cells include low, medium, and high. **b,** The percentage (%) of PDAC patients with specific staining intensity is shown. Staining intensities are divided into three levels using Cutoff Finder (AMPK: 0,<1.56,>1.56; P-AMPK: 0,<1.46,>1.46). Data were analyzed by Felix Schicktanz (TUM, Department of Pathology, PD Dr. Katja Steiger, Prof. Dr. med. Wilko Weichert).

Unexpectedly, we did not observe a statistically significant association between staining intensity and a specific PDAC subtype, grade, or survival (Fig. 12a,b,c).

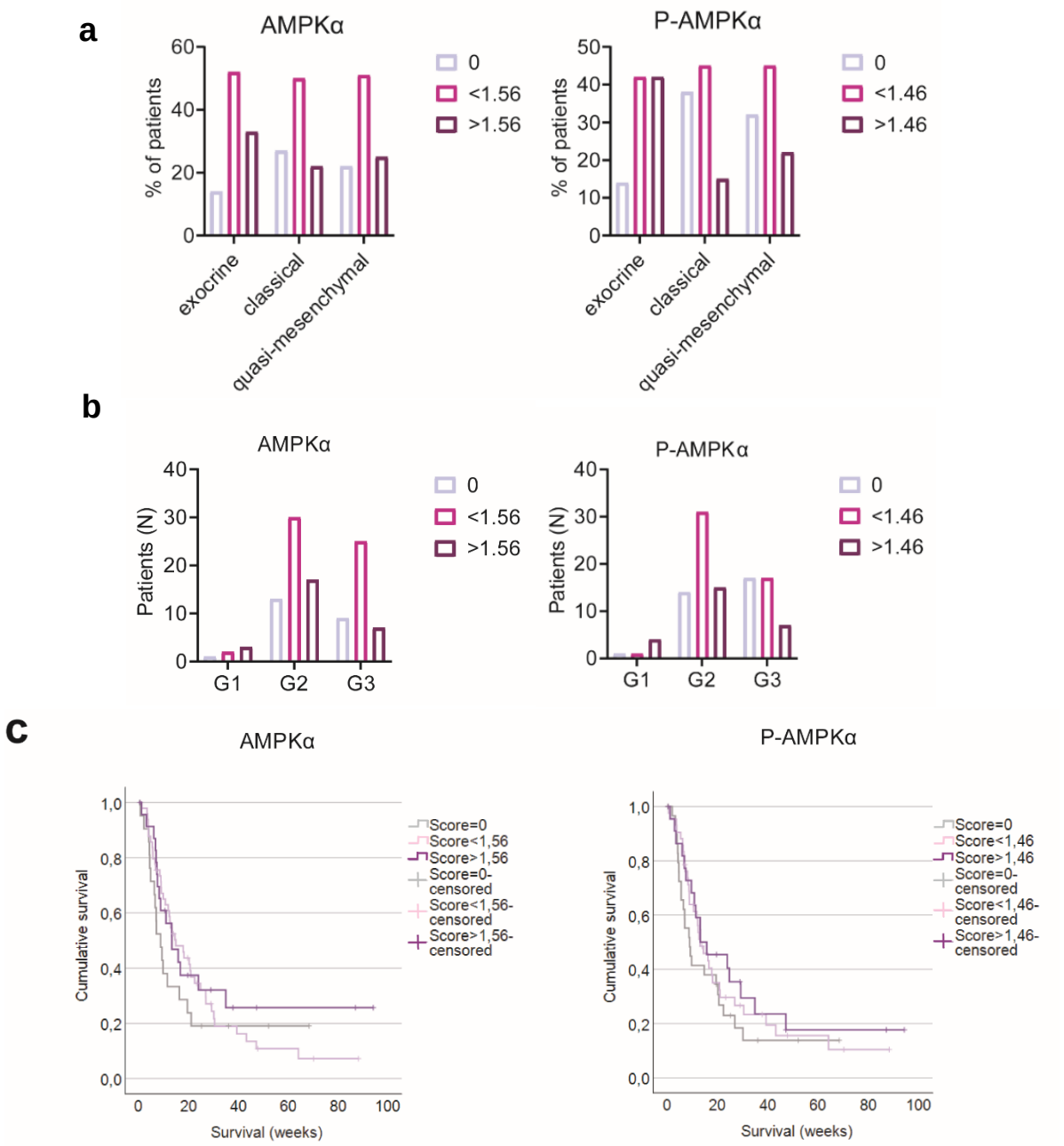

Figure 12 | AMPKα and clinical parameters. Staining intensities are divided into three levels using cut-off finder (AMPKα: 0,<1.56,>1.56; P-AMPKα: 0,<1.46,>1.46). **a,** Quantification of P-AMPKα and AMPKα stained PDACs in exocrine (N = 21), classical (N = 44), and quasi-mesenchymal (N = 31) subtypes. The percentage (%) of PDAC patients with specific subtypes and staining intensity is shown. **b,** Quantification of PAMPKα and AMPKα stained pancreatic cancers classified as G1 (N = 6), G2 (N = 60), G3 (N= 41). The number (N) of PDAC patients with specific grading and staining intensity is shown. **c,** Cumulative survival of pancreatic cancer patients based on staining intensities of P-AMPKα and AMPKα.

Taken together, PDAC cells are characterized by higher *PRKAA1* levels compared to healthy tissue and we observed high expression and phosphorylation of AMPKα in a subset of PDACs.

24 *Prkaa1* Is Associated with a Metastatic and Undifferentiated PDAC Phenotype in Experimental Models

To explore the potential role of PRKAA1, we investigated PRKAA1 in the context of undifferentiated cells and metastasis. The DepMap portal provides data on the metastatic potential of human cancer cell lines (Jin et al. 2020). Jin et al. employed an advanced barcoding strategy to determine the metastatic growth of cancer cell lines in immunodeficient mice and computed the relative metastatic potential for each cell line (Figure 13a). By correlating the metastatic potential of the available PDAC cell lines with protein array data, we found AMPKα as having the highest Pearson correlation coefficient (R=0.51) (Figure 13b). Intriguingly, we observed no correlation between the phosphorylation of AMPKα and the metastatic potential. To further investigate this correlation, we accessed proteomic data and obtained similar results (Figure 13c).

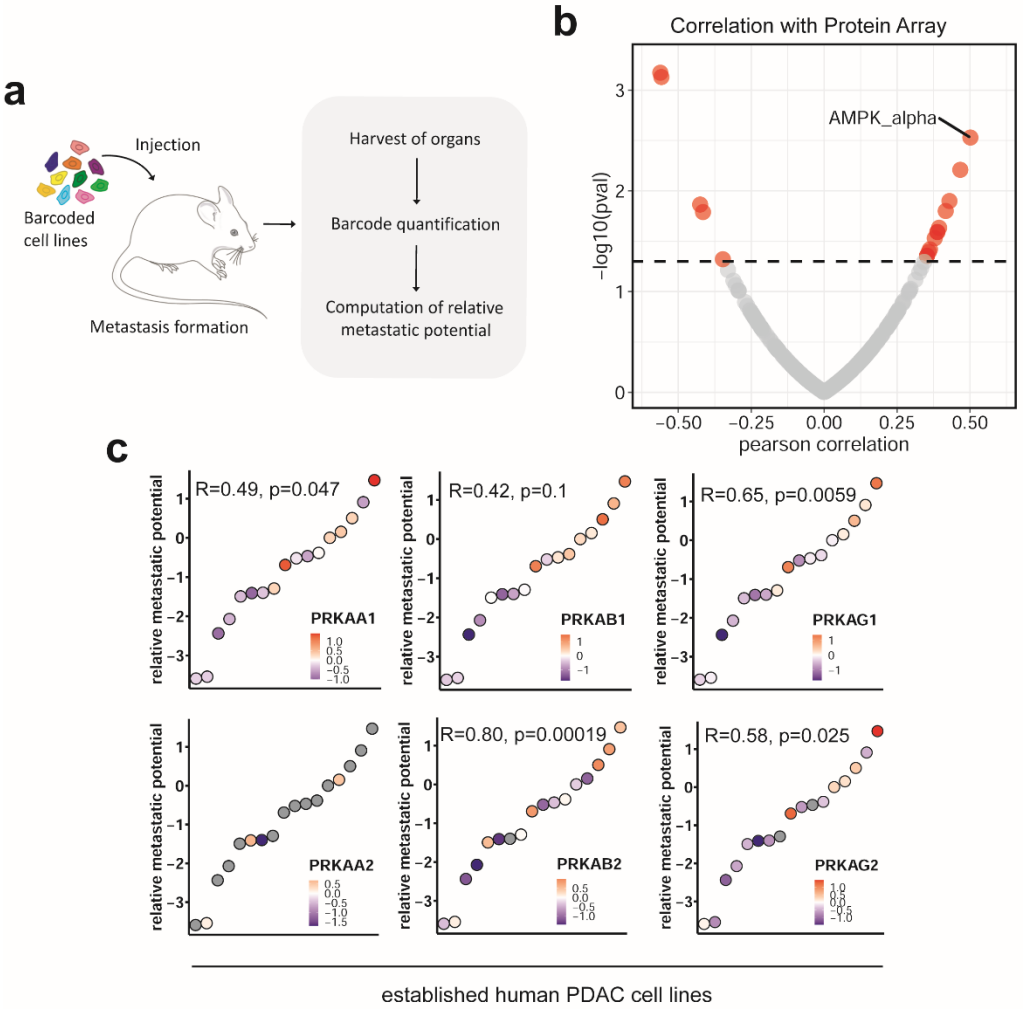

Figure 13 | Correlation of AMPK with the metastatic potential of human PDAC cell lines. Data was accessed via https://depmap.org/. **a,** Scheme of *in vivo* barcoding strategy to determine the metastatic potential of human cancer cell lines in mouse xenografts. Cancer cell lines were barcoded, pooled, and injected into immunodeficient mice. After metastatic growth, organs were harvested, and DNA barcodes were quantified by next-generation

sequencing. The metastatic potential of each cell was quantified as barcode enrichment relative to the abundance in the pre-injected population.**b,** Correlation of protein array data with metastatic potential in human PDAC cell lines. On the x-axis, the Pearson correlation coefficient is shown. On the y-axis, -log10(pval) is shown. **c,** Correlation of AMPK subunit expression with metastatic potential in human PDAC cell lines. PDAC cell lines are ordered by their relative metastatic potential on the x-axis. Relative AMPK subunit expression determined by proteomics is color-coded. Pearson correlation coefficient (R) and p-value (p) are shown.

In addition to the established long-term culture cells, we extended our data by including primary murine cell cultures to strengthen our findings. In collaboration with AG Saur's and AG Rad's labs at the Klinikum rechts der Isar, which have a vast resource of primary murine cell cultures known to recapitulate human disease (Mueller et al. 2018), we investigated the connection between AMPK and metastasis. A total of 38 murine *KRAS*^{G12D} cell lines were analyzed for their AMPK subunit expression and clustered accordingly (Figure 14a). Three main clusters were identified and named based on their AMPK expression levels as Low, High-2, and High-1. These clusters were further analyzed for the presence of metastasis in mice (No, Yes), the cellular morphology (mesenchymal, quasi-epithelial, quasi-mesenchymal, epithelial) of the cell lines, the grading of the respective tumors (Undifferentiated, G3, G2, G1) and their annotated murine PDAC cluster (mCluster) (C1, C2a, C2b, C2c, outlier). Quantification of metastatic PDACs in the different clusters revealed a significantly higher frequency of metastasis in the AMPK-High 1 and 2 cluster compared to the AMPK-Low cluster, with no significant difference between High-1 and High-2 clusters (Figure 14b). We also observed a significant difference in mCluster, with enrichment of cell lines of C1 in the High-A cluster (Figure 14c). The C1 mCluster is considered more aggressive compared to the C2 clusters. Furthermore, tumors of High-1 cell lines were mainly graded as undifferentiated (Figure 14d) and, although no statistically significant relationship was observed, High-1 cell lines were characterized by a mainly mesenchymal morphology (Figure 14e).

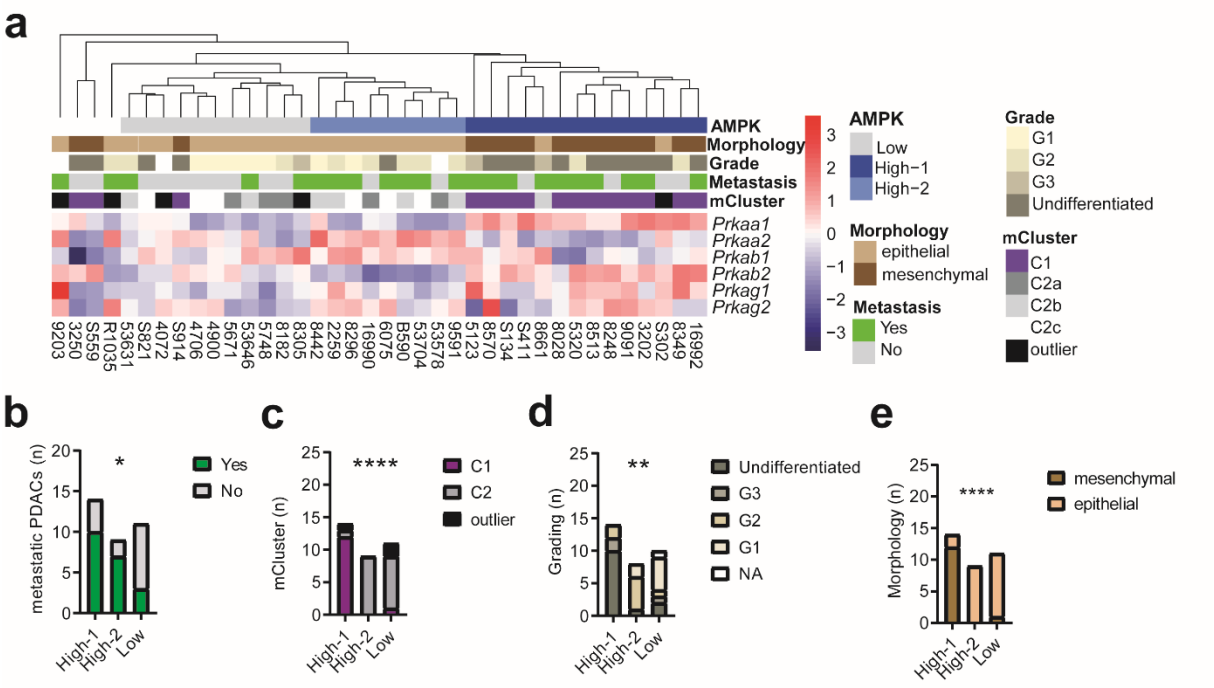

Figure 14 | AMPK in murine PDAC model. a, Heatmap of AMPK subunit expression in murine *Kras*^{G12D} cell lines (n=38). Subunit expression was determined using RNA-Seq. Annotations are given for AMPK cluster (Low, High-2, High-1), metastasis formation (No, Yes) the cellular morphology (mesenchymal, quasi-epithelial, quasi-mesenchymal, epithelial) of the cell lines, the grading of the respective tumors (Undifferentiated, G3, G2, G1) and their annotated murine PDAC cluster (mCluster) (C1, C2a, C2b, C2c, outlier). Clustering method: average, clustering distance: euclidean. **b,** Quantification of metastatic PDACs in AMPK clusters. Statistical analysis was performed by chi squared test. **c,** Quantification of mClusters in AMPK clusters. Statistical analysis was performed by chi squared test. **d,** Quantification of grading of the respective tumors in AMPK clusters. Statistical analysis was performed by chi squared test. **e,** Quantification of the cellular morphology (mesenchymal, quasi-epithelial, quasi-mesenchymal, epithelial) in AMPK clusters. *:p-value<0.05, **:p-value<0.01, ****:p-value<0.0001.

In summary, our findings indicate that elevated expression of *Prkaa1* is associated with a metastatic and undifferentiated PDAC phenotype in primary mouse and established human cell lines.

25 *Prkaa1* Fosters a Phenotype Switch and Oncogenic Signaling

To investigate the functional role of *Prkaa1* in PDAC, we generated *Prkaa1* overexpressing cell lines under the control of the constitutively active phosphoglycerate kinase (PGK) promoter via lentiviral transduction (Figure 15a). The PGK promoter was chosen due to its ability to maintain physiological expression levels. As described in the introduction, two main transcriptional-based subtypes have been described, the undifferentiated basal and the rather differentiated classical subtype. To investigate whether the function of *Prkaa1* is dependent on

the molecular subtype of PDAC, which is classified into undifferentiated basal and differentiated classical subtypes, we selected two cell lines: 8182, a relatively differentiated cell line from the AMPK-Low cluster, and 9019, an undifferentiated cell line from the AMPK-High-A cluster (Figure 14a). The validation experiments and complete characterization of these cell lines were performed under my supervision and can be found in the doctoral thesis of Franziska Génevaux. Interestingly, we observed that low passaged *Prkaa1* overexpressing 8182 cells exhibited a spherical growth pattern, which could potentially indicate a switch towards an undifferentiated phenotype (Figure 15b). In the mesenchymal 9091 cell line, no morphological difference was observed. To further investigate the subtype-dependent function of *Prkaa1*, we performed RNA-Seq of *Prkaa1* overexpressing cell lines and their controls (PRJEB63203) and analyzed their transcriptional profile using GSEA. While the 8182 *Prkaa1* overexpressing cells showed an enrichment of the HALLMARKs GLYCOLYSIS, EMT, and KRAS UP (Figure 15c), the mesenchymal 9091 *Prkaa1* overexpressing cells showed no regulation (data not shown). Epithelial-to-mesenchymal transition (EMT) is a process during which differentiated epithelial cells acquire mesenchymal features. In cancer, EMT is associated with a pluripotent, stem-cell-like phenotype, and metastasis.

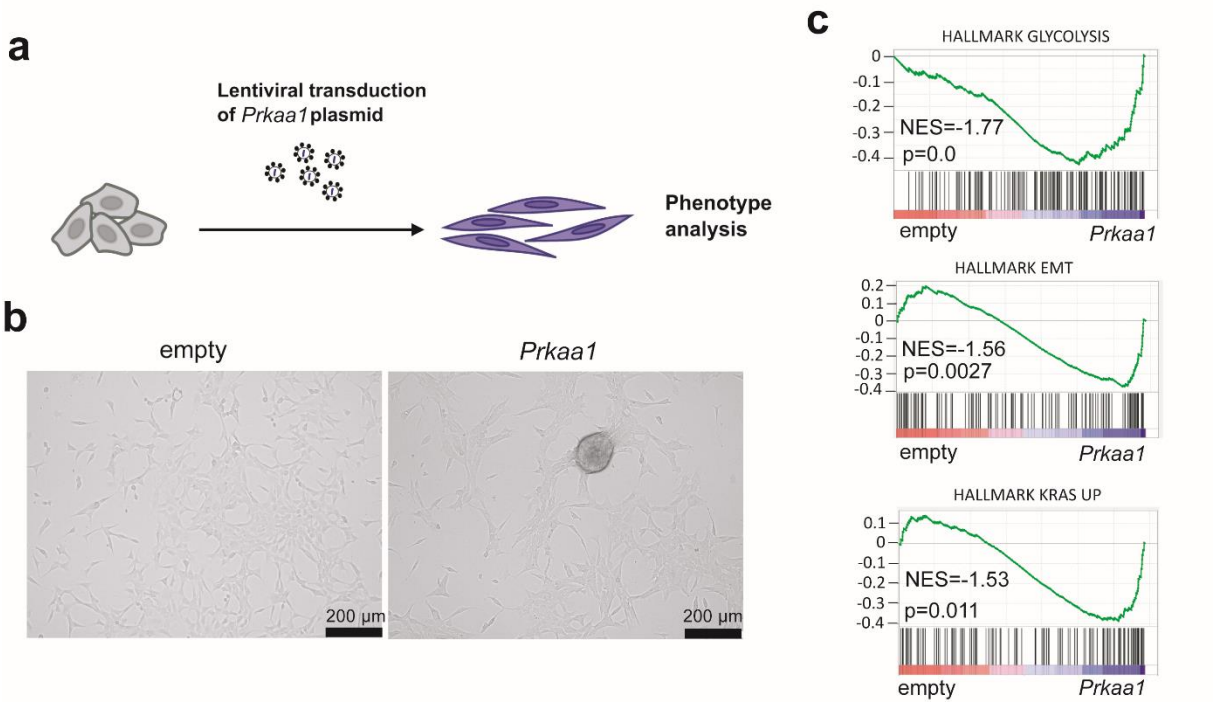

Figure 15 | Characterization of *Prkaa1* overexpressing epithelial PDAC cell line. a, Scheme of generation of *Prkaa1* overexpressing cell lines. Cells were generated by lentiviral transduction of a PGK-vector expressing *Prkaa1*. **b,** Microscopic pictures of 8182 cells with empty or *Prkaa1* vector. The scale bar is shown in the bottom left. **c,** GSEA of RNA-Seq data in 8182 empty vs. 8182 *Prkaa1* cells using the HALLMARK gene set database. Normalized enrichment scores (NES) and p-values (p) are shown. Data can be accessed by PRJEB63203. GSEA: Gene set enrichment analysis.

To explore the possibility that an enhanced metabolic capacity might be responsible for the observed partial phenotype switch, we conducted a Seahorse assay (Figure 16). Our results revealed a slightly elevated extracellular acidification rate (ECAR) in both 8182 and 9091 overexpressing cell lines and an elevated oxygen consumption rate (OCR) only in 8182 *Prkaa1* overexpressing cells.

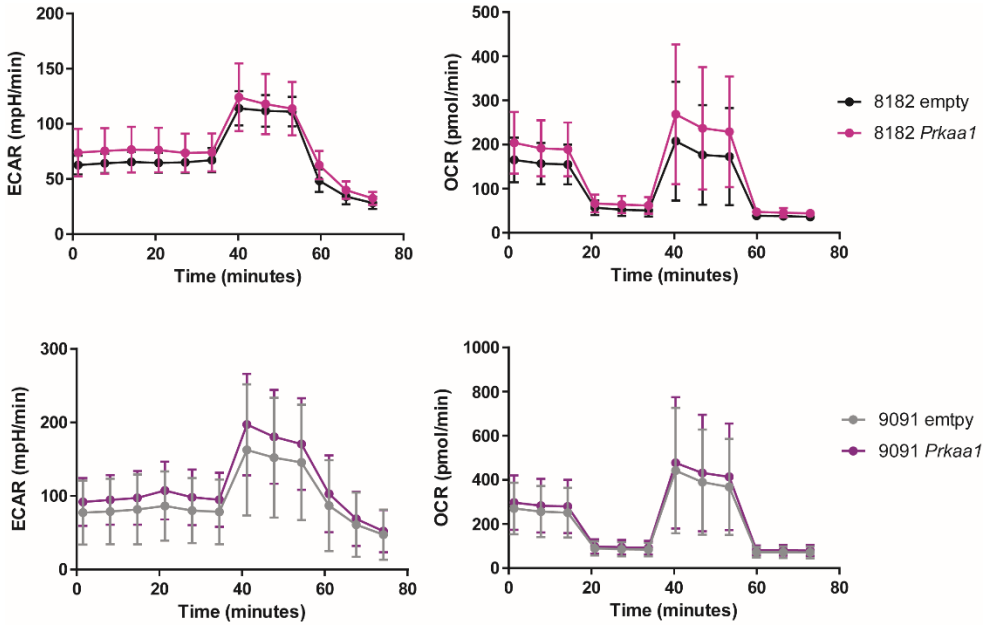

Figure 16 | Seahorse assay of *Prkaa1* overexpressing cell lines. Cell lines are color-coded. **Left:** On the y-axis, the ECAR in mpH/min is shown. On the x-axis the Time in minutes is given. **Right:** On the y-axis, OCR in pmol/min is shown. On the x-axis the Time in minutes is given. Experiments were performed as two biological replicates. ECAR: Extracellular acidification rate, OCR: Oxygen consumption rate. Seahorse assay was performed by Angela Boshnakovska (Georg August University, Göttingen, AG Rehling).

To substantiate our findings of enrichment of the KRAS UP gene set in 8182 *Prkaa1* overexpressing cells, we accessed five publicly available datasets (Figure 17a). These data sets encompass RNA-Seq data of human biospecimens incorporated in The Cancer Genome Atlas (TCGA), International Cancer Genome Consortium (ICGC) and published in (Aung et al. 2018) as well as RNA-Seq and proteomic data of human established PDAC cell lines. We performed correlation analyses between *PRKAA1* and *KRAS, MAPK3*, and *MAPK1* expression levels. We found evidence for a positive association between *PRKAA1* expression and increased expression of *KRAS, MAPK3*, and *MAPK1* on mRNA as well as protein level. Additionally, we accessed protein array data from the depmap portal and found a weak but significant correlation between MAPK1/3 phosphorylation and AMPKα expression across all cancer types, although not significant in PDAC (Figure 17b).

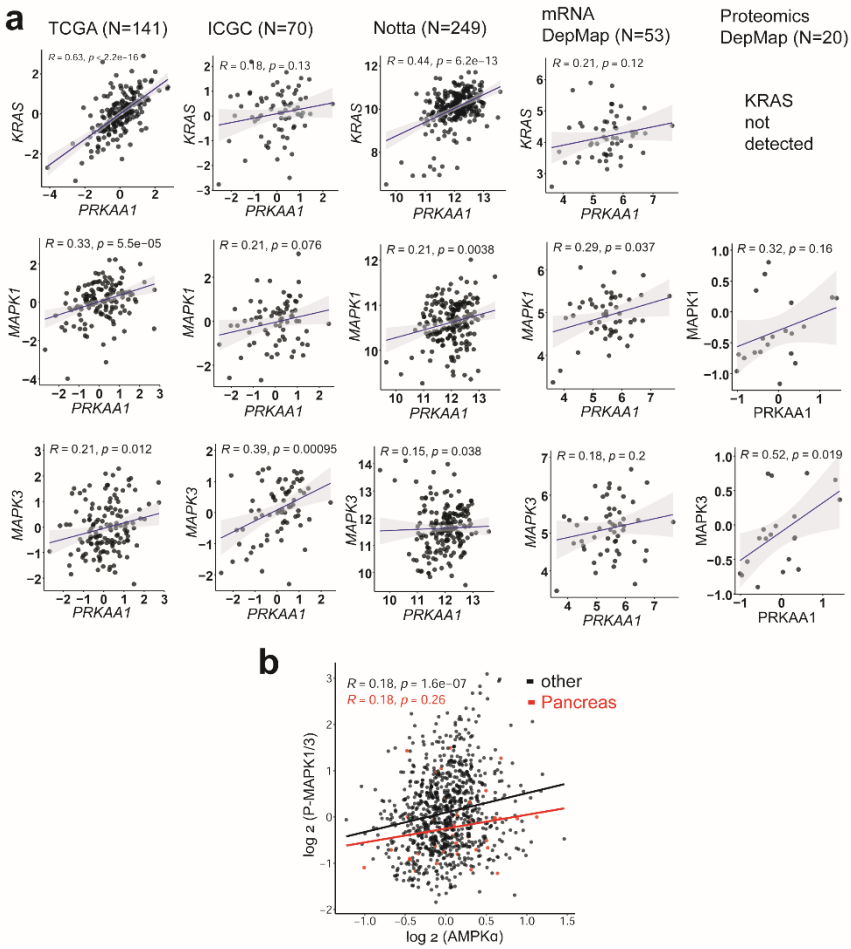

Figure 17 | Correlation of *PRKAA1* with members of KRAS-MEK-ERK pathway. a, Correlation of *PRKAA1* with *KRAS, MAPK1* and *MAPK3* in TCGA, ICGC, Notta, RNA-Seq (https://depmap.org/) and MAPK1 and MAPK3 in proteomics (https://depmap.org/) data. TCGA, ICGC and proteomics data are shown as z-score, Notta and RNA-Seq data are shown as log-transformed values. Number of samples (N), Pearson correlation coefficient (R) and p-value (p) are shown. **b,** Correlation of P-MAPK1/3 at Thr202 and Tyr204 and AMPKα using Protein Array data accessed via https://depmap.org/. Pearson correlation coefficient (R) and p-value (p) for cancer cell lines of the pancreas is indicated in red and for other entities in black. ERK: extracellular signal-regulated kinase MAPK1/3: Mitogen activated protein kinase 1/2, MEK: Mitogen activated protein kinase kinase.

26 *Prkaa1* KO Triggers a Vulnerable Cell State Associated with a Malfunctioning ROS Defence

To expand our understanding of the role of *Prkaa1* in PDAC, we used *Prkaa1* knockout (KO) cell lines generated through CRISPR/Cas9 technology (Falcomatà et al. 2022) (Figure 18a). Three undifferentiated cell lines derived from the AMPK-High-1 (8570, 9091, 8248) cluster were utilized. Each cell line was transduced with two different sgRNAs targeting *Prkaa1* (KO1, KO2), with LacZ serving as the control. The characterization of these cell lines was conducted in collaboration with Thorsten Richter and Jorina Hilbert under my supervision. The success of *Prkaa1* KO was confirmed by Western Blot analysis of AMPKα and phosphorylation of its

downstream target ACC (Figure 18b,c). Additionally, we examined cell growth over four days and observed no significant differences between *Prkaa1* KO and LacZ cells (Figure 18d).

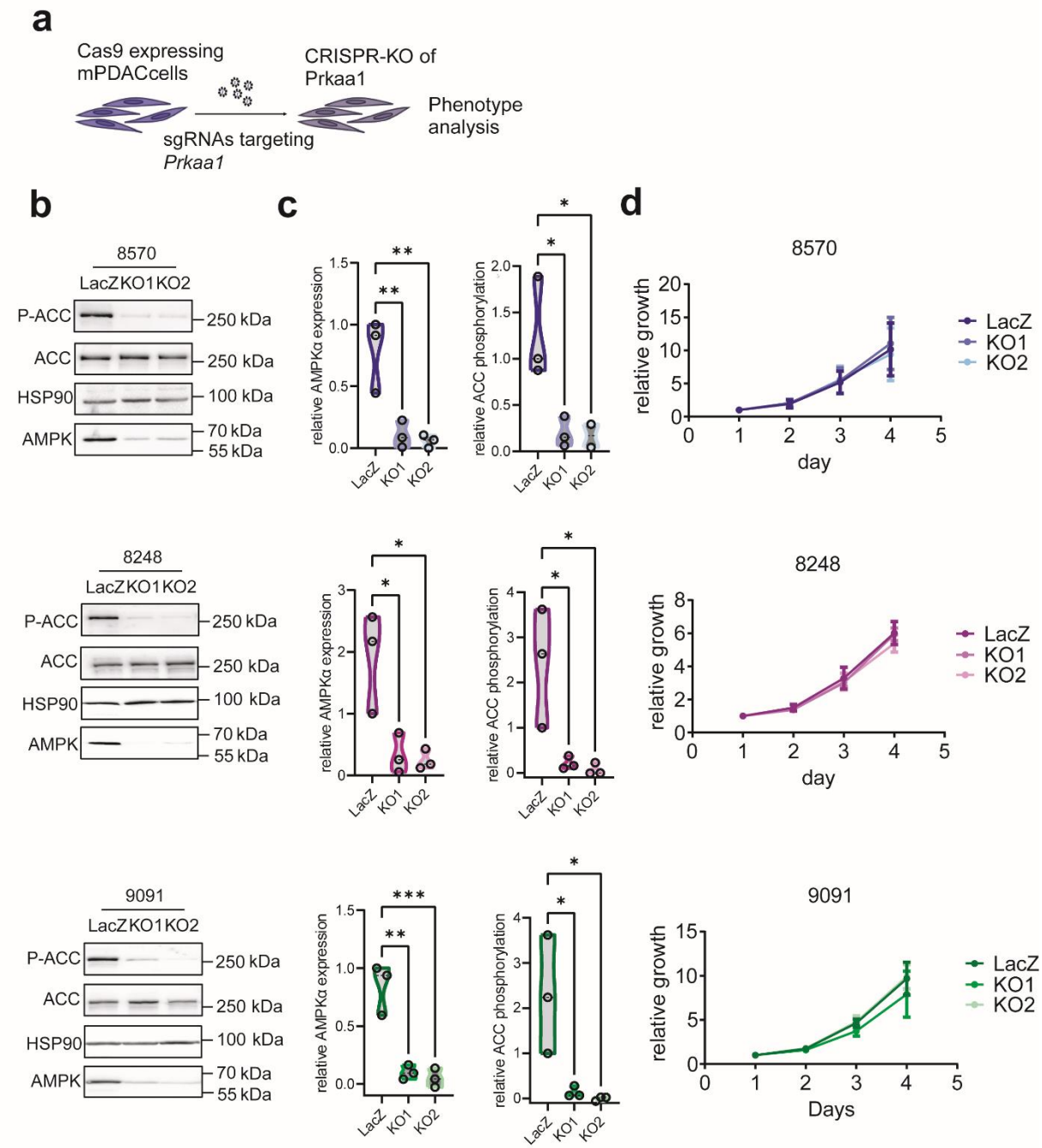

Figure 18 | Characterization of murine *Prkaa1* KO cell lines. **a,** Scheme of generation of *Prkaa1* KO cell lines. CAS9 expressing murine PDAC cell lines were transduced with two different *Prkaa1*-targeting sgRNAs and subsequently their phenotype was analyzed. **b,** Western blots of AMPK pathway in control (LacZ) and *Prkaa1* KO (KO1, KO2) cells. AMPK pathway was investigated using AMPKα, P-ACC, and ACC antibodies. HSP90 was used as a loading control. **c,** Quantification of **b,**. For statistical analysis, one-way ANOVA with Tukey's multiple comparison was performed. **d,** Growth curves of control (LacZ) and *Prkaa1* KO (KO1, KO2) cells. 1000 cells were seeded in 96-well plates and viability was measured each day for four subsequent days. Relative growth to day one is plotted on the y-axis. The experiment was performed with three technical replicates and two (8248) or three

(8570, 9091) biological replicates. ACC: Acetyl-CoA carboxylase, HSP90: Heat shock protein 90, P-: Phosphorylation, ns: not significant, *: p<0.05, **: p<0.01, ***: p<0.005, ****: p<0.001.

We proceeded by performing RNA-Seq of *Prkaa1* KOs and their respective control cells (PRJEB63203) revealing significant differential gene expression in 8248 and 9091 *Prkaa1* KO cells, but no significant changes in 8570 *Prkaa1* KO cells (Figure 19a). To further support the association between *Prkaa1* and an undifferentiated phenotype, we performed a pre-ranked GSEA using specifically the HALLMARK EMT gene set, and consistent with our expectations, we observed a depletion of this signature in both 8248 and 9091 *Prkaa1* KO cells (Figure 18b).

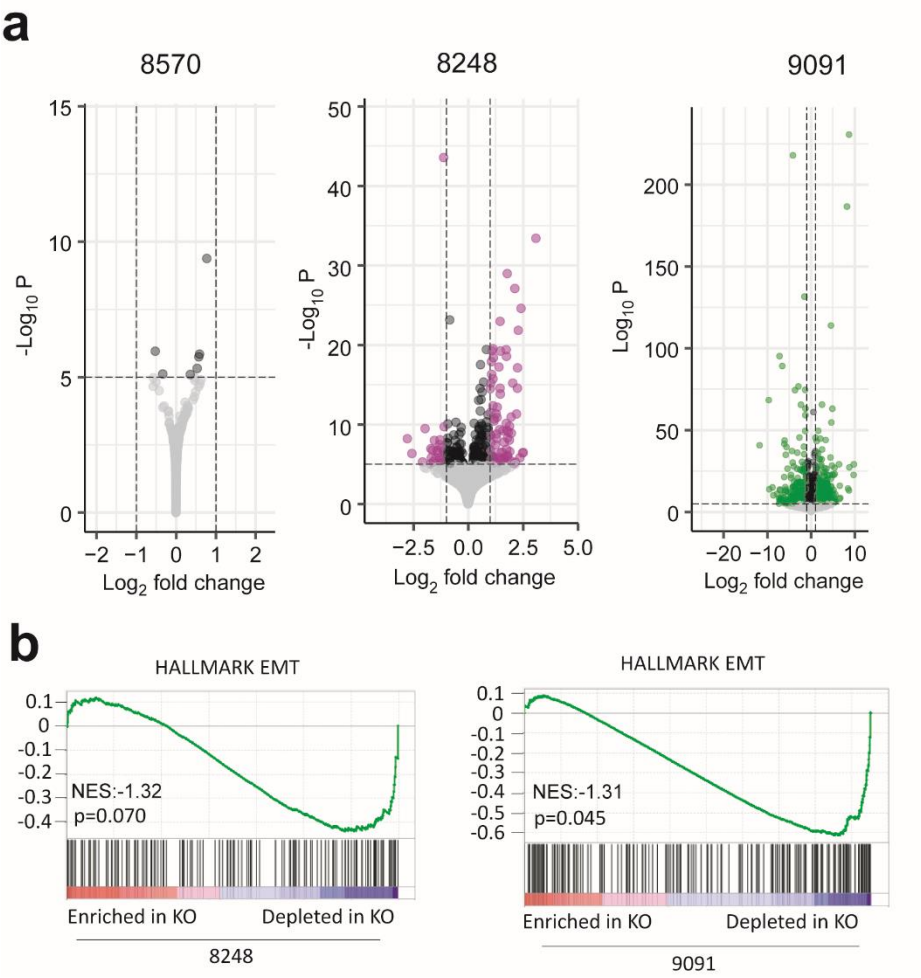

Figure 19 | RNA-Seq Analysis of *Prkaa1* KO cell lines. a, Volcano plot of differently expressed genes in LacZ vs. *Prkaa1* KO cells determined by RNA-Seq. Log_2 fold change is plotted on the x-axis and the log_{10} p-value is plotted on the y-axis. mRNA of three (8570, 9091) or four (8248) biological replicates was used for processing. **b,** GSEA of RNA-Seq data in LacZ vs. KO cells using the EMT-HALLMARK gene set. Normalized enrichment scores (NES) and p-values (p) are shown. Data can be accessed by PRJEB63203. EMT: Epitehlial to mesenchymal transition.

Given that *Prkaa1* KO PDAC cell lines can be generated with similar proliferation rates as their LacZ controls, *Prkaa1* is not deemed an essential gene under normal growth conditions. However, we investigated the cellular fitness of *Prkaa1* KO cell lines by measuring basal caspase activity (Figure 20). Intriguingly, we observed an induction of Caspase 3/7 activity in 8248 and 9091 *Prkaa1* KO cells, suggesting a concealed dysregulation in these cell lines.

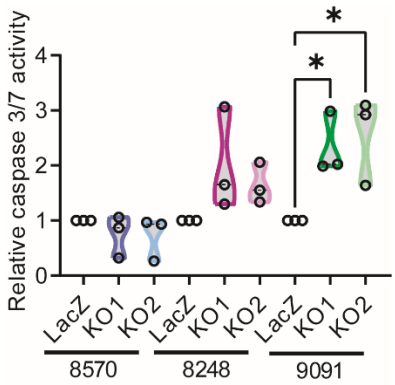

Figure 20 | Basal levels of Caspase 3/7 activity in *Prkaa1* KO cells. Relative caspase 3/7 activity in LacZ vs. KO1 and KO2 cells. Caspase 3/7 activity was normalized to LacZ cells. Experiments were performed as two technical and three biological replicates. For statistical analysis, one-way ANOVA with Tukey's multiple comparisons was performed. *: $p<0.05$. Caspase 3/7 assay was performed by Thorsten Richter and Jorina Hilbert under my supervision.

Given the well-established function of AMPK in regulating energy metabolism, we explored the metabolic capacity and resilience of PDAC cells in the absence of *Prkaa1* using the Seahorse assay (Figure 21). Surprisingly, contrary to our initial expectations, *Prkaa1* KO cells showed only minor deficits. Among the different KO cell lines, the 8570 KO cells, which showed the least differential gene expression, displayed a decrease in ECAR, suggesting potential metabolic alterations. Interestingly, these cells also exhibited a slight increase in maximal OCR. Conversely, the 8248 KO cells displayed both an increased ECAR and OCR, indicating a shift towards enhanced metabolic activity. Meanwhile, in the 9091 KO1 cells, no clear trend was observed. These findings collectively indicate that there are heterogeneous metabolic changes occurring in *Prkaa1* KO PDAC cells, without a clear and consistent pattern observed across all cell lines.

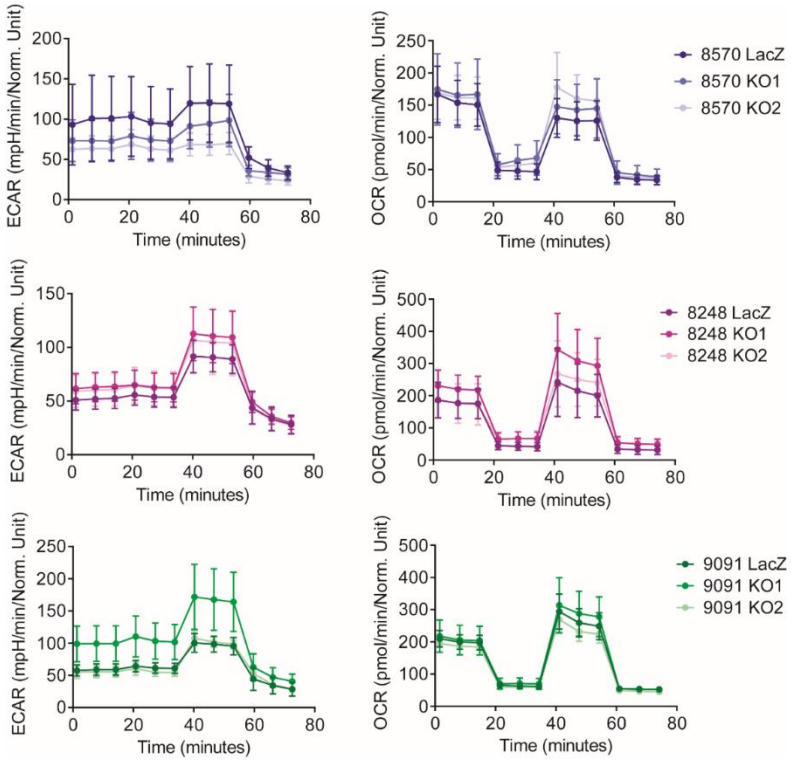

Figure 21 | Seahorse assay of *Prkaa1* KO cell lines. Cell lines are color-coded. **Left:** On the y-axis, the ECAR in mpH/min is shown. On the x-axis, the Time in minutes is given. **Right:** On the y-axis, OCR in pmol/min is shown. On the x-axis, the Time in minutes is given. Experiments were performed as two biological replicates. ECAR: Extracellular acidification rate, OCR: Oxygen consumption rate. Seahorse assay was performed by Angela Boshnakovska (Georg August University, Göttingen, AG Rehling).

Furthermore, we assessed the survival of *Prkaa1* KO cells under growth factor-depleted conditions (Figure 22a). Consistent with the Seahorse assay results, we observed a minor disadvantage of *Prkaa1* KO cells in such conditions (Figure 22b,c).

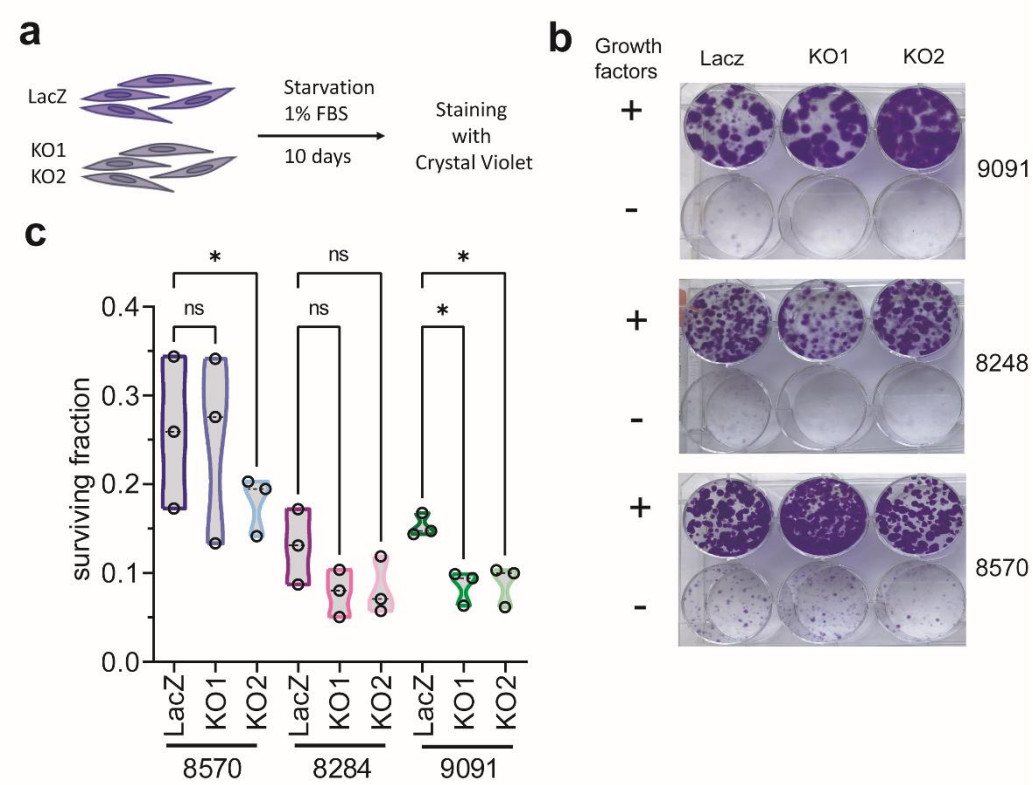

Figure 22 | Survival of *Prkaa1* KO cells under growth factor depletion. a, Scheme of growth factor starvation experiment. Cells were grown for 10 days with 10% or 1% FBS and subsequently, cells were stained with crystal violet for quantification. **b,** Clonogenic assay of LacZ, KO1, and KO2 of 8248, 8570, and 9091 cells in the presence of 10% or 1% FBS for 10 days. Experiments were performed as three biological replicates. **c,** Quantification of surviving fraction of **b,.** One-way ANOVA with Fisher LSD test was performed. ns: not significant, *: $p<0.05$.

In summary, our observations indicated that *Prkaa1* KO cells exhibited only minor metabolic deteriorations in the glycolytic capacity as well as oxidative phosphorylation.

To further investigate *Prkaa1*-associated vulnerabilities, we designed a drug screening experiment using 8570 LacZ, KO1, and KO2 cells treated with 119 drugs in clinical use or preclinical investigation (Figure 23a). Subsequently, we conducted validation experiments in other KO cell lines, as well as combinatorial treatment with PF-3758309, our potential AMPK inhibitor (described in section 26). The results are detailed in the bachelor thesis of Thorsten Richter and the doctoral thesis of Jorina Hilbert. Notably, we discovered that *Prkaa1* KO cells are more sensitive to the ROS inducer Erastin (Figure 23b).

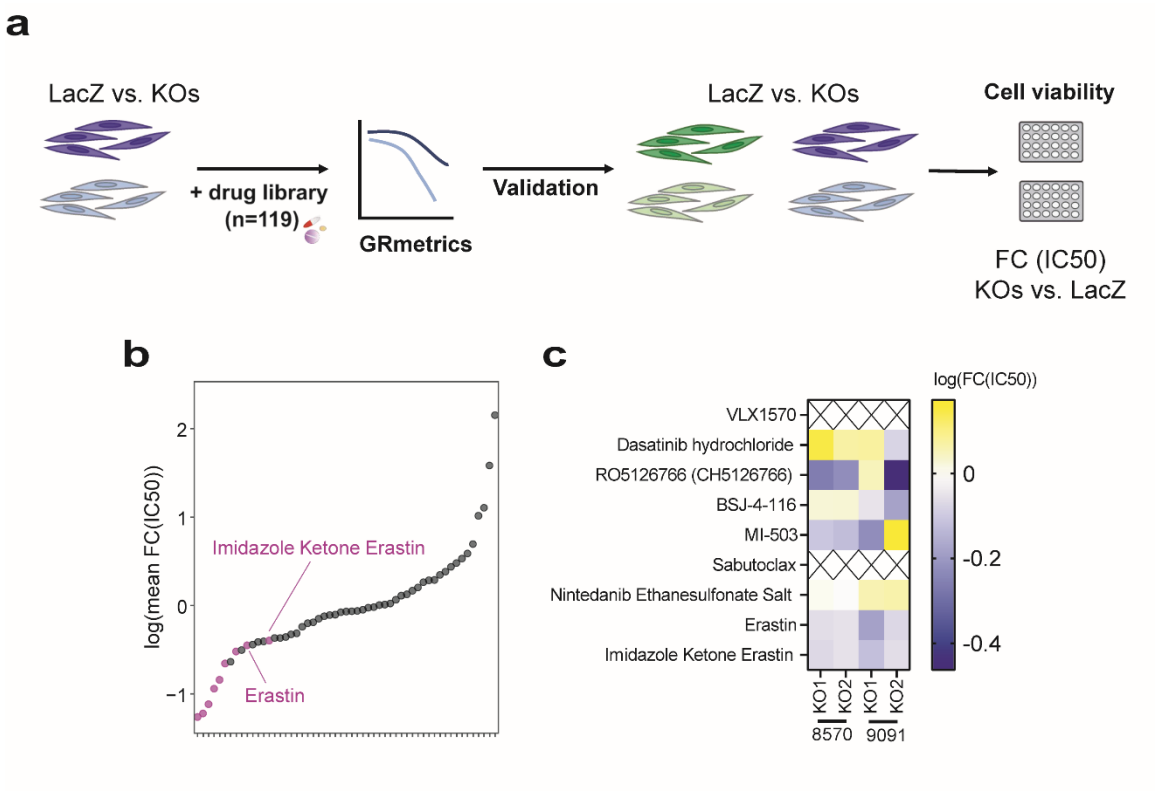

Figure 23 | Drug Screen to uncover *Prkaa1*-dependent processes and associated vulnerabilities in PDAC cells. a, Scheme of drug screen and validation workflow. 8570 LacZ, KO1, and KO2 cells were treated with a drug library containing 119 compounds with a 7-fold dilution under clinical testing. After 72 hours, cell viability was measured and dose-response curves were generated by applying the GRmetrics package. Screening hits were defined as FC(IC50) of *Prkaa1* vs. empty < 0.7. Potential hits were first validated in LacZ and KOs of 8570 and 9091 cells. **b,** Dot plot of log (FC(IC50)) in 8570 LacZ vs KOs. Drugs are ordered according to their mean FC(IC50). Highlighted are drugs with FC(IC50)<0.7 in both KOs and the top hit Erastin as well as its analog Imidazole Ketone Erastin. **c,** Heatmap of $\log_{10}$(FC(IC50)) of potential drug screen hits in LacZ vs. KO1 and KO2 of 8570 and 9091 cells. Log(FC(IC50))) is color-coded. X indicates a false positive hit which was not further investigated. The drug screen was performed by Jorina Hilbert and myself. FC(IC50): fold change (inhibitory concentration 50).

Our findings were further supported by RNA-Seq data from our *Prkaa1* overexpressing cell lines (Figure 24a), which exhibited upregulation in signatures associated with ROS detoxification and defense, including KEGG_DRUG_METABLISM_CYTOCHROME_P450, KEGG_METABOLISM_OF_XENOBIOTICS_BY_CYTOCHROME_P450 and KEGG_GLUTATHIONE_METABOLISM. Interestingly, in the *Prkaa1* KO cells, the 8248 KOs showed a depletion of KEGG_DRUG_METABOLISM_CYTOCHROME_P450, while the 9091 KOs showed enrichment of KEGG_DRUG_METABOLISM_CYTOCHROME_P450, KEGG_METABOLISM_OF_XENOBIOTICS_BY_CYTOCHROME_P450, and KEGG_GLUTATHIONE_METABOLISM (Figure 24b). Given that signatures of similar pathways were among the top 5 regulated signatures in all cell lines, these results suggest that *Prkaa1* plays an essential role in drug metabolism and Glutathione homeostasis in PDAC cells.

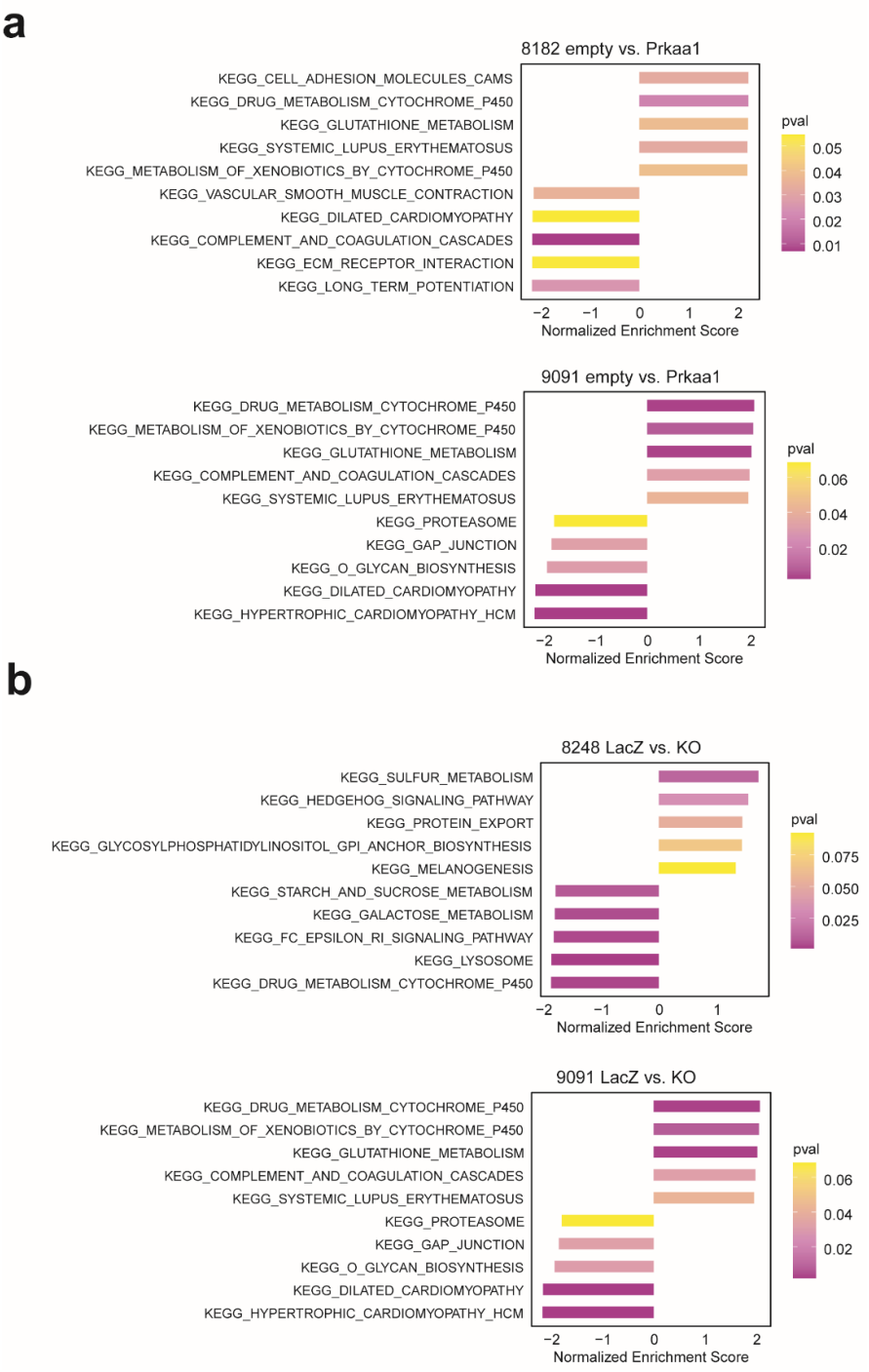

Figure 24 | GSEA of KEGG gene sets in *Prkaa1* models. GSEA of RNA-Seq data of **a,** empty vs. *Prkaa1* overexpressing cells and **b,** LacZ vs. KO cells using the KEGG gene set database. Depicted are the top 5 enriched and depleted KEGG gene sets. Normalized enrichment scores are shown on the x-axis and p-values (pval) are color-coded. RNA isolation was performed by Franziska Génevaux, Jorina Hilbert and myself. Analysis was done by myself. Data can be accessed by PRJEB63203. GSEA: Gene set enrichment analysis.

27 Drug Screen Uncovers Potential AMPKi

Based on the findings presented it appears that *Prkaa1* might play a supportive role in PDAC cells. We found a connection of *Prkaa1* with mesenchymal and metastatic murine PDAC cell lines as well as an increased metastatic potential in a murine xenograft model. Moreover, we found a possible connection between *Prkaa1* with drug metabolism and glutathione homeostasis. As a result, targeting AMPK could potentially represent a novel therapeutic strategy for PDAC. However, the lack of specificity in currently available AMPK inhibitors poses a challenge.

Therefore, our experiments were designed to identify a novel and highly specific inhibitor targeting AMPK by repurposing drugs already in clinical development.

In the doctoral thesis supervised by me, Franziska Génevaux has provided results in the discovery of a novel AMPKi, specifically PF-3758309. Through a comprehensive drug screen of compounds under clinical investigation, PF-3758309 emerged as the top hit associated with resistance in *Prkaa1* overexpressing cells (Figure 25a,b,c). Originally designed as a p21-activated kinase 4 (PAK4) inhibitor with demonstrated anti-tumor activity in *in vivo* models (Murray et al. 2010), PF-3758309 had also undergone a phase I clinical trial (NCT00932126) with no safety concerns, although the study was terminated.

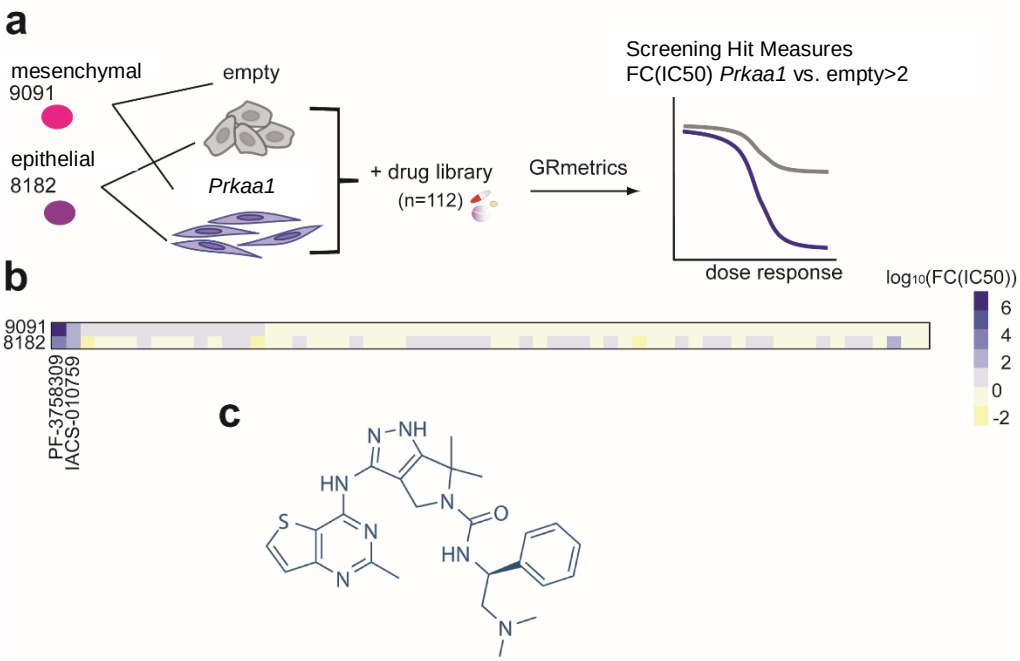

Figure 25 | Drug screen identifies PF-3758309 as AMPKi. a, Experimental setup of drug screen in empty and *Prkaa1* cell lines. 9091 and 8182 empty and *Prkaa1* cell lines were treated with a 7-fold dilution of a drug library containing 112 compounds under clinical testing. After 72 hours, cell viability was measured and dose-response curves were generated by applying the GRmetrics package. Screening hits were defined as FC(IC50) of *Prkaa1* vs. empty > 2. **b,** Heatmap of log10 (FC(IC50)) in 9091 and 8182 cells. **c,** Chemical structure of PF-3758309

(https://www.selleckchem.com/). The drug screen was performed by Franziska Génevaux under my supervision. FC(IC50): Fold change (inhibitory concentration 50).

We validated the findings that *Prkaa1* drives resistance towards PF-3758309 in long-term clonogenic assays (Figure 26a,b).

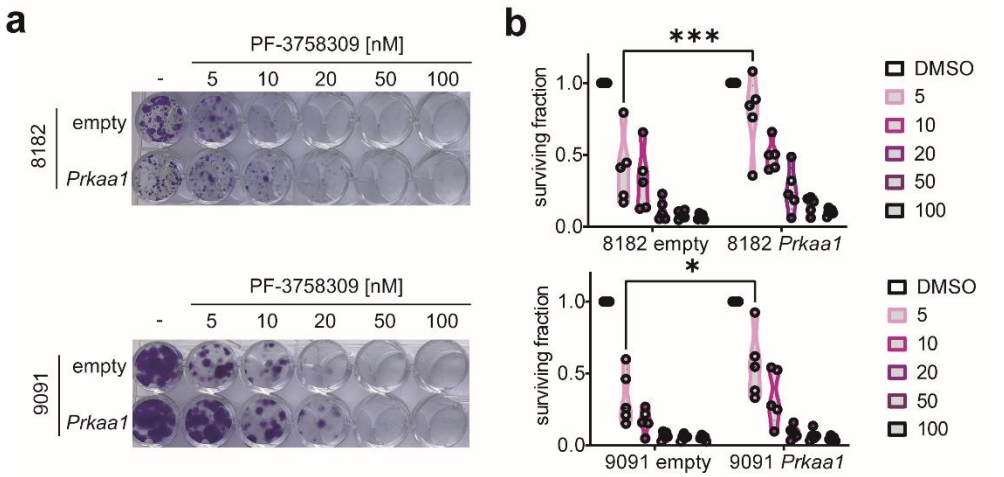

Figure 26 | Clonogenic of *Prkaa1* overexpressing cell lines treated with PF-3758309. a, Clonogenic assay of empty and *Prkaa1* overexpressing cells treated with different concentrations of PF-3758309 for 8 days. **b,** Quantification of **a,**. On the y-axis, the surviving fraction of empty and *Prkaa1* overexpressing cells treated with different concentrations of PF-3758309 after 8 days. Experiments were performed as five biological replicates. For statistical analysis, two-way ANOVA with Bonferoni's multiple comparison was performed.

Furthermore, the resistance of cells towards PF-3758309 in relation to *Prkaa1* was corroborated in the Cancer Target Discovery and Development (CTD^2) screen accessed via depmap (Figure 27).

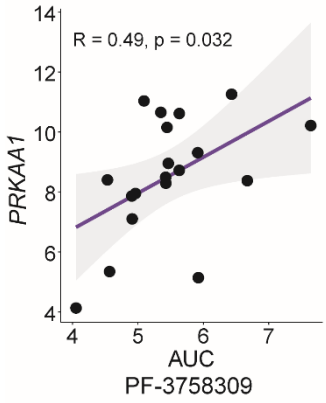

Figure 27 | Resistance markers of PF-3758309. Correlation of *PRKAA1* with CTD^2 AUC of PF-3758309 (https://depmap.org/) and proteomic (https://depmap.org/) data. Pearson correlation coefficient (R) and p-value (p) are shown. AUC: Area under curve.

In summary, our results demonstrate consistent associations of PF-3758309 with AMPK across multiple datasets, providing further evidence supporting its potential as an AMPKi.

28 Deconvolution of Target Space of PF-3758309

To validate the binding of PF-3758309 to AMPK and elucidate its global target footprint, we utilized kinobead technology, which allows for broad-range inhibitor-protein affinity profiling (Figure 28a). For this analysis, we employed 8182 empty and *Prkaa1* overexpressing cells and identified overlapping target kinases based on the following filtering criteria: EC50 < 500 nM, R2>0.8, and bottom of curve < 0.2. As depicted in Figure 28b, all AMPK1 subunits were detected, along with the intended target PAK4 for PF-3758309. Notably, the affinity of PF-3758309 towards the AMPK subunits was found to be higher compared to PAK4. Furthermore, PF-3758309 showed the lowest EC50 for PRKAA1 among 243 kinase inhibitors profiled in https://www.proteomicsdb.org/ (Figure 28c).

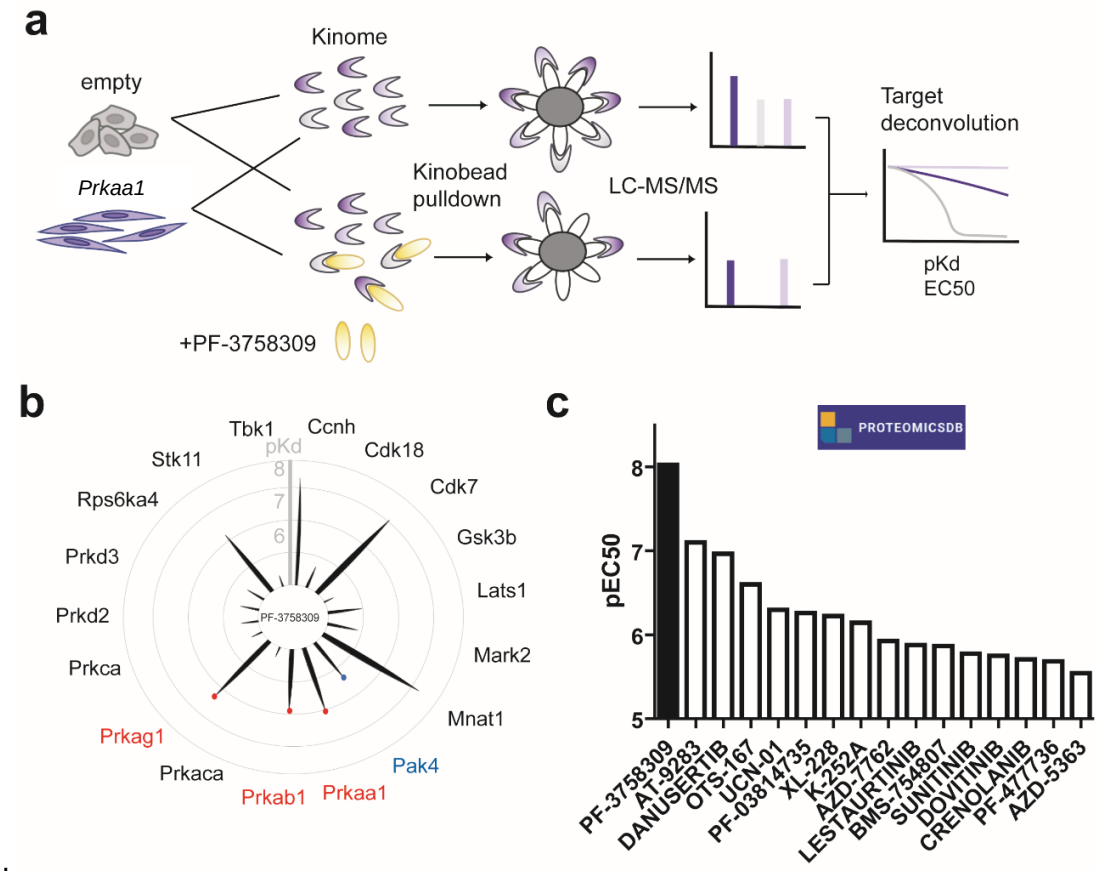

Figure 28 | Kinobeads pulldown to identify targets of PF-3758309. a, Target deconvolution strategy using the kinobead technology. The kinome of empty and *Prkaa1* overexpressing cells was pulled down using broad-range kinobeads either in presence of different concentrations of PF-3758309 or without. Kinases were detected via LC-MS/MS. Targets were ranked according to EC50<500 nM, R2>0.8, and bottom of curve<0.2. **b,** Radar plot of identified targets of PF-3758309 and their pKd. Spike length indicates the pKd of the respective kinase. AMPK subunits are indicated in red. The intended target Pak4 is indicated in blue. **c,** pEC50 of kinase inhibitors against

PRKAA1 downloaded from https://www.proteomicsdb.org/. Kinase inhibitors are ordered based on pEC50. The kinobeads assay was performed by Stefanie Höfer (Technical University Munich, AG Kuster). EC50: Effective concentration 50, LC-MS/MS: Liquid Chromatography with tandem mass spectrometry, Pak4: p21-activated kinase 4, pEC50: -$\log_{10}$(EC50), pKd: -$\log_{10}$(Dissosiation constante).

To gain a deeper understanding of interacting kinases and pulled-down complexes, we performed a string analysis of the designated PF-3758309 target kinases (Figure 29a). Our findings revealed the presence of two prominent complexes that were pulled down: the CDK-activating kinase (CAK)-complexes and the LKB1-AMPK-complex. Remarkably, our analysis also revealed that AMPK is specifically targeted by PF-3758309 with high potency, as evidenced by an EC50 below 20 nM (Figure 29b).

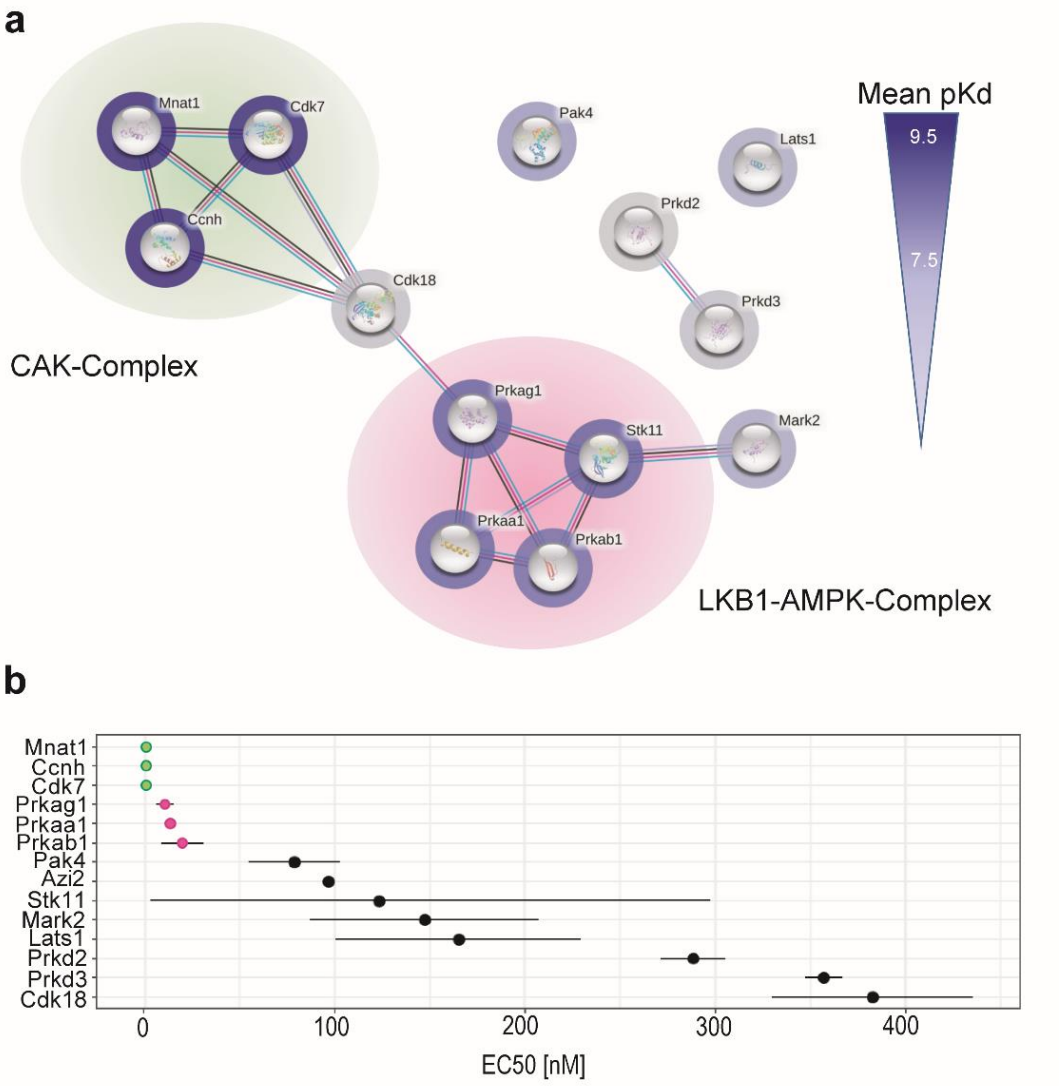

Figure 29 | Network and interaction analysis of PF-3758309-bound proteins. a, String analysis of designated PF-3758309. Mean pKd is indicated by color of border around kinases. Complexes are highlighted in green and pink. **b,** EC50 of kinases targeted by PF-3758309 below 500 nM in 8182 empty and *Prkaa1* overexpressing cells. CAK: CDK-activating kinase, EC50: Effective concentration 50, LKB1: Liver kinase B1, pKd: negative log(Dissosiation constante).

To molecularly analyze the binding of PF-3758309 to key kinases identified in the Kinobead assay, we conducted docking experiments focusing on the kinases with the highest affinity, namely AMPKα, CDK7, and PAK4 (Figure 30). Among the available crystal and cryoEM structures of AMPKα, only three (PDB structures 4RER, 6C9F, and 6C9H) exhibited a docking solution resembling the binding mode of PF-3758309 in PAK4 (PDB ID 2X4Z). In AMPKα, PF-3758309 binds to the ATP pocket and forms hydrogen bonds with Glu96 and Val98, similar to its interaction with PAK4. Additionally, hydrophobic interactions were observed with other residues. Similar binding modes were also observed in the docking pose of PF-3758309 with CDK7. These energetically favorable interactions observed in the studied kinase structures align well with the experimentally determined binding and provide valuable insights for further optimization of the inhibitor's interaction with AMPK.

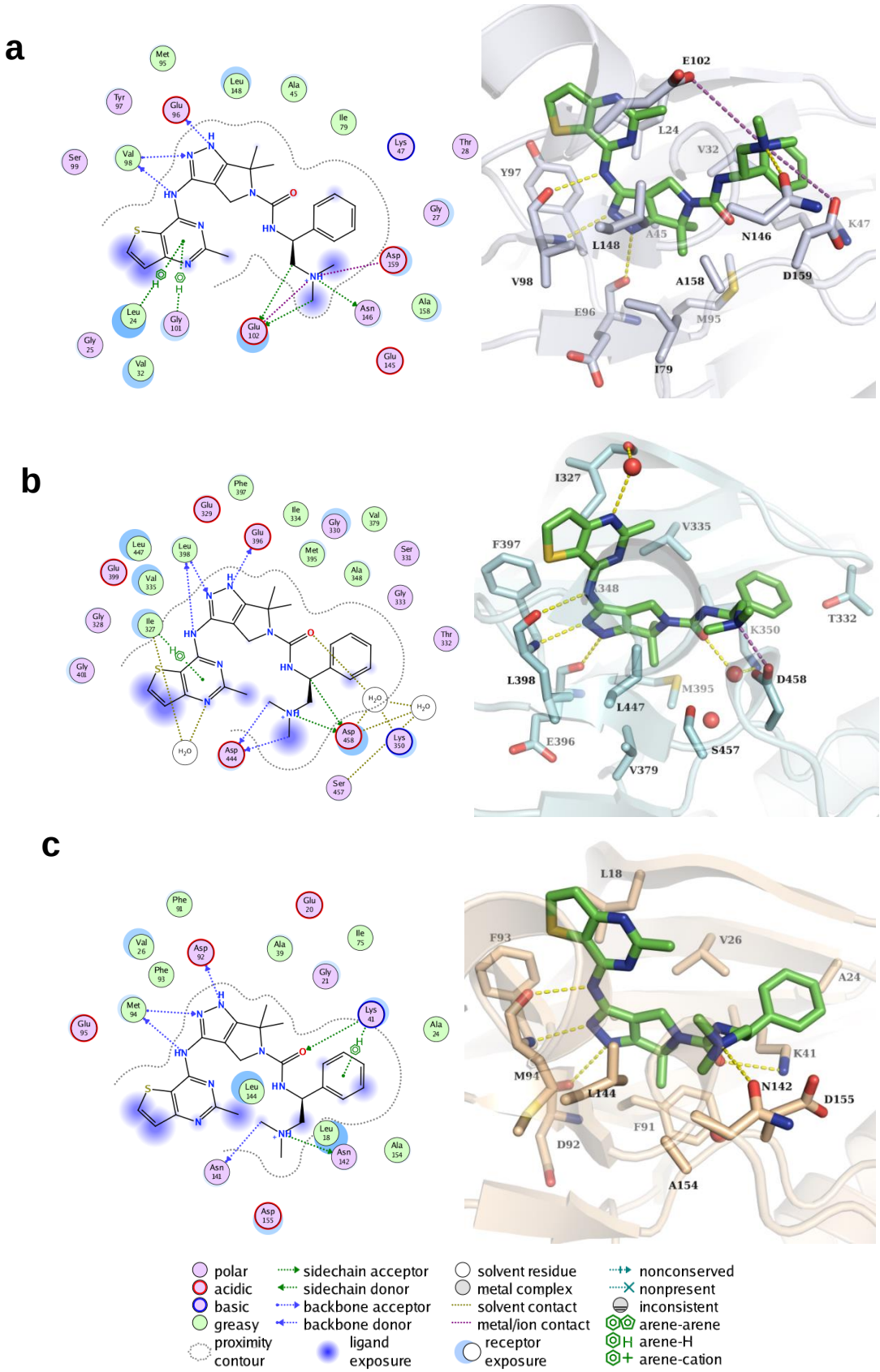

Figure 30 | Docking analysis of PF-3758309 to ATP-binding pocket of AMPKα, PAK4 and CDK7. Predicted interaction of **a,** AMPKα (PDB ID 6C9F), **b,** PAK4 (PDB ID 2XZ4), **c,** CDK7 (PDB ID 7B5Q) with docked PF-03758309. Left: 2D plot of kinase-ligand interaction. Right: 3D representation of the binding of the inhibitor (colored green) to the ATP pocket. Hydrogen bonds are shown as yellow-colored dashed lines. Salt bridges are shown as

magenta-colored dashed lines. Water molecules are displayed as red spheres. The analysis was performed by Abdallah M. Alfayomy (University of Freiburg, Freiburg, Prof. Dr, Wolfgang Sippl).

To demonstrate that PF-3758309 does not only bind to AMPK but also inhibits its downstream signaling, we investigated the phosphorylation of ACC, a well-known downstream target of AMPK, with Western blot (Figure 31a,b). Our findings revealed a significant inhibition of AMPK signaling, as evidenced by the blockage of ACC phosphorylation, which occurred within a similar concentration range as determined in the Kinobeads assay.

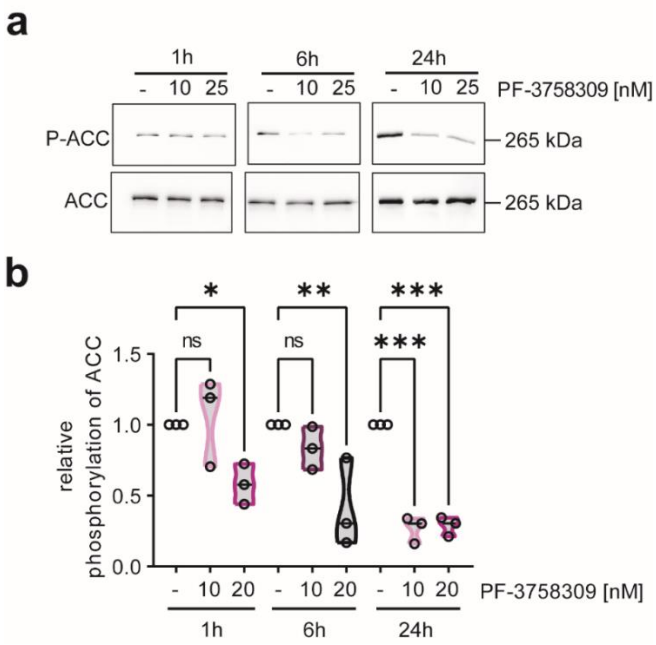

Figure 31 | Western blot of AMPK signaling upon PF-3758309 treatment. a, Western blot and **b,** quantification of AMPK signaling upon PF-3758309 treatment. Cells were treated with 10 or 20 nM of PF-3758309 or left as vehicle-treated controls. Protein was harvested after 1, 6 and 24 hours. AMPK inhibition was investigated by P-ACC and ACC antibodies. P-ACC was normalized to ACC. HSP90 served as loading control. Experiments were performed as three biological replicates. For statistical analysis, one-way ANOVA with Bonferroni's multiple comparison was performed. ACC: Acetyl-CoA carboxylase, HSP90: Heat shock protein 90, P-: Phosphorylation, ns: not significant, *: $p<0.05$, **: $p<0.01$, ***: $p<0.005$.

Collectively, our results indicate that PF-3758309 binds AMPK and blocks its downstream signaling at nanomolar concentrations.

29 PF-3758309 Is Effective Across PDAC Models

To assess the potential anti-tumor efficacy of PF-3758309 in PDAC, we conducted cell viability assays with 7-fold drug dilutions after three days of treatment and determined the IC50 values (Figure 32a,b,c). Our study included a comprehensive panel of 36 murine cell lines, 19

established PDAC cell lines, 5 patient-derived cell lines, and 7 organoids. The majority of the models exhibited an IC50 below 500 nM, indicating significant sensitivity to PF-3758309. Remarkably, prolonged exposure to PF-3758309 further enhanced efficacy in organoids, with complete loss of viability observed at 10 nM of the compound (Figure 32d).

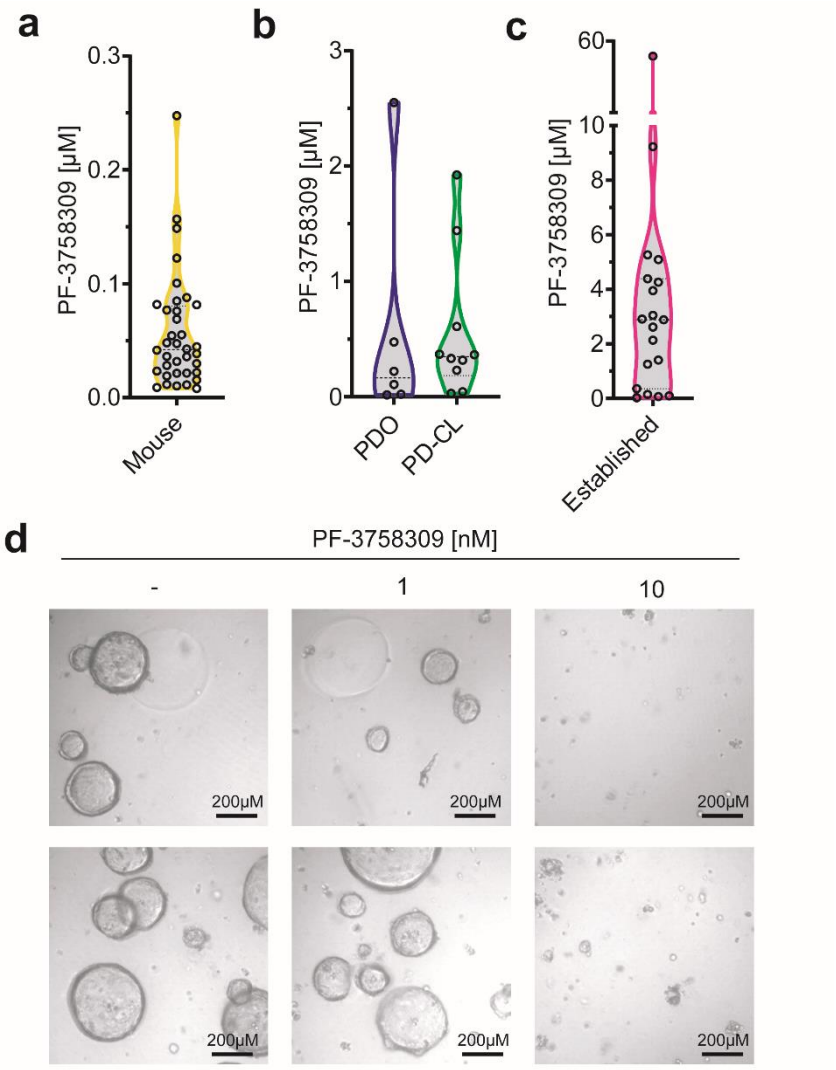

Figure 32 | Efficacy of PF-3758309 across PDAC models. a, IC50 of PF-3758309 after 3 days in murine cell lines. **b,** IC50 of PF-3758309 after 3 days in PDOs and PD-CLs. **c,** IC50 of PF-3758309 in established cell lines derived from depmap. **d,** Microscopic pictures of PDOs treated with different concentrations of PF-3758309 after 7 days. The scale bar is shown in the bottom right. Two biological replicates are depicted. Pharmacotyping of PDOs was performed by Felix Orben (Technical University Munich, Prof. Dr. Günter Schneider) and Constanza Tapia (Georg August University, Göttingen, Prof. Dr. Günter Schneider). IC50: Inhibitory concentration 50, PD-CL: Patient-derived cell lines, PDO: Patient-derived organoids.

Furthermore, we conducted single sample gene set variation analysis (ssGSVA) of the KEGG gene sets in the panel of the primary murine cell lines, and found

KEGG_CITRATE_CYCLE_TCA_CYCLE to be the top gene set that correlated with sensitivity to PF-3758309 (Figure 33).

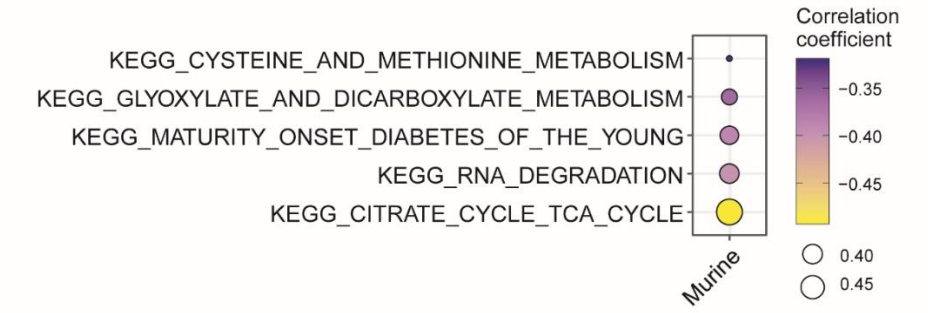

Figure 33 | Sensitivity marker for PF-3758309 based on KEGG signatures. Pearson correlation coefficient of ssGSVA of KEGG gene sets and IC50 of murine PDAC cell lines. The correlation coefficient is indicated by color and size. The top 5 negatively correlated KEGG gene sets are depicted. IC50: Inhibitory concentration 50, ssGSVA: Single sample gene set variation analysis.

Given that PF-3758309 targets AMPK, a key metabolic enzyme, we postulated that treatment with PF-3758309 may lead to impaired metabolic capacity. To test this hypothesis, we conducted a Seahorse assay on cells treated with PF-3758309 for 6 hours (Figure 34). Our findings revealed that PF-3758309 treatment resulted in decreased ECAR but not OCR in the cell line tested.

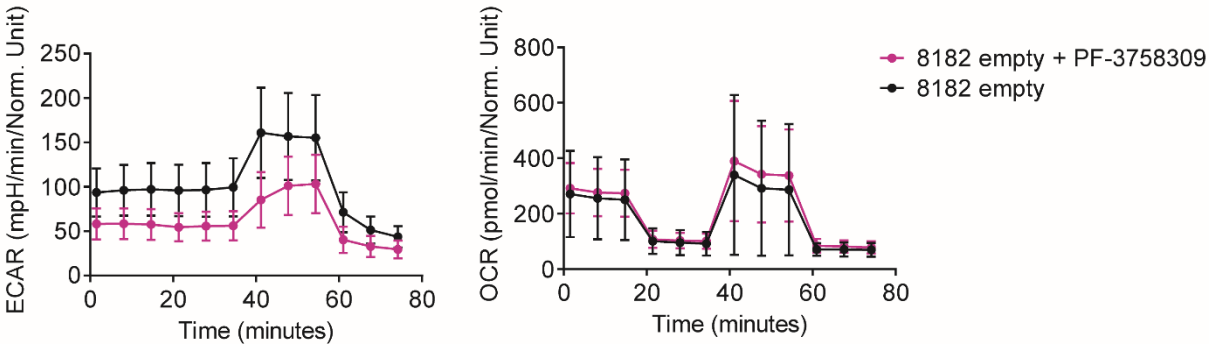

Figure 34 | Seahorse assay upon PF-3758309 treatment. 8182 empty cells were treated with 100 nM PF-3758309 for 6 hours. Cell lines are color-coded. **Left:** On the y-axis, the ECAR in mpH/min is shown. On the x-axis, the time in minutes is given. **Right:** On the y-axis, OCR in pmol/min is shown. On the x-axis, the Time in minutes is given. Experiments were performed as two biological replicates. ECAR: Extracellular acidification rate, OCR: Oxygen consumption rate. Seahorse assay was performed by Angela Boshnakovska (Georg August University, Göttingen, Prof. Dr. Peter Rehling).

Collectively, our data underscore the potential of repurposing PF-3758309 as an AMPK inhibitor. PF-3758309 demonstrated significant efficacy in various PDAC models, indicating its promising therapeutic utility.

Discussion

30 AMPK as a Potential Metastatic Driver

Although AMPK is the main downstream effector of the tumor suppressor LKB1, the role which AMPK plays in tumorigenesis and progression of PDAC is incompletely understood. Given that AMPK is a trimeric complex compromising two variants of the α and β subunits and three variants of the γ subunit, it is important to note that the specific composition of the assembled AMPK complex influences its interaction with downstream effectors and needs to be further investigated.

In this thesis, we mainly focused on PRKAA1. We found that *PRKAA1* is upregulated in PDAC compared to healthy tissue. Although no correlation between AMPKα and a specific subtype was found in immunohistochemistry staining of a human PDAC cohort, *Prkaa1* was associated with an undifferentiated and metastatic phenotype in xenografts of human established cell lines and murine PDAC models. The differences observed between murine models and human PDAC cohorts may be attributed to several factors. Firstly, metastatic patients are often ineligible for surgery and thus, underrepresented in the patient cohort. This sampling bias may explain the missing link between *Prkaa1* and a mesenchymal phenotype. Additionally, it is important to consider the differences in experimental conditions between murine models and human studies. Murine models and established cell lines allow for experiments to be conducted under controlled conditions over relatively short durations. On the other hand, human studies involve a multitude of factors that can influence outcomes, including individual variations, environmental influences, and diverse treatment approaches. This complexity in human studies can affect the interpretation and generalization of results. Furthermore, the genetic background of mice is relatively homogeneous compared to the intricate mutational landscape found in humans. This genetic variation among humans can potentially obscure the role of PRKAA1 in PDAC, suggesting that its involvement might be secondary to other factors. While human studies are considered the gold standard in clinical research, it becomes crucial to remove or account for these overriding factors to specifically study the role of PRKAA1.

As mentioned in the introduction, the role of AMPK in PDAC is not clear. The main drawbacks of the mentioned studies are short-term knockdowns and usage of unspecific inhibitors as well as activators, which do not allow for definite conclusions.

In our study, we overcame these limitations by using constitutive overexpressing models as well as KOs generated by CRISPR/Cas9. We observed that physiological overexpression of *Prkaa1* alone, without any other stimuli, was sufficient to induce a partial phenotype switch in relatively differentiated cells.

These findings are in contrast to studies that have demonstrated the role of AMPK in constraining EMT. For instance, Chou et al. in 2014 showed this effect by pharmacological activation of AMPK as well as siRNA-based knockdown of AMPK, in breast and prostate cancer cell lines (Chou et al. 2014). Similarly, a recent study published by the Jargong lab in 2020 reported that low expression of AMPKα1 was associated with poor clinical outcomes in metastatic breast cancer (Yi et al. 2020). *In vitro* experiments further supported these findings, as silencing of AMPKα1 led to the inhibition of cell-cell interactions through loss of E-cadherin, resulting in an invasive phenotype (Yi et al. 2020).

Nevertheless, *in vivo* studies show the opposite. Cai et al. showed that inoculating shAMPKa1 expressing 4T1 breast cancer cells into mammary fat pads resulted in a reduced number of nodules per lung (Cai et al. 2020). *In vitro* experiments exposing the cells to glucose deprivation or oxidative stress *in vitro*, shAMPKa1-expressing 4T1 cells had a decreased survival rate. By further revealing that AMPK phosphorylates the pyruvate dehydrogenase complex (PDHc), the rate-limiting enzyme of the TCA cycle that controls pyruvate influx, Cai et al. provided a molecular basis for these observed phenomena and highlighted another AMPK-controlled circuit that is crucial for metastasis development.

In addition, Saxena et al. demonstrated that the other AMPKα subunit, *Prkaa2*, is mandatory for the execution of the EMT program in response to physiological cues such as hypoxia and transforming growth factor β (TGFβ) in various malignant cell types (Saxena et al. 2018). Notably, the extent of the EMT program depended on whether the cells already possessed the requisite EMT machinery. By injecting cells that stably express scrambled shRNA or AMPKα2 shRNA through the tail vein of nude mice, the researchers detected less lung metastasis when using AMPKα2 shRNA expressing cells. Mechanistically, Saxena et al. demonstrated that AMPK mediates its invasive effects via the upregulation of twist family basic helix–loop–helix transcription factor 1 (TWIST1) gene expression and its increased nuclear localization. TWIST1 is widely known for cell lineage determination and differentiation of the mesoderm and is a prime example of a transcription factor essential in cancer metastasis (Xu et al. 2017; Yang et al. 2004, 2008).

Although our data highlights the significance of *Prkaa1* in influencing the phenotype of PDAC cells, the molecular mechanisms underlying this role remain unclear and require further experimental elucidation. Moreover, it would be important to investigate the extent of phenotype switch in the presence of EMT inducers or blockers, as well as under cellular stress, in order to gain a more comprehensive understanding of how *Prkaa1* regulates EMT in different cellular contexts. These investigations are warranted and represent an important next step in advancing our understanding of AMPK-modulated PDAC biology.

It is well established that the KRAS-MEK-ERK pathway drives PDAC progression as well as metastasis (Ischenko, Petrenko, and Hayman 2014; Mueller et al. 2018). In contrast to the general belief that AMPK blocks proliferative signaling, we found that *Prkaa1* correlates with the oncogenic KRAS-MEK-ERK pathway. Further studies found also paradoxical activation of the oncogenic AKT-mTOR-axis. Strikingly, AMPK was shown to promote Akt survival signaling under various stresses suggesting AMPK can both decrease and increase mTOR activity depending on the cellular context (Han et al. 2018). Han et al provided evidence that AMPK phosphorylates S-Phase Kinase Associated Protein 2 (SKP2) at Ser256 which in turn drives K63-linked ubiquitination and activation of AKT. This newly identified AMPK-SKP2-AKT pathway provides a new perspective on the premise of the opposite roles of AMPK and mTOR. These findings highlight that *Prkaa1* can foster oncogenic signaling.

Contrary to our initial expectations, we observed that *Prkaa1* KO cells exhibited similar growth rates compared to the LacZ control cells. Similarly, the Seahorse assay did not reveal any clear trends in metabolic function and we observed only a mild advantage of *Prkaa1* in growth factor-depleted conditions. Notably, 8570 showed the highest metabolic alterations among the three KO cell lines, despite no differential gene expression observed. One possible explanation could be the presence of excessive nutrients in the *in vitro* culture conditions, which may have masked any effects of potential metabolic impairments.

In this context, previous studies have shown that AMPK is required under conditions of nutrient depletion, such as essential amino acids (Ghislat et al. 2012) or cysteine (Yuan et al. 2021) deprivation. Additionally, AMPK has been implicated in the regulation of iron metabolism (Merrill et al. 2012; Wang et al. 2022). To gain a deeper understanding of the nutrient dependencies of *Prkaa1* KO cells, it would be valuable to repeat these experiments using media cocktails that are specifically formulated to lack certain nutrients. This approach would not only help elucidate the role of *Prkaa1* in regulating cellular growth and metabolism but also provide further insights into pharmacological targets for PDAC therapy in combination with AMPK inhibition.

31 AMPK and Redox Metabolism

Our research findings suggest that under *in vitro* culture conditions *Prkaa1* may not be an essential gene, as *Prkaa1* KO cells show similar growth rates as their control counterparts. However, we hypothesized that *Prkaa1* KO cells may be more vulnerable to cellular stresses. To investigate this further, we conducted a drug screen in *Prkaa1* KO cells to identify potential bottlenecks. Our results revealed that Erastin is a pan-vulnerability among *Prkaa1* KO cells.

Erastin is a small molecule compound that has gained attention in the field of cancer research. It was initially identified through a high-throughput screening approach as a compound that selectively induces cell death in cancer cells harboring *RAS*^{V12} mutations (Dolma et al. 2003). Erastin is thought to exert its action by targeting two specific components: (i) system xc− (Yan et al. 2022) and (ii) voltage-dependent anion channels (VDACs) (Yagoda et al. 2007).

System xc− is a Na+-independent cystine–glutamate antiporter that consists of two subunits: the transmembrane transporter protein SLC7A11 (xCT) and the single-pass transmembrane regulatory subunit SLC3A2. This antiporter facilitates the exchange of extracellular l-cystine and intracellular l-glutamate, which are crucial precursors for the synthesis of glutathione essential for cellular defense against oxidative stress. (Bannai and Kitamura 1980; Lewerenz et al. 2013)

On the other hand, VDACs are a class of porin ion channels with three isoforms (VDAC1, VDAC2, and VDAC3). They are the most abundant proteins in the outer mitochondrial membrane and serve as general diffusion pores for small hydrophilic molecules such as ATP, ADP, P_i, and respiratory substrates. The voltage-sensitive reversible closure of VDACs is regulated by various factors, including the interaction with dimeric tubulin (Rostovtseva et al. 2008), binding of hexokinase 2 (Haloi et al. 2021) or α-synuclein (Rosencrans et al. 2021), which has significant implications for cellular processes.

One of the consequences of VDAC closure is the reduction of oxidative metabolism within mitochondria due to the restricted entry of substrates into the mitochondria. This metabolic state promotes the upregulation of glycolysis as an alternative energy-generating pathway. Additionally, the closure of VDACs contributes to a decrease in the generation of ROS through reduced activity of the electron transport chain. Furthermore, the closure also prevents the release of pro-apoptotic proteins from the mitochondria, thus inhibiting the initiation of apoptosis. (Varughese, Buchanan, and Pitt 2021)

As mentioned, Erastin interacts with both system xc− and VDACs. By targeting system xc−, Erastin disrupts the exchange of cystine and glutamate, thereby inhibiting GSH synthesis and compromising redox homeostasis (Sato et al. 2018). Simultaneously, Erastin increases the conductance of VDACs leading to enhanced oxidative metabolism and upregulation of ROS production (Maldonado et al. 2013; Yagoda et al. 2007).

The combined targeting of system xc− and VDACs by Erastin disrupts redox homeostasis resulting in an unique form of cell death known as ferroptosis. Ferroptosis is distinguished by an iron-dependent and uncontrolled buildup of lipid peroxidation, ultimately resulting in cell death (X. Jiang, Stockwell, and Conrad 2021). In recent years, ferroptosis has emerged as a

promising therapeutic approach to combat refractory patients and chemotherapy-resilient cancer cells (Hangauer et al. 2017; Viswanathan et al. 2017).

As highlighted in the introduction, *Prkaa1* plays a crucial role in regulating various interfaces that are important for redox homeostasis, and thus, *Prkaa1* may prevent ferroptosis. For instance, it directly phosphorylates antioxidant transcription factors including members of the FoxO transcription factor family (Greer et al. 2007; Yun et al. 2014) as well as NRF2 (Joo et al. 2016). Moreover, it blocks metabolic pathways which consume NADPH including fatty acid synthesis through phosphorylation of ACC1/2 (Jeon et al. 2012) while maintaining continuous TCA flux (Cai et al. 2020; Kumazoe et al. 2017) for NADPH production.

Furthermore, our RNA-Seq analysis of both *Prkaa1* overexpressing and *Prkaa1* KO cell lines revealed that gene sets related to glutathione metabolism were among the top regulated, further supporting the role of *Prkaa1* in redox homeostasis by glutathione-dependent antioxidant defenses.

Notably, our results suggest that inducing ferroptotic cell death could be a vulnerability of PDAC cells, particularly in the absence of surveillance by *Prkaa1*.

32 PF-3758309 as AMPKi

One main step to broaden the understanding of AMPK in cancer and to increase its therapeutic possibility is the development of specific AMPK inhibitors. Currently available pharmacological AMPK inhibitors and activators have been drawn criticism due to their off-target effects and indirect mechanism of action. Nevertheless, promising anti-tumor efficacy has been demonstrated for Dorsomorphin as well as BAY-3827. For instance, BAY-3758 has been tested in androgen-dependent prostate cancer models (Lemos et al. 2021), while Dorsomorphin has shown effectiveness in hematological cancers (Liu et al. 2020) as well as in PDAC (Duong et al. 2012). These preliminary findings suggest that AMPK inhibition might hold therapeutic value in cancer therapy.

To address the limitations of using experimental drugs, we pursued drug repurposing as a strategy to identify AMPK-targeting compounds. We initiated a drug screen including 112 compounds currently under clinical testing and identified PF-3758309 as the top compound associated with resistance in *Prkaa1* overexpressing PDAC cell lines. We further validated the binding of PF-3758309 to AMPK as well as the inhibition of AMPK signaling at low nanomolar doses. Importantly, PF-3758309 demonstrated efficacy across PDAC models. Although in short-term assays, the IC50 of cell lines was above the effective concentration where PF-3758309 exhibited higher selectivity, in long-term assays, cells did not survive 10-20 nM.

Notably, PF-3758309 was previously tested in a clinical trial involving solid tumors and no safety concerns were raised (NCT00932126). However, despite the administration of PF-3758309, the patients experienced relapses, leading to the termination of the study. This contradicts our *in vitro* data where we show a potent killing as well as *in vivo* data where PF-3758309 blocked the growth of multiple human tumor xenografts (Murray et al. 2010).

One possible explanation for this discrepancy could be that elevated levels of *Prkaa1* confer resistance to PF-3758309. As discussed earlier, cancer cells often exhibit elevated levels of *Prkaa1* compared to healthy tissue. Regarding the fact that *Prkaa1* KO cells grow similarly to their control cells under *in vitro* culture conditions, inhibiting solely AMPK might not be enough to generate an effective response in PDAC. Moreover, our experimental setup revealed one murine PDAC cell line, 8570, to be AMPK-independent when no selection pressure was applied. Therefore, we propose combination therapy to overcome *Prkaa1*-driven resistance to PF-3758309. Promising candidates for combination therapy are ROS-inducing agents as discovered by our drug screen of *Prkaa1* KO cells. Our results indicate that PDAC cells may be dependent on *Prkaa1* for glutathione-dependent antioxidant defenses making this a rational therapeutic approach that merits further investigation.

While we show that PF-3758309 efficiently targets AMPK, our data also reveals PF-3758309 has off-target effects. We found that especially the CAK-complex, including CDK7, Menage A Trois 1 (MNAT1) and cyclin H was targeted at very low doses of PF-3758309. Interestingly, CDK7 has been identified as a potential target for cancer therapy. CDK7 plays a critical role in the regulation of the cell cycle and transcriptional regulation through the phosphorylation of RNA polymerase II at CTD Ser7 (Akhtar et al. 2009; Glover-Cutter et al. 2009) and Ser5 (Ebmeier et al. 2017). Inhibition of CDK7 has been shown to disrupt transcriptional elongation and cause cell cycle arrest in cancer cells (Olson et al. 2019; Sun et al. 2020), making it an attractive target for cancer therapy. Moreover, there are currently ongoing clinical trials using CDK7 inhibitors, namely SY-5609 and Q901, in advanced solid tumors (NCT04247126, NCT05394103).

Although we provide evidence for the cross-species efficacy of PF-3758309, the mode of action of this compound requires further exploration. In addition, while our cell-based studies are informative, they should be complemented with *in vivo* experiments to take into account the effects of the immune system as well as hepatic drug metabolism. These findings can then inform structure-based optimization efforts to improve the potency and selectivity of the compound.

In summary, our data underscore the importance of conducting in-depth drug profiling to fully understand the mode of action of a compound and realize its full potential as an inhibitor.

Additionally, we corroborate the value of drug repurposing by discovering PF-3758309 as AMPKi which could serve as a scaffold for the development of advanced and more specific molecules in the future.

33 Conclusion

In conclusion, this work has contributed to highlight the context-dependent role of *Prkaa1* in PDAC. The findings demonstrate that *Prkaa1* (i) has the capacity to shape the phenotype of PDAC cells and (ii) is connected to drug metabolism as well as glutathione homeostasis while (III) its absence renders cells susceptible to ferroptotic stimuli. Moreover, these results underscore the significance of *Prkaa1* as a potential therapeutic target in PDAC and suggest that targeting this pathway may represent a promising approach for the development of new treatments for this deadly disease.

Due to the lack of clinically available AMPKi, a drug repurposing approach was employed to build upon previous research and expedite translation into an approved drug with clinical potential. Notably, the findings demonstrate that the Pak4 inhibitor PF-3758309, which has been part of Phase I clinical trial, can be repurposed as an AMPKi. Furthermore, the results provide evidence for the potential anti-cancer efficacy of PF-3758309 as an AMPKi in various *in vitro* PDAC models and thus lay the foundation for a promising pharmacological option for PDAC treatment with AMPKi.

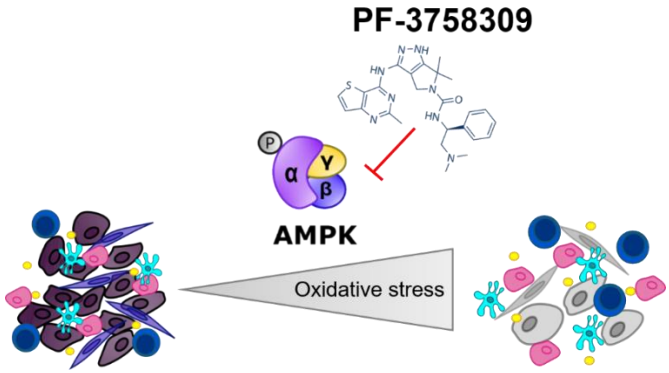

Figure 35 | Graphical abstract of this thesis. PDACs rely on AMPK to uphold their oxidative stress defense. Inhibition of AMPK by PF-3758309 in combination with oxidative stress caused by other agents or environmental factors may be a promising therapeutic approach for the treatment of PDAC.

34 Limitations and Outlook

The presented results might represent a first step forward to broaden the spectrum of actionable targets in PDAC therapy. However, it still harbors limitations and underexplored aspects.

Further studies are warranted to elucidate the precise mechanism by which *Prkaa1* protects against oxidative stress, as well as to identify the key regulatory nodes of *Prkaa1* that modulate phenotype plasticity with respect to EMT. In this study, I focused on *Prkaa1* in advanced PDAC. It is crucial to consider the specific time points during cancer development, progression, and metastatic cascade, as *Prkaa1* may exert distinct functions at different stages of these processes.

Moreover, AMPK has been demonstrated to play a pivotal role in immune regulation. Therefore, *in vivo* studies utilizing mice with a functional immune system are imperative to unravel the intricate interplay of AMPK in this context. In addition, AMPK is a trimeric complex, consisting of two isoforms of the α and β subunits, as well as three isoforms for the γ subunit. It is important to note that the composition of the assembled AMPK complex also influences its downstream effectors. Thus, combinations of AMPK complex assembly need to be further investigated.

Although the presented findings revealed that PF-3758309 effectively inhibits AMPK, it is worth noting that its binding of the CAK complex raises concerns about unspecific inhibitory effects. Therefore, further chemical optimization of PF-3758309 is warranted to minimize off-target effects. Moreover, considering the recruiter functions of AMPK, additional strategies such as proteolysis targeting chimera (PROTAC) development or molecular glues should be explored, as mere AMPK inhibition may not be sufficient to fully block AMPK signal transduction and output.

References

Akhtar, Md. Sohail, Martin Heidemann, Joshua R. Tietjen, David W. Zhang, Rob D. Chapman, Dirk Eick, and Aseem Z. Ansari. 2009. "TFIIH Kinase Places Bivalent Marks on the Carboxy-Terminal Domain of RNA Polymerase II." *Molecular Cell* 34(3):387–93. doi: 10.1016/j.molcel.2009.04.016.

Anon. 2022. "The KRASG12D Inhibitor MRTX1133 Elucidates KRAS-Mediated Oncogenesis." *Nature Medicine* 28(10):2017–18. doi: 10.1038/s41591-022-02008-6.

Aung, Kyaw L., Sandra E. Fischer, Robert E. Denroche, Gun-Ho Jang, Anna Dodd, Sean Creighton, Bernadette Southwood, Sheng-Ben Liang, Dianne Chadwick, Amy Zhang, Grainne M. O'Kane, Hamzeh Albaba, Shari Moura, Robert C. Grant, Jessica K. Miller, Faridah Mbabaali, Danielle Pasternack, Ilinca M. Lungu, John M. S. Bartlett, Sangeet Ghai, Mathieu Lemire, Spring Holter, Ashton A. Connor, Richard A. Moffitt, Jen Jen Yeh, Lee Timms, Paul M. Krzyzanowski, Neesha Dhani, David Hedley, Faiyaz Notta, Julie M. Wilson, Malcolm J. Moore, Steven Gallinger, and Jennifer J. Knox. 2018. "Genomics-Driven Precision Medicine for Advanced Pancreatic Cancer: Early Results from the COMPASS Trial." *Clinical Cancer Research* 24(6):1344–54. doi: 10.1158/1078-0432.CCR-17-2994.

Australian Pancreatic Cancer Genome Initiative, Nicola Waddell, Marina Pajic, Ann-Marie Patch, David K. Chang, Karin S. Kassahn, Peter Bailey, Amber L. Johns, David Miller, Katia Nones, Kelly Quek, Michael C. J. Quinn, Alan J. Robertson, Muhammad Z. H. Fadlullah, Tim J. C. Bruxner, Angelika N. Christ, Ivon Harliwong, Senel Idrisoglu, Suzanne Manning, Craig Nourse, Ehsan Nourbakhsh, Shivangi Wani, Peter J. Wilson, Emma Markham, Nicole Cloonan, Matthew J. Anderson, J. Lynn Fink, Oliver Holmes, Stephen H. Kazakoff, Conrad Leonard, Felicity Newell, Barsha Poudel, Sarah Song, Darrin Taylor, Nick Waddell, Scott Wood, Qinying Xu, Jianmin Wu, Mark Pinese, Mark J. Cowley, Hong C. Lee, Marc D. Jones, Adnan M. Nagrial, Jeremy Humphris, Lorraine A. Chantrill, Venessa Chin, Angela M. Steinmann, Amanda Mawson, Emily S. Humphrey, Emily K. Colvin, Angela Chou, Christopher J. Scarlett, Andreia V. Pinho, Marc Giry-Laterriere, Ilse Rooman, Jaswinder S. Samra, James G. Kench, Jessica A. Pettitt, Neil D. Merrett, Christopher Toon, Krishna Epari, Nam Q. Nguyen, Andrew Barbour, Nikolajs Zeps, Nigel B. Jamieson, Janet S. Graham, Simone P. Niclou, Rolf Bjerkvig, Robert Grützmann, Daniela Aust, Ralph H. Hruban, Anirban Maitra, Christine A. Iacobuzio-Donahue, Christopher L. Wolfgang, Richard A. Morgan, Rita T. Lawlor, Vincenzo Corbo, Claudio Bassi, Massimo Falconi, Giuseppe Zamboni, Giampaolo Tortora, Margaret A. Tempero, Anthony J. Gill, James R. Eshleman, Christian Pilarsky, Aldo Scarpa, Elizabeth A. Musgrove, John V. Pearson, Andrew V. Biankin, and Sean M. Grimmond. 2015. "Whole Genomes Redefine the Mutational Landscape of Pancreatic Cancer." *Nature* 518(7540):495–501. doi: 10.1038/nature14169.

Bannai, S., and E. Kitamura. 1980. "Transport Interaction of L-Cystine and L-Glutamate in Human Diploid Fibroblasts in Culture." *Journal of Biological Chemistry* 255(6):2372–76. doi: 10.1016/S0021-9258(19)85901-X.

Barugola, Giuliano, Stefano Partelli, Stefano Marcucci, Nora Sartori, Paola Capelli, Claudio Bassi, Paolo Pederzoli, and Massimo Falconi. 2009. "Resectable Pancreatic Cancer: Who Really Benefits From Resection?" *Annals of Surgical Oncology* 16(12):3316–22. doi: 10.1245/s10434-009-0670-7.

Berk-Krauss, Juliana, Jennifer A. Stein, Jeffrey Weber, David Polsky, and Alan C. Geller. 2020. "New Systematic Therapies and Trends in Cutaneous Melanoma Deaths Among US Whites, 1986–2016." *American Journal of Public Health* 110(5):731–33. doi: 10.2105/AJPH.2020.305567.

Biancur, Douglas E., Kevin S. Kapner, Keisuke Yamamoto, Robert S. Banh, Jasper E. Neggers, Albert S. W. Sohn, Warren Wu, Robert T. Manguso, Adam Brown, David E. Root, Andrew J. Aguirre, and Alec C. Kimmelman. 2021. "Functional Genomics Identifies Metabolic Vulnerabilities in Pancreatic Cancer." *Cell Metabolism* 33(1):199-210.e8. doi: 10.1016/j.cmet.2020.10.018.

Biankin, Andrew V., Nicola Waddell, Karin S. Kassahn, Marie-Claude Gingras, Lakshmi B. Muthuswamy, Amber L. Johns, David K. Miller, Peter J. Wilson, Ann-Marie Patch, Jianmin Wu, David K. Chang, Mark J.

Cowley, Brooke B. Gardiner, Sarah Song, Ivon Harliwong, Senel Idrisoglu, Craig Nourse, Ehsan Nourbakhsh, Suzanne Manning, Shivangi Wani, Milena Gongora, Marina Pajic, Christopher J. Scarlett, Anthony J. Gill, Andreia V. Pinho, Ilse Rooman, Matthew Anderson, Oliver Holmes, Conrad Leonard, Darrin Taylor, Scott Wood, Qinying Xu, Katia Nones, J. Lynn Fink, Angelika Christ, Tim Bruxner, Nicole Cloonan, Gabriel Kolle, Felicity Newell, Mark Pinese, R. Scott Mead, Jeremy L. Humphris, Warren Kaplan, Marc D. Jones, Emily K. Colvin, Adnan M. Nagrial, Emily S. Humphrey, Angela Chou, Venessa T. Chin, Lorraine A. Chantrill, Amanda Mawson, Jaswinder S. Samra, James G. Kench, Jessica A. Lovell, Roger J. Daly, Neil D. Merrett, Christopher Toon, Krishna Epari, Nam Q. Nguyen, Andrew Barbour, Nikolajs Zeps, Nipun Kakkar, Fengmei Zhao, Yuan Qing Wu, Min Wang, Donna M. Muzny, William E. Fisher, F. Charles Brunicardi, Sally E. Hodges, Jeffrey G. Reid, Jennifer Drummond, Kyle Chang, Yi Han, Lora R. Lewis, Huyen Dinh, Christian J. Buhay, Timothy Beck, Lee Timms, Michelle Sam, Kimberly Begley, Andrew Brown, Deepa Pai, Ami Panchal, Nicholas Buchner, Richard De Borja, Robert E. Denroche, Christina K. Yung, Stefano Serra, Nicole Onetto, Debabrata Mukhopadhyay, Ming-Sound Tsao, Patricia A. Shaw, Gloria M. Petersen, Steven Gallinger, Ralph H. Hruban, Anirban Maitra, Christine A. Iacobuzio-Donahue, Richard D. Schulick, Christopher L. Wolfgang, Richard A. Morgan, Rita T. Lawlor, Paola Capelli, Vincenzo Corbo, Maria Scardoni, Giampaolo Tortora, Margaret A. Tempero, Karen M. Mann, Nancy A. Jenkins, Pedro A. Perez-Mancera, David J. Adams, David A. Largaespada, Lodewyk F. A. Wessels, Alistair G. Rust, Lincoln D. Stein, David A. Tuveson, Neal G. Copeland, Elizabeth A. Musgrove, Aldo Scarpa, James R. Eshleman, Thomas J. Hudson, Robert L. Sutherland, David A. Wheeler, John V. Pearson, John D. McPherson, Richard A. Gibbs, and Sean M. Grimmond. 2012. “Pancreatic Cancer Genomes Reveal Aberrations in Axon Guidance Pathway Genes.” *Nature* 491(7424):399–405. doi: 10.1038/nature11547.

Bowers, Kevin J., Federico D. Sacerdoti, John K. Salmon, Yibing Shan, David E. Shaw, Edmond Chow, Huafeng Xu, Ron O. Dror, Michael P. Eastwood, Brent A. Gregersen, John L. Klepeis, Istvan Kolossvary, and Mark A. Moraes. 2006. “Molecular Dynamics---Scalable Algorithms for Molecular Dynamics Simulations on Commodity Clusters.” P. 84 in *Proceedings of the 2006 ACM/IEEE conference on Supercomputing - SC ’06*. Tampa, Florida: ACM Press.

Bultot, Laurent, Bruno Guigas, Alexander Von Wilamowitz-Moellendorff, Liliane Maisin, Didier Vertommen, Nusrat Hussain, Monique Beullens, Joan J. Guinovart, Marc Foretz, Benoît Viollet, Kei Sakamoto, Louis Hue, and Mark H. Rider. 2012. “AMP-Activated Protein Kinase Phosphorylates and Inactivates Liver Glycogen Synthase.” *Biochemical Journal* 443(1):193–203. doi: 10.1042/BJ20112026.

Burris, H. A., M. J. Moore, J. Andersen, M. R. Green, M. L. Rothenberg, M. R. Modiano, M. C. Cripps, R. K. Portenoy, A. M. Storniolo, P. Tarassoff, R. Nelson, F. A. Dorr, C. D. Stephens, and D. D. Von Hoff. 1997. “Improvements in Survival and Clinical Benefit with Gemcitabine as First-Line Therapy for Patients with Advanced Pancreas Cancer: A Randomized Trial.” *Journal of Clinical Oncology* 15(6):2403–13. doi: 10.1200/JCO.1997.15.6.2403.

Cai, Zhen, Chien-Feng Li, Fei Han, Chunfang Liu, Anmei Zhang, Che-Chia Hsu, Danni Peng, Xian Zhang, Guoxiang Jin, Abdol-Hossein Rezaeian, Guihua Wang, Weina Zhang, Bo-Syong Pan, Chi-Yun Wang, Yu-Hui Wang, Shih-Ying Wu, Shun-Chin Yang, Fang-Chi Hsu, Ralph B. D’Agostino, Christina M. Furdui, Gregory L. Kucera, John S. Parks, Floyd H. Chilton, Chih-Yang Huang, Fuu-Jen Tsai, Boris Pasche, Kounosuke Watabe, and Hui-Kuan Lin. 2020. “Phosphorylation of PDHA by AMPK Drives TCA Cycle to Promote Cancer Metastasis.” *Molecular Cell* 80(2):263-278.e7. doi: 10.1016/j.molcel.2020.09.018.

Carmichael, J., U. Fink, Rc Russell, Mf Spittle, Al Harris, G. Spiessi, and J. Blatter. 1996. “Phase II Study of Gemcitabine in Patients with Advanced Pancreatic Cancer.” *British Journal of Cancer* 73(1):101–5. doi: 10.1038/bjc.1996.18.

Casper, Ephraim S., Mark R. Green, David P. Kelsen, Robert T. Heelan, Thomas D. Brown, Carlos D. Flombaum, Bonnie Trochanowski, and Peter G. Tarassoff. 1994. “Phase II Trial of Gemcitabine (2,2?-Difiuorodeoxycytidine) in Patients with Adenocarcinoma of the Pancreas.” *Investigational New Drugs* 12(1):29–34. doi: 10.1007/BF00873232.

Chan-Seng-Yue, Michelle, Jaeseung C. Kim, Gavin W. Wilson, Karen Ng, Eugenia Flores Figueroa, Grainne M. O'Kane, Ashton A. Connor, Robert E. Denroche, Robert C. Grant, Jessica McLeod, Julie M. Wilson, Gun Ho Jang, Amy Zhang, Anna Dodd, Sheng-Ben Liang, Ayelet Borgida, Dianne Chadwick, Sangeetha Kalimuthu, Ilinca Lungu, John M. S. Bartlett, Paul M. Krzyzanowski, Vandana Sandhu, Hervé Tiriac, Fieke E. M. Froeling, Joanna M. Karasinska, James T. Topham, Daniel J. Renouf, David F. Schaeffer, Steven J. M. Jones, Marco A. Marra, Janessa Laskin, Runjan Chetty, Lincoln D. Stein, George Zogopoulos, Benjamin Haibe-Kains, Peter J. Campbell, David A. Tuveson, Jennifer J. Knox, Sandra E. Fischer, Steven Gallinger, and Faiyaz Notta. 2020. "Transcription Phenotypes of Pancreatic Cancer Are Driven by Genomic Events during Tumor Evolution." *Nature Genetics* 52(2):231–40. doi: 10.1038/s41588-019-0566-9.

Chemical Computing Group ULC. 2019. "Molecular Operating Environment (MOE)."

Chen, Ke, Weikun Qian, Jie Li, Zhengdong Jiang, Liang Cheng, Bin Yan, Junyu Cao, Liankang Sun, Cancan Zhou, Meng Lei, Wanxing Duan, Jiguang Ma, Qingyong Ma, and Zhenhua Ma. 2017. "Loss of AMPK Activation Promotes the Invasion and Metastasis of Pancreatic Cancer through an HSF1-Dependent Pathway." *Molecular Oncology* 11(10):1475–92. doi: 10.1002/1878-0261.12116.

Chen, Zhen, Caoqi Lei, Chao Wang, Nan Li, Mrinal Srivastava, Mengfan Tang, Huimin Zhang, Jong Min Choi, Sung Yun Jung, Jun Qin, and Junjie Chen. 2019. "Global Phosphoproteomic Analysis Reveals ARMC10 as an AMPK Substrate That Regulates Mitochondrial Dynamics." *Nature Communications* 10(1):104. doi: 10.1038/s41467-018-08004-0.

Cheratta, Anees Rahman, Faisal Thayyullathil, Simon A. Hawley, Fiona A. Ross, Abdelmajdid Atrih, Douglas J. Lamont, Siraj Pallichankandy, Karthikeyan Subburayan, Ameer Alakkal, Rachid Rezgui, Alex Gray, D. Grahame Hardie, and Sehamuddin Galadari. 2022. "Caspase Cleavage and Nuclear Retention of the Energy Sensor AMPK-A1 during Apoptosis." *Cell Reports* 39(5):110761. doi: 10.1016/j.celrep.2022.110761.

Chou, Chih-Chien, Kuen-Haur Lee, I.-Lu Lai, Dasheng Wang, Xiaokui Mo, Samuel K. Kulp, Charles L. Shapiro, and Ching-Shih Chen. 2014. "AMPK Reverses the Mesenchymal Phenotype of Cancer Cells by Targeting the Akt–MDM2–Foxo3a Signaling Axis." *Cancer Research* 74(17):4783–95. doi: 10.1158/0008-5472.CAN-14-0135.

Clark, Carolyn E., Sunil R. Hingorani, Rosemarie Mick, Chelsea Combs, David A. Tuveson, and Robert H. Vonderheide. 2007. "Dynamics of the Immune Reaction to Pancreatic Cancer from Inception to Invasion." *Cancer Research* 67(19):9518–27. doi: 10.1158/0008-5472.CAN-07-0175.

Conroy, Thierry, Françoise Desseigne, Marc Ychou, Olivier Bouché, Rosine Guimbaud, Yves Bécouarn, Antoine Adenis, Jean-Luc Raoul, Sophie Gourgou-Bourgade, Christelle De La Fouchardière, Jaafar Bennouna, Jean-Baptiste Bachet, Faiza Khemissa-Akouz, Denis Péré-Vergé, Catherine Delbaldo, Eric Assenat, Bruno Chauffert, Pierre Michel, Christine Montoto-Grillot, and Michel Ducreux. 2011. "FOLFIRINOX versus Gemcitabine for Metastatic Pancreatic Cancer." *New England Journal of Medicine* 364(19):1817–25. doi: 10.1056/NEJMoa1011923.

Daemen, Anneleen, David Peterson, Nisebita Sahu, Ron McCord, Xiangnan Du, Bonnie Liu, Katarzyna Kowanetz, Rebecca Hong, John Moffat, Min Gao, Aaron Boudreau, Rana Mroue, Laura Corson, Thomas O'Brien, Jing Qing, Deepak Sampath, Mark Merchant, Robert Yauch, Gerard Manning, Jeffrey Settleman, Georgia Hatzivassiliou, and Marie Evangelista. 2015. "Metabolite Profiling Stratifies Pancreatic Ductal Adenocarcinomas into Subtypes with Distinct Sensitivities to Metabolic Inhibitors." *Proceedings of the National Academy of Sciences* 112(32). doi: 10.1073/pnas.1501605112.

D.E; Shaw Research. 2021. "Schrödinger Release 2021-3: Desmond Molecular Dynamics System."

DeNicola, Gina M., Florian A. Karreth, Timothy J. Humpton, Aarthi Gopinathan, Cong Wei, Kristopher Frese, Dipti Mangal, Kenneth H. Yu, Charles J. Yeo, Eric S. Calhoun, Francesca Scrimieri, Jordan M. Winter, Ralph H. Hruban, Christine Iacobuzio-Donahue, Scott E. Kern, Ian A. Blair, and David A. Tuveson. 2011.

"Oncogene-Induced Nrf2 Transcription Promotes ROS Detoxification and Tumorigenesis." *Nature* 475(7354):106–9. doi: 10.1038/nature10189.

Dobin, Alexander, Carrie A. Davis, Felix Schlesinger, Jorg Drenkow, Chris Zaleski, Sonali Jha, Philippe Batut, Mark Chaisson, and Thomas R. Gingeras. 2013. "STAR: Ultrafast Universal RNA-Seq Aligner." *Bioinformatics* 29(1):15–21. doi: 10.1093/bioinformatics/bts635.

Dohmen, Marc, Sarah Krieg, Georgios Agalaridis, Xiaoqing Zhu, Saifeldin N. Shehata, Elisabeth Pfeiffenberger, Jan Amelang, Mareike Bütepage, Elena Buerova, Carolina M. Pfaff, Dipanjan Chanda, Stephan Geley, Christian Preisinger, Kei Sakamoto, Bernhard Lüscher, Dietbert Neumann, and Jörg Vervoorts. 2020. "AMPK-Dependent Activation of the Cyclin Y/CDK16 Complex Controls Autophagy." *Nature Communications* 11(1):1032. doi: 10.1038/s41467-020-14812-0.

Dolma, Sonam, Stephen L. Lessnick, William C. Hahn, and Brent R. Stockwell. 2003. "Identification of Genotype-Selective Antitumor Agents Using Synthetic Lethal Chemical Screening in Engineered Human Tumor Cells." *Cancer Cell* 3(3):285–96. doi: 10.1016/S1535-6108(03)00050-3.

Duong, Hong-Quan, Jae Seok Hwang, Hee Jeong Kim, Yeon-Sun Seong, and Insoo Bae. 2012. "BML-275, an AMPK Inhibitor, Induces DNA Damage, G2/M Arrest and Apoptosis in Human Pancreatic Cancer Cells." *International Journal of Oncology* 41(6):2227–36. doi: 10.3892/ijo.2012.1672.

Ebmeier, Christopher C., Benjamin Erickson, Benjamin L. Allen, Mary A. Allen, Hyunmin Kim, Nova Fong, Jeremy R. Jacobsen, Kaiwei Liang, Ali Shilatifard, Robin D. Dowell, William M. Old, David L. Bentley, and Dylan J. Taatjes. 2017. "Human TFIIH Kinase CDK7 Regulates Transcription-Associated Chromatin Modifications." *Cell Reports* 20(5):1173–86. doi: 10.1016/j.celrep.2017.07.021.

Egan, Daniel F., David B. Shackelford, Maria M. Mihaylova, Sara Gelino, Rebecca A. Kohnz, William Mair, Debbie S. Vasquez, Aashish Joshi, Dana M. Gwinn, Rebecca Taylor, John M. Asara, James Fitzpatrick, Andrew Dillin, Benoit Viollet, Mondira Kundu, Malene Hansen, and Reuben J. Shaw. 2011. "Phosphorylation of ULK1 (HATG1) by AMP-Activated Protein Kinase Connects Energy Sensing to Mitophagy." *Science* 331(6016):456–61. doi: 10.1126/science.1196371.

Epik, Schrödinger, LLC. 2021. "Schrödinger Release 2021-4: Protein Preparation Wizard."

Falcomatà, Chiara, Stefanie Bärthel, Sebastian A. Widholz, Christian Schneeweis, Juan José Montero, Albulena Toska, Jonas Mir, Thorsten Kaltenbacher, Jeannine Heetmeyer, Jonathan J. Swietlik, Jing-Yuan Cheng, Bianca Teodorescu, Oliver Reichert, Constantin Schmitt, Kathrin Grabichler, Andrea Coluccio, Fabio Boniolo, Christian Veltkamp, Magdalena Zukowska, Angelica Arenas Vargas, Woo Hyun Paik, Moritz Jesinghaus, Katja Steiger, Roman Maresch, Rupert Öllinger, Tim Ammon, Olga Baranov, Maria S. Robles, Julia Rechenberger, Bernhard Kuster, Felix Meissner, Maximilian Reichert, Michael Flossdorf, Roland Rad, Marc Schmidt-Supprian, Günter Schneider, and Dieter Saur. 2022. "Selective Multi-Kinase Inhibition Sensitizes Mesenchymal Pancreatic Cancer to Immune Checkpoint Blockade by Remodeling the Tumor Microenvironment." *Nature Cancer* 3(3):318–36. doi: 10.1038/s43018-021-00326-1.

Faubert, Brandon, Gino Boily, Said Izreig, Takla Griss, Bozena Samborska, Zhifeng Dong, Fanny Dupuy, Christopher Chambers, Benjamin J. Fuerth, Benoit Viollet, Orval A. Mamer, Daina Avizonis, Ralph J. DeBerardinis, Peter M. Siegel, and Russell G. Jones. 2013. "AMPK Is a Negative Regulator of the Warburg Effect and Suppresses Tumor Growth In Vivo." *Cell Metabolism* 17(1):113–24. doi: 10.1016/j.cmet.2012.12.001.

Flaherty, Keith T., Robert J. Gray, Alice P. Chen, Shuli Li, Lisa M. McShane, David Patton, Stanley R. Hamilton, P. Mickey Williams, A. John Iafrate, Jeffrey Sklar, Edith P. Mitchell, Lyndsay N. Harris, Naoko Takebe, David J. Sims, Brent Coffey, Tony Fu, Mark Routbort, James A. Zwiebel, Larry V. Rubinstein, Richard F. Little, Carlos L. Arteaga, Robert Comis, Jeffrey S. Abrams, Peter J. O'Dwyer, Barbara A. Conley, and for the NCI-MATCH team. 2020. "Molecular Landscape and Actionable Alterations in a Genomically Guided Cancer Clinical Trial: National Cancer Institute Molecular Analysis for Therapy Choice (NCI-MATCH)." *Journal of Clinical Oncology* 38(33):3883–94. doi: 10.1200/JCO.19.03010.

Friedlander, Sharon Y. Gidekel, Gerald C. Chu, Eric L. Snyder, Nomeda Girnius, Gregory Dibelius, Denise Crowley, Eliza Vasile, Ronald A. DePinho, and Tyler Jacks. 2009. “Context-Dependent Transformation of Adult Pancreatic Cells by Oncogenic K-Ras.” *Cancer Cell* 16(5):379–89. doi: 10.1016/j.ccr.2009.09.027.

Friesner, Richard A., Jay L. Banks, Robert B. Murphy, Thomas A. Halgren, Jasna J. Klicic, Daniel T. Mainz, Matthew P. Repasky, Eric H. Knoll, Mee Shelley, Jason K. Perry, David E. Shaw, Perry Francis, and Peter S. Shenkin. 2004. “Glide: A New Approach for Rapid, Accurate Docking and Scoring. 1. Method and Assessment of Docking Accuracy.” *Journal of Medicinal Chemistry* 47(7):1739–49. doi: 10.1021/jm0306430.

Friesner, Richard A., Robert B. Murphy, Matthew P. Repasky, Leah L. Frye, Jeremy R. Greenwood, Thomas A. Halgren, Paul C. Sanschagrin, and Daniel T. Mainz. 2006. “Extra Precision Glide: Docking and Scoring Incorporating a Model of Hydrophobic Enclosure for Protein−Ligand Complexes.” *Journal of Medicinal Chemistry* 49(21):6177–96. doi: 10.1021/jm051256o.

Ghislat, Ghita, Maria Patron, Rosario Rizzuto, and Erwin Knecht. 2012. “Withdrawal of Essential Amino Acids Increases Autophagy by a Pathway Involving Ca2+/Calmodulin-Dependent Kinase Kinase-β (CaMKK-β).” *Journal of Biological Chemistry* 287(46):38625–36. doi: 10.1074/jbc.M112.365767.

Glover-Cutter, Kira, Stéphane Larochelle, Benjamin Erickson, Chao Zhang, Kevan Shokat, Robert P. Fisher, and David L. Bentley. 2009. “TFIIH-Associated Cdk7 Kinase Functions in Phosphorylation of C-Terminal Domain Ser7 Residues, Promoter-Proximal Pausing, and Termination by RNA Polymerase II.” *Molecular and Cellular Biology* 29(20):5455–64. doi: 10.1128/MCB.00637-09.

Greenwood, Jeremy R., David Calkins, Arron P. Sullivan, and John C. Shelley. 2010. “Towards the Comprehensive, Rapid, and Accurate Prediction of the Favorable Tautomeric States of Drug-like Molecules in Aqueous Solution.” *Journal of Computer-Aided Molecular Design* 24(6–7):591–604. doi: 10.1007/s10822-010-9349-1.

Greer, Eric L., Philip R. Oskoui, Max R. Banko, Jay M. Maniar, Melanie P. Gygi, Steven P. Gygi, and Anne Brunet. 2007. “The Energy Sensor AMP-Activated Protein Kinase Directly Regulates the Mammalian FOXO3 Transcription Factor.” *Journal of Biological Chemistry* 282(41):30107–19. doi: 10.1074/jbc.M705325200.

Gunderson, Andrew J., Tomoko Yamazaki, Kayla McCarty, Michaela Phillips, Alejandro Alice, Shelly Bambina, Lauren Zebertavage, David Friedman, Benjamin Cottam, Pippa Newell, Michael J. Gough, Marka R. Crittenden, Pieter Van der Veken, and Kristina H. Young. 2019. “Blockade of Fibroblast Activation Protein in Combination with Radiation Treatment in Murine Models of Pancreatic Adenocarcinoma” edited by M. Korc. *PLOS ONE* 14(2):e0211117. doi: 10.1371/journal.pone.0211117.

Gwinn, Dana M., David B. Shackelford, Daniel F. Egan, Maria M. Mihaylova, Annabelle Mery, Debbie S. Vasquez, Benjamin E. Turk, and Reuben J. Shaw. 2008. “AMPK Phosphorylation of Raptor Mediates a Metabolic Checkpoint.” *Molecular Cell* 30(2):214–26. doi: 10.1016/j.molcel.2008.03.003.

Halgren, Thomas A., Robert B. Murphy, Richard A. Friesner, Hege S. Beard, Leah L. Frye, W. Thomas Pollard, and Jay L. Banks. 2004. “Glide: A New Approach for Rapid, Accurate Docking and Scoring. 2. Enrichment Factors in Database Screening.” *Journal of Medicinal Chemistry* 47(7):1750–59. doi: 10.1021/jm030644s.

Haloi, Nandan, Po-Chao Wen, Qunli Cheng, Meiying Yang, Gayathri Natarajan, Amadou K. S. Camara, Wai-Meng Kwok, and Emad Tajkhorshid. 2021. “Structural Basis of Complex Formation between Mitochondrial Anion Channel VDAC1 and Hexokinase-II.” *Communications Biology* 4(1):667. doi: 10.1038/s42003-021-02205-y.

Hanahan, Douglas. 2022. “Hallmarks of Cancer: New Dimensions.” *Cancer Discovery* 12(1):31–46. doi: 10.1158/2159-8290.CD-21-1059.

Hanahan, Douglas, and Robert A. Weinberg. 2011. “Hallmarks of Cancer: The Next Generation.” *Cell* 144(5):646–74. doi: 10.1016/j.cell.2011.02.013.

Hangauer, Matthew J., Vasanthi S. Viswanathan, Matthew J. Ryan, Dhruv Bole, John K. Eaton, Alexandre Matov, Jacqueline Galeas, Harshil D. Dhruv, Michael E. Berens, Stuart L. Schreiber, Frank McCormick, and Michael T. McManus. 2017. “Drug-Tolerant Persister Cancer Cells Are Vulnerable to GPX4 Inhibition.” *Nature* 551(7679):247–50. doi: 10.1038/nature24297.

Hänzelmann, Sonja, Robert Castelo, and Justin Guinney. 2013. “GSVA: Gene Set Variation Analysis for Microarray and RNA-Seq Data.” *BMC Bioinformatics* 14(1):7. doi: 10.1186/1471-2105-14-7.

Harder, Edward, Wolfgang Damm, Jon Maple, Chuanjie Wu, Mark Reboul, Jin Yu Xiang, Lingle Wang, Dmitry Lupyan, Markus K. Dahlgren, Jennifer L. Knight, Joseph W. Kaus, David S. Cerutti, Goran Krilov, William L. Jorgensen, Robert Abel, and Richard A. Friesner. 2016. “OPLS3: A Force Field Providing Broad Coverage of Drug-like Small Molecules and Proteins.” *Journal of Chemical Theory and Computation* 12(1):281–96. doi: 10.1021/acs.jctc.5b00864.

Hawley, Simon A., Fiona A. Ross, Graeme J. Gowans, Priyanka Tibarewal, Nicholas R. Leslie, and D. Grahame Hardie. 2014. “Phosphorylation by Akt within the ST Loop of AMPK-A1 down-Regulates Its Activation in Tumour Cells.” *Biochemical Journal* 459(2):275–87. doi: 10.1042/BJ20131344.

Heinzlmeir, Stephanie, Küster, Bernhard. 2017. “When Chemical Proteomics Meets Medicinal Chemistry: Guided Drug Discovery towards EPHA2 Inhibitors.”

Hemminki, Akseli, David Markie, Ian Tomlinson, Egle Avizienyte, Stina Roth, Anu Loukola, Graham Bignell, William Warren, Maria Aminoff, Pia Höglund, Heikki Järvinen, Paula Kristo, Katarina Pelin, Maaret Ridanpää, Reijo Salovaara, Tumi Toro, Walter Bodmer, Sylviane Olschwang, Anne S. Olsen, Michael R. Stratton, Albert De La Chapelle, and Lauri A. Aaltonen. 1998. “A Serine/Threonine Kinase Gene Defective in Peutz–Jeghers Syndrome.” *Nature* 391(6663):184–87. doi: 10.1038/34432.

Hemminki, Akseli, Ian Tomlinson, David Markie, Heikki Järvinen, Pertti Sistonen, Anna-Maria Björkqvist, Sakari Knuutila, Reijo Salovaara, Walter Bodmer, Darryl Shibata, Albert De La Chapelle, and Lauri A. Aaltonen. 1997. “Localization of a Susceptibility Locus for Peutz-Jeghers Syndrome to 19p Using Comparative Genomic Hybridization and Targeted Linkage Analysis.” *Nature Genetics* 15(1):87–90. doi: 10.1038/ng0197-87.

Herrero-Martín, Griselda, Maria Høyer-Hansen, Celina García-García, Claudia Fumarola, Thomas Farkas, Abelardo López-Rivas, and Marja Jäättelä. 2009. “TAK1 Activates AMPK-Dependent Cytoprotective Autophagy in TRAIL-Treated Epithelial Cells.” *The EMBO Journal* 28(6):677–85. doi: 10.1038/emboj.2009.8.

Hiraoka, Nobuyoshi, Kaoru Onozato, Tomoo Kosuge, and Setsuo Hirohashi. 2006. “Prevalence of FOXP3+ Regulatory T Cells Increases During the Progression of Pancreatic Ductal Adenocarcinoma and Its Premalignant Lesions.” *Clinical Cancer Research* 12(18):5423–34. doi: 10.1158/1078-0432.CCR-06-0369.

Hoppe, Sven, Holger Bierhoff, Ivana Cado, Andrea Weber, Marcel Tiebe, Ingrid Grummt, and Renate Voit. 2009. “AMP-Activated Protein Kinase Adapts RRNA Synthesis to Cellular Energy Supply.” *Proceedings of the National Academy of Sciences* 106(42):17781–86. doi: 10.1073/pnas.0909873106.

Hu, Mingyue, Xiangxu Chen, Li Ma, Yu Ma, Yuan Li, Huihui Song, Jiajia Xu, Lingna Zhou, Xiaoxue Li, Yuhui Jiang, Bo Kong, and Peilin Huang. 2019. “AMPK Inhibition Suppresses the Malignant Phenotype of Pancreatic Cancer Cells in Part by Attenuating Aerobic Glycolysis.” *Journal of Cancer* 10(8):1870–78. doi: 10.7150/jca.28299.

Hung, Chien-Min, Portia S. Lombardo, Nazma Malik, Sonja N. Brun, Kristina Hellberg, Jeanine L. Van Nostrand, Daniel Garcia, Joshua Baumgart, Ken Diffenderfer, John M. Asara, and Reuben J. Shaw. 2021.

"AMPK/ULK1-Mediated Phosphorylation of Parkin ACT Domain Mediates an Early Step in Mitophagy." *Science Advances* 7(15):eabg4544. doi: 10.1126/sciadv.abg4544.

Hurley, Rebecca L., Laura K. Barré, Sumintra D. Wood, Kristin A. Anderson, Bruce E. Kemp, Anthony R. Means, and Lee A. Witters. 2006. "Regulation of AMP-Activated Protein Kinase by Multisite Phosphorylation in Response to Agents That Elevate Cellular CAMP." *Journal of Biological Chemistry* 281(48):36662–72. doi: 10.1074/jbc.M606676200.

Hwang, William L., Karthik A. Jagadeesh, Jimmy A. Guo, Hannah I. Hoffman, Payman Yadollahpour, Jason W. Reeves, Rahul Mohan, Eugene Drokhlyansky, Nicholas Van Wittenberghe, Orr Ashenberg, Samouil L. Farhi, Denis Schapiro, Prajan Divakar, Eric Miller, Daniel R. Zollinger, George Eng, Jason M. Schenkel, Jennifer Su, Carina Shiau, Patrick Yu, William A. Freed-Pastor, Domenic Abbondanza, Arnav Mehta, Joshua Gould, Conner Lambden, Caroline B. M. Porter, Alexander Tsankov, Danielle Dionne, Julia Waldman, Michael S. Cuoco, Lan Nguyen, Toni Delorey, Devan Phillips, Jaimie L. Barth, Marina Kem, Clifton Rodrigues, Debora Ciprani, Jorge Roldan, Piotr Zelga, Vjola Jorgji, Jonathan H. Chen, Zackery Ely, Daniel Zhao, Kit Fuhrman, Robin Fropf, Joseph M. Beechem, Jay S. Loeffler, David P. Ryan, Colin D. Weekes, Cristina R. Ferrone, Motaz Qadan, Martin J. Aryee, Rakesh K. Jain, Donna S. Neuberg, Jennifer Y. Wo, Theodore S. Hong, Ramnik Xavier, Andrew J. Aguirre, Orit Rozenblatt-Rosen, Mari Mino-Kenudson, Carlos Fernandez-del Castillo, Andrew S. Liss, David T. Ting, Tyler Jacks, and Aviv Regev. 2022. "Single-Nucleus and Spatial Transcriptome Profiling of Pancreatic Cancer Identifies Multicellular Dynamics Associated with Neoadjuvant Treatment." *Nature Genetics* 54(8):1178–91. doi: 10.1038/s41588-022-01134-8.

Inoki, Ken, Tianqing Zhu, and Kun-Liang Guan. 2003. "TSC2 Mediates Cellular Energy Response to Control Cell Growth and Survival." *Cell* 115(5):577–90. doi: 10.1016/S0092-8674(03)00929-2.

Ischenko, Irene, Oleksi Petrenko, and Michael J. Hayman. 2014. "Analysis of the Tumor-Initiating and Metastatic Capacity of PDX1-Positive Cells from the Adult Pancreas." *Proceedings of the National Academy of Sciences* 111(9):3466–71. doi: 10.1073/pnas.1319911111.

Jäger, Sibylle, Christoph Handschin, Julie St.-Pierre, and Bruce M. Spiegelman. 2007. "AMP-Activated Protein Kinase (AMPK) Action in Skeletal Muscle via Direct Phosphorylation of PGC-1α." *Proceedings of the National Academy of Sciences* 104(29):12017–22. doi: 10.1073/pnas.0705070104.

Jänne, Pasi A., Gregory J. Riely, Shirish M. Gadgeel, Rebecca S. Heist, Sai-Hong I. Ou, Jose M. Pacheco, Melissa L. Johnson, Joshua K. Sabari, Konstantinos Leventakos, Edwin Yau, Lyudmila Bazhenova, Marcelo V. Negrao, Nathan A. Pennell, Jun Zhang, Kenna Anderes, Hirak Der-Torossian, Thian Kheoh, Karen Velastegui, Xiaohong Yan, James G. Christensen, Richard C. Chao, and Alexander I. Spira. 2022. "Adagrasib in Non–Small-Cell Lung Cancer Harboring a *KRAS* ^{G12C} Mutation." *New England Journal of Medicine* 387(2):120–31. doi: 10.1056/NEJMoa2204619.

Jenne, Dieter E., Heike Reomann, Jun-ichi Nezu, Waltraut Friedel, Steffan Loff., Reinhard Jeschke, Oliver Müller, Walter Back, and Michael Zimmer. 1998. "Peutz-Jeghers Syndrome Is Caused by Mutations in a Novel Serine Threoninekinase." *Nature Genetics* 18(1):38–43. doi: 10.1038/ng0198-38.

Jeon, Sang-Min, Navdeep S. Chandel, and Nissim Hay. 2012. "AMPK Regulates NADPH Homeostasis to Promote Tumour Cell Survival during Energy Stress." *Nature* 485(7400):661–65. doi: 10.1038/nature11066.

Jia, Jingyue, Bhawana Bissa, Lukas Brecht, Lee Allers, Seong Won Choi, Yuexi Gu, Mark Zbinden, Mark R. Burge, Graham Timmins, Kenneth Hallows, Christian Behrends, and Vojo Deretic. 2020. "AMPK, a Regulator of Metabolism and Autophagy, Is Activated by Lysosomal Damage via a Novel Galectin-Directed Ubiquitin Signal Transduction System." *Molecular Cell* 77(5):951-969.e9. doi: 10.1016/j.molcel.2019.12.028.

Jiang, Xuejun, Brent R. Stockwell, and Marcus Conrad. 2021. "Ferroptosis: Mechanisms, Biology and Role in Disease." *Nature Reviews Molecular Cell Biology* 22(4):266–82. doi: 10.1038/s41580-020-00324-8.

Jiang, Yuejing, Ying Dong, Yifeng Luo, Shangwen Jiang, Fei-Long Meng, Minjia Tan, Jia Li, and Yi Zang. 2021. "AMPK-Mediated Phosphorylation on 53BP1 Promotes c-NHEJ." *Cell Reports* 34(7):108713. doi: 10.1016/j.celrep.2021.108713.

Jin, Xin, Zelalem Demere, Karthik Nair, Ahmed Ali, Gino B. Ferraro, Ted Natoli, Amy Deik, Lia Petronio, Andrew A. Tang, Cong Zhu, Li Wang, Danny Rosenberg, Vamsi Mangena, Jennifer Roth, Kwanghun Chung, Rakesh K. Jain, Clary B. Clish, Matthew G. Vander Heiden, and Todd R. Golub. 2020. "A Metastasis Map of Human Cancer Cell Lines." *Nature* 588(7837):331–36. doi: 10.1038/s41586-020-2969-2.

Jones, Russell G., David R. Plas, Sara Kubek, Monica Buzzai, James Mu, Yang Xu, Morris J. Birnbaum, and Craig B. Thompson. 2005. "AMP-Activated Protein Kinase Induces a P53-Dependent Metabolic Checkpoint." *Molecular Cell* 18(3):283–93. doi: 10.1016/j.molcel.2005.03.027.

Jones, Siân, Xiaosong Zhang, D. Williams Parsons, Jimmy Cheng-Ho Lin, Rebecca J. Leary, Philipp Angenendt, Parminder Mankoo, Hannah Carter, Hirohiko Kamiyama, Antonio Jimeno, Seung-Mo Hong, Baojin Fu, Ming-Tseh Lin, Eric S. Calhoun, Mihoko Kamiyama, Kimberly Walter, Tatiana Nikolskaya, Yuri Nikolsky, James Hartigan, Douglas R. Smith, Manuel Hidalgo, Steven D. Leach, Alison P. Klein, Elizabeth M. Jaffee, Michael Goggins, Anirban Maitra, Christine Iacobuzio-Donahue, James R. Eshleman, Scott E. Kern, Ralph H. Hruban, Rachel Karchin, Nickolas Papadopoulos, Giovanni Parmigiani, Bert Vogelstein, Victor E. Velculescu, and Kenneth W. Kinzler. 2008. "Core Signaling Pathways in Human Pancreatic Cancers Revealed by Global Genomic Analyses." *Science* 321(5897):1801–6. doi: 10.1126/science.1164368.

Joo, Min Sung, Won Dong Kim, Ki Young Lee, Ji Hyun Kim, Ja Hyun Koo, and Sang Geon Kim. 2016. "AMPK Facilitates Nuclear Accumulation of Nrf2 by Phosphorylating at Serine 550." *Molecular and Cellular Biology* 36(14):1931–42. doi: 10.1128/MCB.00118-16.

Jorgensen, William L., David S. Maxwell, and Julian Tirado-Rives. 1996. "Development and Testing of the OPLS All-Atom Force Field on Conformational Energetics and Properties of Organic Liquids." *Journal of the American Chemical Society* 118(45):11225–36. doi: 10.1021/ja9621760.

Jorgensen, William L., and Julian Tirado-Rives. 1988. "The OPLS [Optimized Potentials for Liquid Simulations] Potential Functions for Proteins, Energy Minimizations for Crystals of Cyclic Peptides and Crambin." *Journal of the American Chemical Society* 110(6):1657–66. doi: 10.1021/ja00214a001.

Joseph, Biny K., Hsing-Yin Liu, Jamie Francisco, Devanshi Pandya, Melissa Donigan, Christina Gallo-Ebert, Caroline Giordano, Adam Bata, and Joseph T. Nickels. 2015. "Inhibition of AMP Kinase by the Protein Phosphatase 2A Heterotrimer, PP2APpp2r2d." *Journal of Biological Chemistry* 290(17):10588–98. doi: 10.1074/jbc.M114.626259.

Karasic, Thomas B., Mark H. O'Hara, Arturo Loaiza-Bonilla, Kim A. Reiss, Ursina R. Teitelbaum, Erkut Borazanci, Ana De Jesus-Acosta, Colleen Redlinger, Jessica A. Burrell, Daniel A. Laheru, Daniel D. Von Hoff, Ravi K. Amaravadi, Jeffrey A. Drebin, and Peter J. O'Dwyer. 2019. "Effect of Gemcitabine and Nab-Paclitaxel With or Without Hydroxychloroquine on Patients With Advanced Pancreatic Cancer: A Phase 2 Randomized Clinical Trial." *JAMA Oncology* 5(7):993. doi: 10.1001/jamaoncol.2019.0684.

Kawaguchi, Takumi, Kiyoshi Osatomi, Hiromi Yamashita, Tsutomu Kabashima, and Kosaku Uyeda. 2002. "Mechanism for Fatty Acid 'Sparing' Effect on Glucose-Induced Transcription." *Journal of Biological Chemistry* 277(6):3829–35. doi: 10.1074/jbc.M107895200.

Kim, Joungmok, Young Chul Kim, Chong Fang, Ryan C. Russell, Jeong Hee Kim, Weiliang Fan, Rong Liu, Qing Zhong, and Kun-Liang Guan. 2013. "Differential Regulation of Distinct Vps34 Complexes by AMPK in Nutrient Stress and Autophagy." *Cell* 152(1–2):290–303. doi: 10.1016/j.cell.2012.12.016.

Kim, Joungmok, Mondira Kundu, Benoit Viollet, and Kun-Liang Guan. 2011. "AMPK and MTOR Regulate Autophagy through Direct Phosphorylation of Ulk1." *Nature Cell Biology* 13(2):132–41. doi: 10.1038/ncb2152.

Kleeff, Jorg, Murray Korc, Minoti Apte, Carlo La Vecchia, Colin D. Johnson, Andrew V. Biankin, Rachel E. Neale, Margaret Tempero, David A. Tuveson, Ralph H. Hruban, and John P. Neoptolemos. 2016. "Pancreatic Cancer." *Nature Reviews Disease Primers* 2(1):16022. doi: 10.1038/nrdp.2016.22.

Klein, Alison P., Kieran A. Brune, Gloria M. Petersen, Michael Goggins, Anne C. Tersmette, G. Johan A. Offerhaus, Constance Griffin, John L. Cameron, Charles J. Yeo, Scott Kern, and Ralph H. Hruban. 2004. "Prospective Risk of Pancreatic Cancer in Familial Pancreatic Cancer Kindreds." *Cancer Research* 64(7):2634–38. doi: 10.1158/0008-5472.CAN-03-3823.

Koo, Seung-Hoi, Lawrence Flechner, Ling Qi, Xinmin Zhang, Robert A. Screaton, Shawn Jeffries, Susan Hedrick, Wu Xu, Fayçal Boussouar, Paul Brindle, Hiroshi Takemori, and Marc Montminy. 2005. "The CREB Coactivator TORC2 Is a Key Regulator of Fasting Glucose Metabolism." *Nature* 437(7062):1109–14. doi: 10.1038/nature03967.

Kopp, Janel L., Guido von Figura, Erin Mayes, Fen-Fen Liu, Claire L. Dubois, John P. Morris, Fong Cheng Pan, Haruhiko Akiyama, Christopher V. E. Wright, Kristin Jensen, Matthias Hebrok, and Maike Sander. 2012. "Identification of Sox9-Dependent Acinar-to-Ductal Reprogramming as the Principal Mechanism for Initiation of Pancreatic Ductal Adenocarcinoma." *Cancer Cell* 22(6):737–50. doi: 10.1016/j.ccr.2012.10.025.

Krauß, Lukas, Bettina C. Urban, Sieglinde Hastreiter, Carolin Schneider, Patrick Wenzel, Zonera Hassan, Matthias Wirth, Katharina Lankes, Andrea Terrasi, Christine Klement, Filippo M. Cernilogar, Rupert Öllinger, Niklas de Andrade Krätzig, Thomas Engleitner, Roland M. Schmid, Katja Steiger, Roland Rad, Oliver H. Krämer, Maximilian Reichert, Gunnar Schotta, Dieter Saur, and Günter Schneider. 2022. "HDAC2 Facilitates Pancreatic Cancer Metastasis." *Cancer Research* 82(4):695–707. doi: 10.1158/0008-5472.CAN-20-3209.

Kumazoe, Motofumi, Mika Takai, Shun Hiroi, Chieri Takeuchi, Mai Kadomatsu, Takashi Nojiri, Hiroaki Onda, Jaehoon Bae, Yuhui Huang, Kanako Takamatsu, Shuya Yamashita, Kenji Kangawa, and Hirofumi Tachibana. 2017. "The FOXO3/PGC-1β Signaling Axis Is Essential for Cancer Stem Cell Properties of Pancreatic Ductal Adenocarcinoma." *Journal of Biological Chemistry* 292(26):10813–23. doi: 10.1074/jbc.M116.772111.

Laderoute, Keith R., Khalid Amin, Joy M. Calaoagan, Merrill Knapp, Theresamai Le, Juan Orduna, Marc Foretz, and Benoit Viollet. 2006. "5'-AMP-Activated Protein Kinase (AMPK) Is Induced by Low-Oxygen and Glucose Deprivation Conditions Found in Solid-Tumor Microenvironments." *Molecular and Cellular Biology* 26(14):5336–47. doi: 10.1128/MCB.00166-06.

Langendorf, Christopher G., and Bruce E. Kemp. 2015. "Choreography of AMPK Activation." *Cell Research* 25(1):5–6. doi: 10.1038/cr.2014.163.

Leick, Lotte, Joachim Fentz, Rasmus S. Biensø, Jakob G. Knudsen, Jacob Jeppesen, Bente Kiens, Jørgen F. P. Wojtaszewski, and Henriette Pilegaard. 2010. "PGC-1α Is Required for AICAR-Induced Expression of GLUT4 and Mitochondrial Proteins in Mouse Skeletal Muscle." *American Journal of Physiology-Endocrinology and Metabolism* 299(3):E456–65. doi: 10.1152/ajpendo.00648.2009.

Lemos, Clara, Volker K. Schulze, Simon J. Baumgart, Ekaterina Nevedomskaya, Tobias Heinrich, Julien Lefranc, Benjamin Bader, Clara D. Christ, Hans Briem, Lara P. Kuhnke, Simon J. Holton, Ulf Bömer, Philip Lienau, Franz Von Nussbaum, Carl F. Nising, Marcus Bauser, Andrea Hägebarth, Dominik Mumberg, and Bernard Haendler. 2021. "The Potent AMPK Inhibitor BAY-3827 Shows Strong Efficacy in Androgen-Dependent Prostate Cancer Models." *Cellular Oncology* 44(3):581–94. doi: 10.1007/s13402-020-00584-8.

Leprivier, Gabriel, Marc Remke, Barak Rotblat, Adrian Dubuc, Abigail-Rachele F. Mateo, Marcel Kool, Sameer Agnihotri, Amal El-Naggar, Bin Yu, Syam Prakash Somasekharan, Brandon Faubert, Gaëlle Bridon, Cristina E. Tognon, Joan Mathers, Ryan Thomas, Amy Li, Adi Barokas, Brian Kwok, Mary Bowden, Stephanie Smith, Xiaochong Wu, Andrey Korshunov, Thomas Hielscher, Paul A. Northcott, Jason D.

Galpin, Christopher A. Ahern, Ye Wang, Martin G. McCabe, V. Peter Collins, Russell G. Jones, Michael Pollak, Olivier Delattre, Martin E. Gleave, Eric Jan, Stefan M. Pfister, Christopher G. Proud, W. Brent Derry, Michael D. Taylor, and Poul H. Sorensen. 2013. "The EEF2 Kinase Confers Resistance to Nutrient Deprivation by Blocking Translation Elongation." *Cell* 153(5):1064–79. doi: 10.1016/j.cell.2013.04.055.

Lewerenz, Jan, Sandra J. Hewett, Ying Huang, Maria Lambros, Peter W. Gout, Peter W. Kalivas, Ann Massie, Ilse Smolders, Axel Methner, Mathias Pergande, Sylvia B. Smith, Vadivel Ganapathy, and Pamela Maher. 2013. "The Cystine/Glutamate Antiporter System x_c^- in Health and Disease: From Molecular Mechanisms to Novel Therapeutic Opportunities." *Antioxidants & Redox Signaling* 18(5):522–55. doi: 10.1089/ars.2011.4391.

Li, Shan, Zeno Lavagnino, Delphine Lemacon, Lingzhen Kong, Alessandro Ustione, Xuewen Ng, Yuanya Zhang, Yingchun Wang, Bin Zheng, Helen Piwnica-Worms, Alessandro Vindigni, David W. Piston, and Zhongsheng You. 2019. "Ca2+-Stimulated AMPK-Dependent Phosphorylation of Exo1 Protects Stressed Replication Forks from Aberrant Resection." *Molecular Cell* 74(6):1123-1137.e6. doi: 10.1016/j.molcel.2019.04.003.

Li, Yu, Shanqin Xu, Maria M. Mihaylova, Bin Zheng, Xiuyun Hou, Bingbing Jiang, Ogyi Park, Zhijun Luo, Etienne Lefai, John Y. J. Shyy, Bin Gao, Michel Wierzbicki, Tony J. Verbeuren, Reuben J. Shaw, Richard A. Cohen, and Mengwei Zang. 2011. "AMPK Phosphorylates and Inhibits SREBP Activity to Attenuate Hepatic Steatosis and Atherosclerosis in Diet-Induced Insulin-Resistant Mice." *Cell Metabolism* 13(4):376–88. doi: 10.1016/j.cmet.2011.03.009.

Liang, Jiyong, Shan H. Shao, Zhi-Xiang Xu, Bryan Hennessy, Zhiyong Ding, Michelle Larrea, Seiji Kondo, Dan J. Dumont, Jordan U. Gutterman, Cheryl L. Walker, Joyce M. Slingerland, and Gordon B. Mills. 2007. "The Energy Sensing LKB1–AMPK Pathway Regulates P27kip1 Phosphorylation Mediating the Decision to Enter Autophagy or Apoptosis." *Nature Cell Biology* 9(2):218–24. doi: 10.1038/ncb1537.

Liao, Yang, Gordon K. Smyth, and Wei Shi. 2014. "FeatureCounts: An Efficient General Purpose Program for Assigning Sequence Reads to Genomic Features." *Bioinformatics* 30(7):923–30. doi: 10.1093/bioinformatics/btt656.

Ling, Naomi X. Y., Adrian Kaczmarek, Ashfaqul Hoque, Elizabeth Davie, Kevin R. W. Ngoei, Kaitlin R. Morrison, William J. Smiles, Gabriella M. Forte, Tingting Wang, Shervi Lie, Toby A. Dite, Christopher G. Langendorf, John W. Scott, Jonathan S. Oakhill, and Janni Petersen. 2020. "MTORC1 Directly Inhibits AMPK to Promote Cell Proliferation under Nutrient Stress." *Nature Metabolism* 2(1):41–49. doi: 10.1038/s42255-019-0157-1.

Liu, Zhao, Guizhong Zhang, Shiran Huang, Jian Cheng, Tian Deng, Xiaoxu Lu, Funmilayo Oladunni Adeshakin, Qian Chen, and Xiaochun Wan. 2020. "Induction of Apoptosis in Hematological Cancer Cells by Dorsomorphin Correlates with BAD Upregulation." *Biochemical and Biophysical Research Communications* 522(3):704–8. doi: 10.1016/j.bbrc.2019.11.157.

Lomberk, Gwen, Yuna Blum, Rémy Nicolle, Asha Nair, Krutika Satish Gaonkar, Laetitia Marisa, Angela Mathison, Zhifu Sun, Huihuang Yan, Nabila Elarouci, Lucile Armenoult, Mira Ayadi, Tamas Ordog, Jeong-Heon Lee, Gavin Oliver, Eric Klee, Vincent Moutardier, Odile Gayet, Benjamin Bian, Pauline Duconseil, Marine Gilabert, Martin Bigonnet, Stephane Garcia, Olivier Turrini, Jean-Robert Delpero, Marc Giovannini, Philippe Grandval, Mohamed Gasmi, Veronique Secq, Aurélien De Reyniès, Nelson Dusetti, Juan Iovanna, and Raul Urrutia. 2018. "Distinct Epigenetic Landscapes Underlie the Pathobiology of Pancreatic Cancer Subtypes." *Nature Communications* 9(1):1978. doi: 10.1038/s41467-018-04383-6.

Lopez-Mejia, Isabel C., Sylviane Lagarrigue, Albert Giralt, Laia Martinez-Carreres, Nadège Zanou, Pierre-Damien Denechaud, Judit Castillo-Armengol, Carine Chavey, Meritxell Orpinell, Brigitte Delacuisine, Anita Nasrallah, Caterina Collodet, Lianjun Zhang, Benoît Viollet, D. Grahame Hardie, and Lluis Fajas. 2017. "CDK4 Phosphorylates AMPKα2 to Inhibit Its Activity and Repress Fatty Acid Oxidation." *Molecular Cell* 68(2):336-349.e6. doi: 10.1016/j.molcel.2017.09.034.

Lu, Jianlin, Yuanyuan Huang, Li Zhan, Ming Wang, Leilei Xu, McKay Mullen, Jianye Zang, Guowei Fang, Zhen Dou, Xing Liu, Wei Liu, Minerva Garcia-Barrio, and Xuebiao Yao. 2021. "AMPKα2 Activation by an Energy-Independent Signal Ensures Chromosomal Stability during Mitosis." *IScience* 24(4):102363. doi: 10.1016/j.isci.2021.102363.

Madhavi Sastry, G., Matvey Adzhigirey, Tyler Day, Ramakrishna Annabhimoju, and Woody Sherman. 2013. "Protein and Ligand Preparation: Parameters, Protocols, and Influence on Virtual Screening Enrichments." *Journal of Computer-Aided Molecular Design* 27(3):221–34. doi: 10.1007/s10822-013-9644-8.

Makohon-Moore, Alvin P., Karen Matsukuma, Ming Zhang, Johannes G. Reiter, Jeffrey M. Gerold, Yuchen Jiao, Lisa Sikkema, Marc A. Attiyeh, Shinichi Yachida, Corinne Sandone, Ralph H. Hruban, David S. Klimstra, Nickolas Papadopoulos, Martin A. Nowak, Kenneth W. Kinzler, Bert Vogelstein, and Christine A. Iacobuzio-Donahue. 2018. "Precancerous Neoplastic Cells Can Move through the Pancreatic Ductal System." *Nature* 561(7722):201–5. doi: 10.1038/s41586-018-0481-8.

Maldonado, Eduardo N., Kely L. Sheldon, David N. DeHart, Jyoti Patnaik, Yefim Manevich, Danyelle M. Townsend, Sergey M. Bezrukov, Tatiana K. Rostovtseva, and John J. Lemasters. 2013. "Voltage-Dependent Anion Channels Modulate Mitochondrial Metabolism in Cancer Cells." *Journal of Biological Chemistry* 288(17):11920–29. doi: 10.1074/jbc.M112.433847.

Martina, Jose A., Yong Chen, Marjan Gucek, and Rosa Puertollano. 2012. "MTORC1 Functions as a Transcriptional Regulator of Autophagy by Preventing Nuclear Transport of TFEB." *Autophagy* 8(6):903–14. doi: 10.4161/auto.19653.

Martina, José A., Heba I. Diab, Li Lishu, Lim Jeong-A, Simona Patange, Nina Raben, and Rosa Puertollano. 2014. "The Nutrient-Responsive Transcription Factor TFE3 Promotes Autophagy, Lysosomal Biogenesis, and Clearance of Cellular Debris." *Science Signaling* 7(309). doi: 10.1126/scisignal.2004754.

Masoud, Rawand, Gabriela Reyes-Castellanos, Sophie Lac, Julie Garcia, Samir Dou, Laetitia Shintu, Nadine Abdel Hadi, Tristan Gicquel, Abdessamad El Kaoutari, Binta Diémé, Fabrice Tranchida, Laurie Cormareche, Laurence Borge, Odile Gayet, Eddy Pasquier, Nelson Dusetti, Juan Iovanna, and Alice Carrier. 2020. "Targeting Mitochondrial Complex I Overcomes Chemoresistance in High OXPHOS Pancreatic Cancer." *Cell Reports Medicine* 1(8):100143. doi: 10.1016/j.xcrm.2020.100143.

McDonald, Oliver G., Xin Li, Tyler Saunders, Rakel Tryggvadottir, Samantha J. Mentch, Marc O. Warmoes, Anna E. Word, Alessandro Carrer, Tal H. Salz, Sonoko Natsume, Kimberly M. Stauffer, Alvin Makohon-Moore, Yi Zhong, Hao Wu, Kathryn E. Wellen, Jason W. Locasale, Christine A. Iacobuzio-Donahue, and Andrew P. Feinberg. 2017. "Epigenomic Reprogramming during Pancreatic Cancer Progression Links Anabolic Glucose Metabolism to Distant Metastasis." *Nature Genetics* 49(3):367–76. doi: 10.1038/ng.3753.

Merrill, John F., David M. Thomson, Shalene E. Hardman, Squire D. Hepworth, Shelby Willie, and Chad R. Hancock. 2012. "Iron Deficiency Causes a Shift in AMP-Activated Protein Kinase (AMPK) Subunit Composition in Rat Skeletal Muscle." *Nutrition & Metabolism* 9(1):104. doi: 10.1186/1743-7075-9-104.

Mihaylova, Maria M., Debbie S. Vasquez, Kim Ravnskjaer, Pierre-Damien Denechaud, Ruth T. Yu, Jacqueline G. Alvarez, Michael Downes, Ronald M. Evans, Marc Montminy, and Reuben J. Shaw. 2011. "Class IIa Histone Deacetylases Are Hormone-Activated Regulators of FOXO and Mammalian Glucose Homeostasis." *Cell* 145(4):607–21. doi: 10.1016/j.cell.2011.03.043.

Moffitt, Richard A., Raoud Marayati, Elizabeth L. Flate, Keith E. Volmar, S. Gabriela Herrera Loeza, Katherine A. Hoadley, Naim U. Rashid, Lindsay A. Williams, Samuel C. Eaton, Alexander H. Chung, Jadwiga K. Smyla, Judy M. Anderson, Hong Jin Kim, David J. Bentrem, Mark S. Talamonti, Christine A. Iacobuzio-Donahue, Michael A. Hollingsworth, and Jen Jen Yeh. 2015. "Virtual Microdissection Identifies Distinct Tumor- and Stroma-Specific Subtypes of Pancreatic Ductal Adenocarcinoma." *Nature Genetics* 47(10):1168–78. doi: 10.1038/ng.3398.

Mueller, Sebastian, Thomas Engleitner, Roman Maresch, Magdalena Zukowska, Sebastian Lange, Thorsten Kaltenbacher, Björn Konukiewitz, Rupert Öllinger, Maximilian Zwiebel, Alex Strong, Hsi-Yu Yen, Ruby Banerjee, Sandra Louzada, Beiyuan Fu, Barbara Seidler, Juliana Götzfried, Kathleen Schuck, Zonera Hassan, Andreas Arbeiter, Nina Schönhuber, Sabine Klein, Christian Veltkamp, Mathias Friedrich, Lena Rad, Maxim Barenboim, Christoph Ziegenhain, Julia Hess, Oliver M. Dovey, Stefan Eser, Swati Parekh, Fernando Constantino-Casas, Jorge de la Rosa, Marta I. Sierra, Mario Fraga, Julia Mayerle, Günter Klöppel, Juan Cadiñanos, Pentao Liu, George Vassiliou, Wilko Weichert, Katja Steiger, Wolfgang Enard, Roland M. Schmid, Fengtang Yang, Kristian Unger, Günter Schneider, Ignacio Varela, Allan Bradley, Dieter Saur, and Roland Rad. 2018. "Evolutionary Routes and KRAS Dosage Define Pancreatic Cancer Phenotypes." *Nature* 554(7690):62–68. doi: 10.1038/nature25459.

Mullard, Asher. 2022. "BRAF plus MEK Inhibitor Combo Secures Tumour-Agnostic FDA Approval." *Nature Reviews Drug Discovery* 21(8):548–548. doi: 10.1038/d41573-022-00117-y.

Murray, Brion W., Chuangxing Guo, Joseph Piraino, John K. Westwick, Cathy Zhang, Jane Lamerdin, Eleanor Dagostino, Daniel Knighton, Cho-Ming Loi, Michael Zager, Eugenia Kraynov, Ian Popoff, James G. Christensen, Ricardo Martinez, Susan E. Kephart, Joseph Marakovits, Shannon Karlicek, Simon Bergqvist, and Tod Smeal. 2010. "Small-Molecule P21-Activated Kinase Inhibitor PF-3758309 Is a Potent Inhibitor of Oncogenic Signaling and Tumor Growth." *Proceedings of the National Academy of Sciences* 107(20):9446–51. doi: 10.1073/pnas.0911863107.

Nicolle, Rémy, Yuna Blum, Pauline Duconseil, Charles Vanbrugghe, Nicolas Brandone, Flora Poizat, Julie Roques, Martin Bigonnet, Odile Gayet, Marion Rubis, Nabila Elarouci, Lucile Armenoult, Mira Ayadi, Aurélien de Reyniès, Marc Giovannini, Philippe Grandval, Stephane Garcia, Cindy Canivet, Jérôme Cros, Barbara Bournet, Louis Buscail, Vincent Moutardier, Marine Gilabert, Juan Iovanna, and Nelson Dusetti. 2020. "Establishment of a Pancreatic Adenocarcinoma Molecular Gradient (PAMG) That Predicts the Clinical Outcome of Pancreatic Cancer." *EBioMedicine* 57:102858. doi: 10.1016/j.ebiom.2020.102858.

Ning, Junyu, Gang Xi, and David R. Clemmons. 2011. "Suppression of AMPK Activation via S485 Phosphorylation by IGF-I during Hyperglycemia Is Mediated by AKT Activation in Vascular Smooth Muscle Cells." *Endocrinology* 152(8):3143–54. doi: 10.1210/en.2011-0155.

Nishio, Kohei, Kenjiro Kimura, Ryosuke Amano, Sadaaki Yamazoe, Go Ohrira, Bunzo Nakata, Kosei Hirakawa, and Masaichi Ohira. 2017. "Preoperative Predictors for Early Recurrence of Resectable Pancreatic Cancer." *World Journal of Surgical Oncology* 15(1):16. doi: 10.1186/s12957-016-1078-z.

Noll, Elisa M., Christian Eisen, Albrecht Stenzinger, Elisa Espinet, Alexander Muckenhuber, Corinna Klein, Vanessa Vogel, Bernd Klaus, Wiebke Nadler, Christoph Rösli, Christian Lutz, Michael Kulke, Jan Engelhardt, Franziska M. Zickgraf, Octavio Espinosa, Matthias Schlesner, Xiaoqi Jiang, Annette Kopp-Schneider, Peter Neuhaus, Marcus Bahra, Bruno V. Sinn, Roland Eils, Nathalia A. Giese, Thilo Hackert, Oliver Strobel, Jens Werner, Markus W. Büchler, Wilko Weichert, Andreas Trumpp, and Martin R. Sprick. 2016. "CYP3A5 Mediates Basal and Acquired Therapy Resistance in Different Subtypes of Pancreatic Ductal Adenocarcinoma." *Nature Medicine* 22(3):278–87. doi: 10.1038/nm.4038.

Notta, Faiyaz, Michelle Chan-Seng-Yue, Mathieu Lemire, Yilong Li, Gavin W. Wilson, Ashton A. Connor, Robert E. Denroche, Sheng-Ben Liang, Andrew M. K. Brown, Jaeseung C. Kim, Tao Wang, Jared T. Simpson, Timothy Beck, Ayelet Borgida, Nicholas Buchner, Dianne Chadwick, Sara Hafezi-Bakhtiari, John E. Dick, Lawrence Heisler, Michael A. Hollingsworth, Emin Ibrahimov, Gun Ho Jang, Jeremy Johns, Lars G. T. Jorgensen, Calvin Law, Olga Ludkovski, Ilinca Lungu, Karen Ng, Danielle Pasternack, Gloria M. Petersen, Liran I. Shlush, Lee Timms, Ming-Sound Tsao, Julie M. Wilson, Christina K. Yung, George Zogopoulos, John M. S. Bartlett, Ludmil B. Alexandrov, Francisco X. Real, Sean P. Cleary, Michael H. Roehrl, John D. McPherson, Lincoln D. Stein, Thomas J. Hudson, Peter J. Campbell, and Steven Gallinger. 2016. "A Renewed Model of Pancreatic Cancer Evolution Based on Genomic Rearrangement Patterns." *Nature* 538(7625):378–82. doi: 10.1038/nature19823.

Olson, Calla M., Yanke Liang, Alan Leggett, Woojun D. Park, Lianbo Li, Caitlin E. Mills, Selma Z. Elsarrag, Scott B. Ficarro, Tinghu Zhang, Robert Düster, Matthias Geyer, Taebo Sim, Jarrod A. Marto, Peter K. Sorger,

Ken D. Westover, Charles Y. Lin, Nicholas Kwiatkowski, and Nathanael S. Gray. 2019. “Development of a Selective CDK7 Covalent Inhibitor Reveals Predominant Cell-Cycle Phenotype.” *Cell Chemical Biology* 26(6):792-803.e10. doi: 10.1016/j.chembiol.2019.02.012.

Orben, Felix, Katharina Lankes, Christian Schneeweis, Zonera Hassan, Hannah Jakubowsky, Lukas Krauß, Fabio Boniolo, Carolin Schneider, Arlett Schäfer, Janine Murr, Christoph Schlag, Bo Kong, Rupert Öllinger, Chengdong Wang, Georg Beyer, Ujjwal M. Mahajan, Yonggan Xue, Julia Mayerle, Roland M. Schmid, Bernhard Kuster, Roland Rad, Christian J. Braun, Matthias Wirth, Maximilian Reichert, Dieter Saur, and Günter Schneider. 2022. “Epigenetic Drug Screening Defines a PRMT5 Inhibitor–Sensitive Pancreatic Cancer Subtype.” *JCI Insight* 7(10):e151353. doi: 10.1172/jci.insight.151353.

Paquette, Mathieu, Leeanna El-Houjeiri, Linda C. Zirden, Pietri Puustinen, Paola Blanchette, Hyeonju Jeong, Kurt Dejgaard, Peter M. Siegel, and Arnim Pause. 2021. “AMPK-Dependent Phosphorylation Is Required for Transcriptional Activation of TFEB and TFE3.” *Autophagy* 17(12):3957–75. doi: 10.1080/15548627.2021.1898748.

Parekh, Swati, Christoph Ziegenhain, Beate Vieth, Wolfgang Enard, and Ines Hellmann. 2016. “The Impact of Amplification on Differential Expression Analyses by RNA-Seq.” *Scientific Reports* 6(1):25533. doi: 10.1038/srep25533.

Peschke, Katja, Hannah Jakubowsky, Arlett Schäfer, Carlo Maurer, Sebastian Lange, Felix Orben, Raquel Bernad, Felix N. Harder, Matthias Eiber, Rupert Öllinger, Katja Steiger, Melissa Schlitter, Wilko Weichert, Ulrich Mayr, Veit Phillip, Christoph Schlag, Roland M. Schmid, Rickmer F. Braren, Bo Kong, Ihsan Ekin Demir, Helmut Friess, Roland Rad, Dieter Saur, Günter Schneider, and Maximilian Reichert. 2022. “Identification of Treatment-induced Vulnerabilities in Pancreatic Cancer Patients Using Functional Model Systems.” *EMBO Molecular Medicine* 14(4). doi: 10.15252/emmm.202114876.

Pinkosky, Stephen L., John W. Scott, Eric M. Desjardins, Brennan K. Smith, Emily A. Day, Rebecca J. Ford, Christopher G. Langendorf, Naomi X. Y. Ling, Tracy L. Nero, Kim Loh, Sandra Galic, Ashfaqul Hoque, William J. Smiles, Kevin R. W. Ngoei, Michael W. Parker, Yan Yan, Karsten Melcher, Bruce E. Kemp, Jonathan S. Oakhill, and Gregory R. Steinberg. 2020. “Long-Chain Fatty Acyl-CoA Esters Regulate Metabolism via Allosteric Control of AMPK B1 Isoforms.” *Nature Metabolism* 2(9):873–81. doi: 10.1038/s42255-020-0245-2.

Pishvaian, Michael J., Edik M. Blais, Jonathan R. Brody, Emily Lyons, Patricia DeArbeloa, Andrew Hendifar, Sam Mikhail, Vincent Chung, Vaibhav Sahai, Davendra P. S. Sohal, Sara Bellakbira, Dzung Thach, Lola Rahib, Subha Madhavan, Lynn M. Matrisian, and Emanuel F. Petricoin. 2020. “Overall Survival in Patients with Pancreatic Cancer Receiving Matched Therapies Following Molecular Profiling: A Retrospective Analysis of the Know Your Tumor Registry Trial.” *The Lancet Oncology* 21(4):508–18. doi: 10.1016/S1470-2045(20)30074-7.

Raghavan, Srivatsan, Peter S. Winter, Andrew W. Navia, Hannah L. Williams, Alan DenAdel, Kristen E. Lowder, Jennyfer Galvez-Reyes, Radha L. Kalekar, Nolawit Mulugeta, Kevin S. Kapner, Manisha S. Raghavan, Ashir A. Borah, Nuo Liu, Sara A. Väyrynen, Andressa Dias Costa, Raymond W. S. Ng, Junning Wang, Emma K. Hill, Dorisanne Y. Ragon, Lauren K. Brais, Alex M. Jaeger, Liam F. Spurr, Yvonne Y. Li, Andrew D. Cherniack, Matthew A. Booker, Elizabeth F. Cohen, Michael Y. Tolstorukov, Isaac Wakiro, Asaf Rotem, Bruce E. Johnson, James M. McFarland, Ewa T. Sicinska, Tyler E. Jacks, Ryan J. Sullivan, Geoffrey I. Shapiro, Thomas E. Clancy, Kimberly Perez, Douglas A. Rubinson, Kimmie Ng, James M. Cleary, Lorin Crawford, Scott R. Manalis, Jonathan A. Nowak, Brian M. Wolpin, William C. Hahn, Andrew J. Aguirre, and Alex K. Shalek. 2021. “Microenvironment Drives Cell State, Plasticity, and Drug Response in Pancreatic Cancer.” *Cell* 184(25):6119-6137.e26. doi: 10.1016/j.cell.2021.11.017.

Reinecke, Maria, Benjamin Ruprecht, Sandra Poser, Svenja Wiechmann, Mathias Wilhelm, Stephanie Heinzlmeir, Bernhard Kuster, and Guillaume Médard. 2019. “Chemoproteomic Selectivity Profiling of PIKK and PI3K Kinase Inhibitors.” *ACS Chemical Biology* 14(4):655–64. doi: 10.1021/acschembio.8b01020.

Robert Koch Institute. 2022. *Retrieved October 10, 2022, from Https://Www.Krebsdaten.de/Krebs/EN/Database/Databasequery_step1_node.Html*.

Rosencrans, William M., Vicente M. Aguilella, Tatiana K. Rostovtseva, and Sergey M. Bezrukov. 2021. "α-Synuclein Emerges as a Potent Regulator of VDAC-Facilitated Calcium Transport." *Cell Calcium* 95:102355. doi: 10.1016/j.ceca.2021.102355.

Rostovtseva, Tatiana K., Kely L. Sheldon, Elnaz Hassanzadeh, Claire Monge, Valdur Saks, Sergey M. Bezrukov, and Dan L. Sackett. 2008. "Tubulin Binding Blocks Mitochondrial Voltage-Dependent Anion Channel and Regulates Respiration." *Proceedings of the National Academy of Sciences* 105(48):18746–51. doi: 10.1073/pnas.0806303105.

Ryan, David P., Theodore S. Hong, and Nabeel Bardeesy. 2014. "Pancreatic Adenocarcinoma." *New England Journal of Medicine* 371(11):1039–49. doi: 10.1056/NEJMra1404198.

Sasaki, Koji, Sara S. Strom, Susan O'Brien, Elias Jabbour, Farhad Ravandi, Marina Konopleva, Gautam Borthakur, Naveen Pemmaraju, Naval Daver, Preetesh Jain, Sherry Pierce, Hagop Kantarjian, and Jorge E. Cortes. 2015. "Relative Survival in Patients with Chronic-Phase Chronic Myeloid Leukaemia in the Tyrosine-Kinase Inhibitor Era: Analysis of Patient Data from Six Prospective Clinical Trials." *The Lancet Haematology* 2(5):e186–93. doi: 10.1016/S2352-3026(15)00048-4.

Sato, Mami, Ryosuke Kusumi, Shinji Hamashima, Sho Kobayashi, Satoru Sasaki, Yuhei Komiyama, Takuji Izumikawa, Marcus Conrad, Shiro Bannai, and Hideyo Sato. 2018. "The Ferroptosis Inducer Erastin Irreversibly Inhibits System Xc− and Synergizes with Cisplatin to Increase Cisplatin's Cytotoxicity in Cancer Cells." *Scientific Reports* 8(1):968. doi: 10.1038/s41598-018-19213-4.

Sato, R., J. L. Goldstein, and M. S. Brown. 1993. "Replacement of Serine-871 of Hamster 3-Hydroxy-3-Methylglutaryl-CoA Reductase Prevents Phosphorylation by AMP-Activated Kinase and Blocks Inhibition of Sterol Synthesis Induced by ATP Depletion." *Proceedings of the National Academy of Sciences* 90(20):9261–65. doi: 10.1073/pnas.90.20.9261.

Schaffer, Bethany E., Rebecca S. Levin, Nicholas T. Hertz, Travis J. Maures, Michael L. Schoof, Pablo E. Hollstein, Bérénice A. Benayoun, Max R. Banko, Reuben J. Shaw, Kevan M. Shokat, and Anne Brunet. 2015. "Identification of AMPK Phosphorylation Sites Reveals a Network of Proteins Involved in Cell Invasion and Facilitates Large-Scale Substrate Prediction." *Cell Metabolism* 22(5):907–21. doi: 10.1016/j.cmet.2015.09.009.

Schrödinger, LLC. 2021a. "Schrödinger Release 2021-3: ConfGen."

Schrödinger, LLC. 2021b. "Schrödinger Release 2021-3: Epik."

Schrödinger, LLC. 2021c. "Schrödinger Release 2021-3: Glide."

Schrödinger, LLC. 2021d. "Schrödinger Release 2021-3: LigPrep."

Schrödinger, LLC. 2021e. "Schrödinger Release 2021-3: Maestro."

Schrödinger, LLC. n.d. "PyMOL Molecular Graphics System."

Settembre, Carmine, Roberto Zoncu, Diego L. Medina, Francesco Vetrini, Serkan Erdin, SerpilUckac Erdin, Tuong Huynh, Mathieu Ferron, Gerard Karsenty, Michel C. Vellard, Valeria Facchinetti, David M. Sabatini, and Andrea Ballabio. 2012. "A Lysosome-to-Nucleus Signalling Mechanism Senses and Regulates the Lysosome via MTOR and TFEB: Self-Regulation of the Lysosome via MTOR and TFEB." *The EMBO Journal* 31(5):1095–1108. doi: 10.1038/emboj.2012.32.

Shelley, John C., Anuradha Cholleti, Leah L. Frye, Jeremy R. Greenwood, Mathew R. Timlin, and Makoto Uchimaya. 2007. "Epik: A Software Program for PK a Prediction and Protonation State Generation for

Drug-like Molecules." *Journal of Computer-Aided Molecular Design* 21(12):681–91. doi: 10.1007/s10822-007-9133-z.

Shi, Chanjuan, Ralph H. Hruban, and Alison P. Klein. 2009. "Familial Pancreatic Cancer." *Archives of Pathology & Laboratory Medicine* 133(3):365–74. doi: 10.5858/133.3.365.

Shivakumar, Devleena, Joshua Williams, Yujie Wu, Wolfgang Damm, John Shelley, and Woody Sherman. 2010. "Prediction of Absolute Solvation Free Energies Using Molecular Dynamics Free Energy Perturbation and the OPLS Force Field." *Journal of Chemical Theory and Computation* 6(5):1509–19. doi: 10.1021/ct900587b.

Sicklick, Jason K., Shumei Kato, Ryosuke Okamura, Maria Schwaederle, Michael E. Hahn, Casey B. Williams, Pradip De, Amy Krie, David E. Piccioni, Vincent A. Miller, Jeffrey S. Ross, Adam Benson, Jennifer Webster, Philip J. Stephens, J. Jack Lee, Paul T. Fanta, Scott M. Lippman, Brian Leyland-Jones, and Razelle Kurzrock. 2019. "Molecular Profiling of Cancer Patients Enables Personalized Combination Therapy: The I-PREDICT Study." *Nature Medicine* 25(5):744–50. doi: 10.1038/s41591-019-0407-5.

Siegel, Rebecca L., Kimberly D. Miller, Hannah E. Fuchs, and Ahmedin Jemal. 2022. "Cancer Statistics, 2022." *CA: A Cancer Journal for Clinicians* 72(1):7–33. doi: 10.3322/caac.21708.

Siegel, Rebecca L., Kimberly D. Miller, and Ahmedin Jemal. 2017. "Cancer Statistics, 2017." *CA: A Cancer Journal for Clinicians* 67(1):7–30. doi: 10.3322/caac.21387.

Siegel, Rebecca L., Kimberly D. Miller, Nikita Sandeep Wagle, and Ahmedin Jemal. 2023. "Cancer Statistics, 2023." *CA: A Cancer Journal for Clinicians* 73(1):17–48. doi: 10.3322/caac.21763.

Sinha, Rohit A., Brijesh K. Singh, Jin Zhou, Yajun Wu, Benjamin L. Farah, Kenji Ohba, Ronny Lesmana, Jessica Gooding, Boon-Huat Bay, and Paul M. Yen. 2015. "Thyroid Hormone Induction of Mitochondrial Activity Is Coupled to Mitophagy via ROS-AMPK-ULK1 Signaling." *Autophagy* 11(8):1341–57. doi: 10.1080/15548627.2015.1061849.

Skoulidis, Ferdinandos, Bob T. Li, Grace K. Dy, Timothy J. Price, Gerald S. Falchook, Jürgen Wolf, Antoine Italiano, Martin Schuler, Hossein Borghaei, Fabrice Barlesi, Terufumi Kato, Alessandra Curioni-Fontecedro, Adrian Sacher, Alexander Spira, Suresh S. Ramalingam, Toshiaki Takahashi, Benjamin Besse, Abraham Anderson, Agnes Ang, Qui Tran, Omar Mather, Haby Henary, Gataree Ngarmchamnanrith, Gregory Friberg, Vamsidhar Velcheti, and Ramaswamy Govindan. 2021. "Sotorasib for Lung Cancers with *KRAS* p.G12C Mutation." *New England Journal of Medicine* 384(25):2371–81. doi: 10.1056/NEJMoa2103695.

Son, Jaekyoung, Costas A. Lyssiotis, Haoqiang Ying, Xiaoxu Wang, Sujun Hua, Matteo Ligorio, Rushika M. Perera, Cristina R. Ferrone, Edouard Mullarky, Ng Shyh-Chang, Ya'an Kang, Jason B. Fleming, Nabeel Bardeesy, John M. Asara, Marcia C. Haigis, Ronald A. DePinho, Lewis C. Cantley, and Alec C. Kimmelman. 2013. "Glutamine Supports Pancreatic Cancer Growth through a KRAS-Regulated Metabolic Pathway." *Nature* 496(7443):101–5. doi: 10.1038/nature12040.

Stahmann, Nadine, Angela Woods, Katrin Spengler, Amanda Heslegrave, Reinhard Bauer, Siegfried Krause, Benoit Viollet, David Carling, and Regine Heller. 2010. "Activation of AMP-Activated Protein Kinase by Vascular Endothelial Growth Factor Mediates Endothelial Angiogenesis Independently of Nitric-Oxide Synthase." *Journal of Biological Chemistry* 285(14):10638–52. doi: 10.1074/jbc.M110.108688.

Steinberg, Gregory R., and D. Grahame Hardie. 2022. "New Insights into Activation and Function of the AMPK." *Nature Reviews Molecular Cell Biology*. doi: 10.1038/s41580-022-00547-x.

Sun, Bowen, Seth Mason, Robert C. Wilson, Starr E. Hazard, Yubao Wang, Rong Fang, Qiwei Wang, Elizabeth S. Yeh, Meixiang Yang, Thomas M. Roberts, Jean J. Zhao, and Qi Wang. 2020. "Inhibition of the Transcriptional Kinase CDK7 Overcomes Therapeutic Resistance in HER2-Positive Breast Cancers." *Oncogene* 39(1):50–63. doi: 10.1038/s41388-019-0953-9.

Tadros, Saber, Surendra K. Shukla, Ryan J. King, Venugopal Gunda, Enza Vernucci, Jaime Abrego, Nina V. Chaika, Fang Yu, Audrey J. Lazenby, Lyudmyla Berim, Jean Grem, Aaron R. Sasson, and Pankaj K. Singh. 2017. "*De Novo* Lipid Synthesis Facilitates Gemcitabine Resistance through Endoplasmic Reticulum Stress in Pancreatic Cancer." *Cancer Research* 77(20):5503–17. doi: 10.1158/0008-5472.CAN-16-3062.

Tang, Yichen, Xuejun Xu, Shixiang Guo, Chaobin Zhang, Yan Tang, Yi Tian, Bing Ni, Binfeng Lu, and Huaizhi Wang. 2014. "An Increased Abundance of Tumor-Infiltrating Regulatory T Cells Is Correlated with the Progression and Prognosis of Pancreatic Ductal Adenocarcinoma" edited by H. Shiku. *PLoS ONE* 9(3):e91551. doi: 10.1371/journal.pone.0091551.

Tang, Zefang, Chenwei Li, Boxi Kang, Ge Gao, Cheng Li, and Zemin Zhang. 2017. "GEPIA: A Web Server for Cancer and Normal Gene Expression Profiling and Interactive Analyses." *Nucleic Acids Research* 45(W1):W98–102. doi: 10.1093/nar/gkx247.

Topal, Halit, Raymond Aerts, Annouschka Laenen, André Collignon, Joris Jaekers, Joachim Geers, and Baki Topal. 2022. "Survival After Minimally Invasive vs Open Surgery for Pancreatic Adenocarcinoma." *JAMA Network Open* 5(12):e2248147. doi: 10.1001/jamanetworkopen.2022.48147.

Toyama, Erin Quan, Sébastien Herzig, Julien Courchet, Tommy L. Lewis, Oliver C. Losón, Kristina Hellberg, Nathan P. Young, Hsiuchen Chen, Franck Polleux, David C. Chan, and Reuben J. Shaw. 2016. "AMP-Activated Protein Kinase Mediates Mitochondrial Fission in Response to Energy Stress." *Science* 351(6270):275–81. doi: 10.1126/science.aab4138.

Tran, Eric, Dhanalakshmi Chinnasamy, Zhiya Yu, Richard A. Morgan, Chyi-Chia Richard Lee, Nicholas P. Restifo, and Steven A. Rosenberg. 2013. "Immune Targeting of Fibroblast Activation Protein Triggers Recognition of Multipotent Bone Marrow Stromal Cells and Cachexia." *Journal of Experimental Medicine* 210(6):1125–35. doi: 10.1084/jem.20130110.

Varughese, Joyce T., Susan K. Buchanan, and Ashley S. Pitt. 2021. "The Role of Voltage-Dependent Anion Channel in Mitochondrial Dysfunction and Human Disease." *Cells* 10(7):1737. doi: 10.3390/cells10071737.

Vaziri-Gohar, Ali, Joel Cassel, Farheen S. Mohammed, Mehrdad Zarei, Jonathan J. Hue, Omid Hajihassani, Hallie J. Graor, Yellamelli V. V. Srikanth, Saadia A. Karim, Ata Abbas, Erin Prendergast, Vanessa Chen, Erryk S. Katayama, Katerina Dukleska, Imran Khokhar, Anthony Andren, Li Zhang, Chunying Wu, Bernadette Erokwu, Chris A. Flask, Mahsa Zarei, Rui Wang, Luke D. Rothermel, Andrea M. P. Romani, Jessica Bowers, Robert Getts, Curtis Tatsuoka, Jennifer P. Morton, Ilya Bederman, Henri Brunengraber, Costas A. Lyssiotis, Joseph M. Salvino, Jonathan R. Brody, and Jordan M. Winter. 2022. "Limited Nutrient Availability in the Tumor Microenvironment Renders Pancreatic Tumors Sensitive to Allosteric IDH1 Inhibitors." *Nature Cancer* 3(7):852–65. doi: 10.1038/s43018-022-00393-y.

Viswanathan, Vasanthi S., Matthew J. Ryan, Harshil D. Dhruv, Shubhroz Gill, Ossia M. Eichhoff, Brinton Seashore-Ludlow, Samuel D. Kaffenberger, John K. Eaton, Kenichi Shimada, Andrew J. Aguirre, Srinivas R. Viswanathan, Shrikanta Chattopadhyay, Pablo Tamayo, Wan Seok Yang, Matthew G. Rees, Sixun Chen, Zarko V. Boskovic, Sarah Javaid, Cherrie Huang, Xiaoyun Wu, Yuen-Yi Tseng, Elisabeth M. Roider, Dong Gao, James M. Cleary, Brian M. Wolpin, Jill P. Mesirov, Daniel A. Haber, Jeffrey A. Engelman, Jesse S. Boehm, Joanne D. Kotz, Cindy S. Hon, Yu Chen, William C. Hahn, Mitchell P. Levesque, John G. Doench, Michael E. Berens, Alykhan F. Shamji, Paul A. Clemons, Brent R. Stockwell, and Stuart L. Schreiber. 2017. "Dependency of a Therapy-Resistant State of Cancer Cells on a Lipid Peroxidase Pathway." *Nature* 547(7664):453–57. doi: 10.1038/nature23007.

Von Hoff, Daniel D., Thomas Ervin, Francis P. Arena, E. Gabriela Chiorean, Jeffrey Infante, Malcolm Moore, Thomas Seay, Sergei A. Tjulandin, Wen Wee Ma, Mansoor N. Saleh, Marion Harris, Michele Reni, Scot Dowden, Daniel Laheru, Nathan Bahary, Ramesh K. Ramanathan, Josep Tabernero, Manuel Hidalgo, David Goldstein, Eric Van Cutsem, Xinyu Wei, Jose Iglesias, and Markus F. Renschler. 2013. "Increased Survival in Pancreatic Cancer with Nab-Paclitaxel plus Gemcitabine." *New England Journal of Medicine* 369(18):1691–1703. doi: 10.1056/NEJMoa1304369.

Voss, Martin, James Paterson, Ian R. Kelsall, Cristina Martín-Granados, C. James Hastie, Mark W. Peggie, and Patricia T. W. Cohen. 2011. “Ppm1E Is an in Cellulo AMP-Activated Protein Kinase Phosphatase.” *Cellular Signalling* 23(1):114–24. doi: 10.1016/j.cellsig.2010.08.010.

Wang, Cheng, Wencheng Zhang, Wenjing Xu, Zhaoyu Liu, and Kai Huang. 2022. “AMP-activated Protein Kinase A1 Phosphorylates PHD2 to Maintain Systemic Iron Homeostasis.” *Clinical and Translational Medicine* 12(5). doi: 10.1002/ctm2.854.

Warburg, Otto. 1956. “On the Origin of Cancer Cells.” *Science* 123(3191):309–14. doi: 10.1126/science.123.3191.309.

Watts, K. Shawn, Pranav Dalal, Robert B. Murphy, Woody Sherman, Rich A. Friesner, and John C. Shelley. 2010. “ConfGen: A Conformational Search Method for Efficient Generation of Bioactive Conformers.” *Journal of Chemical Information and Modeling* 50(4):534–46. doi: 10.1021/ci100015j.

Weekes, John, Kathryn L. Ball, F. Barry Caudwell, and D. Grahame Hardie. 1993. “Specificity Determinants for the AMP-Activated Protein Kinase and Its Plant Homologue Analysed Using Synthetic Peptides.” *FEBS Letters* 334(3):335–39. doi: 10.1016/0014-5793(93)80706-Z.

Weerasekara, Vajira K., David J. Panek, David G. Broadbent, Jeffrey B. Mortenson, Andrew D. Mathis, Gideon N. Logan, John T. Prince, David M. Thomson, J. Will Thompson, and Joshua L. Andersen. 2014. “Metabolic-Stress-Induced Rearrangement of the 14-3-3ζ Interactome Promotes Autophagy via a ULK1- and AMPK-Regulated 14-3-3ζ Interaction with Phosphorylated Atg9.” *Molecular and Cellular Biology* 34(24):4379–88. doi: 10.1128/MCB.00740-14.

Woods, Angela, Jennet R. Williams, Phillip J. Muckett, Faith V. Mayer, Maria Liljevald, Mohammad Bohlooly-Y, and David Carling. 2017. “Liver-Specific Activation of AMPK Prevents Steatosis on a High-Fructose Diet.” *Cell Reports* 18(13):3043–51. doi: 10.1016/j.celrep.2017.03.011.

Wouters, Olivier J., Martin McKee, and Jeroen Luyten. 2020. “Estimated Research and Development Investment Needed to Bring a New Medicine to Market, 2009-2018.” *JAMA* 323(9):844. doi: 10.1001/jama.2020.1166.

Wu, Ning, Bin Zheng, Adam Shaywitz, Yossi Dagon, Christine Tower, Gary Bellinger, Che-Hung Shen, Jennifer Wen, John Asara, Timothy E. McGraw, Barbara B. Kahn, and Lewis C. Cantley. 2013. “AMPK-Dependent Degradation of TXNIP upon Energy Stress Leads to Enhanced Glucose Uptake via GLUT1.” *Molecular Cell* 49(6):1167–75. doi: 10.1016/j.molcel.2013.01.035.

Xu, Yixiang, Dong-Kee Lee, Zhen Feng, Yan Xu, Wen Bu, Yi Li, Lan Liao, and Jianming Xu. 2017. “Breast Tumor Cell-Specific Knockout of *Twist1* Inhibits Cancer Cell Plasticity, Dissemination, and Lung Metastasis in Mice.” *Proceedings of the National Academy of Sciences* 114(43):11494–99. doi: 10.1073/pnas.1618091114.

Yagoda, Nicholas, Moritz Von Rechenberg, Elma Zaganjor, Andras J. Bauer, Wan Seok Yang, Daniel J. Fridman, Adam J. Wolpaw, Inese Smukste, John M. Peltier, J. Jay Boniface, Richard Smith, Stephen L. Lessnick, Sudhir Sahasrabudhe, and Brent R. Stockwell. 2007. “RAS–RAF–MEK-Dependent Oxidative Cell Death Involving Voltage-Dependent Anion Channels.” *Nature* 447(7146):865–69. doi: 10.1038/nature05859.

Yan, Renhong, Enjun Xie, Yaning Li, Jin Li, Yuanyuan Zhang, Ximin Chi, Xueping Hu, Lei Xu, Tingjun Hou, Brent R. Stockwell, Junxia Min, Qiang Zhou, and Fudi Wang. 2022. “The Structure of Erastin-Bound XCT–4F2hc Complex Reveals Molecular Mechanisms Underlying Erastin-Induced Ferroptosis.” *Cell Research* 32(7):687–90. doi: 10.1038/s41422-022-00642-w.

Yang, Jing, Sendurai A. Mani, Joana Liu Donaher, Sridhar Ramaswamy, Raphael A. Itzykson, Christophe Come, Pierre Savagner, Inna Gitelman, Andrea Richardson, and Robert A. Weinberg. 2004. “Twist, a Master Regulator of Morphogenesis, Plays an Essential Role in Tumor Metastasis.” *Cell* 117(7):927–39. doi: 10.1016/j.cell.2004.06.006.

Yang, Muh-Hwa, Min-Zu Wu, Shih-Hwa Chiou, Po-Min Chen, Shyue-Yih Chang, Chung-Ji Liu, Shu-Chun Teng, and Kou-Juey Wu. 2008. "Direct Regulation of TWIST by HIF-1α Promotes Metastasis." *Nature Cell Biology* 10(3):295–305. doi: 10.1038/ncb1691.

Yang, Shenghong, Xiaoxu Wang, Gianmarco Contino, Marc Liesa, Ergun Sahin, Haoqiang Ying, Alexandra Bause, Yinghua Li, Jayne M. Stommel, Giacomo Dell'Antonio, Josef Mautner, Giovanni Tonon, Marcia Haigis, Orian S. Shirihai, Claudio Doglioni, Nabeel Bardeesy, and Alec C. Kimmelman. 2011. "Pancreatic Cancers Require Autophagy for Tumor Growth." *Genes & Development* 25(7):717–29. doi: 10.1101/gad.2016111.

Yang, Yunlei, Deniz Atasoy, Helen H. Su, and Scott M. Sternson. 2011. "Hunger States Switch a Flip-Flop Memory Circuit via a Synaptic AMPK-Dependent Positive Feedback Loop." *Cell* 146(6):992–1003. doi: 10.1016/j.cell.2011.07.039.

Yarchoan, Mark, Alexander Hopkins, and Elizabeth M. Jaffee. 2017. "Tumor Mutational Burden and Response Rate to PD-1 Inhibition." *New England Journal of Medicine* 377(25):2500–2501. doi: 10.1056/NEJMc1713444.

Yi, Yong, Deshi Chen, Juan Ao, Wenhua Zhang, Jianqiao Yi, Xiaokun Ren, Junjie Fei, Fengtian Li, Mengmeng Niu, Hu Chen, Yangkun Luo, Zhijun Luo, and Zhi-Xiong Jim Xiao. 2020. "Transcriptional Suppression of AMPKα1 Promotes Breast Cancer Metastasis upon Oncogene Activation." *Proceedings of the National Academy of Sciences* 117(14):8013–21. doi: 10.1073/pnas.1914786117.

Ying, Haoqiang, Alec C. Kimmelman, Costas A. Lyssiotis, Sujun Hua, Gerald C. Chu, Eliot Fletcher-Sananikone, Jason W. Locasale, Jaekyoung Son, Hailei Zhang, Jonathan L. Coloff, Haiyan Yan, Wei Wang, Shujuan Chen, Andrea Viale, Hongwu Zheng, Ji-hye Paik, Carol Lim, Alexander R. Guimaraes, Eric S. Martin, Jeffery Chang, Aram F. Hezel, Samuel R. Perry, Jian Hu, Boyi Gan, Yonghong Xiao, John M. Asara, Ralph Weissleder, Y. Alan Wang, Lynda Chin, Lewis C. Cantley, and Ronald A. DePinho. 2012. "Oncogenic Kras Maintains Pancreatic Tumors through Regulation of Anabolic Glucose Metabolism." *Cell* 149(3):656–70. doi: 10.1016/j.cell.2012.01.058.

Yu, Paul B., Charles C. Hong, Chetana Sachidanandan, Jodie L. Babitt, Donna Y. Deng, Stefan A. Hoyng, Herbert Y. Lin, Kenneth D. Bloch, and Randall T. Peterson. 2008. "Dorsomorphin Inhibits BMP Signals Required for Embryogenesis and Iron Metabolism." *Nature Chemical Biology* 4(1):33–41. doi: 10.1038/nchembio.2007.54.

Yuan, Mengqiu, Ronghui Yan, Yi Zhang, Yue Qiu, Zetan Jiang, Haiying Liu, Ying Wang, Linchong Sun, Huafeng Zhang, and Ping Gao. 2021. "CARS Senses Cysteine Deprivation to Activate AMPK for Cell Survival." *The EMBO Journal* 40(21). doi: 10.15252/embj.2021108028.

Yun, Hee, Seolhui Park, Min-Jung Kim, Woo Kyeom Yang, Dong Uk Im, Ki Ryeol Yang, Jongki Hong, Wonchae Choe, Insug Kang, Sung Soo Kim, and Joohun Ha. 2014. "AMP-Activated Protein Kinase Mediates the Antioxidant Effects of Resveratrol through Regulation of the Transcription Factor FoxO1." *FEBS Journal* 281(19):4421–38. doi: 10.1111/febs.12949.

Zhang, Chen-Song, Simon A. Hawley, Yue Zong, Mengqi Li, Zhichao Wang, Alexander Gray, Teng Ma, Jiwen Cui, Jin-Wei Feng, Mingjiang Zhu, Yu-Qing Wu, Terytty Yang Li, Zhiyun Ye, Shu-Yong Lin, Huiyong Yin, Hai-Long Piao, D. Grahame Hardie, and Sheng-Cai Lin. 2017. "Fructose-1,6-Bisphosphate and Aldolase Mediate Glucose Sensing by AMPK." *Nature* 548(7665):112–16. doi: 10.1038/nature23275.

Zhang, Deyi, Wei Wang, Xiujie Sun, Daqian Xu, Chenyao Wang, Qian Zhang, Huafei Wang, Wenwen Luo, Yan Chen, Huaiyong Chen, and Zhixue Liu. 2016. "AMPK Regulates Autophagy by Phosphorylating BECN1 at Threonine 388." *Autophagy* 12(9):1447–59. doi: 10.1080/15548627.2016.1185576.

Zhao, Yawei, Qingyang Wang, Guihua Qiu, Silei Zhou, Zhaofei Jing, Jingyang Wang, Wendie Wang, Junxia Cao, Kun Han, Qianqian Cheng, Beifen Shen, Yingyu Chen, Weiping J. Zhang, Yuanfang Ma, and Jiyan Zhang. 2015. "RACK1 Promotes Autophagy by Enhancing the Atg14L-Beclin 1-Vps34-Vps15 Complex

Formation upon Phosphorylation by AMPK." *Cell Reports* 13(7):1407–17. doi: 10.1016/j.celrep.2015.10.011.

Zhu, Andrew X., Teresa Macarulla, Milind M. Javle, R. Kate Kelley, Sam J. Lubner, Jorge Adeva, James M. Cleary, Daniel V. T. Catenacci, Mitesh J. Borad, John A. Bridgewater, William P. Harris, Adrian G. Murphy, Do-Youn Oh, Jonathan R. Whisenant, Maeve A. Lowery, Lipika Goyal, Rachna T. Shroff, Anthony B. El-Khoueiry, Christina X. Chamberlain, Elia Aguado-Fraile, Sung Choe, Bin Wu, Hua Liu, Camelia Gliser, Shuchi S. Pandya, Juan W. Valle, and Ghassan K. Abou-Alfa. 2021. "Final Overall Survival Efficacy Results of Ivosidenib for Patients With Advanced Cholangiocarcinoma With *IDH1* Mutation: The Phase 3 Randomized Clinical ClarIDHy Trial." *JAMA Oncology* 7(11):1669. doi: 10.1001/jamaoncol.2021.3836.

Zhu, Xiphias Ge, Aleksey Chudnovskiy, Lou Baudrier, Benjamin Prizer, Yuyang Liu, Benjamin N. Ostendorf, Norihiro Yamaguchi, Abolfozl Arab, Bernardo Tavora, Rebecca Timson, Søren Heissel, Elisa de Stanchina, Henrik Molina, Gabriel D. Victora, Hani Goodarzi, and Kıvanç Birsoy. 2021. "Functional Genomics In Vivo Reveal Metabolic Dependencies of Pancreatic Cancer Cells." *Cell Metabolism* 33(1):211-221.e6. doi: 10.1016/j.cmet.2020.10.017.

Zmijewski, Jaroslaw W., Sami Banerjee, Hongbeom Bae, Arnaud Friggeri, Eduardo R. Lazarowski, and Edward Abraham. 2010. "Exposure to Hydrogen Peroxide Induces Oxidation and Activation of AMP-Activated Protein Kinase*." *Journal of Biological Chemistry* 285(43):33154–64. doi: 10.1074/jbc.M110.143685.

Supplemental Data

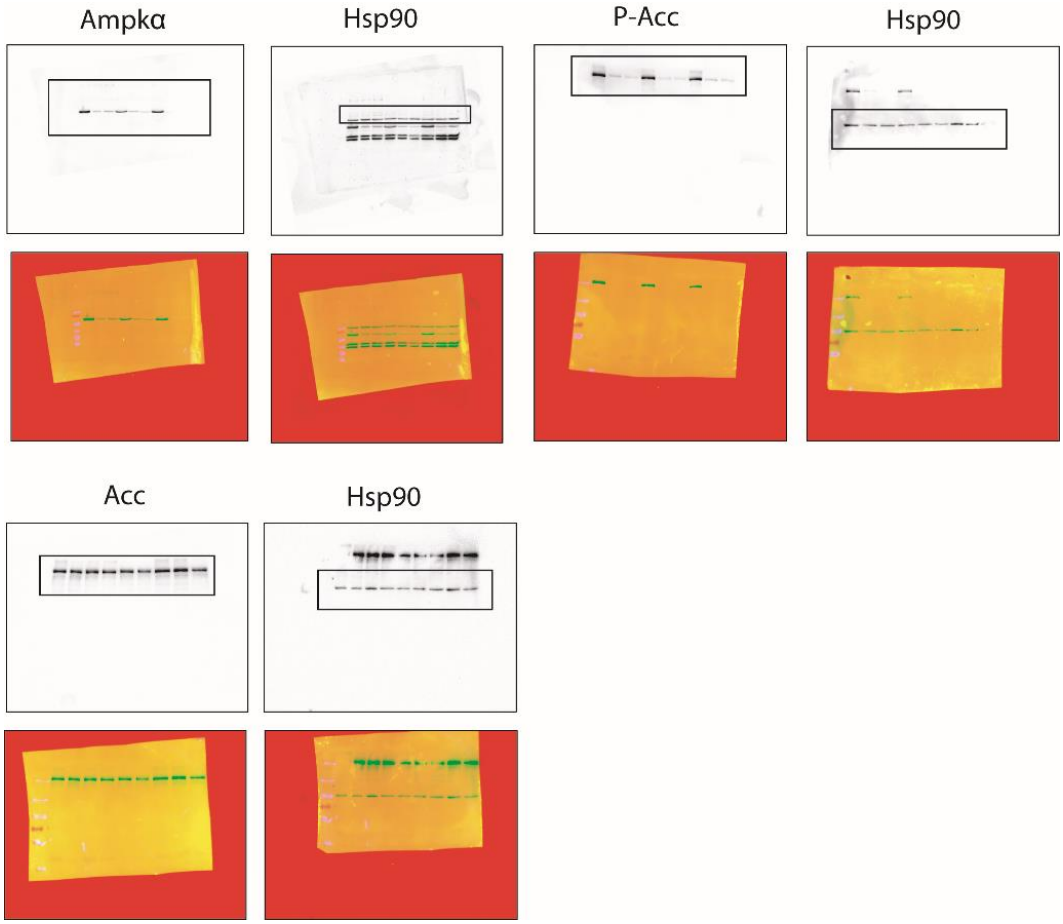

Figure 36 | Raw Western blots of murine 8570 *Prkaa1* KO cell lines. Raw Western blots of AMPK pathway in control (LacZ) and *Prkaa1* KO (KO1, KO2) cells. Three biological replicates are shown. AMPK pathway was investigated using AMPKα, P-ACC, and ACC antibodies. HSP90 was used as a loading control. ACC: Acetyl-CoA carboxylase, HSP90: Heat shock protein 90, P-: Phosphorylation.

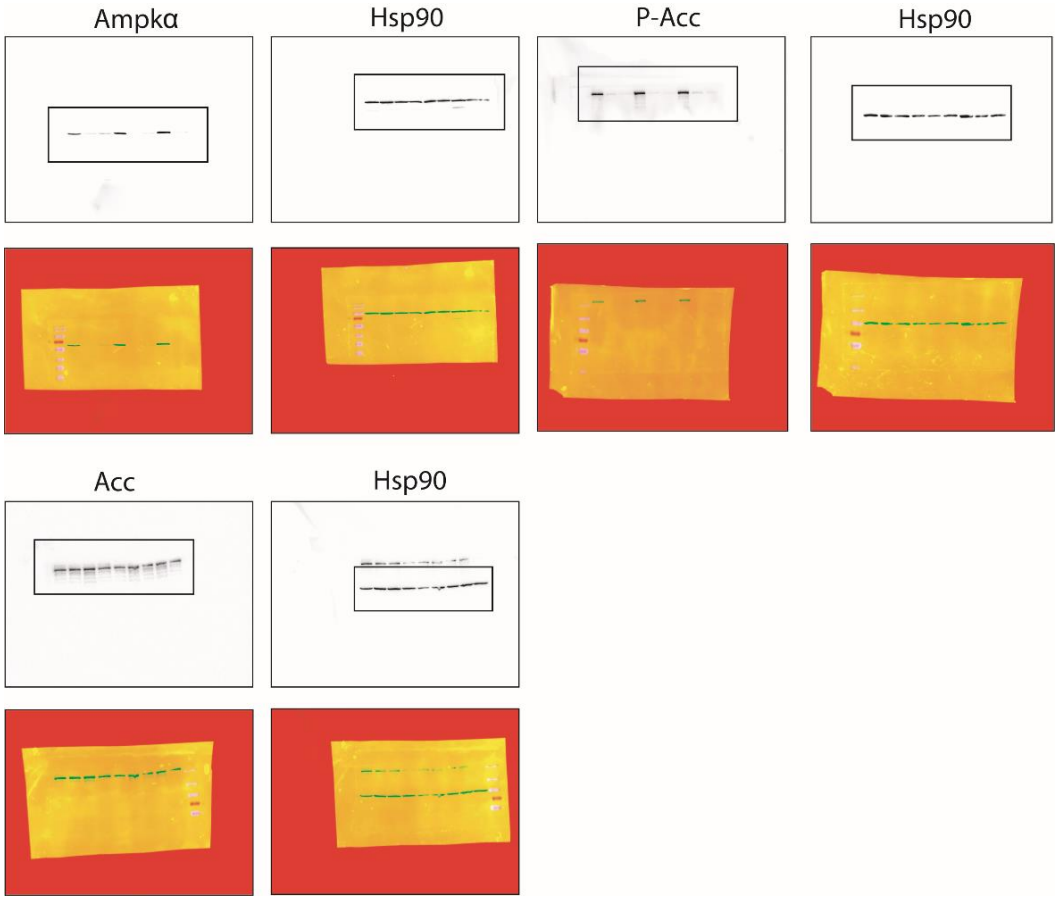

Figure 37 | Raw Western blots of murine 8248 *Prkaa1* KO cell lines. Raw Western blots of AMPK pathway in control (LacZ) and Prkaa1 KO (KO1, KO2) cells. Three biological replicates are shown. AMPK pathway was investigated using AMPKα, P-ACC, and ACC antibodies. HSP90 was used as a loading control. ACC: Acetyl-CoA carboxylase, HSP90: Heat shock protein 90, P-: Phosphorylation.

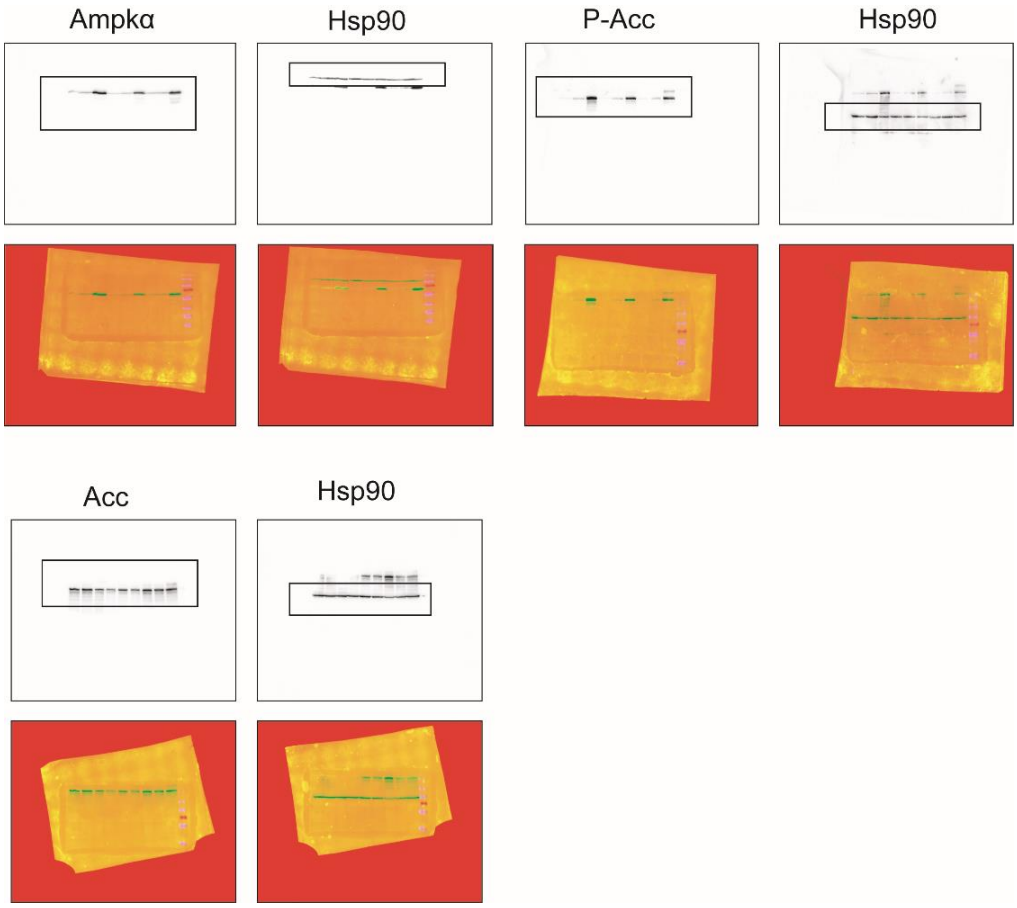

Figure 38 | Raw Western blots of murine 9091 *Prkaa1* KO cell lines. Raw Western blots of AMPK pathway in control (LacZ) and *Prkaa1* KO (KO1, KO2) cells. Three biological replicates are shown. AMPK pathway was investigated using AMPKα, P-ACC, and ACC antibodies. HSP90 was used as a loading control. ACC: Acetyl-CoA carboxylase, HSP90: Heat shock protein 90, P-: Phosphorylation.

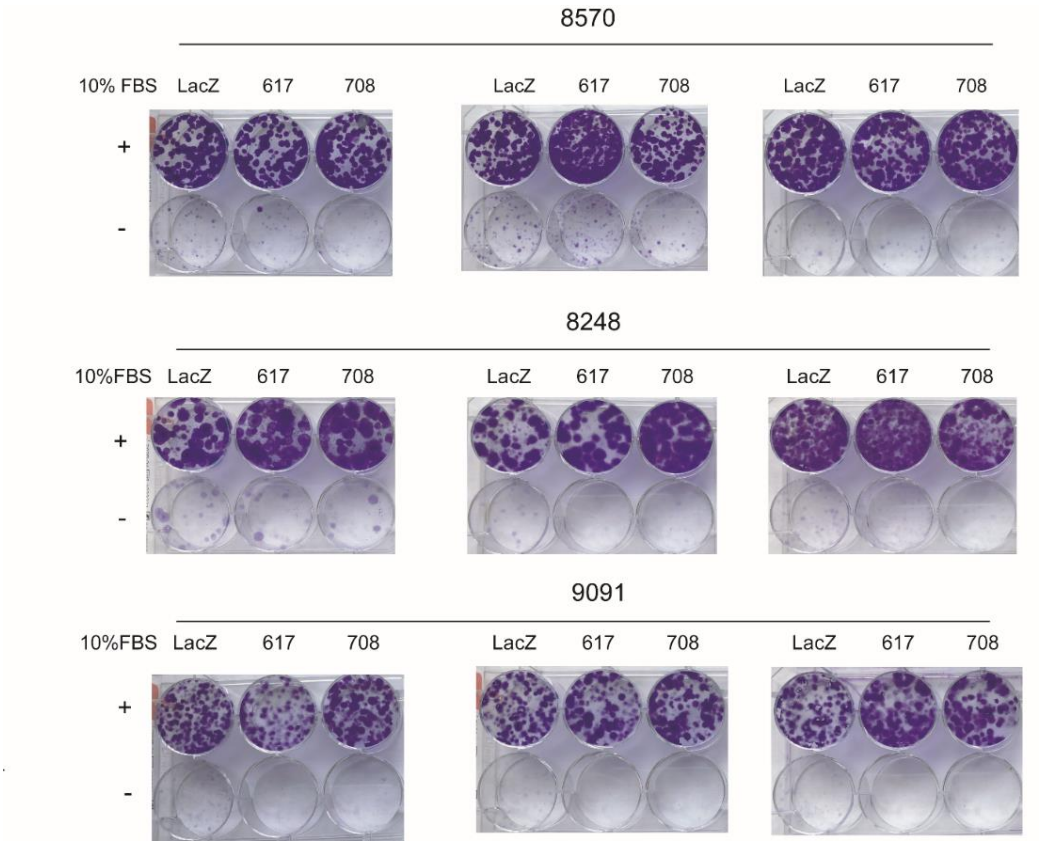

Figure 39 | Clonogenic assays of murine LacZ and *Prkaa1* KO cells under growth factor depletion. Clonogenic assay of LacZ, KO1, and KO2 of 8248, 8570, and 9091 cells in the presence of 10% or 1% FBS for 10 days. Experiments were performed as three biological replicates.

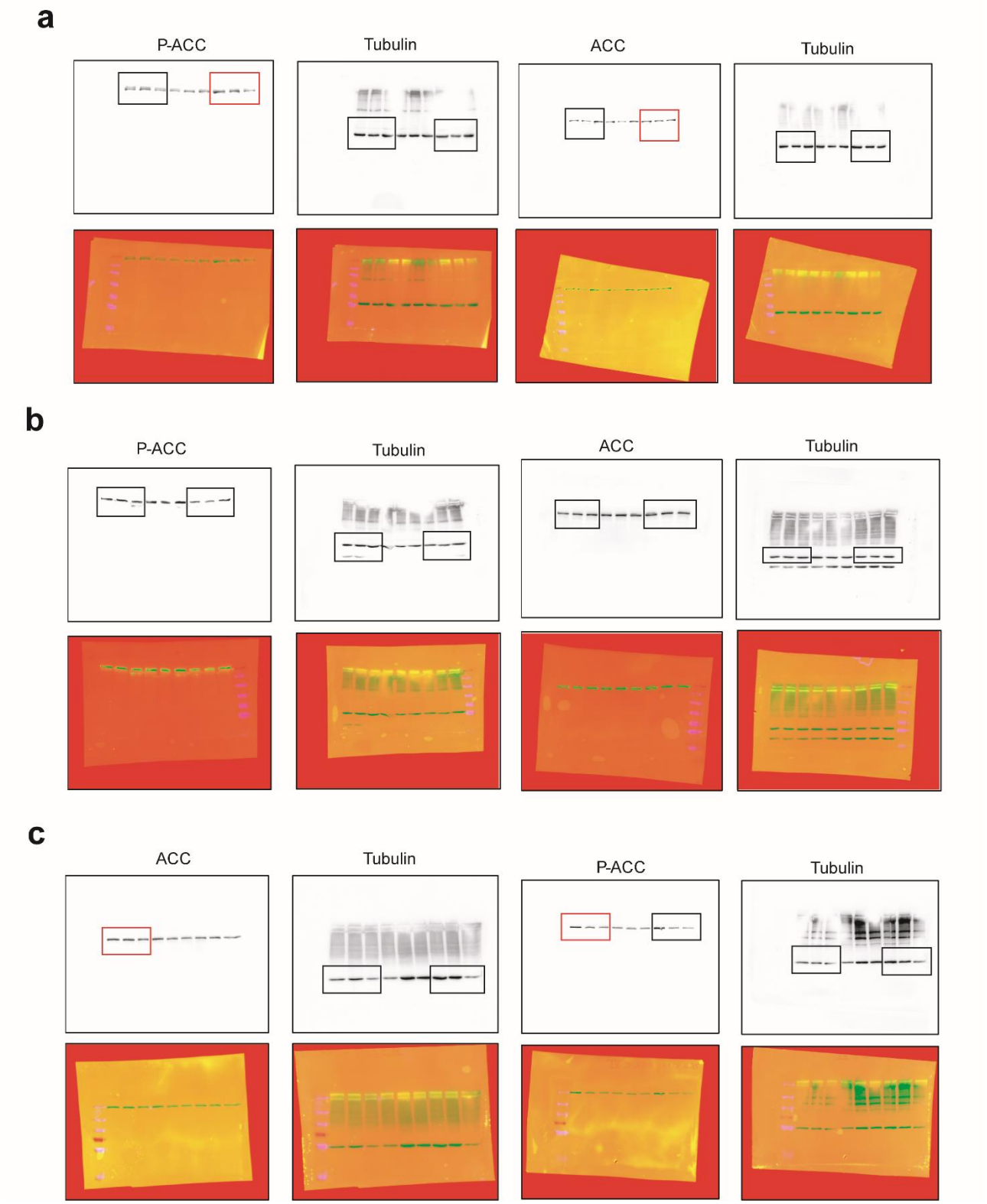

Figure 40 | Raw Western blots of AMPK signaling upon PF-3758309 treatment. Western blots of **a,** replicate 1 **b,** replicate 2 **c,** replicate 3 of AMPK signaling upon PF-3758309 treatment. Cells were treated with 10 or 20 nM of PF-3758309 or left as vehicle-treated controls. Protein was harvested after 1 and 6. AMPK inhibition was investigated by P-ACC and ACC antibodies. P-ACC was normalized to ACC. HSP90 served as loading control. Experiments were performed as three biological replicates. Boxes indicate bands which were used for

quantification. Red boxes indicate bands which were choosen for result section. ACC: Acetyl-CoA carboxylase, HSP90: Heat shock protein 90, P-: Phosphorylation.

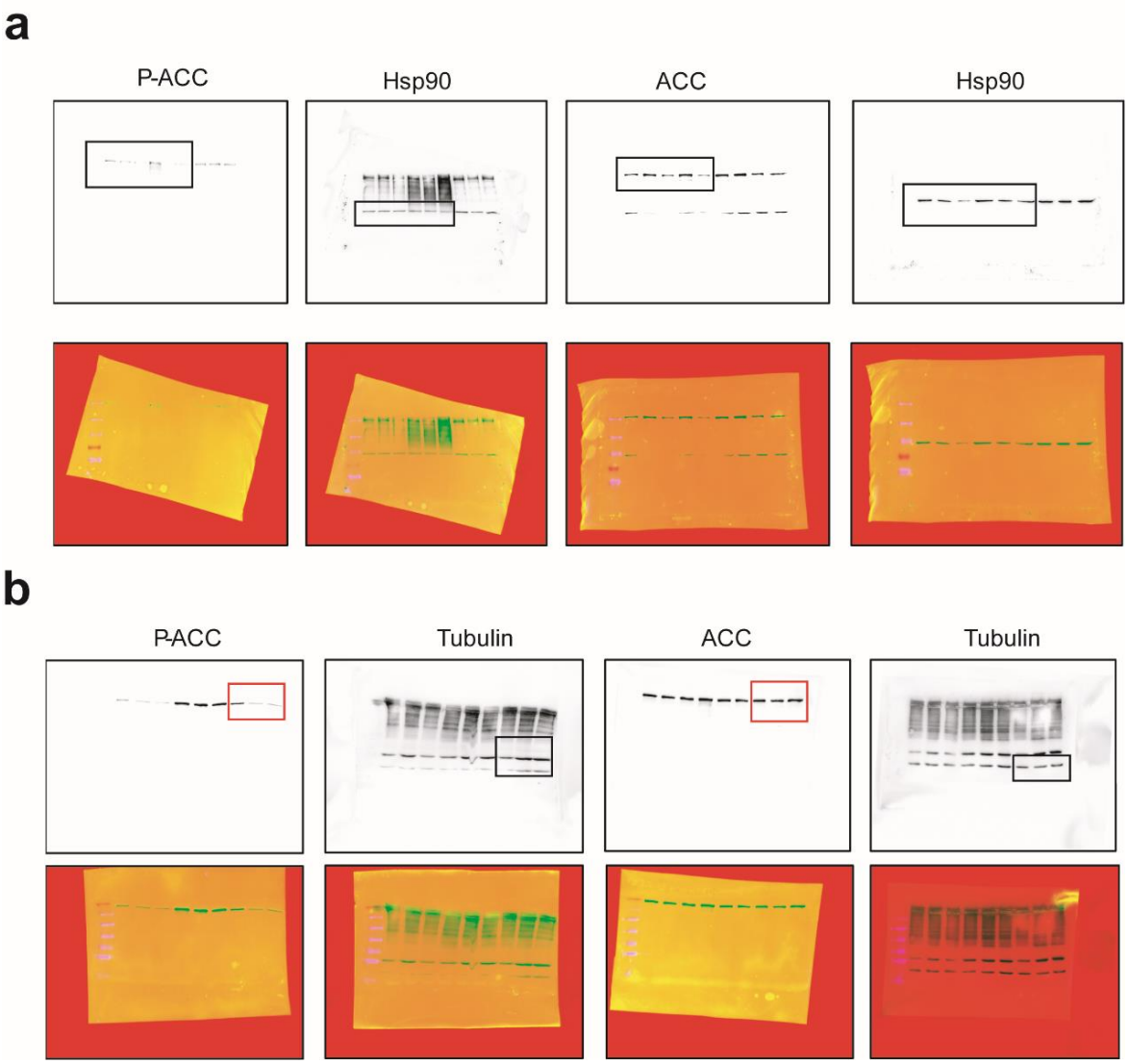

Figure 41 | Raw Western blots of AMPK signaling upon PF-3758309 treatment. Western blots of **a,** replicate 1 and replicate 2 and **b,** replicate 3 of AMPK signaling upon PF-3758309 treatment. Cells were treated with 10 or 20 nM of PF-3758309 or left as vehicle-treated controls. Protein was harvested after 24 hours. AMPK inhibition was investigated by P-ACC and ACC antibodies. P-ACC was normalized to ACC. HSP90 served as loading control. Experiments were performed as three biological replicates. Boxes indicate bands which were used for quantification. Red boxes indicate bands which were choosen for result section. ACC: Acetyl-CoA carboxylase, HSP90: Heat shock protein 90, P-: Phosphorylation.

Table 21 | List of kinase protein structures downloaded from the Protein Databank as well as Glide redocking results for selected kinases. Details for AMPKα, PAK4 and CDK7 are listed. RMSD: Root Mean Square Deviation.

PDB ID	Deposite Date	Resolution Å	RMSD redocking Å
AMPKα			
2H6D	2006-05-31	1.85	
2OOX	2007-01-26	2.60	
2OOY	2007-01-26	2.88	
2QR1	2007-07-27	2.70	
2QRC	2007-07-28	2.70	
2QRD	2007-07-28	2.41	
2QRE	2007-07-28	3.01	
2V92	2007-08-20	2.40	
2V9J	2007-08-23	2.53	
2Y8L	2011-02-07	2.50	
2Y8Q	2011-02-09	2.80	
2YA3	2011-02-17	2-50	
2YA3	2011-02-17	2.50	
2YZA	2007-05-04	3.02	
3AQV	2010-11-19	2.08	
4CFE	2013-11-14	3.02	
4CFF	2013-11-14	3.92	
4CFH	2013-11-18	3.24	
4EAG	2012-03-22	2.70	
4EAI	2012-03-22	2.29	
4EAJ	2012-03-22	2.61	
4EAK	2012-03-22	2.50	
4EAL	2012-03-22	2.51	
4QFG	2014-05-20	3.46	
4QFR	2014-05-21	3.34	
4QFS	2014-05-21	3.55	
4RER	2014-09-23	4.05	0.293
4REW	2014-09-24	4.58	
4ZHX	2015-04-27	2.99	
5EZV	2015-11-26	2.99	
5ISO	2016-03-15	2.63	

5KQ5	2016-07-05	3.41	
5T5T	2016-08-31	3.46	
5UFU	2017-01-05	3.45	
6B1U	2017-09-19	2.77	
6B2E	2017-09-19	3.80	
6BX6	2017-12-17	2.90	
6C9F	2018-01-26	2.92	0.505
6C9H	2018-01-26	2.65	0.316
6C9J	2018-01-26	3.05	
6E4T	2018-07-18	3.40	
6E4U	2018-07-18	3.27	
6E4W	2018-07-18	3.35	
7JHG	2020-07-20	3.47	
7JHH	2020-07-20	3.92	
7JIJ	2020-07-23	5.50	
7M74	2021-03-26	3.93	
7MYJ	2021-05-21	2.95	
PAK4			
2X4Z	2010-02-03	2.10	0.441
CDK7			
7B5O	2020-12-05	2.50	0.560
7B5Q	2020-12-05	2.50	1.167

Table 22 | IC50 and AUC of drug screen in 8570 *Prkaa1* KO cells. 8570 LacZ, KO1, and KO2 cells were treated with a drug library containing 119 compounds with a 7-fold dilution under clinical testing. After 72 hours, cell viability was measured and dose-response curves were generated by applying the GRmetrics package. AUC, area under the curve, IC50: inhibitory concentration 50.

agent	**8570 LacZ**		**8570 KO1**		**8570 KO2**	
	IC50 [µM]	AUC	IC50 [µM]	AUC	IC50 [µM]	AUC
Abexinostat (PCI-24781)	0.2581	0.4741	x	0.4886	0.2377	0.4814
Adavoserti b	0.2014	0.4301	0.1846	0.4366	0.1093	0.4067
AZ 628	0.7834	0.6563	3.3340	0.8681	4.2907	0.7707
AZ191	2.1202	0.7787	2.5905	0.8818	3.3958	0.8210

AZD1480	4.4915	0.9061	4.4561	0.8444	5.5812	0.8511
AZD7762	0.3618	0.5348	0.6956	0.6015	0.6070	0.6159
BAY-876	0.1083	0.5548	0.4355	0.5060	1.4288	0.7229
BAY 11-7082	1.5921	0.6873	3.4104	0.8217	0.8380	0.5909
BSJ-4-116	0.7489	0.6437	0.2554	0.4506	0.3287	0.4955
CB-839	0.0142	0.1351	0.0134	0.1276	0.0170	0.1408
CCF642	0.9272	0.6179	1.1399	0.7442	1.1316	0.7058
Cobimetinib	0.0405	0.3393	x	0.3171	0.0420	0.3089
Colchicine	0.0191	0.1897	0.0192	0.1759	0.0172	0.1765
Crizotinib (PF-02341066)	0.6885	0.5909	0.6983	0.6334	0.5208	0.5535
Danusertib (PHA-739358)	0.8026	0.6405	1.2440	0.6590	0.8895	0.6927
Dasatinib hydrochloride	0.5277	0.6085	0.1849	0.5911	0.1263	0.4715
Deguelin	0.0667	0.3475	0.1666	0.4848	0.2012	0.4886
Dinaciclib (SCH727965)	0.0589	0.2623	0.0599	0.2551	0.0364	0.2093
Erastin	0.7062	0.5593	0.4582	0.5889	0.4415	0.5603
Etoposide	Inf	0.6980	0.2595	0.4436	0.2342	0.4559
Fluorouracil (5-Fluoracil, 5-FU)	1.8668	0.7383	0.9242	0.6428	1.6894	0.7542
Fluvastatin Sodium	1.0809	0.6729	1.8577	0.7804	1.8146	0.8156
Gemcitabine	0.0179	0.1227	0.0288	0.1559	0.0238	0.1294
GMX1778 (CHS828)	0.1633	0.4905	0.2023	0.4327	0.2222	0.4954
GSK461364	0.0124	0.1444	#NAME?	0.1338	0.0142	0.1627
HTH-01-015	4.8087	0.8935	3.8014	0.9082	2.3728	0.7740
Imidazole Ketone Erastin	1.0842	0.6631	0.7350	0.5937	0.7222	0.6595
Indisulam	Inf	0.8847	3.5988	0.7675	4.0717	0.7905

Irinotecan HCl Trihydrate	4.3659	0.8402	3.9270	0.8247	2.1174	0.7914
Ixazomib Citrate (MLN9708)	0.0550	0.2773	0.0804	0.3227	0.0899	0.3476
JIB-04	0.1340	0.3662	0.1213	0.3729	0.1267	0.3566
KX2-391	0.0227	0.1813	0.0237	0.1850	0.0188	0.1722
Lys05	1.1159	0.7098	0.9835	0.5983	1.2060	0.6405
Masitinib (AB1010)	5.7493	0.9327	6.1795	0.9400	4.1843	0.8427
MI-2 (MALT1 inhibitor)	1.2764	0.6963	1.6077	0.6793	2.5144	0.7931
MI-503	4.2727	0.9205	1.0789	0.6883	2.6034	0.7206
Mubritinib (TAK 165)	0.3606	0.5625	0.2784	0.5100	0.1028	0.3973
Napabucasin	0.9710	0.6536	0.5475	0.6519	1.2776	0.7191
Nintedanib Ethanesulfonate Salt	4.5623	0.8537	3.0121	0.8449	2.4084	0.7792
NMS-873	0.1981	0.4418	0.4497	0.5140	0.3436	0.4917
OF-1	4.8161	0.8604	4.6441	0.8747	5.0286	0.8838
Onalespib (AT13387)	0.0640	0.2788	0.0559	0.2602	0.0364	0.2017
Onametostat (JNJ-64619178)	0.6583	0.6106	1.1688	0.6474	Inf	0.5673
OTX015	0.0999	0.4097	0.1511	0.4860	0.0848	0.3915
Paclitaxel	0.0181	0.1655	0.0194	0.1714	0.0159	0.1692
Panobinostat (LBH589)	0.0147	0.1388	0.0104	0.1206	0.0099	0.1093
Pevonedistat (MLN4924)	2.8629	0.7942	2.9410	0.7717	1.9883	0.7385
PF-3758309	0.0269	0.2404	0.0109	0.2018	0.0247	0.2387
Plinabulin (NPI-2358)	0.0209	0.1484	0.0216	0.1816	0.0211	0.1594
Ponatinib (AP24534)	0.8722	0.5946	0.7370	0.6946	0.7045	0.6665
Rabusertib (LY2603618)	1.5161	0.8092	1.5819	0.8176	1.2488	0.7270

Rigosertib (ON-01910)	0.1335	0.4009	0.4698	0.5573	0.3364	0.5265
RO5126766 (CH5126766)	0.4844	0.5592	0.0828	0.5067	0.2343	0.5155
RSL3	0.3369	0.4866	0.3588	0.5196	0.2454	0.5887
Sabutoclax	1.4474	0.7089	0.8684	0.6182	0.6322	0.5829
Sapanisertib (INK 128, MLN0128)	0.0233	0.2334	0.0188	0.2395	0.0283	0.2178
SP2509	0.3793	0.4749	0.1467	0.3892	0.3115	0.4905
STF-31	Inf	0.7863	0.6170	0.5940	1.4182	0.6864
Subasumstat (TAK-981)	0.2760	0.5377	0.2397	0.4943	0.1938	0.4789
Tozasertib (VX-680, MK-0457)	0.1119	0.4494	0.0946	0.4187	0.0544	0.3359
VLX1570	0.1871	0.3899	0.0576	0.3150	0.0483	0.2404
Volasertib (BI 6727)	0.0318	0.2152	0.0361	0.2352	0.0361	0.2260

Table 23 | IC50 and AUC of drug screen in *Prkaa1* overexpressing cell lines. Empty and *Prkaa1* overexpressing cell lines of 8182 and 9091 were treated with a drug library containing 118 compounds with a 7-fold dilution under clinical testing. After 72 hours, cell viability was measured and dose-response curves were generated by applying the GRmetrics package. AUC, area under the curve, IC50: inhibitory concentration 50.

agent	8182 empty		8182 *Prkaa1*		9091 empty		9091 *Prkaa1*	
	IC50 [µM]	AUC	IC50 [µM]	AUC	IC50 [µM]	AUC	IC50 [µM]	AUC
4EGI-1	Inf	0.9087	Inf	0.9765	Inf	0.9651	47.4372	0.9319
A-1210477	Inf	0.9921	Inf	0.8768	Inf	0.9911	Inf	0.9774
A1874	1.3400	0.6909	1.6566	0.7681	1.9627	0.7676	2.4145	0.8036
A-196	Inf	0.9652	Inf	0.8802	Inf	0.9419	Inf	0.9916
Abexinostat (PCI-24781)	0.3537	0.5214	0.6299	0.6935	0.2796	0.4700	0.3427	0.4861
Adavosertib MK-1775	0.2012	0.5047	0.1207	0.4285	0.2585	0.4917	0.4259	0.5420
Alisertib (MLN8237)	0.5245	0.6920	1.1055	0.7415	0.4570	0.6298	0.4801	0.6524
Alpelisib (BYL719)	2.9294	0.7518	1.8004	0.7270	11.9574	0.8295	22.9783	0.8565
apx 2009 100mM	0.4142	0.4998	0.5968	0.5970	0.4638	0.5279	0.5948	0.5588
Azacitidine	5.5982	0.8641	2.8018	0.7903	8.3128	0.9057	8.4602	0.8611
AZD	0.4311	0.5309	0.6669	0.5995	0.5618	0.5587	Inf	0.7768
AZD1208	Inf	0.8841	Inf	0.8519	Inf	0.9561	Inf	0.9196
AZD5153	0.1175	0.4052	0.0897	0.4020	0.0913	0.3869	0.0909	0.4234
AZD6738	1.0468	0.7016	0.7992	0.6207	1.8808	0.7374	3.4821	0.8079
AZD7762	0.4308	0.5438	0.3954	0.5477	0.6474	0.6336	1.3211	0.6831
BAY-876	0.0312	0.2175	0.0168	0.2046	0.1009	0.3416	0.1998	0.4291
BI-3406	Inf	0.9546	Inf	1.0696	Inf	0.9877	Inf	0.9651
BI-78D3	1.9200	0.7173	1.7721	0.6851	2.0873	0.7421	2.4169	0.7698

BI-847325	0.0604	0.2697	0.0556	0.2789	0.1085	0.3878	0.1982	0.4234
BI-D1870	5.6013	0.8264	4.1905	0.8262	0.6438	0.7345	1.4389	0.7625
Birinapant	Inf	1.0005	Inf	1.1468	Inf	0.9114	Inf	0.9277
BRD4770	Inf	1.0244	Inf	0.9573	Inf	0.9793	Inf	0.9816
BX-795	1.3498	0.7197	2.8435	0.9187	1.8699	0.7329	1.8433	0.7391
BX-912	5.6372	0.8405	8.4807	0.8936	7.5122	0.8960	8.3726	0.9048
Carfilzomib (PR-171)	0.0121	0.0404	x	0.0137	0.0390	0.1635	0.0494	0.1955
CB-839	0.0147	0.1659	0.0200	0.1863	0.0223	0.1587	0.0192	0.1414
Chloroquin	2.1918	0.8089	2.5508	0.7815	6.3516	0.9066	Inf	1.0014
COH000	1.3640	0.6500	1.0221	0.6062	1.5786	0.7056	2.1194	0.7642
CPI-455 HCl	Inf	0.9793	Inf	1.0133	Inf	0.9505	Inf	0.9809
Crenigacestat (LY3039478)	Inf	0.7799	Inf	0.9938	Inf	0.8858	Inf	0.8467
CUDC-101	2.9208	0.8395	3.3925	0.9211	1.5468	0.7374	1.4417	0.7009
CW069	Inf	0.9467	Inf	0.9532	Inf	0.9849	Inf	0.9803
Danusertib	4.1106	0.7910	5.1209	0.7934	2.4493	0.7889	Inf	0.8887
EED226	Inf	1.0069	Inf	1.0288	Inf	0.9771	Inf	0.9722
Elesclomol (STA-4783)	0.0329	0.1728	0.0302	0.1539	0.0329	0.1510	0.0374	0.1739
Entrectinib (RXDX-101)	1.5359	0.7118	1.5359	0.7417	2.3698	0.7577	3.3397	0.8106
Enzastaurin (LY317615)	14.3621	0.9225	Inf	0.9143	Inf	0.9690	Inf	0.9688
EOAI3402143	0.4659	0.5301	0.5185	0.5368	0.5520	0.5609	0.6134	0.5762
Epacadostat	Inf	1.0359	Inf	0.9694	Inf	1.0213	Inf	0.9918

(INCB024360)								
Erastin	1.2390	0.7216	1.9312	0.7631	0.4030	0.5235	0.4837	0.5460
Erdafitinib (JNJ-42756493)	5.0656	0.8830	3.3696	0.8156	4.1708	0.8227	4.1836	0.8240
FT113	Inf	0.9472	Inf	1.1242	62.2237	0.9430	77.4247	0.9118
Galunisertib (LY2157299)	Inf	0.8661	872.7859	0.8327	Inf	0.9145	Inf	0.9347
GDC	1.4828	0.6908	0.8154	0.6248	2.9689	0.7483	2.6142	0.4959
GSK2837808A	Inf	0.9082	Inf	1.0107	Inf	0.9426	Inf	0.9726
GSK J1	Inf	0.9631	Inf	0.9147	Inf	0.9761	210.0514	0.9473
GSK2656157	6.3363	0.9080	Inf	0.9199	10.9436	0.9482	Inf	0.9228
GSK2830371	Inf	0.8753	Inf	0.8842	Inf	0.9194	Inf	0.9407
GSK467	Inf	0.9530	Inf	0.9192	Inf	0.9711	Inf	0.9862
GSK503	4.3153	0.8272	6.7525	0.9739	12.5746	0.9207	14.8525	0.9324
GSK591	Inf	0.8611	Inf	0.8663	Inf	0.8277	195.6005	0.8226
HTH-01-015	2.9841	0.8146	3.5415	0.8916	9.3389	0.9524	7.2990	0.8685
HTH-02-006	2.1200	0.7384	3.4680	0.8659	2.1454	0.7445	Inf	0.9170
IACS	0.0372	0.2112	0.1074	0.3182	0.0514	0.2379	1.7639	0.5674
IM156	1.4354	0.7399	1.0510	0.6387	1.7218	0.7344	1.6598	0.7630
Indirubin	90.9059	0.8945	Inf	0.8978	Inf	0.9014	Inf	0.8332
Ispinesib (SB-715992)	x	0.2732	x	0.1985	x	0.3188	x	0.3568
JIB-04	0.1326	0.3749	0.2386	0.4261	0.1088	0.3549	0.1644	0.3908
JNJ1 1mM	Inf	0.8319	13.7297	0.8232	Inf	0.8025	Inf	0.8197
JNJ-64619178	0.1787	0.3988	0.2840	0.4468	0.3365	0.4705	0.4118	0.4945
KU-60019	4.7490	0.8418	4.9551	0.9772	10.7098	0.9526	11.4297	0.9263
Lapatinib (GW-572016)	2.5593	0.7586	Inf	0.7881	6.4590	0.9070	5.7569	0.8837

Ditosylate								
LB100	Inf	1.0009	Inf	0.9316	5.3167	0.8579	51.8014	0.9183
Linsitinib (OSI-906)	6.6548	0.8700	Inf	0.7646	74.8229	0.8739	81.4272	0.9108
LJH685	Inf	0.9416	Inf	1.0655	Inf	0.9672	Inf	0.8588
LLY-507	1.4133	0.7117	1.2179	0.6777	2.7248	0.8039	1.9984	0.7380
Luminespib (AUY-922, NVP-AUY922)	0.0147	0.0779	0.0313	0.1612	0.0228	0.1249	0.0347	0.1893
MI-463	0.5393	0.5440	0.7822	0.5890	3.9545	0.7953	3.3330	0.7951
Milciclib (PHA-848125)	0.4220	0.5262	0.7267	0.6018	0.3976	0.5145	0.6788	0.5697
MK-2206 2HCl	2.4174	0.7632	1.3994	0.6891	5.7342	0.8499	7.9917	0.8382
ml093 10mM	0.3955	0.5933	0.1021	0.3597	0.6597	0.7022	0.6821	0.6906
ML264	Inf	0.7144	14.3171	0.9229	Inf	0.9029	Inf	0.9654
ML324	5.5299	0.8853	7.4989	0.9258	5.0879	0.8549	5.8379	0.8707
MX69	Inf	0.9518	Inf	1.0452	Inf	0.9707	Inf	0.9506
MYCi975	6.4864	0.8752	5.3136	0.8619	6.0239	0.8942	6.2442	0.9122
Napabucasin	1.0140	0.6456	0.8703	0.6281	0.8959	0.6275	1.1326	0.6728
NMS-873	0.1358	0.3733	0.1292	0.3337	0.3296	0.4955	0.2387	0.4317
None1	Inf	1.0737	Inf	0.9935	Inf	0.9052	Inf	0.9299
None2	Inf	0.9556	Inf	0.9678	Inf	0.9709	Inf	1.0113
None3	Inf	0.9339	Inf	0.9093	Inf	0.9545	Inf	0.9807
None4	Inf	1.0132	Inf	1.0197	Inf	0.9875	Inf	0.9753
None5	Inf	0.9747	Inf	0.9013	Inf	1.0046	Inf	1.0168
NSC87877	Inf	0.9367	Inf	1.0156	Inf	0.9938	Inf	0.9387
NVP-CGM097	4.0486	0.8240	4.3254	0.8682	5.1146	0.8214	4.7516	0.8078
Orantinib (TSU-68,	348.9172	0.8546	Inf	0.9448	Inf	0.9292	Inf	0.9422

SU6668)								
OTX015	0.8216	0.6710	0.7006	0.6450	0.6768	0.6636	0.7883	0.6498
P22077	11.5618	0.9407	Inf	0.9716	10.7473	1.0100	20.2984	0.9677
Pelitinib (EKB-569)	0.4454	0.5677	0.3957	0.5184	2.0318	0.7689	1.4134	0.6940
Pevonedistat (MLN4924)	0.4448	0.5750	0.3680	0.5155	0.4617	0.5648	0.6030	0.5909
PF-3758309	0.0169	0.2633	0.0896	0.3686	0.0164	0.2496	204.6274	0.6719
Phenformin	Inf	0.8428	Inf	0.8635	Inf	0.7644	Inf	0.8827
Poziotinib (HM781-36B)	2.4288	0.7313	1.0475	0.6066	11.2499	0.8500	16.7697	0.9021
Pracinostat (SB939)	0.7259	0.6606	0.7209	0.6493	0.4341	0.5383	0.5510	0.5540
PRT4165	30.3145	0.9050	Inf	1.1841	432.3617	0.9630	Inf	0.9682
PTC-209 HBr	0.3355	0.5270	1.1673	0.6478	0.5881	0.6094	0.4295	0.5733
PX-478 2HCl	Inf	0.9433	Inf	0.9153	Inf	0.9694	198.0158	0.9443
RI-1	Inf	0.9547	Inf	1.0706	Inf	1.0306	170.6847	0.9380
Rigosertib (ON-01910)	0.3205	0.4924	0.5686	0.6287	0.4959	0.6138	0.4869	0.6511
RO5126766 (CH5126766)	2.0797	0.7493	2.0578	0.7509	Inf	0.8654	Inf	0.9513
Ruxolitinib	Inf	0.9180	Inf	1.0230	Inf	1.0000	13.5482	0.9815
Sapanisertib (INK 128, MLN0128)	0.0888	0.3429	0.0659	0.3433	0.0651	0.3037	0.0603	0.3036
Saracatinib (AZD0530)	0.6877	0.6330	0.9597	0.6832	2.3570	0.7724	2.8379	0.7928

Selisistat (EX 527)	Inf	0.9594	Inf	1.0180	Inf	0.9785	Inf	1.0028
SF1670	1.2675	0.6723	1.4760	0.7479	1.0772	0.6729	1.2119	0.6860
SGC707	Inf	0.9345	Inf	0.9828	Inf	1.0073	Inf	0.9702
STF-083010	Inf	0.9872	Inf	1.0670	Inf	1.0112	Inf	0.9931
TAK-243	0.5491	0.6237	0.5243	0.5889	0.1935	0.3958	0.1649	0.3895
Tak981 10mM	0.6814	0.6975	0.2228	0.4453	1.3547	0.7759	3.0940	0.8047
Thiomyristoyl	9.4823	0.9566	Inf	0.9970	Inf	0.9487	9.6771	0.9356
Trametinib (GSK1120212)	0.0297	0.2183	0.0526	0.2443	0.4733	0.6141	0.9255	0.6514
Ulixertinib (BVD-523, VRT752271)	1.6147	0.7010	3.3157	0.8365	Inf	0.9228	12.2969	0.8607
UNC0379	3.3948	0.8321	2.1063	0.7467	6.5939	0.9294	8.1968	0.9747
UNC0638	1.1740	0.7149	1.1027	0.6580	4.3448	0.8294	3.9114	0.8353
UNC1999	2.8090	0.7728	4.6546	0.8638	5.8555	0.9170	8.0430	0.9359
USP2528 inhibitor AZ1	4.6715	0.9044	3.2847	0.8209	5.6504	0.8776	7.6302	0.9402
Veliparib (ABT-888)	31.7519	0.9185	Inf	0.9290	44.6236	0.8906	126.9987	0.9260
WZ4003	3.5574	0.7729	4.4702	0.8336	7.1751	0.8799	7.1854	0.8976